Università di Roma "Sapienza"

Facoltà di Scienze Matematiche, Fisiche e Naturali

Scuola di Dottorato Vito Volterra

Dottorato in Astronomia

Low Frequency Noise Suppression for the Development of Gravitational Astronomy

Author:

Luca Naticchioni

Supervisor:

Prof. Fulvio Ricci

Coordinator:

Prof. Roberto Capuzzo Dolcetta

XXVI ciclo 2010/2013

A.A. 2012/2013

Table of Contents

Introduzione

L'esistenza delle onde gravitazionali, prevista dalla teoria della Relatività generale, fu dimostrata indirettamente per la prima volta grazie all'osservazione del decadimento orbitale della pulsar binaria PSR 1913+16, per la cui scoperta R.A. Hulse e J.H. Taylor furono insigniti del premio Nobel nel 1993. A partire da questa prima evidenza osservativa, la ricerca di una rivelazione diretta delle onde gravitazionali è divenuta negli anni uno dei principali temi della fisica sperimentale, non solo per la verifica della teoria in se, ma anche e soprattutto per la possibilità di aprire una nuova finestra astronomica sul nostro universo. Infatti molti oggetti astrofisici, come ad esempio stelle di neutroni e buchi neri, possono essere studiati direttamente solo attraverso la loro emissione gravitazionale. Inoltre, poichè l'interazione delle onde gravitazionali con la materia è molto debole, la degradazione delle informazioni da queste trasportate risulta trascurabile e la loro rivelazione ci permetterebbe di comprendere la struttura interna delle sorgenti massive che le emettono, fornendo un punto di vista complementare a quello dell'astronomia e della cosmologia tradizionali.

La rivelazione diretta deve affrontare l'estrema debolezza della radiazione gravitazionale, di conseguenza è necessario disporre di rivelatori caratterizzati da un'altissima sensibilità per essere in grado di osservare l'effetto quadripolare prodotto dal passaggio di un'onda gravitazionale. I primi tentativi in questo campo sfruttavano massicce barre risonanti e si basavano sulla tecnica sviluppata da J. Weber. Negli ultimi decenni è stata adottata una strategia più promettente basata sull'interferometria, che fornisce il vantaggio di avere rivelatori caratterizzati da una larga banda di osservazione (da pochi Hz ad alcuni kHz) unitamente ad una estrema sensibilità (la deformazione rilevabile è inferiore alla dimensione di un protone). La rete globale di rivelatori interferometrici di prima generazione, composta da Virgo, LIGO, GEO600 e TAMA300, ha dimostrato la fattibilità di questa tecnica; in particolare i rivelatori su scala kilometrica Virgo e LIGO hanno raggiunto una sensibilità sufficientemente alta da porre i primi limiti superiori all'emissione gravitazionale di alcune stelle di neutroni note, come le pulsar del Granchio e della Vela. Nei prossimi anni entreranno in funzione le versioni potenziate di questi rivelatori, costituendo la cosiddetta seconda generazione di interferometri (Advanced Virgo e Advanced LIGO), con cui ci si aspetta di raggiungere una sensibilità tale da permettere le prime rivelazioni dirette di onde gravitazionali. Comunque, anche con questi rivelatori potenziati, il rapporto segnale-rumore sarebbe troppo basso per permettere di sviluppare una astronomia di precisione che possa essere complementare alle osservazioni nelle bande ottica, radio e dei raggi X nello studio dei sistemi e processi astrofisici. Per questa ragione la progettazione di una

nuova - terza - generazione di rivelatori interferometrici è già iniziata, e ha condotto alla proposta di un osservatorio europeo denominato Einstein Telescope (ET). Con una sensibilità considerevolmente migliorata questi nuovi rivelatori apriranno l'era dell'astronomia gravitazionale, contribuendo alla definizione di una completa *multimessenger astronomy*. In particolare, per allargare la banda di rivelazione nel range delle basse frequenze (fino a $\sim 1\ Hz$), dove sarebbe possibile rilevare molti segnali gravitazionali di interesse, come ad esempio quelli emessi da stelle di neutroni rotanti, è richiesta una ulteriore riduzione del rumore a bassa frequenza rispetto a quella che si avrà nei rivelatori di seconda generazione.

Nella banda delle basse frequenze la principale limitazione alla sensibilità dell'interferometro deriva dal rumore termico, e alle frequenze più basse, dai rumori sismico e newtoniano. La soppressione del rumore termico richiederà l'adozione di estesi apparati criogenici, in modo tale da raffreddare le masse di test a $T \sim 10\ K$, cosicché sarà anche necessario lo sviluppo di sensori di posizione di alta sensibilità, compatibili con la criogenia, per il controllo delle sospensioni e dei payload del rivelatore. L'attenuazione del rumore sismico è già stata ottenuta nella prima generazione di rivelatori per mezzo di lunghe catene di sospensione composte da oscillatori verticali e orizzontali (come ad esempio il superattenuatore di Virgo), cosicché per avere una ulteriore riduzione del rumore sismico sarà necessario individuare un sito con sismicità ambientale inferiore a quella tipica degli attuali rivelatori di superficie; inoltre, le fluttuazioni della densità di massa prodotte dalle perturbazioni sismiche inducono un gradiente gravitazionale variabile (definito rumore newtoniano) che cortocircuita l'intero filtro della sospensione e agisce direttamente sulle masse di test dell'interferometro. Per ridurre questi due rumori di natura sismica, la terza generazione di rivelatori sarà costruita in infrastrutture sotterranee, dove le onde superficiali di Rayleigh sono attenuate, e gli strati rocciosi circostanti sono più omogenei e stabili, riduendo così le fluttuazioni di densità di massa. La fattibilità di un interferometro criogenico e sotterraneo è già stata testata dal prototipo di rivelatore interferometrico giapponese CLIO, situato nello stesso sito dove è attualmente in costruzione KAGRA (precedentemente noto come LCGT), il primo interferometro su scala kilometrica basato su questi approcci. Per i suddetti aspetti, questo rivelatore di seconda generazione rappresenterà il precursore di quelli di terza generazione come ET, perciò è già iniziata una collaborazione scientifica tra i gruppi di ricerca impegnati nei due progetti.

Il mio lavoro sperimentale è focalizzato sulla soppressione dei suddetti rumori a bassa frequenza, di conseguenza questa tesi è strutturata in due paralleli campi di ricerca: la caratterizzazione sismica di un potenziale sito per la costruzione dell'Einstein Telescope, e lo sviluppo di un accelerometro verticale criogenico che possa essere usato come sensore inerziale di posizione, analogamente a quelli usati a temperatura ambiente nel superattenuatore di Virgo, ma anche per la misura delle vibrazioni introdotte dagli apparati criogenici, cosa che ho fatto con le misure svolte nei cristati di KAGRA e presentate nella conclusione di questa tesi.

Lo schema di questa tesi è suddiviso in tre parti principali: nella prima parte introduco i fondamenti dell'astronomia gravitazionale, dalla teoria dell'emissione gravitazionale e delle sorgenti astrofisiche agli esperimenti per l'osservazione gravitazionale diretta; nella seconda parte discuto i rumori a bassa frequenza e la loro

attenuazione a livello teorico; nella terza parte presento il lavoro sperimentale che ho svolto in questo contesto. Ogni parte è composta di due capitoli, strutturati come segue:

Nel *primo capitolo* descrivo la derivazione delle onde gravitazionali a partire dalle equazioni di campo di Einstein, discutendo le loro proprietà e le sorgenti astrofisiche e cosmologiche, specialmente quelle la cui emissione è localizzata a basse frequenze.

Nel *secondo capitolo* descrivo la rivelazione interferometrica diretta delle onde gravitazionali e le principali sorgenti di rumore che ne limitano la sensibilità, concludendo con una panoramica sui rivelatori presenti e futuri.

Nel *terzo capitolo* discuto le principali caratteristiche dei rumori sismico e newtoniano, e le strategie necessarie per la loro attenuazione, in particolare nei rivelatori di terza generazione.

Nel *quarto capitolo* discuto la teoria del rumore termico, dal caso ideale dell'oscillatore armonico smorzato al caso reale dei sistemi dissipativi meccanici e delle componenti ottiche di un interferometro.

Nel *quinto capitolo* presento il mio lavoro sperimentale svolto nell'ambito della caratterizzazione sismica su lungo periodo del sito di Sos Enattos in Sardegna (proposto per ospitare l'Einstein Telescope), dalla costruzione e installazione della strumentazione di una rete sotterranea di sensori all'analisi dei dati sismici e meteorologici raccolti nell'arco di un anno.

In conclusione, nel *sesto capitolo*, presento il mio lavoro sperimentale per lo sviluppo di un accelerometro verticale criogenico, dalla progettazione ai test e alle calibrazioni a temperature criogeniche ($T = 20\ K$). In questo capitolo presento anche i risultati ottenuti dall'installazione di questo sensore nei criostati che ospiteranno le masse di test di KAGRA, nelle quali ho verificato il corretto funzionamento del sensore anche a $T = 8\ K$ e ho misurato le vibrazioni dello schermo termico interno dei suddetti criostati. Queste misure hanno condotto ad una prima stima basata su risultati empirici del rumore vibrazionale aggiuntivo che sarà introdotto a livello delle masse di test dai refrigeratori criogenici.

Introduction

The existence of gravitational radiation, predicted by the General Relativity theory, was indirectly demonstrated by the observation of the orbital decay in the binary pulsar 1913+16, for which R.A. Hulse and J.H. Taylor were awarded with the Nobel Prize in 1993. From then on, the direct detection of gravitational waves became a main issue in the experimental physics, not only for the verification of the theory itself but, most important, because it can open a new "observation window" of the universe. In fact, many astronomical objects, such as neutron stars and black holes, can be directly studied only through their gravitational emission. Moreover, since its interaction with matter is intrinsically weak, the degradation of informations carried by gravitational waves is negligible, and their revelation will allow us to understand the internal structure of massive objects which emit them, and will also provide a complementary point of view to the traditional astronomy and cosmology.

The direct detection must face the extreme weakness of gravitational radiation, hence very high sensitive detectors are required in order to reveal the quadrupolar effect produced by the passage of gravitational waves. The first attempts in this field were based on massive resonant bars, relying on the pioneering technique developed by J. Weber. In recent decades a more promising strategy based on interferometry was developed, providing the advantage of a wide-frequency detection-band (from few Hz to some kHz) jointly to an extreme sensitivity (the detectable strain is smaller than the size of a proton). The global network of first generation interferometric detectors, composed of Virgo, LIGO, GEO600 and TAMA300, demonstrated the feasibility of such a technique; in particular the kilometric-scale detectors Virgo and LIGO achieved a sensitivity high enough to determine the first upper limits for the gravitational emission of some known neutron stars, such as the Crab and Vela pulsars. In the next few years the upgraded version of these detectors, namely the second generation of detectors (such as Advanced Virgo and Advanced LIGO) will become operational and are expected to achieve the first direct detections of gravitational waves. However, the signal-to-noise ratio (SNR) of these first detections will be too low for precise astronomical studies of the gravitational wave sources and for complementing optical, radio and X-ray observations in the study of fundamental systems and processes in the Universe. For this reason the investigation on the design of a new, namely third, generation of detectors is already started, leading to the proposal of the European Einstein Telescope (ET). With a considerably improved sensitivity these new machines will open the era of routine gravitational wave astronomy, leading to the birth of a complete multimessenger astronomy. In particular, to enlarge the detector bandwidth in the range

of 1 Hz, where interesting gravitational signals, such as those emitted by rotating neutron stars, can be detected, a further reduction of the so-called low-frequency noise, with respect to the second generation detectors, is required.

In this low-frequency band the main limitation to the sensitivity of an interferometric detector arises from the thermal noise, and at lower frequencies, from the seismic and Newtonian noises. The suppression of the thermal noise will require the implementation of a cryogenic apparatus, in order to cool the test masses down to $\sim 10\ K$, so that the development of position-control devices capable of cryogenic operations will be also necessary for the suspension and payload control. The seismic attenuation was already obtained in first generation detectors by means of long suspension chains of vertical and horizontal oscillators (e.g. the superattenuator of Virgo), so that a further reduction requires a smaller seismic noise at the input of the suspension system; moreover, mass density fluctuations produced by the seismic motion induce also a stochastic gravitational field (the so-called Newtonian or gravity-gradient noise) which shunts the suspension and couples directly to the mirrors of the interferometer. In order to suppress these two seismically-generated noises, third generation interferometers will be constructed in underground sites, where Rayleigh surface waves are attenuated, and the surrounding rock layers are more homogeneous and stable, reducing the density fluctuations. The feasibility of a cryogenic and underground interferometer was already tested by the Japanese prototype-detector CLIO, in the same site where is currently under construction KAGRA (formerly known as LGCT), the first full-scale interferometric detector based on these approaches. For these aspects, this second generation detector will be the forerunner of third generation interferometers such as ET, therefore a collaboration between the two scientific collaborations has been established.

My experimental work is focused on the suppression of these low noise sources, so that this thesis is structured in two parallel fields of research: the seismic characterization of a potential site for the construction of the Einstein Telescope, and the development, calibration and test of a cryogenic vertical accelerometer, which can be used as a position control device, analogously to those used in the actual room-temperature superattenuator of Virgo, but also to check the vibrations introduced by the cryogenic apparatus, as I did with the measurements I performed on the cryostats of KAGRA, presented at the end of this thesis.

The scheme of this thesis is subdivided in three main parts: in the first part I introduce the foundations of the gravitational astronomy, from the theory and the astrophysical sources to the experiments which will lead to the gravitational observations; in the second part I discuss the theory of low frequency noise sources and their suppression; in the third part I present the experimental work I performed in this context. Every part is composed of two chapters, structured as follows.

In the *first chapter* I describe the derivation of gravitational waves from the Einstein's field equations, discussing their properties and the astrophysical and cosmological sources, especially those whose emission is expected at low frequencies.

In the *second chapter* I describe the direct interferometric detection of gravitational waves and the main noise sources which limit the sensitivity, concluding with an overview of present and future detectors.

In the *third chapter* I discuss the main features of the seismic and Newtonian noises, and the strategies necessary to suppress them, especially in third generation detectors.

In the *fourth chapter* I discuss the theory of thermal noise, from the ideal case of the damped harmonic oscillator to the real dissipative mechanical systems and optical components of the interferometer.

In the *fifth chapter* I present my experimental work on the long-period characterization of the Sos Enattos site in Sardinia (proposed for hosting the Einstein Telescope), from the construction and instrumentation of an underground array of sensors to the analysis of seismic and meteorological data collected in one year of observations.

Finally, in the *sixth chapter* I present my experimental work on the development of a cryogenic vertical accelerometer, from the designing to the cryogenic calibration and tests at $T = 20\ K$. In this chapter I also present the results of the implementation of this device into the cryostats dedicated to the test masses of KAGRA, where I verified the operations of the accelerometer at $T = 8\ K$ and I measured the vibrations of the inner radiation shield of the cryostats. These measurements led to a first experimental estimate of the additional vibrational noise which will be injected by the cryogenic refrigerators to the detector test masses.

Part I

Gravitational Astronomy

Chapter 1

Gravitational Waves

In his famous publication dated 1916 Albert Einstein proposed the revolutionary theory of General Relativity [1] postulating that the gravitational field is described by the curvature of space and time merged together in a 4-dimensional manifold. Such a distortion is produced by its mass and energy content and determines the dynamics of the system, manifesting itself as gravitational attraction. This concept is expressed by a system of partial non-linear differential equations known as the Einstein's field Equations [2]. These equations are satisfied by a wave solution, which leads to the prediction of the existence of gravitational waves produced by variations of mass-energy distribution of a system. Due to the intrinsic weakness of the gravitational interaction, only massive astrophysical objects with rapid changes in their mass-energy distribution could be observed.

In this chapter I will briefly discuss the derivation of gravitational waves from the Einstein field equations, their properties and the astrophysical sources, especially the low frequency ones.

1.1 Einstein's equations

In General Relativity the energy E and the mass m must be considered two aspects of the same physical entity, as expressed by the well-known relation:

$$E = mc^2 \tag{1.1}$$

where c is the light speed. Eq. 1.1 implies that both mass and energy are source of the gravitational field. Hence both must appear in relativistic gravitational field equations, unlike in the Newtonian mechanics where the gravitational field generated by a mass distribution was expressed by the Poisson equation as a function of the mass density ρ:

$$\nabla^2 \phi_g = 4\pi G\rho \tag{1.2}$$

Hence relativistic gravitational field equations should coincide with the eq. 1.2 for non-relativistic speed (i.e. for $v \ll c$) in the weak field limit:

$$\begin{cases} g_{\mu\nu} \approx \eta_{\mu\nu} \\ g_{\mu\nu,0} = 0 \end{cases} \tag{1.3}$$

where $g_{\mu\nu}$ and $\eta_{\mu\nu}$ are respectively the metric and the Minkowsky tensor. The first one is obtained from the derivative of the spacetime coordinates under the transformation $x^\alpha = x^\alpha(\xi^\alpha)$ and it is defined as follows:

$$g_{\mu\nu} = \frac{d\xi^\alpha}{dx^\mu}\frac{d\xi^\beta}{dx^\nu}\eta_{\alpha\beta} \tag{1.4}$$

The Minkowsky tensor is the particular case of the metric tensor for a flat spacetime, being defined by:

$$\eta_{\mu\nu} = \begin{pmatrix} -1 & 0 & 0 & 0 \\ 0 & 1 & 0 & 0 \\ 0 & 0 & 1 & 0 \\ 0 & 0 & 0 & 1 \end{pmatrix} \tag{1.5}$$

Let us introduce also the Christoffel symbols $\Gamma^\alpha_{\mu\nu}$ related to the derivative of the spacetime coordinates and defined by:

$$\Gamma^\alpha_{\mu\nu} = \frac{\partial x^\alpha}{\partial \xi^\lambda}\frac{\partial^2 \xi^\lambda}{\partial x^\mu \partial x^\nu} \tag{1.6}$$

From eq. 1.4 and 1.6 we can obtain the relation between $g_{\mu\nu}$ and $\Gamma^\alpha_{\mu\nu}$:

$$\Gamma^\sigma_{\lambda\mu} = \frac{1}{2}g^{\nu\sigma}\left(g_{\mu\nu,\lambda} + g_{\lambda\nu,\mu} - g_{\lambda\mu,\nu}\right) \tag{1.7}$$

The gravitational field equations we are looking for must also satisfy the principle of general covariance which states:

1. a physical law is true if it continues to be true in absence of gravity, i.e. when $g_{\mu\nu} \to \eta_{\mu\nu}$ and $\Gamma^\alpha_{\mu\nu} \to 0$ it reduces to the laws of Special Relativity (and then it implies the Equivalence Principle);

2. the equations must be covariant (i.e. must be in a tensorial form) in order to preserve the invariance of the form of physical laws under arbitrary differentiable coordinate transformations.

Taking into account the aforesaid considerations it is possible to obtain the general form of the Einstein field Equations [2], which solutions will give the form of $g_{\mu\nu}$ in vacuum or in presence of a gravitational field source:

$$G_{\mu\nu} = R_{\mu\nu} - \frac{1}{2}g_{\mu\nu}R = -\frac{8\pi G}{c^4}T_{\mu\nu} \tag{1.8}$$

where $G_{\mu\nu}$ is the Einstein tensor, $R_{\mu\nu}$ and R are respectively the Ricci tensor and scalar, being the first obtained by the contraction of the Riemann tensor:

$$R_{\mu\nu} = g^{\lambda\alpha}R_{\lambda\mu\alpha\nu} = R^\alpha_{\mu\alpha\nu} \tag{1.9}$$

The tensor $R_{\mu\nu}$ is defined in terms of Christoffel symbols [2] and represents the curvature of the 4-dimensional manifold (i.e. the curvature of the spacetime). Since the Riemann tensor is symmetric, this also applies to the Ricci tensor. Ricci Scalar R is defined by:

$$R = g^{\alpha\beta}R_{\alpha\beta} \tag{1.10}$$

and it is also known as the scalar curvature. Both $R_{\mu\nu}$ and R contain (and are composed starting from) the second derivative of the metric tensor $g_{\mu\nu}$.

The tensor $T_{\mu\nu}$, which appears in the last term of eq. 1.8, is the stress-energy tensor, related to the system mass-energy distribution. It contains informations about the sources of the gravitational field, that is the system mass-energy content. Let us consider a system composed of n non-interacting particles with energy-momentum 4-vector p_n^α:

$$p_n^\alpha = \frac{E_n}{c^2}\frac{d\xi_n^\alpha(t)}{dt} \tag{1.11}$$

and distributed in the points $\xi_n(t)$, the T^{00} component of the stress-energy tensor represents the energy density defined by:

$$P = T^{00} = \sum_n cp_n^0(t)\delta^3(\vec{\xi} - \vec{\xi}_n(t)) \tag{1.12}$$

Similarly the momentum density is represented by the T^{0i} components of the tensor:

$$T = \frac{1}{c}T^{0i} = \sum_n cp_n^i(t)\delta^3(\vec{\xi} - \vec{\xi}_n(t)), \quad i = 1, 2, 3 \tag{1.13}$$

and the last components T^{ki} have to be considered as momentum-currents:

$$T^{ki} = \sum_n p_n^k(t)\frac{d\xi_n^i}{dt}\delta^3(\vec{\xi} - \vec{\xi}_n(t)), \quad i = 1, 2, 3;\ k = 1, 2, 3 \tag{1.14}$$

The general form of the stress-energy tensor can be obtained by substituting eq. 1.11 in eq. 1.12, 1.13 and 1.14:

$$T^{\alpha\beta} = c^2 \sum_n \frac{p_n^\alpha p_n^\beta}{E_n}\delta^3(\vec{\xi} - \vec{\xi}_n(t)) \tag{1.15}$$

Since the Einstein tensor in eq. 1.8 is symmetric, this property is verified also by the stress-energy tensor above defined, which satisfies the conservation law:

$$T^{\mu\nu}_{;\mu} = 0 \tag{1.16}$$

In principle Einstein field equations provide 10 indipendent equations for 10 components of $g_{\mu\nu}$. However the number of independent equations can be reduced if we consider the Bianchi identities for the Riemann tensor:

$$R_{\alpha\beta\mu\nu;\lambda} + R_{\alpha\beta\lambda\mu;\nu} + R_{\alpha\beta\nu\lambda;\mu} = 0 \tag{1.17}$$

Eq. 1.17 implies that:

$$G^{\mu\nu}_{;\mu} = 0 \tag{1.18}$$

The last equation 1.18 provides 4 relations for the tensor $G^{\mu\nu}$, which is the first term of field eq. 1.8, reducing to 6 the number of independent equations and allowing 4 degrees of freedom. The last result implies that if we consider $g_{\mu\nu}$ a solution of eq. 1.8, and the coordinate transformation $x^{\mu'} = x^{\mu'}(x^\alpha)$, then $g'_{\mu\nu} = g_{\mu'\nu'}$ will be again a solution of the field equations, according to the principle of general

covariance. Therefore $g_{\mu\nu}$ and $g'_{\mu\nu}$ represent the same physic solution (i.e. the same geometry) observed from two different coordinate reference systems. The four degrees of freedom obtained by eq. 1.18 disappear once a reference system is chosen, and remarkably it is always possible to choose a reference system where 4 of the 10 components of $g_{\mu\nu}$ are equal to zero.

1.2 Wave solution

Einstein field equations are a system of partial non-linear differential equations, thus it is extremely difficult to find an exact solution which can describe at the same time both the source and the radiation emitted. Infact any solution of eq. 1.8 carries itself energy and momentum which modify continuously the second member of the equation. A solution can be found in simple cases characterized by the existence of symmetries, like in the Swarzschild's solution, otherwise a perturbative approach is needed.

1.2.1 Derivation

The weak-field limit [2] allow us to consider a gravitational radiation carrying not enough energy and momentum to affect its own propagation. In this limit we can describe a linearized gravity approximation: let us consider $g^0_{\mu\nu}$ as an hypothetical exact solution of eq. 1.8 and $h_{\mu\nu}$ as a small perturbation, then the metric tensor of perturbed spacetime will be defined in an appropriate coordinate reference system as follow:

$$\begin{cases} g_{\mu\nu} = g^0_{\mu\nu} + h_{\mu\nu} \\ |h_{\mu\nu}| \ll |g^0_{\mu\nu}| \end{cases} \tag{1.19}$$

The perturbation $h_{\mu\nu}$ will be related to the perturbative term $T'_{\mu\nu}$ of the stress-energy tensor:

$$T_{\mu\nu} = T^0_{\mu\nu} + T'_{\mu\nu} \tag{1.20}$$

In a flat Minkowsky's spacetime eq. 1.19 becomes:

$$\begin{cases} g_{\mu\nu} = \eta_{\mu\nu} + h_{\mu\nu} \\ |h_{\mu\nu}| \ll 1 \end{cases} \tag{1.21}$$

By substituting eq. 1.20 and eq. 1.21 in the Einstein field Equations 1.8 and disregarding non-linear elements, it is possible to obtain the following equation:

$$\Box h_{\mu\nu} - \left[\frac{\partial^2}{\partial x^\lambda \partial x^\mu} h^\lambda_\nu + \frac{\partial^2}{\partial x^\lambda \partial x^\nu} h^\lambda_\mu - \frac{\partial^2}{\partial x^\mu \partial x^\nu} h^\lambda_\lambda \right] = -\frac{16\pi G}{c^4} (T'_{\mu\nu} - \frac{1}{2} g_{\mu\nu} T'^\lambda_\lambda) \tag{1.22}$$

where $\Box$ is the D'Alembert operator in the Minkowsky's spacetime, defined by:

$$\Box = \eta^{\alpha\beta} \frac{\partial}{\partial x^\alpha} \frac{\partial}{\partial x^\beta} = -\frac{1}{c^2} \frac{\partial^2}{\partial t^2} + \nabla^2 \tag{1.23}$$

The four degrees of freedom of Einstein's equations found at the end of section 1.1 allow us to choose a coordinate reference system in which the harmonic gauge condition is satisfied:

$$g^{\mu\nu}\Gamma^{\lambda}_{\mu\nu} = 0 \tag{1.24}$$

The gauge condition chosen in eq. 1.24 reduces the eq. 1.22 to the wave equation:

$$\begin{cases} \Box h_{\mu\nu} = -\frac{16\pi G}{c^4}(T'_{\mu\nu} - \frac{1}{2}g_{\mu\nu}T'^{\lambda}_{\lambda}) \\ \frac{\partial}{\partial x^{\mu}}h^{\mu}_{\nu} = \frac{\partial}{\partial x^{\nu}}h^{\lambda}_{\lambda} \end{cases} \tag{1.25}$$

If we define the tensor:

$$\overline{h}_{\mu\nu} \equiv h_{\mu\nu} - \frac{1}{2}g_{\mu\nu}h^{\lambda}_{\lambda} \tag{1.26}$$

eq. 1.25 at source becomes:

$$\begin{cases} \Box \overline{h}_{\mu\nu} = -\frac{16\pi G}{c^4}T'_{\mu\nu} \\ \frac{\partial}{\partial x^{\mu}}\overline{h}^{\mu}_{\nu} = 0 \end{cases} \tag{1.27}$$

The solution of eq. 1.27 can be written as a retarded potential which represents the gravitational wave calculated in the position $\vec{x}$ and generated by the source described by $T'_{\mu\nu}$ in the spacetime $\vec{x'}$:

$$\overline{h}_{\mu\nu}(t, \vec{x}) = \frac{4G}{c^4}\int \frac{T'_{\mu\nu}(t - |\vec{x} - \vec{x'}|, \vec{x'})}{|\vec{x} - \vec{x'}|}d^3x' \tag{1.28}$$

In the weak-field limit, when the wave propagates in vacuum far from the source, i.e. when $T'_{\mu\nu}$ vanishes, eq. 1.27 becomes:

$$\begin{cases} \Box \overline{h}_{\mu\nu} = 0 \\ \frac{\partial}{\partial x^{\mu}}\overline{h}^{\mu}_{\nu} = 0 \end{cases} \tag{1.29}$$

The eq. 1.29 shows that a perturbation of a flat spacetime propagates as a wave. Because of this we can state that General Relativity theory predicts the existence of gravitational waves. Moreover the double nature of the metric tensor $g_{\mu\nu}$, which describes both the spacetime shape and the gravitational potential, indicates that metric perturbation coincides with gravitational perturbation. As said above eq. 1.29 is a wave equation hence its solution can be written in terms of a monochromatic plane wave, considering only the real part:

$$\overline{h}_{\mu\nu} = \mathcal{R}e\left\{A_{\mu\nu}e^{ik_{\lambda}x^{\lambda}}\right\} \tag{1.30}$$

where the wave amplitude is expressed by the polarization tensor $A_{\mu\nu}$ and k_{λ} is the wave vector.

1.2.2 Main properties

Let us derive the main properties of gravitational waves. By substituting the solution 1.30 in the first equation of 1.29 we obtain for the wave vector k_{λ} the following condition:

$$\eta^{\mu\nu}k_{\mu}k_{\nu} = 0 \tag{1.31}$$

Eq. 1.31 implies that 1.30 is solution of eq. 1.29 only if k_λ is a null vector or a light-like vector; it means that a gravitational wave moves at the speed of light c. By substituting the solution 1.30 in the second equation of 1.29 we find that:

$$\eta^{\mu\lambda}\frac{\partial}{\partial x^\mu}\overline{h}_{\lambda\nu} = 0 \tag{1.32}$$

which implies:

$$k_\mu A^\lambda_\nu = 0 \tag{1.33}$$

From Eq. 1.33 we find that the harmonic gauge condition implies the orthogonality of the polarization tensor $A_{\mu\nu}$ and the wave vector k_λ, being the last one defined by:

$$k_\lambda = \left(\frac{\omega}{c}, \vec{k}\right) \tag{1.34}$$

and its light-like nature implies that:

$$-(k_0)^2 + \sum_{i=x,y,z} k_i^2 = 0 \tag{1.35}$$

hence, considering eq. 1.34 and 1.35, we can write the wave frequency as follows:

$$\omega = ck_0 = c\sqrt{\sum_{i=x,y,z} k_i^2} \tag{1.36}$$

Only two components of $h_{\mu\nu}$ have a physical meaning, representing the degrees of freedom. Let us consider a wave propagating in a flat spacetime along the direction $x^1 = x$; since $h_{\mu\nu}$ does not depend on y and z, eq. 1.29 can be written in the following way:

$$\begin{cases} \left(-\frac{\partial^2}{c^2\partial t^2} + \frac{\partial^2}{\partial x^2}\right)\overline{h}^\mu_\nu = 0 \\ \frac{\partial}{\partial x^\mu}\overline{h}^\mu_\nu = 0 \end{cases} \tag{1.37}$$

and then $\overline{h}^\mu_\nu$ is an arbitrary function of $t \pm \frac{x}{c}$. If the wave is progressive, the second equation of 1.37 becomes:

$$\frac{\partial}{\partial x^\mu}\overline{h}^\mu_\nu = \frac{1}{c}\frac{\partial}{\partial t}\overline{h}^t_\nu + \frac{\partial}{\partial x}\overline{h}^x_\nu = \frac{1}{c}\frac{\partial}{\partial\left(t - \frac{x}{c}\right)}\left[\overline{h}^t_\nu - \overline{h}^x_\nu\right] = 0 \tag{1.38}$$

Integrating the time-dependent part of eq. 1.38 we obtain:

$$\begin{cases} \overline{h}^t_t = \overline{h}^x_t \\ \overline{h}^t_x = \overline{h}^x_x \\ \overline{h}^t_y = \overline{h}^x_y \\ \overline{h}^t_z = \overline{h}^x_z \end{cases} \tag{1.39}$$

The harmonic gauge allows us to apply the infinitesimal transformation of coordinates:

$$x^{\mu'} = x^\mu + \xi^\mu \tag{1.40}$$

given the condition:

$$\Box\xi^{\mu} = 0 \tag{1.41}$$

The infinitesimal transformation 1.40 can be chosen in order to cancel the following elements:

$$\begin{cases} \overline{h}^{t}_{x} = \overline{h}^{t}_{y} = \overline{h}^{t}_{z} = 0 \\ \overline{h}^{y}_{y} + \overline{h}^{z}_{z} = 0 \end{cases} \tag{1.42}$$

From the relations 1.39 and 1.42 we obtain:

$$\overline{h}^{x}_{x} = \overline{h}^{x}_{y} = \overline{h}^{x}_{z} = \overline{h}^{t}_{t} = 0 \tag{1.43}$$

Moreover, since $h^{\mu}_{\mu} = 0$, from eq. 1.26 we obtain that $\overline{h}^{\mu}_{\nu} \equiv h^{\mu}_{\nu}$, and finally we can write $h_{\mu\nu}$ as follows:

$$h_{\mu\nu} = \begin{pmatrix} 0 & 0 & 0 & 0 \\ 0 & 0 & 0 & 0 \\ 0 & 0 & h_{yy} & h_{yz} \\ 0 & 0 & h_{yz} & -h_{yy} \end{pmatrix} \tag{1.44}$$

Hence from the gauge chosen above in 1.40 we obtained that h^{μ}_{ν} coincides with $\overline{h}^{\mu}_{\nu}$ and is traceless. It means that a plane gravitational wave propagating along the x direction is described by the matrix h^{μ}_{ν} with only two non-zero components in the plane yz orthogonal to the propagation direction. Therefore the transformation 1.40 is known as transverse-traceless gauge, or simply TT-gauge. The two non-zero components of h^{μ}_{ν} correspond to the two possible polarization states: the *plus* polarization and the *cross* polarization, usually known as A_{+} and $A_{\times}$, with the related amplitudes h_{+} and $h_{\times}$.

The two non-zero elements of the matrix 1.44, corresponding to the two polarization states, can be written as follow:

$$\begin{aligned} h_{yy} = -h_{zz} &= 2\mathcal{R}e\left\{h_{+}e^{i\omega\left(t-\frac{x}{c}\right)}\right\} \\ h_{yz} = -h_{zy} &= 2\mathcal{R}e\left\{h_{\times}e^{i\omega\left(t-\frac{x}{c}\right)}\right\} \end{aligned} \tag{1.45}$$

1.2.3 Interaction with matter

The simplest case we can study is the effect produced by the passage of a gravitational wave on a single particle at rest in a fixed frame. Let us consider the general equation of motion of a particle with respect to spacetime coordinates ξ^{μ}:

$$\frac{d^2\xi^{\alpha}}{d\tau^2} = 0 \tag{1.46}$$

where τ is the proper time. If we consider the coordinate transformation $x^{\alpha} = x^{\alpha}(\xi^{\alpha})$ and the definition 1.6, the equation of motion becomes:

$$\frac{d^2x^{\alpha}}{d\tau^2} + \Gamma^{\alpha}_{\mu\nu}\left[\frac{dx^{\mu}}{d\tau}\frac{dx^{\nu}}{d\tau}\right] \equiv \frac{U^{\alpha}}{d\tau} + \Gamma^{\alpha}_{\mu\nu}U^{\mu}U^{\nu} = 0 \tag{1.47}$$

Eq. 1.47 is known as geodesic equation and describes the motion of the particle along the geodesic of the spacetime curved by the gravitational wave passage.

Initially the particle is at rest, i.e. $U^\alpha = (1, 0, 0, 0)$ at $t = 0$. From eq. 1.47 and relation 1.7, considering the TT-gauge, we obtain the expression of the acceleration induced by the gravitational wave:

$$\left.\frac{U^\alpha}{d\tau}\right|_{t=0} = -\Gamma^\alpha_{00} = -\frac{1}{2}\eta^{\alpha\beta}\left(h_{\beta 0,0} + h_{0\beta,0} - h_{00,\beta}\right) = 0 \tag{1.48}$$

From eq. 1.48 it comes out that a gravitational wave will not cause any acceleration to a particle at rest.

Let us study instead what happens when we consider a system of two test masses considering their relative motion in a fixed frame [3]. Let the particles A and B be at rest at $t = 0$ and let them be located along the x-axis, with A placed in the origin of the frame of reference and B at the distance $x = l_{AB}$ from the origin. We can calculate the relative displacement Δl_{AB} of the two masses as follows:

$$\begin{aligned}\Delta l_{AB} = \int |ds^2|^{1/2} = \int |g_{\mu\nu}dx^\mu dx^\nu|^{1/2} = \int_0^\epsilon |g_{xx}|^{1/2}dx \\ \approx |g_{xx}(x=0)|^{1/2}\epsilon \approx [1 + \frac{1}{2}h_{xx}(x=0)]l_{AB}\end{aligned} \tag{1.49}$$

Therefore from eq. 1.49 it is evident that the passage of a gravitational wave causes an oscillation of the relative displacement Δl_{AB} at the same frequency of the wave. Moreover, the effect is directly proportional to the wave amplitude h_{xx} and to the initial distance l_{AB}.

In more general terms, it can be proved [2] that under the TT-gauge:

$$\delta x^j = \delta x^j_0 + \frac{1}{2}\eta^{ji}h_{ik}\delta x^k_0 \tag{1.50}$$

Eq. 1.50 shows that the test masses are accelerated only in the plane orthogonal to the propagation direction of the wave.

Let us highlight the effect produced by an incoming monochromatic gravitational wave *plus* or *cross* polarized on a circular-shape distribution of non-interacting point masses: if the wave is propagating along the z-axis, we can write the matrix form of $h_{\mu\nu}$ as we did in eq. 1.44:

$$h_{\mu\nu} = \begin{pmatrix} 0 & 0 & 0 & 0 \\ 0 & h_+(t-\frac{z}{c}) & h_\times(t-\frac{z}{c}) & 0 \\ 0 & h_\times(t-\frac{z}{c}) & -h_+(t-\frac{z}{c}) & 0 \\ 0 & 0 & 0 & 0 \end{pmatrix} \tag{1.51}$$

Let us use the *Fermi coordinates* $\hat{x}^\mu$ to describe the movement of the considered point masses in a *quasi*-Newtonian way; eq. 1.50 in the time domain becomes:

$$\hat{x}^i(t) = x^i_0 + \frac{1}{2}h_{ij}(t,0)x^j_0 \tag{1.52}$$

Using 1.51 in eq. 1.52 we obtain:

$$\begin{cases} \hat{x}(t) = x_0 + \frac{1}{2}(h_+x_0 + h_\times y_0)e^{i\omega t} \\ \hat{y}(t) = y_0 + \frac{1}{2}(h_\times x_0 - h_+ y_0)e^{i\omega t} \\ \hat{z}(t) = z_0 \end{cases} \tag{1.53}$$

From eq. 1.53 we note that a circle of particles will be deformed as the gravitational wave passes, by alternative contractions and elongations along the $\hat{x}$ and $\hat{y}$ axes, for the *plus* polarization, and along the lines $\hat{y} = \hat{x}$ and $\hat{y} = -\hat{x}$ for the *cross* polarization. This deformation will be modulated at the wave frequency.

It is evident that this tidal effect on test masses can be used for a direct detection of gravitational waves, as we shall see in chapter 2.

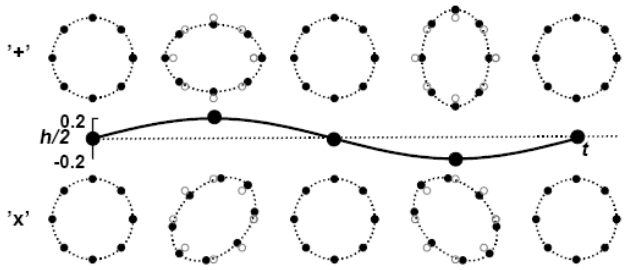

Figure 1.1: Tidal effect produced by the passage of a gravitational wave propagating along the z-axis on a ring of particles at rest on the xy-plane. The oscillation axis of *plus* polarization are $\pi/4$ rotated with respect to those of *cross* polarization.

1.2.4 Emission and intensity

Let us consider the reasonable hypothesis that a source of gravitational waves is confined within a region of dimension ϵ smaller than the emitted wavelength, i.e. $\epsilon \ll \lambda_{gw} \equiv \frac{2\pi c}{\omega}$, it follows that $\epsilon\omega \ll c$. We can write the typical speed at the source as $v \approx \epsilon\omega$ and then we deduce that $v \ll c$. Hence we shall consider non-relativistic speed in the emission processes of the source.

The mass distribution of the source can be expressed in terms of multipole components. The monopole term is the total mass itself, i.e. M, which is conserved in a closed isolated system. The dipole term is defined by:

$$D = \sum_k m_k x_k \tag{1.54}$$

In analogy with electromagnetism, the power emitted by a gravitational dipole is given by $P \propto \ddot{D}^2$, i.e. is proportional to the second power of the dipole second derivative:

$$\ddot{D} = \sum_k m_k \ddot{x}_k = \sum_k m_k \dot{v}_k = \sum_k \dot{p}_k \tag{1.55}$$

where p_k is the linear momentum of the k-th mass element. In eq. 1.55 we considered the equivalence between gravitational and inertial mass, i.e. the *Equivalence Principle* [2]. Since also the total momentum must be conserved in a closed isolated system, i.e. $\sum_k p_k = const$, it follows that the last term of eq. 1.55 vanishes, therefore a gravitational dipole will not emit radiation.

From the aforesaid considerations based on the conservation of mass and linear and angular momentum (which are implied in the conservation of the stress-energy

tensor expressed by eq. 1.16) it follows that the first contribution to the emission of gravitational waves is due to the next term in the multipole expansion: the quadrupole momentum $Q_{\mu\nu}$. It can be expressed in its integral form as follows [4]:

$$Q_{\mu\nu} = \int (3x'_\mu x'_\nu - r^2\delta_{\mu\nu})\rho(\overrightarrow{x'})d^3x' \tag{1.56}$$

where r is the distance between the source and the observer, and $\rho(\overrightarrow{x'})$ is the energy density of the source. Using the solution of eq. 1.28 in the non-relativistic and far-field approximation we can write the gravitational wave amplitude $\overline{h}_{\mu\nu}$ in terms of the second derivative of the gravitational quadrupole momentum [4]:

$$\overline{h}_{\mu\nu}(t,r) \approx \frac{8\pi}{3}\frac{G}{c^4}\frac{1}{r}\ddot{Q}_{\mu\nu} \tag{1.57}$$

From eq. 1.56 and 1.57 it is clear that spherically or axially-symmetric systems cannot emit gravitational waves.

In order to estimate the order of magnitude of the perturbation intensity, we should approximate the quadrupole momentum, and then its second derivative, as follows:

$$Q \approx \epsilon M R^2 \tag{1.58}$$

$$\ddot{Q} \approx \epsilon \frac{MR^2}{T^2} \tag{1.59}$$

where ϵ is the coefficient of asymmetry of the mass distribution, M is the total mass of the source, R is its typical dimension and T the typical timescale of the system. The speed of the mass elements of the system can be expressed as $v = \frac{R}{T}$, hence substituting the expression of v in $\ddot{Q}$, the eq. 1.57 becomes [4]:

$$\overline{h} \sim \frac{1}{r}\frac{GM}{c^2}\left(\frac{v}{c}\right)^2 \tag{1.60}$$

From the eq. 1.60 we note that the amplitude decreases with the distance from the source as $\frac{1}{r}$. Moreover, the smallness of the factor $\frac{G}{c^2} \approx 10^{-29} m^3/s^4 kg$ makes negliglible the effect except for those astronomical sources with masses at least of the order of 10^{30} kg. The last term of eq. 1.60 shows that also the typical speed of mass elements in the source should be comparable with c in order to have a significant effect.

It is possible to obtain a more detailed expression of the gravitational wave amplitude from the lowest order term of a spherical multipole expansion for the spatial coordinates [5]:

$$\bar{h}_{jk} = \frac{2G}{c^4 r}\ddot{Q}_{jk}\left(t - \frac{r}{c}\right) + \frac{4G}{3c^5 r}\left[\epsilon_{pqj}\ddot{\mathcal{S}}_{kp}\left(t - \frac{r}{c}\right) + \epsilon_{pqk}\ddot{\mathcal{S}}_{jp}\left(t - \frac{r}{c}\right)\right] n_q \tag{1.61}$$

where repeated indices imply the summation, ϵ_{ijk} is the antisymmetric tensor, $\mathcal{S}_{mn}$ is the current quadrupole momentum and n_q is the propagation versor. Eq. 1.61 is widely used to estimate the gravitational wave amplitudes in astrophysical context: if the system dynamics is dominated by bulk mass motions (e.g. in the *chirp* of inspiral binary systems, see sec. 1.3.2) the gravitational radiation is well described by the first term of the equation. The eq. 1.61 can be used also in the case of f-mode, r-mode (in particular the second term of the equation) and secular instabilities in order to estimate the related gravitational emission (see sec. 1.3.4).

1.2.5 Luminosity

The local stress-energy tensor of a gravitational wavefield propagating through a flat spacetime is given by the Isaacson expression [2]:

$$T_{\alpha\beta} = \frac{1}{32\pi} \left\langle \overline{h}_{jk,\alpha} \overline{h}^{jk}_{,\beta} \right\rangle \tag{1.62}$$

where with the angle brackets we indicate the averages over regions of the same size of a wavelength and times of the same length of a period of the gravitational wave. The T^{0i} component of the stress-energy, that we have already introduced as the momentum density in sec. 1.1, represents the energy flux of a wave in the x^i direction. In the quadrupole approximation we can obtain the gravitational wave luminosity by integrating the eq. 1.62 over a distant sphere [4]:

$$L^*_{gw} = \frac{dE_{gw}}{dt} = \frac{1}{5} \left(\sum_{j,k} \dddot{Q}_{jk} \dddot{Q}_{jk} - \frac{1}{3} \dddot{Q}^2 \right) \tag{1.63}$$

where we introduced Q as the trace of the matrix Q_{jk}. The expression 1.63 is dimensionless since we assumed geometrized units (i.e. $c = G = 1$). Equation 1.63 must be multiplied by the scale factor $L_0 = c^5/G = 3.6 \times 10^{52}\ W$ in order to obtain the luminosity with its proper dimensions:

$$L_{gw} = L_0 L^*_{gw} \tag{1.64}$$

Usually the astrophysical sources (see sec. 1.3) emit a fraction of L_0, but in some cases the gravitational wave luminosity can come close to L_0, greater than the typical electromagnetic luminosities: by comparison the luminosity of the Sun is only $L_\odot = 3.8 \times 10^{26}\ W$, and that of a typical galaxy would be $L_{gal} \sim 10^{37}\ W$. By combining eq. 1.61 and 1.63, assuming geometrized units and considering the source at great distance, we can derive the expression for the apparent luminosity of radiation in terms of gravitational wave amplitude [2]:

$$F \sim \frac{|\dot{h}|^2}{16\pi} \tag{1.65}$$

The eq. 1.65 is useful to make an order-of-magnitude estimate of the gravitational wave amplitude emitted by a source for which the energy emission rate is known. Let us consider a source, placed at a distance r, which radiates the energy E in a time T with a typical frequency f; since $\dot{h} = 2\pi f h$ and $F \sim E/(4\pi r^2 T)$, we obtain:

$$h \sim \frac{1}{\pi f r} \sqrt{\frac{E}{T}} \tag{1.66}$$

From eq. 1.66 we note that, as in other branches of astronomy, the detectability of a source depends on its apparent luminosity and on the observation time. However in eq. 1.66 we should also consider the dependence on frequency: two sources with the same energy flux but with different emission frequencies are not equally easy to detect, since higher frequency signals will have smaller amplitudes.

1.3 Astrophysical sources

The gravitational radiation is expected to be present over a wide range of frequencies, therefore we can classify the astrophysical sources depending on their emission band:

- very low frequency ($10^{-18} - 10^{-2} Hz$)
  - stochastic background (gravitational fluctuations from the primordial universe, stochastic background due to astrophysical and cosmological sources)
  - compact binary systems early inspiral (black holes binaries in particular); *quasi-periodic* sources.
- low frequency ($10^{-2} - 10^{2} Hz$)
  - compact binary systems coalescence (white dwarves, neutron stars, intermediate-mass black holes); *quasi-periodic* sources.
  - spinning neutron stars; *periodic* sources.
- high frequency ($10^{2} - 10^{4} Hz$)
  - compact binary mergers; *transient* sources.
  - neutron star's instabilities; *transient* sources.
  - gravitational collapses (supernovae, gamma-ray burst progenitors such as hypernovae and collapsars); *transient* sources.
  - stochastic background (expected by string theory and inflation model)

Many of these sources (e.g. binary black holes) can be observed directly only through their gravitational radiation, others could have an electromagnetic or neutrino counterpart (see sec. 1.4). Moreover, since the interaction between gravitational radiation and matter is extremely low, gravitational waves carry almost intact informations about the source which emitted them. *Quasi-periodic* and *periodic* sources also give the advantage of allowing the signal integration over time, increasing the related amplitude SNR as the square root of the observation time[6]:

$$SNR_{amp} \propto \frac{\sqrt{T_{obs}}}{\sqrt{S_n(f_0)}} h(f_0) \tag{1.67}$$

where S_n is the related noise power and f_0 is the typical emission frequency. Obviously, a gravitational wave signal would not have such a simple single frequency modulation f_0 in the detector frame: a ground-based detector will have at least the frequency modulations due to the motions of the Earth. However in principle the SNR increase with time can still be valid using data analysis techniques such as matched filtering [6].

In this section I will discuss the astrophysical sources of gravitational radiation, showing that low-frequency sources are very promising candidates for direct gravitational wave observations in ground-based detectors. A useful parameter to

evaluate the number of gravitational signals coming from every kind of source is the detection rate $\dot{N}$ [7]. It depends on the emission rate R per unit time and per galaxy (e.g. coalescence events) and on the number of observable galaxies N_G, and is defined by:

$$\dot{N} = RN_G \tag{1.68}$$

The number of observable galaxies obviously depends on the horizon distance D_{hor} related to the detector sensitivity. It can be expressed with a good approximation by the following formula:

$$N_G = \frac{4}{3}\pi \left(\frac{D_{hor}}{Mpc}\right)^3 (2.26)^{-3}(1.16 \times 10^{-2}) \tag{1.69}$$

where $1/2.26$ is a correction factor which takes into account the average over all sky locations, and $1.16 \times 10^{-2} Mpc^{-3}$ is the extrapolated density of Milky Way equivalent galaxies in space.

1.3.1 Stochastic background

The gravitational wave stochastic background is a superposition of waves arriving at random times and from random directions from a large number of unresolved sources, i.e. from those sources with an angular size smaller than the angular resolution of the detector. Such a gravitational wave field would be measured by a detector as a time-series noise, which should have a Gaussian-normal distribution function, given the central limit theorem and considering a large number of overlapping sources. This background signal is composed of two contributions:

1. the primordial background, produced by quantum fluctuations that created the CGWB (*cosmic gravitational wave background*) in the early universe.

2. the astrophysical background, produced by the evolution of galaxies and stellar objects, like those that will be described in the next subsections.

The energy density of a field of gravitational waves can be derived from eq. 1.62 multiplied by the factor c^2/G^2, considering that the element T_{00} represents the energy density ρ_{gw}:

$$\rho_{gw} = \frac{c^2}{32\pi G^2} \left\langle \dot{h}_{jk}\dot{h}^{jk} \right\rangle \tag{1.70}$$

Usually, the energy density related to a random field of gravitational waves is function of frequency. In geometrized units the energy density of a plane wave is the same as its flux, then from eq. 1.65 we can derive:

$$\rho_{gw}(f) = \frac{\pi}{4} f^2 h^2 \tag{1.71}$$

In this case the wave field is a random variable, then h^2 must be replaced by a statistical mean square amplitude per unit frequency defined $S_{gw}(f)$. Therefore the energy density per unit frequency will be proportional to $f^2 S_{gw}(f)$. It is usual to consider the energy density per unit logarithm of the frequency, which introduce

a multiplication by f. By averaging over all directions of the wave and over all the independent polarization components, it is possible to derive [8]:

$$\frac{d\rho_{gw}}{d\ln f} = 4\pi^2 f^3 S_{gw}(f) \tag{1.72}$$

The spectrum of the gravitational stochastic background is characterized by the dimensionless parameter $\Omega_{gw}(f)$ [8], which can be interpreted as the fraction of the closure energy density that is stored in random gravitational waves in a frequency bin delimited by f and $e \times f$. It is defined, as usual in cosmology, by:

$$\Omega_{gw}(f) = \frac{1}{\rho_{cr}} \frac{d\rho_{gw}}{d\ln f} \tag{1.73}$$

In eq. 1.73 f is the frequency in the observer frame and ρ_{cr} is the critical energy density required to make flat the Universe today, which is given in terms of the Hubble constant $H_0 \equiv 100 \times h_{100}\ km/s/Mpc$ as:

$$\rho_{cr} = \frac{3}{8\pi} \frac{c^2 H_0^2}{G} \approx 9.0 \times 10^{-10} J/m^3 \tag{1.74}$$

where we used the estimate $H_0 \approx 72\ km/s/Mpc$. Some cosmological models assume a frequency-independent Ω_{gw}, but in general we should consider a dependence on frequency expressed by the function $H(f)$, in such a way that it can describe any spectrum of gravitational radiation, e.g. a flat spectrum, a black body spectrum or any other specific frequency-dependent energy distribution. If the source of radiation is *scale-free*, which means that the emission process does not have any characteristic length or time scale, then it will produce a power-law spectrum in which Ω_{gw} is a power of f. The explicit frequency-dependence of Ω_{gw} can be derived using a plane wave expansion of the metric perturbations in eq. 1.70 [8], and combining it with eq. 1.73 and 1.74:

$$\Omega_{gw}(f) = \frac{32\pi^3}{3H_0^2} f^3 H(f) \tag{1.75}$$

From eq. 1.72, considering eq. 1.73 and 1.74, we can also derive:

$$S_{gw}(f) = \frac{3H_0^2}{10\pi^2} f^{-3} \Omega_{gw}(f) \tag{1.76}$$

where $S_{gw}(f)$ can be interpreted as the strain spectral noise density induced on an interferometric detector (see chapter 2) by an incident isotropic gravitational wave background. The energy density fraction Ω_{gw} can be used to define the so called *chirp*-amplitude, a dimensionless gravitational wave strain $h_c = \Delta L/L$ that would be produced in the arms of a detector and in a bandwidth which coincides with the observation frequency. It is defined by the following equation [9]:

$$h_c(f) = 3 \times 10^{-20} h_{100} \sqrt{\Omega_{gw}} \frac{100Hz}{f} \tag{1.77}$$

Observational constraints on the stochastic background

From non-gravitational wave astronomy observations we can set constraints on the energy density fraction Ω_{gw}. The strongest constraint comes from the high degree of isotropy in the CMBR (*cosmic microwave background radiation*). The *Sachs Wolfe effect* [10] establishes the connection between the temperature anisotropies of the CMBR and gravitational waves: variations in the density of the cosmological fluid and gravitational wave perturbations result in the temperature fluctuations of CMBR, even if the last scattering surface was perfectly uniform in temperature. From the observations of $\delta T/T$ by satellite missions like COBE and WMAP it is possible to give a constraint on the energy density fraction of gravitational wave of cosmological origin that were present at the time of last scattering [8]:

$$\Omega_{gw}(f)h_{100}^2 < 7 \times 10^{-11} \left(\frac{H_0}{f}\right)^2 \tag{1.78}$$

Since $H_0 = 3.2 \times 10^{-18} h_{100}\ Hz$, it follows that this limit applies only in a narrow band of very low frequencies (i.e. $10^{-18} < f < 10^{-16} Hz$) where we obtain $\Omega_{gw}(f = 10^{-18} Hz)h_{100}^2 < 7 \times 10^{-11}$. Other cosmological constraints could be placed by the measurement of the B-mode CMBR polarization spectrum by the data obtained by other satellite missions like PLANCK.

Another constraint comes from the *millisecond* pulsars (see sec. 1.3.4). The extreme regularity of their pulses, observed over decades, places a tight constraint on $\Omega_{gw}(f)$ at frequencies equal to the inverse of the observation time [11]. In order to obtain such a constraint we need to measure their timing residuals $\Delta t/t$, which in principle can highlight the passage of a gravitational wave. Let us consider a gravitational wave passing by us from a direction transverse to our line-of-sight to the pulsar, assuming a wavelenght $\lambda = 8\ ly$ and considering the emitting pulsar as a perfect clock signal. When one of the maxima of the gravitational wave is passing by the Earth, we should observe a small delay between the pulses (i.e. a kind of gravitational redshifting); then four years later, when a minimum of the gravitational wave is passing by the Earth, we should observe the pulses more closely spaced togheter (i.e. a kind of blueshifting). Such a system could be considered as a single-arm gravitational wave detector, with an arm length $L = 8\ ly$. Then the size of the gravitational wave strain is limited by [8]:

$$h_c \leq \frac{\Delta L}{L} = \frac{\Delta t}{t} \tag{1.79}$$

where we put $L = ct = 8\ ly$ and $\Delta t \sim \mu s$. From eq. 1.77 and 1.79, and considering that the timing residual which is of the order of $\Delta t/t \sim \mu s/y < 10^{-14}$, we obtain the constraint:

$$\Omega_{gw}(f \sim 10^{-8} Hz)h_{100}^2 < 10^{-8} \tag{1.80}$$

Another observational constraint is given by the standard model of the Big Bang nucleosynthesis (BBN), which fits the observed abundances of light elements in the universe and constrains some cosmological parameters, e.g. the expansion rate of the universe at the time of nucleosynthesis. This rate is related to the energy density of the universe at that time, and then also to the energy density

in a cosmological gravitational wave background. Usually the constraint is given in terms of number of massles neutrinos permitted at the time of nucleosynthesis, that is $N_\nu \leq 3.4$ [12]:

$$\int \Omega_{gw}^{NS}(f) h_{100}^2 d(\ln f) \leq y(N_\nu) \left(\frac{\rho_{rad}}{\rho_{cr}} \right) \tag{1.81}$$

where ρ_{rad} is the radiation energy density. We can derive the present day limit considering that the radiation energy density redshifts proportionally to $(1+z)^{-1}$. Therefore, from eq. 1.81 we obtain:

$$\int \Omega_{gw}(f) h_{100}^2 d(\ln f) \leq 7 \times 10^{-2} (1 + z_{eq})^{-1} \sim 10^{-5} \tag{1.82}$$

where we considered the redshift at the time of equivalence between radiation and matter densities $z_{eq} \sim 3400$ [13].

Cosmological background emission

Let us examine the main cosmological processes in the early universe which determines the spectrum of $\Omega_{gw}(f)$.

- **Inflationary models**. These are a class of cosmological models which assume that the early universe undergoes a phase in which the energy density of the universe was dominated by the vacuum energy Λ, resulting in a very rapid expansion lasted from 10^{-36} s to 10^{-32} s after the initial singularity. In cosmology the predictions of these models are in good agreement with many observational evidences, e.g. they explain the flatness of the universe and the CMBR features. The energy density fraction Ω_{gw} can be obtained as a function of the energy density of vacuum ρ_Λ [14, 15]:

  $$\Omega_{gw}(f) = \frac{16}{9} \frac{\rho_\Lambda}{\rho_P} (1 + z_{eq})^{-1} \tag{1.83}$$

  where we have introduced the Planck energy density $\rho_P = c^7/\hbar G^2$. The dependence on $\hbar$ is related to the fact that this kind of background can be considered as a parametrically-amplified zero-point energy [14]. The spectral shape of Ω_{gw} is almost flat in the typical frequency band of ground-based detectors.

- **Cosmic strings**. These are a class of one-dimensional objects which might have formed during a phase transition as the universe cooled, in analogy with topological defects which can form during the phase transitions of liquid crystals. Cosmic strings can be described as topologically-stable scalar/gauge field configurations characterized by a mass per unit length μ. They are always generated in form of loops, but if the loop is larger than the Hubble length we will consider it as an infinite string. The length of the loop is defined as the total energy of the loop divided by μ. An important property of loops is that they have a tension equal to their μ, therefore this large

tension causes a relativistic oscillation of the cosmic string: in general a non-circular loop will oscillate quasi-periodically. Another important property is that a loop is stable against all types of decay, except for the emission of gravitational waves. The expression of Ω_{gw} for a stochastic gravitational wave background generated by a cosmic string network can be written as [14]:

$$\Omega_{gw}(f) = \frac{16\pi}{9}\frac{A\gamma}{\alpha}\left(\frac{G\mu}{c^2}\right)^2(\beta^{3/2}-1)(1+z_{eq})^{-1} \tag{1.84}$$

Eq. 1.84 depends on not completely known parameters: the number of long strings per horizon volume A, the radiation rate coefficient from a typical loop γ, the mass per unit length μ, the size of a loop at formation α and the ratio of death-time and birth-time for cosmic string loops β. From some estimates of these parameters it seems possible that an eventual stochastic cosmic string background could be within the sensitivity range of advanced detectors (see chapter 2), with a spectral shape of Ω_{gw} fairly flat in their frequency band.

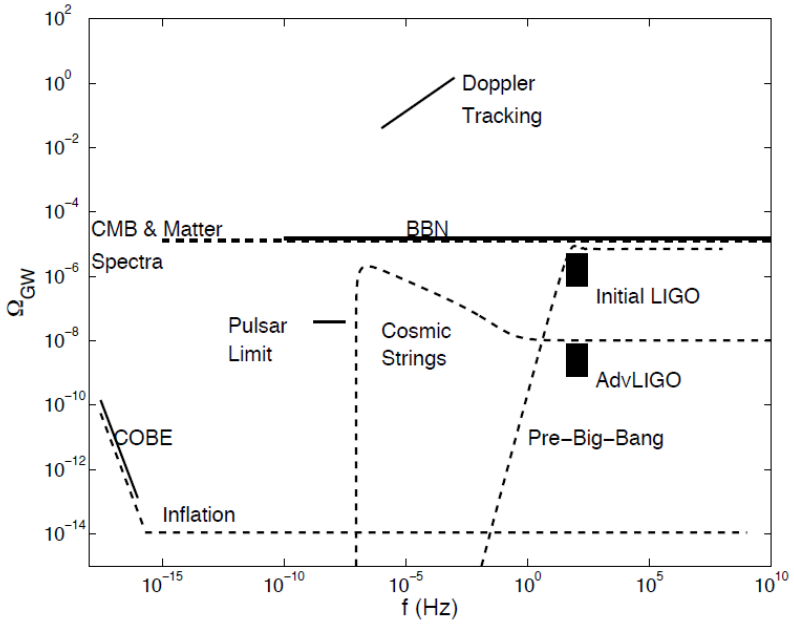

Figure 1.2: Theoretical predictions of the cosmological stochastic background and observational constraints [16]. The *Doppler tracking* constraint in the mHz-band is obtained using the Earth and a distant interplanetary spacecraft as free-falling particles of a single-arm detector, measuring $\Delta\nu/\nu$ of a microwave tracking link between them compared to a highly stable clock. The squares indicates the sensitivity limits of initial and advanced ground-base interferometric detectors (see chapter 2).

- **First-order phase transitions**. These transitions occurs in an expanding and cooling universe, when its temperature T_u has dropped below the characteristic energy of the phase transition, i.e. when $KT_u < E_{trans}$. In

this condition, bubbles of the new low energy density phase form within the old high energy density phase, and they expand rapidly, converting the difference in energy density per volume into kinetic energy of the expanding bubble boundaries. This energy density difference is parameterized in $\alpha = \rho_{vac}/\rho_{therm}$. Bubbles can collide at relativistic speed with non-symmetric events, generating gravitational radiation. The spectral shape produced by this mechanism will be strongly peaked at a typical frequency f_{max} related to the time at which the phase transition and bubble collisions have occurred, and it is a function of the the temperature T_{ph} of the phase transition. In the standard model of electro-weak phase transition the estimate of this frequency is: $f_{max} \sim 10^{-3}\ Hz$. Considering this mechanism, the energy density fraction will be [16]:

$$\Omega_{gw}(f_{max})h^2_{100} \propto 10^{-6}\left(\frac{H_{trans}}{\beta}\right)^2\left(\frac{100}{N_{dof}}\right)^{1/3} \tag{1.85}$$

where H_{trans} is the Hubble constant at the time of phase transition, β is given by the bubble nucleation rate $\Gamma = \Gamma_0 \exp(-\beta t)$ and N_{dof} is the number of the relativistic degree of freedom (in GUT models $N_{dof} \sim 10^2$). It would be very optimistic to assume a strongly first order transition, however from eq. 1.85 we can estimate the gravitational wave fractional energy density produced during the electro-week phase transition (at $T_{ph} \sim 10^2\ GeV$) that is $\Omega_{gw} \sim 10^{-9}$ at mHz scale frequencies.

Astrophysical background emission

Let us examine the main contributions to the gravitational stochastic background produced by astrophysical sources. Many informations about this kind of sources (e.g. their physical properties and initial mass function) could be provided by the detection this background.

- **Binary neutron stars**. The coalescences of binary neutron stars (see sec. 1.3.2) may radiate energy up to $10^{46}\ J$ in the last seconds of their inspiral trajectory. The frequency range of this emission extends over a wide range of frequencies, with a maximum at about $1.4 - 1.6\ kHz$. Considering the quadrupole approximation, the energy spectrum emitted by a binary system in inspiral phase up to its last stable orbit (i.e. up to its maximum frequency f_{max}) is given by [16]:

$$H(f) \propto \frac{dE_{gw}}{df} = \frac{(G\pi)^{2/3}}{3}\frac{m_1 m_2}{(m_1+m_2)^{1/3}}f^{-1/3} \tag{1.86}$$

where $H(f)$ is the frequency-dependent part of eq. 1.76, m_1 and m_2 are the neutron star masses. Assuming $m_1 = m_2 = 1.4\ M_\odot$, the energy density increases to a maximum given by:

$$\Omega_{gw}(f \approx 600Hz) \sim 2 \times 10^{-9}\dot{\rho} \tag{1.87}$$

where $\dot{\rho}$ is the local coalescence rate in $My^{-1}Mpc^{-3}$. Even with the most pessimistic predictions of this rate, which give $\dot{\rho} \sim 0.035$ (i.e. a galactic

rate of $3My^{-1}$), the background from binaries should be detectable by third-generation gravitational wave detectors (see fig. 1.3 and chapter 2).

- **Rotating neutron stars: bar-modes**. These modes are a dynamical instability associated with the neutron star formation (see sec. 1.3.4), and derive their name from the bar-like deformation they induce on a disk-like object. Numerical simulations [17] predict a maximum of the fractional energy density $\Omega_{gw} \sim 4 \times 10^{-10}$ around 600 Hz.

- **Rotating neutron stars: r-modes**. The contribution to stochastic background produced by this kind of instabilities (see sec. 1.3.4) was investigated by some authors [18] without taking into account for dissipation mechanisms which may reduce the gravitational instability (e.g. effects of the solid crust or the magnetic field). The spectral dependence of fractional energy density calculated for a single source is given by:

$$H(f) \propto \frac{dE_{gw}}{df} = \frac{2E_0}{f_{sup}^2} f \tag{1.88}$$

where $0 < f < f_{sup}$, f_{sup} is equal to 4/3 of the initial rotational frequency and E_0 is the rotational energy lost within the instability window. If we consider neutron stars with radius $R = 10\ km$ and mass $M = 1.4\ M_\odot$, the predicted spectrum is given by:

$$\Omega_{gw}(f) \sim 10^{-12} \xi f_0^3 \tag{1.89}$$

where ξ is the fraction of neutron stars born near the Keplerian velocity and which enter in the instability window. The spectrum of Ω_{gw} have a maximum around $f \sim 900\ Hz$. If $\xi > 0.2\%$ third-generation gravitational wave detectors (see chapter 2) may detect this background radiation.

- **Rotating neutron stars: tri-axial emission**. This emission is produced by rotating neutron stars with a triaxial shape, which may be characterized by a time varying quadrupole momentum, resulting in a gravitational wave emission at twice the rotational frequency. The related Ω_{gw} spectral dependence will be proportional to the total spectral energy emitted by a neutron star with an initial rotational period P_0, decelerating through magnetic dipole torques and gravitational wave emission. It is given by [16]:

$$H(f) \propto \frac{dE_{gw}}{df} = \frac{Kf^3}{1 + (Kf^2)/(\pi^2 I_{zz})} \tag{1.90}$$

where

$$K = \frac{192\pi^4 G I_{zz}^3 \epsilon^2}{5c^5 R^6 B^2} \tag{1.91}$$

R is the radius of the star, $\epsilon = (I_{xx} - Iyy)/I_{zz}$ is its ellipticity, I_{ij} is the principal momentum of inertia, B is the projection of the magnetic dipole in the direction orthogonal to the rotation axis and $0 < f < 2/P_0$. The energy density spectrum can be estimated to be $\Omega_{gw} \sim 1.3 \times 10^{-8}$ at $f = 1.6\ kHz$.

- **Neutron star collapses**. A fraction of the neutron stars may undergo small core collapses, resulting in phase transition to quark matter. This process will release a certain amount of energy through gravitational wave emission: if this class of neutron stars is 1% of the total and the released energy is 5% of the rotational energy ($\sim 2 \times 10^{44}$ J), the fractionary energy density will be $\Omega_{gw} \sim 10^{-10}$ in the kHz-band.

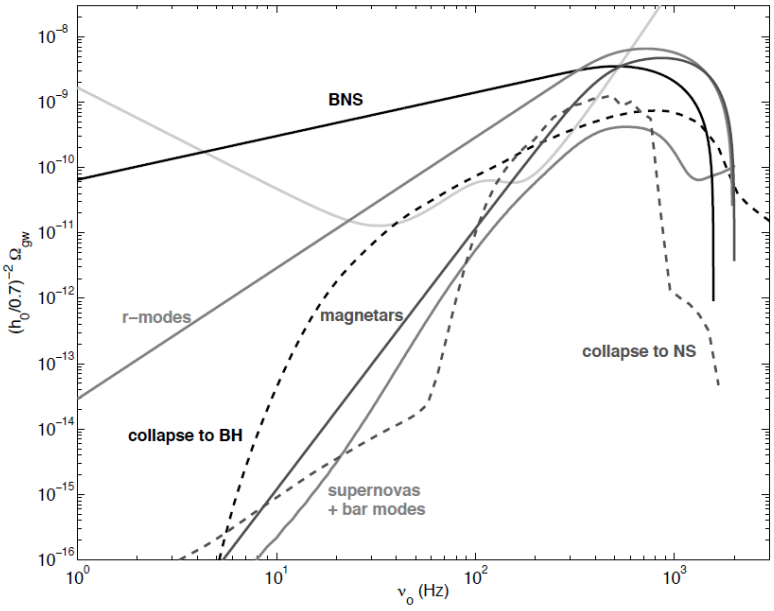

Figure 1.3: Energy density of astrophysical background sources discussed in this section [16]: magnetars (threshold detectable by 3^{rd} generation detectors), binary neutron stars, dynamical bar modes in proto-neutron stars, r-modes assuming that 1% of proto-neutron stars cross the instability window, population II core collapses to neutron stars and to back holes.

- **Core collapses: supernovae to neutron stars**. In a supernova explosion (see sec. 1.3.5) the star envelope is ejected while the core collapses to form a neutron star or a black hole, depending on the initial mass of the progenitor star. This process may emit a large amount of gravitational waves. Some authors calculated the stochastic background produced by the birth of neutron stars at cosmological distances [19], considering the standard cosmological model (with $\Omega_m = 0.3$, $\Omega_\Lambda = 0.7$ and $H_0 = 70$ $km/s/Mpc$), assuming neutron star progenitors with masses $8\ M_\odot < M < 25\ M_\odot$ and a Salpeter initial mass function normalized between $0.1 - 125\ M_\odot$. The resulting background is found to be continuous for Type I supernovae, while is like burst-noise for Type II. The maximum of the Ω_{gw} spectrum is $\Omega_{gw} \sim 3 \times 10^{-12}$ at 700 Hz for Type I and $\Omega_{gw} \sim 3 \times 10^{-13}$ at 100 Hz for Type II. We should remark that this estimates remain uncertain due to the difficult to predict the waveform and the parameters of the supernovae gravitational wave emissions.

- **Core collapses: supernovae to black holes**. Assuming Population II and a mass range of 20 $M_\odot < M < 100\ M_\odot$ for the black hole progenitors, the expected background energy density maximum from these objects is $\Omega_{gw} \sim 5 \times 10^{-10}$ at $f = 500Hz$. If the mass of the progenitors is 8 $M_\odot < M < 20\ M_\odot$, the expected maximum is $\Omega_{gw} \sim 10^{-9}$ at 1 kHz. A general estimate of the gravitational wave background spectrum generated by core collapses supernovae is given by [20]:

$$H(f) \propto \frac{dE_{gw}}{df} = Ae^{-\frac{f-f_0}{2\sigma^2}} \tag{1.92}$$

where 200 $Hz < f_0 < 800\ Hz$ and $\sigma \sim 500$. The background signal generated by these sources might be detectable in third-generation detectors only if the efficiencies ϵ of the emission process are high enough.

Detection of stochastic background

A random signal such as the stochastic background is indistinguishable from instrumental incoherent noise of a single detector, at least considering short observation times. When the random field is produced by astrophysical sources with an anisotropic distribution (e.g. by sources in our galaxy), the detection would be possible having long observation times, as the ground-based detector changes its orientation due to Earth orbital motion, producing a signal modulation.

Another way of detecting the stochastic radiation consists in performing a cross-correlation between two detectors: the random signal measured by one detector is used as a template for the signal measured by the second detector. In principle the local noise of the two detectors will be incoherent and so they will have a low correlation; instead an astrophysical stochastic background will produce a stronger correlation. We have to consider an important remark: the signals can only match well if the gravitational wave wavelength is longer than the separation between the detectors; otherwise a wave maximum will reach a detector before the other producing a time delay, and this will degrade the match. Let us study this method [8]: the simplest possible case is to have two independent coincident and co-aligned gravitational wave detectors, characterized by two outputs:

$$s_1(t) = h_1(t) + n_1(t) \tag{1.93}$$
$$s_2(t) = h_2(t) + n_2(t) \tag{1.94}$$

where we indicate the signal $s_i(t)$ as composed of the gravitational strain $h_i(t)$ produced by the stochastic background, and the intrinsic detector noise $n_i(t)$. We will assume that the two noises are stationary, Gaussian, statistically independent of one another[1] and much larger than the gravitational strain $h(t)$, which will be the same for coincident and co-aligned detectors. We can obtain the correlation signal S by multiplying together the two outputs and integrating over time T:

$$S =< s_1\ s_2 > \equiv \int_{-T/2}^{T/2} s_1(t)s_2(t)dt \tag{1.95}$$

[1] obviously this assumption is unrealistic for the case of coincident and co-aligned detectors, but it is reasonable when considering the case of widely separated detectors.

Since we assumed that detector noise n_i is great if compared to the signal, we can write:

$$\begin{aligned} S &= < h_1\, h_2 > + < n_1\, h_2 > + < h_1\, n_2 > + < n_1\, n_2 > \\ &\approx < h_1\, h_2 > + < n_1\, n_2 > \end{aligned} \tag{1.96}$$

where we have neglected terms like $< n_i\ h_j >$ that are smaller than $< n_i\ n_j >$ but statistically identical. Note that in eq. 1.101 the first term $< h_1\ h_2 >$ will be proportional to the observation time T, since $h_1(t) = h_2(t) = h(t)$; the second term $< n_1\ n_2 >$ can be considered as the random walk of one-dimensional line, and then on the average it grows as $T^{1/2}$. Therefore, increasing the observation time, it is possible in principle to detect a stochastic background signal immersed in any level of noise. From computation [14] we obtain:

$$< h_1\, h_2 > \ \propto\ |\tilde{h}(f)|^2 \Delta f T \propto \Omega_{gw}(f) \Delta f T \tag{1.97}$$

$$< n_1\, n_2 > \ \propto\ |\tilde{n}(f)|^2 (\Delta f T)^{1/2} \tag{1.98}$$

where f is the central frequency of the detector sensitivity band, Δf is the effective bandwidth and we used the *tilde* character to indicate the Fourier transform:

$$\tilde{h}(f) = \int_{-\infty}^{\infty} e^{2\pi i f t} h(t) dt \tag{1.99}$$

If we set the SNR equal to 1, from eq. 1.97 and 1.98 we can write the minimum detectable level of $\Omega_g w$:

$$\Omega_{gw}^{min} \propto |\tilde{n}(f)|^2 (\Delta f T)^{-1/2} \tag{1.100}$$

Let us analyze a more realistic situation, when the arms of the two detectors are not parallel and there is a time delay between them. In this case $h_1 \neq h_2$, resulting in a partial overlap between the gravitational wave strains in the two detectors, that we will indicate with the overlap reduction function $\gamma(f)$. The generalization of eq. 1.95 is given by:

$$S \equiv \int_{-T/2}^{T/2} dt \int_{-T/2}^{T/2} dt' s_1(t) s_2(t') Q(t - t') \tag{1.101}$$

where $Q(t-t')$ is the real filter function, and depends on the relative position and orientation of the two detectors. If we consider two detectors characterized by a narrow bandwidth, located very close to each other and with the same orientations, then the real filter function would be a Dirac delta function $Q(t - t') \equiv \delta(t - t')$, i.e. we would obtain the situation expressed by eq. 1.95. In a general case $Q(t-t')$ is also a function of the spectral characteristic of the stochastic background and detector noise, and so it is related to $\gamma(f)$.

Assuming that the filter function is real, i.e. $\tilde{Q}(-f) = \tilde{Q}^*(f)$, by using the Fourier transform eq. 1.101 in the frequency domain becomes:

$$S \equiv \int_{-\infty}^{\infty} df \int_{-\infty}^{\infty} df' \delta_T(f - f') \tilde{s}_1^*(f) \tilde{s}_2(f') \tilde{Q}(f) \tag{1.102}$$

where the function $\delta_T(f - f')$ is a finite time approximation to the Dirac delta function, being defined by:

$$\delta_T(f - f') = \int_{-T/2}^{T/2} dt\ e^{-2\pi i f t} \equiv \frac{sin(\pi f T)}{\pi f} \tag{1.103}$$

We note that eq. 1.103 reduces to the Dirac delta function in the limit $T \to \infty$. Assuming an isotropic, unpolarized and Gaussian stochastic background we can obtain the strain signal and strain noise Fourier amplitudes [14]:

$$< \tilde{h}_1^*(f)\ \tilde{h}_2(f') > \ = \ \delta(f - f')\frac{3H_0^2}{20\pi^2}\frac{\Omega_{gw}(|f|)\gamma(|f|)}{|f|^3} \tag{1.104}$$

$$< \tilde{n}_i^*(f)\ \tilde{n}_j(f') > \ = \ \frac{1}{2}\delta(f - f')\delta_{ij}P_i(|f|) \tag{1.105}$$

where the two sites are indicated by the indices i, j and $P_i(|f|)$ is the power spectral noise density.

We still have to choose an optimal filter function $Q(f)$ such that the SNR is maximized. Since we assumed that the noise in each detector is uncorrelated with the other, and also with the gravitational wave strain h, we can obtain its Fourier transform expression given by [8]:

$$\tilde{Q}(f) = \lambda\frac{\gamma(|f|)\Omega_{gw}(|f|)}{|f|^3 P_1(|f|)P_2(|f|)} \tag{1.106}$$

where λ is an overall normalization constant. The related expression of the optimal SNR from the cross-correlation is given by:

$$\left(\frac{S}{N}\right)^2 = \frac{9H_O^4 T}{50\pi^4}\int_0^\infty df\frac{\gamma^2(f)\Omega_{gw}^2(f)}{f^6 P_1(f)P_2(f)} \tag{1.107}$$

From 1.107 we note that SNR depends on the spectrum of gravitational wave $\Omega_g(f)$, that is a function that we do not know *a priori*. It means that in practice we need to have a set of such filters to perform a cross-correlation observation.

By using the data collected by the first generation of interferometric detectors (see chapter 2), these cross-correlation methods gave an upper limit on the gravitational wave density fraction $\Omega_{gw} \leq 6.9^{-6}$ at 95% confidence [21]. We remark that this value is lower than other limits set by Big Bang nucleosynthesis ($\Omega_{gw}^{BBN} \leq 10^{-5}$) and from the CMBR measurement experiments ($\Omega_{gw}^{CMBR} \leq 9.5 \times 10^{-6}$).

1.3.2 Compact binary coalescences

Compact binaries consist of neutron stars and/or black holes binary systems. These objects evolve by emitting gravitational radiation which extracts orbital binding energy and angular momentum from the system. Therefore the two components of a compact binary will inspiral toward each other end eventually they will merge. We can describe the evolution of this kind of systems in three phases (see fig. 1.4):

Inspiral A binary system spends hundred of millions of years in this phase. The emission of gravitational waves and the dynamics of the system can be solved in a first approximation using the Newtonian mechanics and, for a more accurate description, the Post-Newtonian approach [22]. Let us consider a system composed of two point masses M_1 and M_2, with a separation a and an orbital period P. If we assume a quasi-circular orbit we know from the third Kepler's law that $G(M_1 + M_2) = v^2 a$, having written the orbital speed as $v = 2\pi a/P$, then we obtain:

$$\left(\frac{v}{c}\right)^2 = G\frac{M_1 + M_2}{ac^2} \tag{1.108}$$

By substituting eq. 1.108 in eq. 1.60, averaging over the orbital period and orientation of the orbital plane, we can derive the expression of the gravitational wave amplitude [23]:

$$h \equiv \sqrt{< h_+^2 > + < h_\times^2 >} = \left(\frac{32}{5}\right)^{1/2} \frac{(\pi f)^{2/3}}{R_0} \frac{G^{5/3}}{c^4} \frac{M_1 M_2}{(M_1 + M_2)^{1/3}} \tag{1.109}$$

where R_0 is the distance of the detector from the source, and f is the emitted gravitational wave frequency, defined by:

$$f = \frac{1}{\pi}\left[\frac{G(M_1 + M_2)}{a^3}\right]^{1/2} \tag{1.110}$$

In eq. 1.109 we observe that the amplitude h depends on a particular combination of the two masses:

$$\mathcal{M} = \left[\frac{(M_1 M_2)^3}{M_1 + M_2}\right]^{1/5} \tag{1.111}$$

$\mathcal{M}$ is called the *chirp*-mass because it largely determines the rate at which the system frequency evolves, or "chirps". Using the definition 1.111 in eq. 1.109 we obtain:

$$h \propto \frac{\mathcal{M}^{5/3} f^{2/3}}{R_0} \tag{1.112}$$

which determines the energy spectrum:

$$\frac{dE}{df} = \frac{(\pi G)^{2/3}}{3} \mathcal{M}^{5/3} f^{-1/3} \tag{1.113}$$

From eq. 1.110 and 1.112 we note that as the two objects approach each other, i.e. a decreases, the emitted gravitational wave frequency and amplitude increase, producing a final signal which is called the *chirp*.

Using the Post-Newtonian expansion of the Einstein's equations we can obtain a more accurate computation of the gravitational wave amplitudes in the inspiral phase. Let us consider a binary system with a *chirp*-mass $\mathcal{M}$,

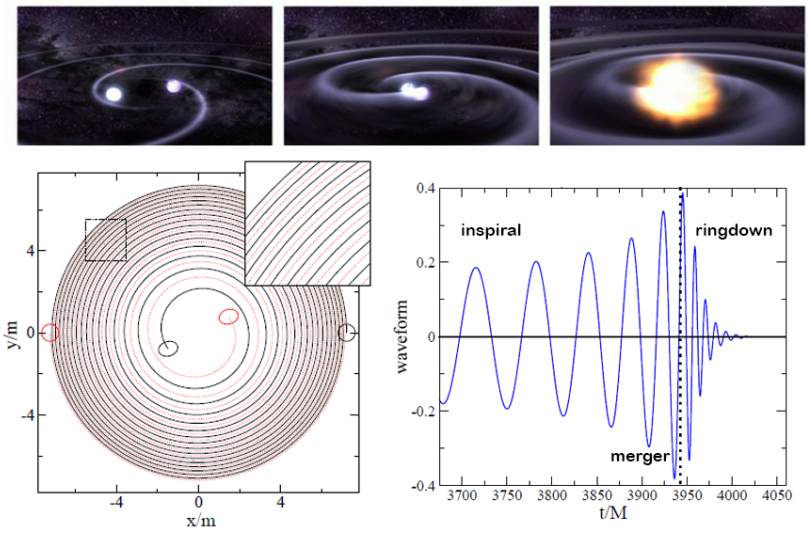

Figure 1.4: Compact binary coalescence: artist's representation, waveform and orbital decay. The inspiral phase emission can be calculated with a Newtonian or Post-Newtonian approach, the merger phase waveform comes from numerical relativity simulations, and the ringdown phase is calculated by the black hole perturbation theory.

placed at a luminosity distance D_L: from Post-Newtonian computations the dominant parts of the two polarization are given by [24]:

$$h_+(t) = 2\frac{\mathcal{M}^{5/3}(\pi f)^{2/3}}{D_L}(1+\cos^2 i)\cos(2\Phi(t)+\Phi_0) \tag{1.114}$$

$$h_\times(t) = -4\frac{\mathcal{M}^{5/3}(\pi f)^{2/3}}{D_L}\cos i \sin(2\Phi(t)+\Phi_0) \tag{1.115}$$

where i is the angle between the orbital angular momentum and the line-of-sight, and $\Phi(t) \equiv \Phi(t; t_0, M_1, M_2)$ is the orbital phase of the equivalent one-body system around the centre of mass of the binary system. Equations 1.114 and 1.115 contain only the dominant terms which oscillates at twice the orbital frequency. In a more accurate approach we should consider also higher order amplitude corrections which contain other harmonics (i.e. phase terms containing $k\Phi(t)$, being k a positive integer number). Moreover, the expressions 1.114 and 1.115 are valid for a system of non-spinning components on a quasi-circular orbit, that is not a rather realistic assumption. A detailed Post-Newtonian calculation must take into account the spin-orbit and the spin-spin couplings between the two components of the binary system, which produce a characteristic modulation in the emitted gravitational signal (see fig. 1.6). The gravitational wave frequency at the end of the inspiral phase, when the two massive objects collide, is given by:

$$f^* \approx 4\left(\frac{M}{M_\odot}\right)^{-1} kHz \tag{1.116}$$

Note that eq. 1.116 is valid only for a system composed of compact objects. Otherwise, if we consider a large stellar object (i.e. a separation between the two bodies larger than the innermost stable circular orbit), we should consider a different proportionality to the factor $1/a$, resulting in a lower transition frequency.

Merger In this phase the two stellar objects are moving at relativistic speed and experiencing extreme gravitational fields, eventually resulting in a violent dynamical fusion that leads to the formation of a black hole, relasing a fraction of their rest-mass energy in gravitational radiation. The Post-Newtonian approximation is no longer valid when the two objects get very close to each other. In this case an accurate description of the system dynamics requires the full non-linear structure of the Einstein's Equations (see. sec. 1.1), as the problem involves strong relativistic gravity and tidal deformations an disruption. An effective way to solve this problem is by means of numerical simulations, which widely investigated the case of binary black holes in the previous years [25]. However the merger phase in the case of binary neutron stars is still not well understood, as it is complicated by many unknown physical effects, such as the equation of state of neutron stars and the effect of their magnetic fields. The timescale of the merger phase is very short: from milliseconds in the case of stellar-mass black holes to seconds in the case of the heaviest black holes. During this phase a significant amount of the progenitor's matter could have such a high angular momentum which can contrast the falling into the black hole horizon. This leads to the formation of a temporary accretion disk around the black hole which can power a gamma-ray burst jet (see sec. 1.3.6). Note that although this phase is very short compared to the system evolution timescale, it can generate a gravitational radiation luminosity close to L_0 (see sec. 1.2.5), exceeding the luminosity of the entire Universe in electromagnetic radiation in that short duration.

Ringdown After the two progenitor neutron stars and/or black holes have merged to form a massive compact object, it settles down to a quiescent state by radiating the deformations inherited during the merger, in the so called ringdown phase. To compute the emitted gravitational radiation after the merger, the perturbation theory can be used, consisting of a superposition of quasi-normal modes of the object formed in the merging. These modes are characterized by a unique signature that depends only on the mass and spin angular momentum in the case of a final black hole. If we consider instead the formation of a neutron star in the merging, the signature will also depend on the equation of state of its supra-nuclear matter. The duration of this phase is comparable to the one of the merging, depending on the mass of the final object; in practice it consists of two to three cycles.

The gravitational signal emitted by a compact binary will last some hours in the typical low frequency band of third-generation ground-based detectors[2].

[2]for a binary composed of two 1.4 $M_\odot$ neutron stars it will be: $\Delta t_{1-5Hz} \sim 10^d$ and $\Delta t_{5-10Hz} \sim 2^h$; for a binary composed of two 20 $M_\odot$ black holes it will be $\Delta t_{1-2Hz} \sim 2^d$ and $\Delta t_{2-10Hz} \sim 1^h$.

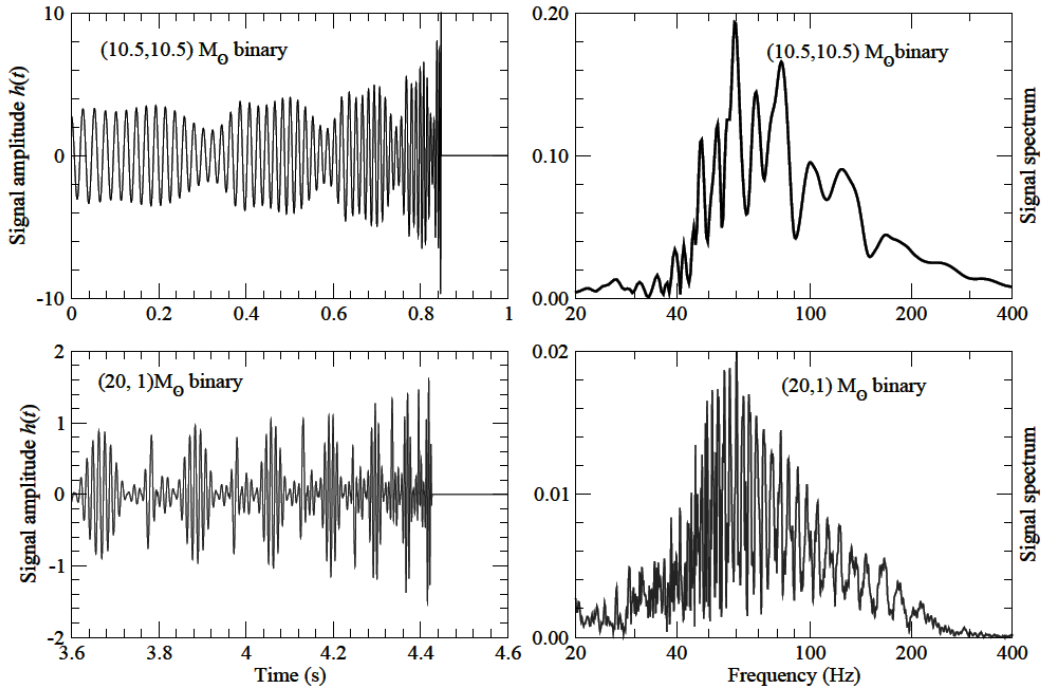

Figure 1.5: Coalescences from compact binary systems [26]: left plots show the time-domain waveforms, right plots show the frequency spectrum. The upper plots are related to a system composed of two equal masses, the lower plots to a system composed of a neutron star - black hole system. In the waveform it is evident the modulation produced by the interaction between the spins of the bodies and the orbital angular momentum. In the second case the signal amplitude is smaller and the duration is longer due to the larger mass ratio of the system, moreover the signal modulation is stronger as the spin-orbit precession of the orbital plane is greater.

Since there are not any direct observation of these events in the electromagnetic window, a prediction for the compact binary mergers would be entirely based on theoretical estimates. In a first approximation the binary merger rate depends on the formation rate of Type II supernovae (see sec. 1.3.5), which are the main progenitors of both neutron stars and black holes. Hence the merger rate is roughly proportional to the star formation rate, and we expect that it increases with redshift. Recently some progenitors of binary black holes have been discovered, such as the IC10 X-1 system, composed of a black hole and a massive Wolf-Rayet star [27]. This kind of progenitors[3] lie in low metallicity environments, and we expect higher formation rates and higher masses in such low metallicity gas clouds. This fact suggests that in the early universe, where fewer generations of stars have produced metals, massive binaries could have formed very frequently. The compact binary formation and merger rates are also increased by mass segregation in the core of protoclusters, where a massive object can easily form a compact binary, being born in a multiple system or substituting the lighter companion in a binary system through a three-body interaction. Moreover, the close approach of other stellar objects in a mass-segregated core of a cluster could extract angular momentum from the compact binary, reducing the coalescence time and therefore statistically increasing the merger rate.

Source	Rate ($Mpc^{-3}Myr^{-1}$)
BNS	$0.1 - 6$
NS-BH	$0.01 - 0.3$
BBH	$2 \times 10^{-3} - 0.04$

Table 1.1: Expected coalescence rates per Mpc^3 and Myr in the local universe ($z \approx 0$) [26] for three kind of compact binary systems: binary neutron stars (BNS), neutron star - black hole (NS-BH) and binary black holes (BBH). A rough estimate of the expected detection rates are given by the multiplication of these coalescence rates by the detector observational horizon.

Intermediate-mass binary black holes

Black holes can be divided into three categories according to their mass: stellar-mass (SBH) with $3\ M_\odot < M <\sim 30\ M_\odot$, intermediate-mass (IMBH) with $10^2 M_\odot < M < 10^4 M_\odot$, and supermassive (SMBH) with $10^4 M_\odot < M < 10^9 M_\odot$. The IMBHs binaries are a promising source of gravitational radiation in future ground-based and space-based gravitational wave detectors. In the early Universe ($z \geq 10$) the negligible metallicity might have enabled the formation of this intermediate-mass black holes from very high-mass Population III stars or via direct collapse of low-rotation gas disks. Observations of quasars out to $z \sim 7$ suggest that these early generation of IMBHs could have acted as initial seeds for progressive SMHN growth. In the present Universe, IMBH will form in globular

[3]usually such compact binary systems composed of a black hole and a massive star have a X-ray counterpart powered by the accretion disk formed around the black hole.

clusters. Since an IMBH will be the most massive object of the cluster, it will quickly sink to the center of it and eventually substitute, through a three-bodies interaction, into a binary system with a compact object companion. Subsequently, close stellar flybys in the dense core of the cluster will remove angular momentum from the system reducing the separation between the binary components, and at the end there will be a merging via an intermediate-mass-ratio inspiral (IMRI) on a timescale of less than $10^9\ yr$. If the stellar binary fraction (f_b) of the globular cluster is sufficiently high ($f_b \geq 10\%$ from recent simulations [28]), two or more IMBHs can form and sink to the center, where they will form a binary composed of two IMBH and eventually merge. Observations and simulations [29] suggest that $f_b \geq 30\%$, therefore the formation of the IMBH binaries in dense and young star clusters could be likely. Moreover, the merger of two stellar clusters (both with an IMBH in their core) could be an alternative mechanism to form this kind of binaries. The detection rate of IMBH coalescences in advanced gravitational wave

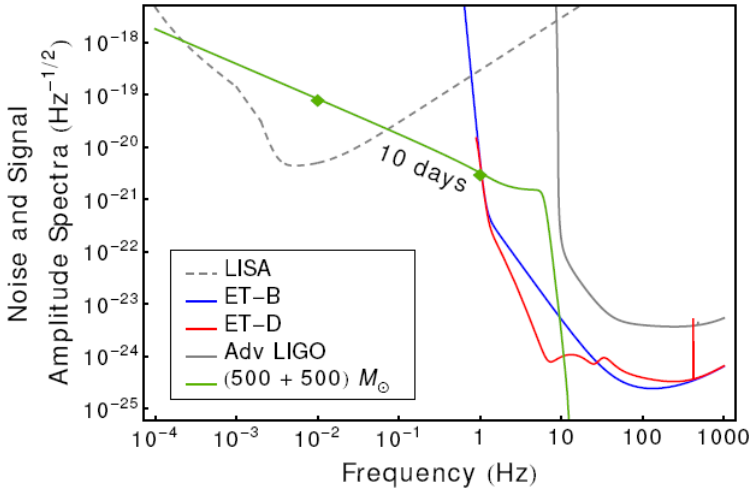

Figure 1.6: Expected gravitational signal amplitude from a binary composed of two IMBH ($500M_\odot - 500M_\odot$) [26]. In the figure there are also reported the design-sensitivity curves for Advanced, third generation and space (LISA) detectors (see chapter 2).

detectors (see chapter 2) can be estimated by:

$$\dot{N}^{2gen}_{IMBH} \sim 40 \left(\frac{g \times g_c}{10^{-2}} \right) \ yr^{-1} \tag{1.117}$$

where g is the fraction of globular clusters hosting a pair of IMBHs and g_c is the fraction of star forming clusters with $10^4 M_\odot < M_{cl} < 10^6 M_\odot$. The detection rate for past first generation detectors and for the future third generation detectors can be obtained multiplying $\dot{N}^{2gen}_{IMBH}$ respectively by a factor 10^{-2} and 10^2 [26].

Massive black holes mergers and captures

A very intense gravitational wave source in the low-frequency band can be expected from the merger of massive and supermassive black holes (SMBH), such as those

in the cores of galaxies. Galactic mergers are likely to give rise to these events, therefore the galactic merger rate gives a rough estimate of SMBH merger rate. Potentially detectable low-frequency gravitational waves can also be generated by low-mass objects (such as smaller black holes, neutron stars white dwarfs or even main sequence stars) orbiting massive black holes in the high density galactic nuclei. This kind of sources probably exists in the nucleus of our own Galaxy, and could be in principle be detectable well beyond the Virgo Cluster. The main constraint for the gravitational wave emission of this objects is whether or not the gravity gradient from the central black hole is sufficient to tidally disrupt the companion object: in this case the disrupted object will form an accretion disk slowly falling into the black hole, with a negligible gravitational radiation emission. In order to avoid the tidal disruption, the Swartzchild radius of the black hole must be large compared with the radius of the infalling object: the black hole must have a mass $10^7 M_\odot < M < 10^8 M_\odot$ for main sequence stars, $10^4 M_\odot$ for white dwarfs and $10 M_\odot$ for neutron star captures.

Cosmology with binary coalescences

In physical cosmology the distance-redshift relation is a crucial measure in order to study the expansion history of the universe, and then to obtain constraints on the cosmological parameters such as the energy densities. In particular, the distance-redshift relation is used to constrain the equation of state and the energy density of the *dark energy*, which is the main contribution to the total mass-energy of the universe and produces the increase of the expansion rate of the universe [30, 31]. The discovery of this acceleration was possible by using electromagnetic *standard candles* such as type Ia supernovae[4] (see sec. 1.3.5) observed at different redshifts z: their apparent luminosity F can be calibrated, since we know their intrinsic peak luminosity L, in order to obtain their luminosity distance, that is $D_L = (L/4\pi F)^{1/2}$. The "distance ladder" based on type Ia supernovae works up to redshifts of a few, while it is necessary to find a completely different kind of sources on larger distance scales. In 1986 it has been shown by Schutz [32] that gravitational wave observations can provide *standard sirens* such as the chirping signal from the coalescence of compact binary systems. For instance the inspiral phase evolution of BBH/BNS systems, descibed above in this subsection, is well modeled and the gravitational wave amplitudes are expressed by eq. 1.114, 1.115. Since the the phase $\Phi(t)$ of the signal is known from Post-Newtonian computation, using matched filters it is possible to measure $\mathcal{M}$, f, t_0 and Φ_0. The remaining unknown angular parameters of eq. 1.114, 1.115 can be derived by a network of three non-co-located detectors measuring three independent combinations of the polarizations and two time delays of the observed signal. From the knowledge of the previous parameters and having properly considered the antenna pattern function of the detectors (see sec. 2.1), from eq. 1.114, 1.115 it is possible to determine the luminosity distance with the fairly high accuracy of $\Delta D_L/D_L \sim 1 - 10\%$ [33]. Obviously gravitational waves do not provide informations about the redshift of the

[4]for this discovery A. Riess, S. Perlmutter and P. Schmidt got the Nobel prize in physics in 2011

emitting source, therefore to study the expansion rate change of the universe the measure of z from an electromagnetic counterpart (e.g. the host galaxy) is needed (see sec. 1.4). Moreover, the redshift z is entangled in the inspiral evolution of the binary systems: since the evolution timescales are redshifted, then the measured masses are also redshifted[5] [33]. Hence the gravitational wave amplitudes emitted in the inspiral phase at cosmological distance and expressed by eq. 1.114, 1.115 must be rewritten with the mapping $\mathcal{M} \rightarrow (1+z)\mathcal{M} = \mathcal{M}_z$. Furthermore, knowing the redshift of the electromagnetic counterpart and considering only local coalescences (i.e. within $z \ll 1$), through the calculation of the luminosity distance D_L, derived from the measurement of the related gravitational signal, it is also possible to measure the Hubble constant, which is defined as $H_0 = cz/D_L$, with a very high accuracy. From the measurement of the masses of coalescing systems and from the relative redshift provided by electromagnetic counterparts it is also possible to study the evolution of the star formation rate $SFR(z)$ and binary fraction $f_b(z)$. In particular, at higher redshift we expect the formation of more massive BHs and so more massive compact binaries. It is caused both by higher SFR and by lower metallicities, which imply lower mass-loss rates in the stellar phase and then the formation of higher masses BHs. Therefore the detection of gravitational wave signals produced by compact binaries may give us valuable informations about their population evolution.

1.3.3 Binary coalescence precursors: PSR1913+16

The existence of gravitational waves is shown indirectly from the study of binary neutron stars that are binary coalescence precursors. Their electromagnetic emission is oriented with the neutron star magnetic field axis, that is misaligned with the rotational spin axis (see fig. 1.9). Therefore, when their emission axis is pointed toward the Earth, the neutron star appears as a pulsating source with a very precise interval between pulses[6]. When the neutron star is part of a compact binary system its pulsating signal is characterized by a modulation equal to their orbital period P. Binary neutron stars emit gravitational radiation loosing orbital energy, therefore in the adiabatic approximation we can express this concept writing:

$$L_{gw} \equiv \frac{dE_{gw}}{dt} = -\frac{dE_{orb}}{dt} \tag{1.118}$$

In eq. 1.118 the luminosity L_{gw} can be derived by equations 1.63 taking into account the factor c^5/G, obtaining:

$$L_{gw} = \frac{32G^4}{5c^5}\frac{\mu^2(M_1+M_2)^3}{a^5} \tag{1.119}$$

where $\mu = (M_1M_2)/(M_1+M_2)$ is the reduced mass and a is the separation between the two compact objects. If we consider a Keplerian orbit, the orbital energy will

[5] this effect make a system with total mass M placed at redshift z indistinguishable from a local system with total mass $(1+z)M$.

[6] because of this characteristic emission a radiating neutron star is often called *pulsar*, i.e. pulsating star.

be given by:

$$E_{orb} = -\frac{1}{2}\frac{G\mu(M_1 + M_2)}{a} \tag{1.120}$$

Hence substituting the time derivative of eq. 1.120 and the eq. 1.119 in eq. 1.118, considering the third Kepler's law: $P^2 = a^3 G M_1 M_2 / 4\pi^2 \mu$, we can derive the orbital period P variation due to the emission of gravitational waves:

$$\frac{dP}{dt} = \frac{3}{2}\frac{P}{E_{orb}} L_{gw} \tag{1.121}$$

Taking also into account the orbital eccentricity e, we can derive a more accurate estimate of the time rate for the change of orbital period from the quadrupole formula (eq. 1.61) applied to a system made of two point-masses in Keplerian orbit [34]:

$$\left\langle \frac{dP}{dt} \right\rangle = -\frac{192\pi}{5c^5}\left(\frac{2\pi G}{P}\right)^{5/3} \frac{M_{ns} M_c}{(M_{ns} + M_c)^{1/3}} \frac{1 + \frac{73}{24}e^2 + \frac{37}{96}e^4}{(1 - e^2)^{7/2}} \tag{1.122}$$

where M_{ns} and M_c are respectively the mass of the neutron star and that of its companion.

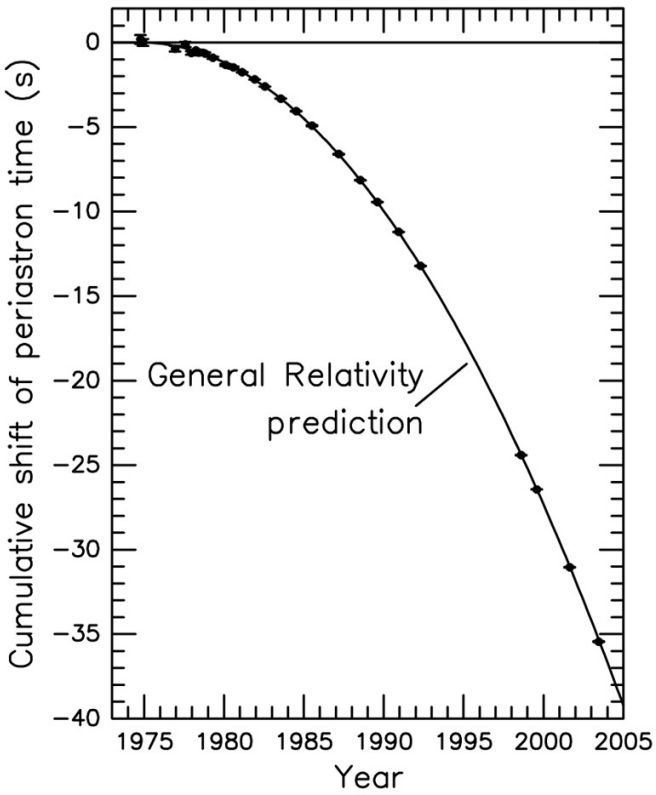

Figure 1.7: The orbital period decay of the binary PSR1913+16. The observational points are in excellent agreement with the emission of gravitational waves predicted by general relativity [35].

In 1974 R. A. Hulse and J. H. Taylor discovered the binary pulsar PSR1913+16, finding a pulse period $p = 59\ ms$ with a modulation $P = 7.752^h$. The masses of the pulsar and its companion are estimated to be respectively $M_{ns} = 1.4398\ M_\odot$ and $M_c = 1.3886\ M_\odot$, with an orbital eccentricity $e = 0.6171$ [35]. From eq. 1.122 they obtained the predicted value of the orbital period decay:

$$\left\langle \frac{dP}{dt} \right\rangle = -(2.402531 \pm 0.000014) \times 10^{-12} \tag{1.123}$$

After 30 years of observations the predicted value of 1.123 is in excellent agreement with the observational one (see fig. 1.7), and their ratio is:

$$R = \left(\frac{dP}{dt}\right)_{obs} \left(\frac{dP}{dt}\right)^{-1}_{GR} = 0.997 \pm 0.002 \tag{1.124}$$

That is a remarkable check of general relativity in particular since it is done in a strong-field regime, and it is a quantitative evidence of the existence of gravitational waves. For this result Hulse and Taylor got the Nobel Prize in 1993.

1.3.4 Isolated neutron stars

There are almost 2000 neutron stars known presently, observed as pulsars either in the radio or X-ray bands. Obviously the electromagnetic detection of neutron stars is biased toward pulsars which have their magnetic field axis aligned with our line-of-sight, therefore we expect at least 10^8 spinning neutron stars considering only our galaxy. Since they are generated from collapsed star cores that reached the Chandrasekhar limit, their mass is $M \sim 1.44\ M_\odot$ (i.e. the *Chandrasekhar mass*); their typical size is related to the Schwarzschild radius: $R_{NS} \sim 10\ km$. Neutron star's electromagnetic emission can be powered by the rotational energy (*rotation-powered pulsars*), by the gravitational potential energy of matter in an accretion disk (*accretion-powered pulsars*, usually X-ray sources) and by the decay of strong magnetic fields (*magnetars*, usually X-ray and γ-ray sources). The parameters of many of these objects have been accurately measured, in particular their frequency f_{rot}, which slows in time (i.e. $\dot{f}_{rot} < 0$) as their rotational period P increases. Depending on this period pulsars can be divided into two categories:

- **millisecond pulsars**, when their orbital period is $P \leq 20\ ms$;
- **long-period pulsars**, when their orbital period is $P > 20\ ms$

A spinning neutron star can be a periodic source of gravitational radiation when it is characterized by a non-axisymmetric mass distribution, giving rise to a time-varying quadrupole momentum. In this case its gravitational wave emission due to a non-negligible ellipticity will occur at twice the rotational frequency of the star, i.e. $f = 2f_{rot}$. The asymmetry may be generated by different effects:

- the neutron star structure may be distorted by the high spinning rate of the pulsar which produces an equatorial bulge, and by strong magnetic field local interactions; because of these effects the rotational axis may not coincide with the symmetry axis;

Figure 1.8: The pulsar at the center of the Crab nebula. It was generated by the supernova explosion observed in 1054 A.D. (SN1054). The rotational period of this pulsar is $P \approx 33.5\ ms$. This picture is a false-color composite of X-ray (in blue, by NASA's Chandra X-ray Observatory), visible band (in green, by NASA's Hubble Space Telescope) and radio band (in red, by NRAO/AUI/NSF) observations.

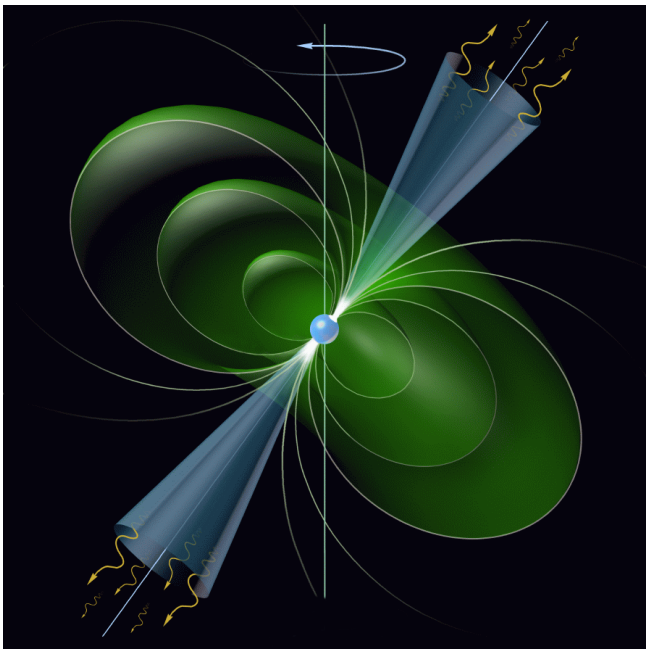

Figure 1.9: Artist's representation of a radiating neutron star; the electromagnetic beams are drawn in blue, magnetic field lines in green. The pulsar is visible in the *EM*-band when the beam intersects periodically with our line of sight.

- inhomogeneities in the star core and/or crust, produced in the neutron star formation or by sudden crustal adjustment (starquakes);
- an accretion disk may surround the neutron star, especially in close binaries, and it can have an angular momentum misaligned with that of the neutron star;
- instabilities (such as glitches and r-modes) in the neutron star fluid.

The expected gravitational radiation amplitude generated by a pulsar is given by [36]:

$$h_0 = \frac{4\pi^2 G}{c^4}\frac{I_{zz}\epsilon f^2}{r} \tag{1.125}$$

where I_{zz} is the star momentum of inertia with respect to the rotation axis, r is the star distance and ϵ is the equatorial ellipticity defined by:

$$\epsilon = \frac{I_{xx} - I_{yy}}{I_{zz}} \tag{1.126}$$

Therefore we can write the two polarization amplitudes in terms of h_0:

$$h_+(t) = h_0 \left(\frac{1+\cos^2 i}{2}\right)\cos\phi(t) \tag{1.127}$$

$$h_\times(t) = h_0 \cos i \sin\phi(t) \tag{1.128}$$

where i is the angle of inclination of the star's rotation axis with respect to the line-of-sight and $\phi(t)$ is the signal phase function, which takes into account timing effects such as the Roemer delay, the gravitational redshift produced by the Sun and by the time dilatation due to Earth's motion, and the Shapiro delay [37] produced by the curvature of spacetime near the Sun. The ellipticity ϵ is not know in principle but it can be estimated by crustal models as a function of the breaking strain U_b. These models indicates that the crustal structure can sustain the maximum ellipticity [38] $\epsilon \leq 2 \times 10^{-4} U_b$, with $U_b \sim 0.1$ [39]. However a rigorous calculation of the allowed maximum ellipticity should take into account also the equation of state of the neutron star's core [40, 41] and the interaction of the inner magnetic field [42, 43] which may produce asymmetries, especially in young neutron stars.

We define the spindown upper limit to the amplitude h_0 of the gravitational radiation emitted by a pulsar by assuming that all the lost rotational energy is converted into gravitational wave emission:

$$\dot{E}_{rot} = \dot{E}_{gw} \tag{1.129}$$

where we have to substitute the expressions of $\dot{E}_{rot}$ and $\dot{E}_{gw}$:

$$\dot{E}_{rot} = I\omega\dot{\omega} \tag{1.130}$$

$$\dot{E}_{gw} = \frac{2c^3}{5G}\omega^2 r^2 (h_0)^2_{sd} \tag{1.131}$$

The angular velocity ω and the distance r are known from electromagnetic observations, and we can assume $I \sim 10^{38}\ kg\ m^2$. Therefore, from eq. 1.129 we obtain the spindown upper limit of the known pulsars $(h_0)^2_{sd}$, which ranges between 10^{-28} and 10^{-24} (see fig. 1.10). The weakness of this signal implies an integration over long periods, with the related data analysis complications, such as those considered above in the signal phase function $\phi(t)$. Using the data acquired in the past years by the interferometric gravitational wave detectors Virgo and LIGO (see chapter 2) it was possible to find the upper limits to the gravitational emission of the pulsars Crab [44] (shown in fig. 1.8) and Vela [36], finding respectively $(h_0)^{Crab}_{obs} < 2.4 \times 10^{-25}$ and $(h_0)^{Vela}_{obs} < 2 \times 10^{-24}$, which are smaller than their spindown upper limits $(h_0)^{Crab}_{sd} < 1.4 \times 10^{-24}$ and $(h_0)^{Vela}_{sd} < 3.29 \times 10^{-24}$. These results implies that the fraction of rotational energy lost converted into gravitational radiation emission is $< 2\%$ for the Crab and $< 35\%$ for the Vela. Moreover, from eq. 1.125 we also obtain a limit to their ellipticity, that is respectively: $\epsilon^{Crab} < 1.3 \times 10^{-4}$ and $\epsilon^{Vela} < 1.1 \times 10^{-3}$. In the next subsections we will analyze some relevant processes involved in the gravitational radiation emission from spinning neutron stars.

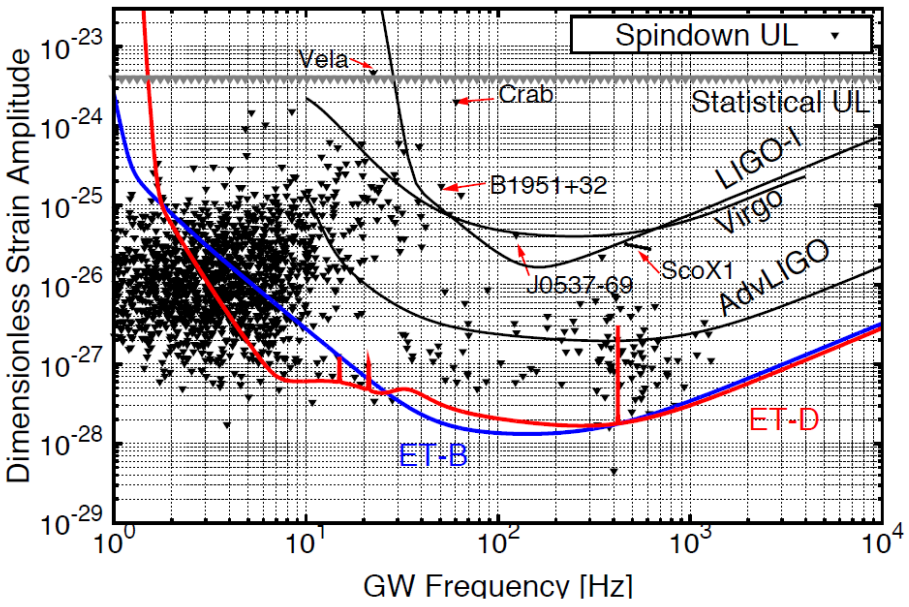

Figure 1.10: Upper limits and spin-down limits for known pulsars [26]. The spindown limit is obtained considering that the rotational energy lost is completely converted into gravitational wave emission. The sensitivity curves of first generation detectors (initial Virgo and LIGO), advanced and third generation detectors (Adv and ET) are drawn, considering an integration time of 2 and 5 years respectively. From this plot it is clear that most of the known pulsars might emit in the low frequency band, especially below 20 Hz.

Glitches

A glitch is a sudden and temporary increase of the angular velocity and spindown rate of the order $10^{-8} \leq \Delta\omega/\omega \leq 10^{-6}$ and $10^{-4} \leq \Delta\dot{\omega}/\dot{\omega} \leq 10^{-2}$, followed by a relaxation phase. It is usually observed in radio pulsars, such as the Crab and the Vela (see fig. 1.11), with typical intervals between these events which ranges between several months and years. The process which produces glitches in a spinning pulsar is still not well understood. It could be related to a transfer of angular momentum from the superfluids components of the inner structure of the neutron star to the crust and the core [45]. Another mechanism which can explain the glitches are repeated starquakes which cause significant internal heating and increased frictional coupling between the crust and the more rapidly rotating neutron superfluid interior [46]; also the interaction with the magnetic moment of the star and its possible angular variation should be taken into account. A pulsar glitch could excite f-modes instabilities (see next subsection), leading to a gravitational wave amplitude $h \propto 10^{-23}$, considering a source at a distance of 10 kpc.

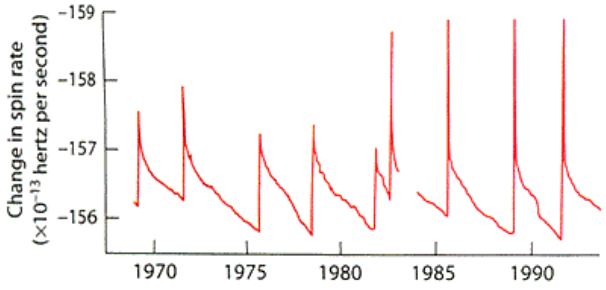

Figure 1.11: Glitches in the Vela pulsar observed between 1970 and 1995 [47]. A typical Vela's glitch produces a frequency change of the order of 10^{-6}, which roughly corresponds to an energy of the order of $10^{35}J$; a fraction of this energy might be radiated as gravitational waves.

Dynamical and secular instabilities

Due to dynamical instability a rotating axisymmetric fluid body becomes unstable to non-axisymmetric deformations. This kind of instability was studied in the classical theory of Newtonian MacLaurin spheroids and it is driven by the parameter β which is defined as the ratio of the rotational energy E_{rot} and the potential energy U_g of the rotating body:

$$\beta = \frac{E_{rot}}{U_g} \tag{1.132}$$

From the Newtonian theory the critical value of eq. 1.132 for an incompressible MacLaurin spheroid is $\beta_{dyn} = 0.27$. For a ratio greater than this value, i.e. for $\beta \geq \beta_{dyn}$, the spheroid becomes dynamically unstable. Relativistic simulations [48] suggest that for a neutron star $\beta_{dyn}^{GR} = 0.25$ and for $\beta \gg \beta_{dyn}^{GR}$ the spheroid forms spiral arms and ejects mass until the remnant reaches a dynamically stable

state, while for $\beta \geq \beta_{dyn}^{GR}$ it does not develop spiral arms nor eject mass but adjusts to form dynamically stable ellipsoidal-like configurations.

A dynamically stable neutron star can retain a β greater than the critical value $\beta_{sec} = 0.1375$, in this case the system may be affected by secular non-axisymmetric instabilities with a timescale greater than the dynamical one. The secular instability may be driven by the viscosity [49] in cold or matter-accreting neutron stars, but this mechanism is generally suppressed by relativistic effects. A more important mechanism is the Chandrasekhar-Friedman-Schutz instability (CFS) [50, 51] related to the gravitational radiation reaction. When the neutron star forms as a result of a collapse, since it is rapidly rotating (i.e. it is characterized by $\beta \geq \beta_{dyn}$), it can evolve in a configuration similar to a Jacobian ellipsoid. This configuration is nearly axisymmetric, therefore the amplitude of the emitted gravitational radiation would be small. When a quasi-stable configuration is reached, it may be possible that β is still greater than β_{sec}, resulting in the development of a secular instability. Let us consider the rotating Jacobian ellipsoid, its rate of radiation of the angular momentum L due to emission of gravitational waves is given by:

$$\frac{dL}{dt} = -\frac{32G}{5c^5}(I_{xx} - I_{yy})^2\omega^5 \tag{1.133}$$

where I_{ii} is the tensor of the momentum of inertia in the equatorial plane and ω is the angular velocity. Due to gravitational radiation reaction the object will evolve toward a MacLaurin spheroid (i.e. a non-radiating configuration) and this process will be characterized by the emission of gravitational waves with increasing frequency[7]. The maximum amplitude of the emitted gravitational waves during the transition from the Jacobi ellipsoid to the MacLaurin spheroid (see fig. 1.12) will be given by:

$$h_0 \approx 8.7 \times 10^{-19} \left(\frac{M}{1.4\ M_\odot}\right)^2 \left(\frac{10\ km}{R}\right) \left(\frac{10\ kpc}{r}\right) \tag{1.134}$$

where R is the radius of the neutron star and r is the distance of the observer, considering a polytropic index[8] $n = 1$ and $\beta = 0.12$. This maximum amplitude is reached at $\nu \sim 1.3\ kHz$. If the final MacLaurin spheroid is characterized by $\beta > \beta_{sec}$ a new secular instability will take place.

Through such an instability the object will evolve to a tri-axial configurations in two ways:

1. the Jacobi sequence, resulting in a tri-axial ellipsoid rigidly rotating around its smallest axis.

2. the Dedekind sequence, resulting in a fixed tri-axial ellipsoid characterized by an internal fluid circulation with constant vorticity. The angular velocity decreases to zero, which implies that the ellipsoid does not emit gravitational radiation.

[7] this emission is called the *spin-up wave*.

[8] neutron stars are well modeled by a polytropic equation of state: $P = k\rho^{(1+1/n)}$, where P is the pressure, ρ is the density and $0.5 < n < 1$ is the polytropic index.

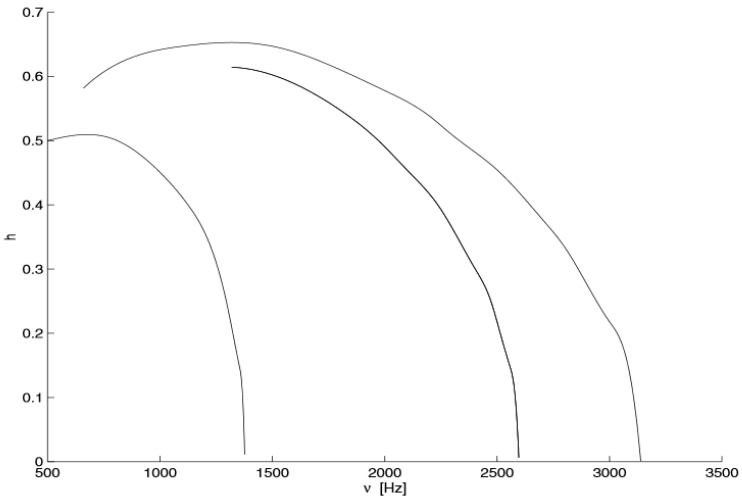

Figure 1.12: Amplitude of gravitational wave emitted by a secularly unstable neutron star, evolving from a Jacobi ellipsoid to a MacLaurin spheroid [52]. The three curves from the upper one correspond respectively to final MacLaurin spheroids with $\beta = 0.02,\ 0.12,\ 0.24$ and polytropic index $n = 1$.

The maximum gravitational wave amplitude from a neutron star described by a polytropic equation of state with index $n = 1$ evolving from a MacLaurin spheroid with $\beta = 0.24$ to a Dedekind ellipsoid will be given by:

$$h_0 \approx 4.2 \times 10^{-20} \left(\frac{M}{1.4\ M_\odot}\right)^2 \left(\frac{10\ km}{R}\right) \left(\frac{10\ kpc}{r}\right) \tag{1.135}$$

reached at a frequency $\nu \sim 500\ Hz$.

Let us remark that the value $\beta = \beta_{sec}$ corresponds to the critical rotation frequency $\nu_{sec} = \omega_{sec}/2\pi$ which has to be compared with the Keplerian frequency at which the centrifugal force balances the gravitational force at the equator:

$$\nu_K \approx \frac{1}{3}\sqrt{\pi G \bar{\rho}} \approx 1.25 \times 10^3 \left(\frac{M}{1.4 M_\odot}\right)^{1/2} \left(\frac{R}{10 km}\right)^{-3/2} Hz \tag{1.136}$$

where $\bar{\rho}$ is the mean density of the star. For rotation frequencies greater than ν_K the object will begin to loose matter forming spiral arms.

Dynamically or secularly unstable stars could develop global azimuthal non-axisymmetric structures that can be characterized in terms of modes m with a spatial structure proportional to $e^{im\Phi}$, where Φ is the azimuthal angle. In the context of gravitational wave astrophysics f-, g-, p-, w- and r-modes have been considered, but f- and r- modes are by far the most important for the gravitational emission.

f-modes In most cases the $m = 2$ mode (f-mode) is the dominant one, the so-called bar-mode instability. It is confined to the surface and can be excited by pulsar glitches. The f-mode becomes unstable for $\beta > \beta_{sec}$ when the

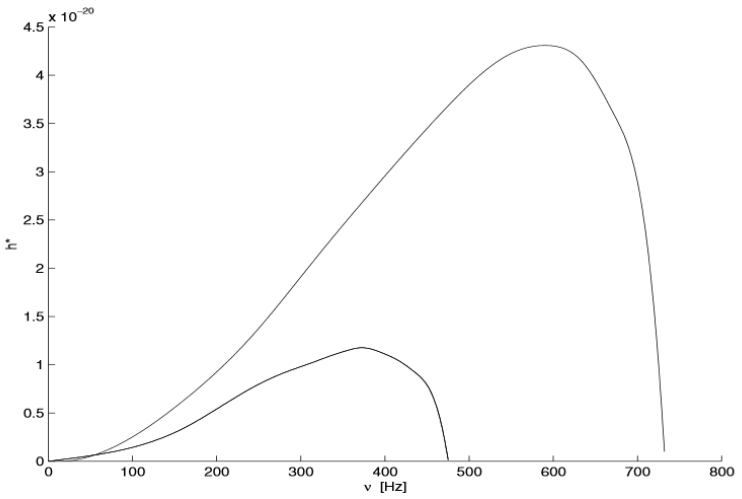

Figure 1.13: Amplitude of gravitational wave emitted by a secularly unstable neutron star, evolving from a MacLaurin spheroid toward a Dedekind ellipsoid [52]. The upper curve correspond to $\beta = 0.24$ and the other to $\beta = 0.20$, both are drawn for a star described by a polytropic equation of state with $n = 0.5$.

frequency ratio between ν_{sec} and ν_k reaches a critical value which depends on the considered equation of state (i.e. on the assumed polytropic index n). The gravitational wave amplitude from a $2R$-long spinning bar is $h_{bar} \propto MR^2\omega^2/r$ at a frequency f which is twice the rotational frequency (it can be obtained by eq. 1.138 and 1.139, taking the value $m = 2$); in the quadrupole approximation, considering the bar ellipticity ϵ, the amplitude is given by:

$$h_{bar} \sim 4.5 \times 10^{-20} \epsilon \left(\frac{f}{500\ Hz}\right)^2 \left(\frac{R}{12\ km}\right)^2 \left(\frac{10\ kpc}{r}\right) \left(\frac{M}{0.7\ M_\odot}\right) \tag{1.137}$$

Rossby modes The r-modes are axial fluid oscillations related to the Coriolis force. Their coupling takes place through the current multipoles ($\mathcal{S}_{mn}$ in eq. 1.61), instead of the mass multipoles. The r-modes can be described as large scale oscillating currents that move along the equipotential surfaces of the rotating star, and for this reason they are also called convective modes [53]. In contrast to the f-modes, which become unstable above a critical rotation rate, r-modes are unstable in a rotating perfect fluid star at all rotation rates. Gravitational radiation makes r-modes unstable if the emission timescale is smaller with respect to the viscous time scale. This condition is well verified if the star angular velocity is greater than a critical value ω_c which depends on the star temperature and on the presence of a solid crust [54]. Therefore the r-mode instability may be relevant in hot, rapidly-rotating neutron stars. In particular, it may lead to a spinning down in new-born neutron stars, losing angular momentum through gravitational radiation.

The frequency σ of the m mode with harmonic index $l = m$ is given by:

$$\sigma_m(\omega) = -\frac{(m-1)(m+2)}{(m+1)}\,\omega \tag{1.138}$$

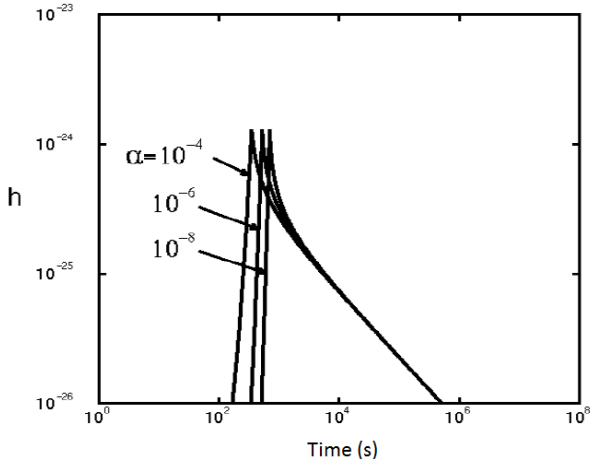

Figure 1.14: Amplitude of gravitational wave emitted when the r-mode instability is excited in a fluid star, for different values of the initial size of the perturbation α. Here it is considered the source distance $r = 20Mpc$ and the initial angular velocity $\omega_0 = 2\pi\nu_k$ [55].

where ω is the angular velocity of the star. The related frequency of the gravitational radiation emitted from such a mode will be:

$$f(\omega) = -\frac{\sigma_m(\omega)}{2\pi} \tag{1.139}$$

At the beginning the amplitude of the mode is small but increases until hydrodynamic effects are no longer negligible and the system reaches a non-linear regime. The maximum value of the emitted gravitational wave is given by:

$$h_0 \approx 1.2 \times 10^{-22} \left(\frac{\omega_0}{\omega_K}\right)^3 \left(\frac{20Mpc}{r}\right) \tag{1.140}$$

Where ω_0 is the initial angular velocity of the star and $\omega_K \equiv 2\pi\nu_K$. Once the non-linear regime is reached, the mode no longer grows due to a saturation effect, and the excess of angular momentum is radiated away through gravitational waves. Consequently, the star spins down until its angular velocity and temperature are sufficiently low to allow the solidification of the crust, damping the mode.

1.3.5 Supernovae

Many of the sources discussed in the previous sections, such as neutron stars and black holes, are formed from gravitational collapses known as Supernovae. These transient sources are characterized by a very high electromagnetic luminosity variation ($|\Delta\mathcal{M}| \sim 20\ mag$) which corresponds to a radiated energy of the order of $10^{42} - 10^{44}\ J$. We can classify the supernovae depending on their progenitor:

1. the gravitational collapse of a white dwarf pushed beyond the Chandrasekhar limit by mass transfer in binary systems;

2. the gravitational collapse of the core of highly evolved massive stars.

According to their light curves and absorption lines in their electromagnetic spectra, the first kind of collapses gives rise to Type Ia supernovae, the second one to Type Ib,c or Type II supernovae.

Type Ia This kind of supernovae are produced by the thermonuclear deflagration of carbon-oxygen white dwarfs in close binary systems, caused by the mass transfer from the companion star (e.g. a giant or supergiant star out of the Main Sequence) to the white dwarf: when its mass exceeds the Chandrasekhar limit, the electron degeneracy pressure no longer can sustain the star structure, which subsequently collapses triggering the thermonuclear synthesis of heavy elements and photodisintegration of iron nuclei. The related luminosity variation is very fast (of the order of hours or days) until it reaches the maximum luminosity $L \approx 4 \times 10^9\ L_\odot$, then it exponentially decays. Supernovae Ia produce consistent peak luminosities and related decais because of the uniform mass of progenitor white dwarfs that explode with the same accretion mechanism. For this reason they are used as a standard candle in cosmology. From the spectral absorption lines it is possible to measure a mass ejection velocity of the order of $10^4\ km/s$.

Type Ib,c This kind of supernovae are produced by the gravitational core collapse of massive stars which have lost their outer envelope of hydrogen, by means of strong stellar winds or due to the interaction with a companion star in a binary system. For this reason they are also called *stripped-core supernovae*. Massive stars which undergo to rapid mass loss, such as Wolf-Rayet stars, are a typical progenitor of such phenomena. Type Ic supernovae may be related to long gamma-ray bursts (see sec.1.3.6).

Type II This kind of supernovae are produced by the gravitational core collapse of massive stars ($8\ M_\odot \geq M \leq 100\ M_\odot$ at ZAMS[9]). During its evolution, the stellar structure is sustained by the balance of the gravitational force and the combination of thermal and electron degeneracy pressures. Once evolved, these stars are characterized by an onion-like structure produced by the progressive thermonuclear synthesis of heavier atomic nuclei. The last possible exoenergetic reaction is the silicon fusion in nickel, which decays in iron, eventually accumulated in the core. The iron-grup nuclei can sustain the overlying stellar structure only by means of electron degeneracy. Once the mass of the iron-core exceeds its effective Chandrasekhar limit, it begins to compress and to heat up, and eventually the star gravitationally collapses. Type II are also called *core-collapse supernovae*. From the their light curve shape it is possible to distinguish two subtypes: $\mathrm{II_P}$ if there is a plateau, $\mathrm{II_L}$ if it is characterized by a linear decrease.

Let us focus on type II supernovae, which are believed to occur at a rate of between 0.01 and 0.1 per year in a Milky Way equivalent galaxy[10]. We can distinguish three main phases: the initial *collapse* of the core to nuclear densities ($\rho \geq \rho_n = 2.7 \times 10^{14} g/cm^3$), the *core bounce* when the nuclear equation of state becomes stiff

[9] *zero age main sequence*, at the beginning of their main sequence phase

[10] at this rate we might expect an event rate of about 1 per 2 years within 5 Mpc

enough to rebound the inner core, and eventually the hydrodynamic *shock wave* which propagates outward from the outer edge of the inner core, colliding with the infalling matter of the outer core and ultimately leads to the disruption of the star. The energy released in this last phase is given by:

$$E_{SN} \sim 3 \times 10^{46} \left(\frac{M}{M_\odot}\right)^2 \left(\frac{10\ km}{R}\right)\ J \tag{1.141}$$

About the 99% of E_{SN} is radiated away by neutrinos in a timescale of $\sim 100\ s$, the 1% is converted into kinetic energy of the ejected outer layers, and only the 0.01% is emitted as electromagnetic radiation. It is still not clear why type II supernovae explode as observed from their light curves and radiated energies, in particular theoretical models and simulations can not explain how the inflow reverses to produce the observed explosion. The main problem arises from the shock wave that should quickly lose energy in the propagation, because of the dissociation of heavy nuclei and the stream of neutrinos which carry away energy from the post-shock region. In such a situation there should be a direct collapse to a black hole without the supernova deflagration. Moreover, we also know from observations that a neutron star can survive the gravitational collapse. Therefore a shock revival mechanism is needed in order to explain the type II supernovae. It should take place as soon as $\sim 1\ s$ after the core bounce in order to produce a compact remnant as a pulsar. Some post-bounce mechanisms have been proposed [56], such as the *neutrino mechanism* (based on neutrino heating), the *magneto-hydrodynamic mechanism* (MHD, based on the the magnetic-field amplification) and the *acoustic mechanism* (based on the strong sound waves emitted by the proto-neutron star instabilities). However the only observational data which may explain the details of this kind of phenomena verifying the proposed models will come from neutrinos and gravitational waves, produced deep inside the supernovae.

Gravitational waves from a supernova

If the collapse is non-spherical, perhaps induced by strong rotation or magnetic field, then gravitational waves could carry away some of the binding energy and angular momentum, depending on the geometry of the collapse. In a typical supernova, recent simulations suggest that gravitational radiation might extract between about 10^{-11} and 10^{-7} of the total available mass-energy, and the gravitational waves could come off in a burst whose frequency might lie in the range of $f \sim 200 - 1000\ Hz$. The gravitational wave amplitude from a supernova is given by [26]:

$$h \approx 1.5 \times 10^{-21} \left(\frac{E}{10^{-7} M_\odot}\right)^{1/2} \left(\frac{1\ ms}{t}\right)^{1/2} \left(\frac{1\ kHz}{f}\right) \left(\frac{10\ kpc}{r}\right) \tag{1.142}$$

where E indicates the energy in equivalent solar masses. For a supernova in our galaxy the typical values of eq. 1.142 are $r = 10\ kpc$, $E = 10^{-8} M_\odot$, $f = 1\ kHz$ and $t = 2\ ms$. During the supernova explosion gravitational waves are produced in three phases [57]:

1. **Bounce**. When the inner core reaches nuclear densities the gravitational collapse is stopped and the infalling matter reaches its peak acceleration. If the collapse itself or the neutrino emission are asymmetric, due to structural asymmetries or to rotation, the strongest gravitational radiation emission takes place. Three kinds of gravitational signals are produced in this phase (see fig. 1.15), associated with different types of collapse:

   - **Type I** models undergo core bounce driven by the stiffening of the nuclear equation of state when the inner core reaches nuclear densities, and ring down quickly into a post-bounce equilibrium. The waveform of this type of collapse is characterized by a large spike at the bounce event and by a subsequent damped ring down.

   - **Type II** models are driven by the rotation, therefore their core bounce is dominated by centrifugal forces at densities $\rho < \rho_n$. Their dynamics is characterized by slow harmonic-oscillator-like damped bounces and re-expansion-collapse cycles. Therefore their waveform shows different signal peaks for every bounce.

   - **Type III** models are characterized by a fast collapse, caused by a very soft subnuclear equation of state or a very efficent electron capture in the core, and consequently by an extremely low mass collapsing inner core. The waveform related to this type of collapses shows a negative spike associated with the bounce, and low-amplitude gravitational waves.

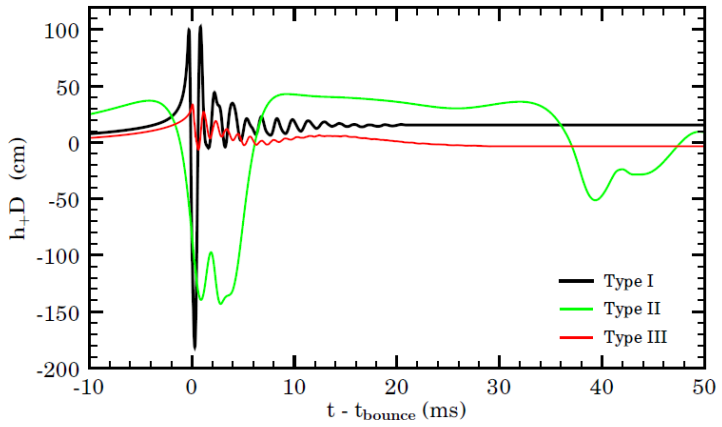

Figure 1.15: Burst gravitational wave signal emitted by the three types of core bounce in a supernova [57]. The amplitude is given in h_+D, where D is the distance from the source.

The characteristic gravitational signal produced in the bounce, in particular for the type I model, depends on the angular velocity of the core, as reported in table 1.2

$\omega_{co}(rad/s)$	$h_{max} \times 10^{-21}$	$E_{GW} \times 10^{-8}(M_{\odot}c^2)$	$f_{peak}(Hz)$
$\leq 1 - 1.5$	≤ 0.5	≤ 0.1	$700 - 800$
$1 - 2$ to $6 - 13$	0.5 to 10	0.1 to 5	$400 - 800$
$\geq 6 - 13$	3.5 to 7.5	0.07 to 0.5	70 to 200

Table 1.2: Gravitational signals expected in the type I core bounce phase from a supernova, as a function of the angular velocity ω_{co} of the pre-collapse iron core [57]; h_{max} is the maximum gravitational wave strain amplitude at 10 kpc, E_{GW} is the energy radiated away by gravitational waves, f_{peak} is the peak frequency of the gravitational wave energy spectrum dE/df.

2. **Post-bounce and convection**. In this phase the convection in the layers above the collapsing core may also produce strong asymmetries, as the convective cells merge into low-mode convection. These mechanisms are intrinsically multi-dimensional and produce rapid variations of the mass quadrupole momentum, resulting in gravitational radiation emission. According to the Schwarzschild-Ledoux criterion, convective overturn develops when there is a negative radial entropy or lepton composition gradients. These may be driven by three kinds of convection [57]:

   - **Prompt convection**. It may start immediately after the bounce. As the stalling bounce shock front passes through the outer core, it leaves behind a negative entropy gradient. Moreover, following neutrino shock breakout and the related burst of electron neutrinos, a negative lepton gradient arises at the outer edge of the proto-neutron star. The two negative gradients generate a convectively unstable region as determined by the aforesaid Schwarzschild-Ledoux criterion. Losses and energy deposition from neutrinos behind the stalling shock front smooth out the large negative entropy gradient in the immediate post-shock region. However, prompt convection can still develop rapidly and last for some milliseconds if significant seed perturbations are present in the post-bounce flow.
   - **Proto-neutron star convection**. The new-born proto-neutron star is convectively unstable in the radial interval $10\ km \geq R \leq 30\ km$, because of the negative radial lepton gradient. Convection starts few tens of milliseconds after the bounce and may last for some seconds as the proto-neutron star slowly contracts and deleptonizes after the supernova explosion. Instabilities, such as g-modes, can distort the convection and themselves lead to gravitational wave emission stronger than that produced by the convection. If the supernova is failed or too weak, a black hole will form: in this case convection and the related gravitational wave emission will stop abruptly.

- **Neutrino convection**. It takes place in the post-shock heating region. The heating produced by neutrinos below the stalling shock front is maximum in the neutrino heating region between the proto-neutron surface and the shock front, and decreases outward. This produces a negative radial entropy gradient and makes the neutrino heating region convectively unstable. Accordingly, convection develop in this region (which extends from ~ 50 to $\sim 200\ km$) within few tens of milliseconds after the bounce.

Process	Typical $\|h\|$ (at 10 kpc)	Typical f Hz	Duration Δt ms	E_{GW} $\times 10^{-10}(M_\odot c^2)$
Prompt convection	$10^{-23} - 10^{-21}$	$50 - 1000$	$0- \sim 30$	$\leq 0.01 - 10$
Proto-NS convection	$2 - 5 \times 10^{-23}$	$300 - 1500$	$500- \sim 10^3$	$\leq 1.3(\frac{\Delta t}{1\ s})$
Neutrino driven convection	$10^{-23} - 10^{-22}$	$100 - 800$	$100- \geq 1000$	$\geq 0.01(\frac{\Delta t}{100\ ms})$

Table 1.3: Estimates calculated from simulations [57] for the typical gravitational wave strain amplitude, the typical emission frequency f, the duration of the emission Δt, and the emitted energy E_{GW} in the convection processes in the post-bounce phase of a supernova.

3. **Proto-neutron star** During its cooling the new-born proto-neutron star may undergo convection, producing asymmetries and therefore emitting gravitational radiation. Other gravitational emission mechanisms in this phase are the neutron star pulsation and bar-mode instabilities (see instabilities in sec. 1.3.4)

1.3.6 Gamma-ray bursts

The gamma-ray bursts (GRBs) are powerful emissions of γ-rays associated with extremely energetic explosions: in the electromagnetic spectrum they are the brightest events known in the universe. The typical observed energy ranges from keV to MeV, and they can last from 10 ms to few minutes. The main features of GRBs are:

- the isotropic distribution;
- the extragalactic origin;
- the absence of bright peristent counterparts;
- the non-thermal spectrum.

Their isotropy and extragalactic origin imply a cosmological nature of this kind of sources, therefore the associated energy released in these phenomena are 10^{44} –

10^{46} J or even more. Moreover the observed millisecond periodic pulsation of some GRBs implies high photon density in a relatively small volume, therefore the astrophysical object producing such phenomena must be compact. The GRB rate measured from satellite detectors, like BATSE and SWIFT, is $\dot{N} \sim 1/day$, from which we can infer a rate $\dot{N}_{MWeg} \sim 10^{-6} - 10^{-9}/year$ for a Milky Way equivalent galaxy, with only a small percentage of them beamed towards Earth.

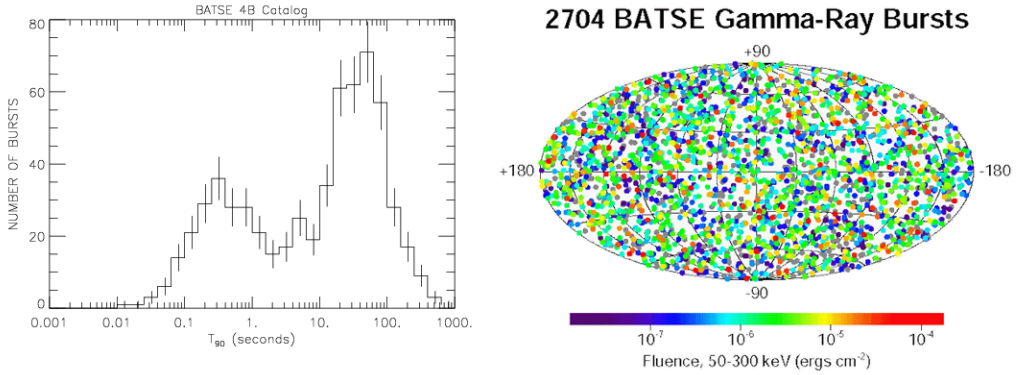

Figure 1.16: *left panel*: bimodal distribution of GRBs' duration, where t_{90} is the time during which the cumulative counts increase from 5% to 95% above the background; *right panel*: isotropy of GRBs from the BATSE (on NASA's Compton Gamma Ray Observatory) survey, with the related energies indicated by different colors.

Despite decades of observations physical mechanisms and counterparts of GRB are still debated. The *fireball* model has been developed in the last years to explain the observed general features of these phenomena. In this model the GRB origin is the jet-like ultrarelativistic flow, pointed to our line-of-sight, which is partially converted to radiation in a optically thin region. The remaining kinetic energy is dissipated via external shocks, resulting in the so-called *afterglow* at longer wavelengths (from X-rays to the microwave and radio band). Relativistic shocks or magnetic reconnection might dissipate the internal energy of the jet, subsequently radiated as synchrotron and blackbody radiation. The observed prompt emission, associated to this phase, implies that γ-rays are emitted after the jet has become transparent to its own radiation. But it this case most of its thermal energy should be radiated as photospheric emission, which instead is not observed. Therefore the energy must be stored in non-thermal components, such as kinetic energy or magnetic fields, and then released after the jet has become transparent. The initial prompt emission, produced within the ultrarelativistic jet, and the afterglow, due to the interaction with the circumburst medium, are clearly evident in the light curves of GRBs, as shown in fig. 1.17. Moreover, the same features observed in GRBs' light curves at various redshift indicates that the physical mechanisms which produce the bursts should be similar [58]. The duration of the observed GRBs is well described by a bimodal distribution, as shown in fig. 1.16, hence we can distinguish between two main classes of burst: *short* and *long* GRB.

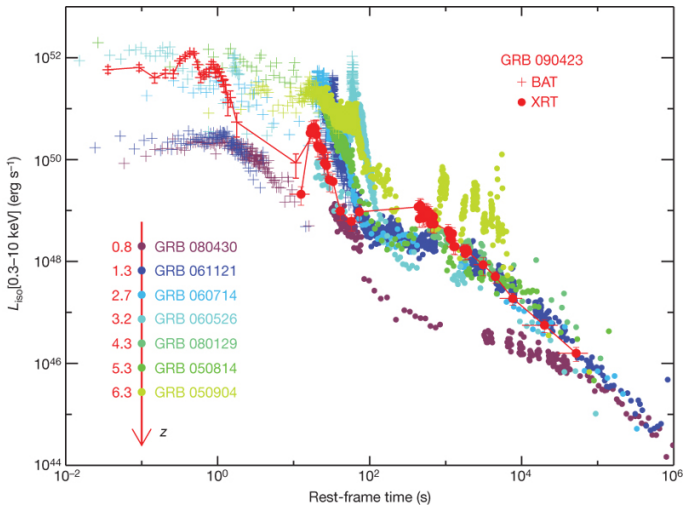

Figure 1.17: Time evolution of the luminosity of a sample of GRBs as function of the redshift z. It is generally evident the transition from the prompt emission phase and the afterglow. GRB090423 (in red, observed by NASA's space telescope Swift) occurred at $z \approx 8.1$ (corresponding to $\sim 13 \times 10^9\ ly$) and its light curve does not have any distinguishing features relative to those of the lower-redshift bursts, suggesting that the physical mechanism that causes the GRB and its interaction with the circumburst medium are similar at every redshifts [58].

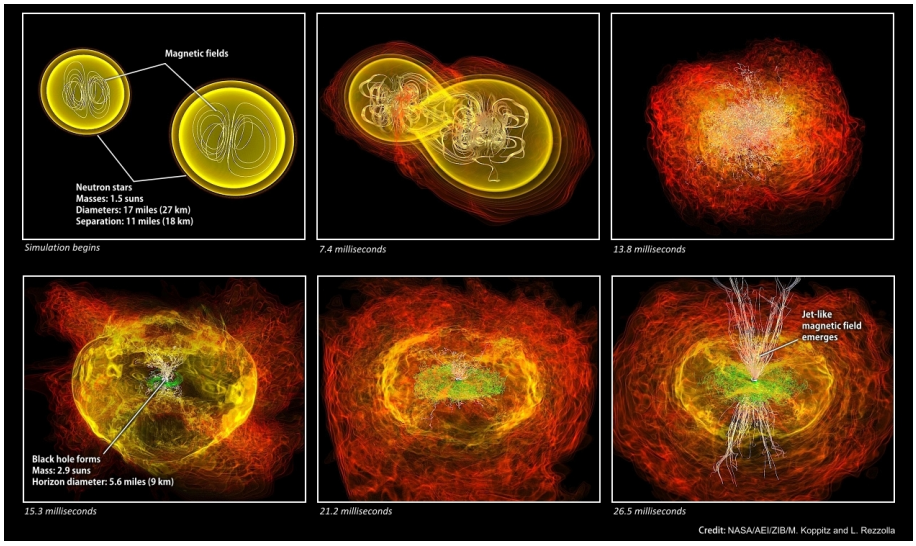

Figure 1.18: The merging of two neutron stars as progenitor of a short gamma-ray burst from a relativistic simulation [59]. Colors from red to yellow indicates increasing densities, the green lines sample the magnetic field in the torus on the equatorial plane, white lines indicate magnetic field outside the torus and near the new-born BH spin axis. The size of the torus extends from $\sim 90\ km$ to $\sim 170\ km$, while the BH horizon has a diameter of $\approx 9\ km$.

Short GRB This class of GRBs are generally observed at low redshifts in galaxies (especially early-type elliptical and lenticular) without active star forming regions. Recent studies and simulations [59] suggest that short GRB may be powered by the merger of binary neutron stars (see fig. 1.18) or neutron star - black hole systems. A small fraction of these events ($< 15\%$) are caused by soft-gamma-ray repeaters (SGRs), that may be related to nuclear explosions in an accreting neutron star[11] which excite f-mode (see instabilities in sec. 1.3.4). A small subset of SGRs can be expained by giant flares on magnetars, a class of neutron stars with extraordinarily large magnetic fields ($10^{14} - 10^{15}\ G$). These flares may be produced by the sudden and violent reconfigurations of complex magnetic field topologies. Three known SGRs are located in our Galaxy, and another one in the Large Magellanic Cloud.

Long GRB They are generally associated with galaxies characterized by late-type star forming regions. Therefore most of long-GRBs are powered by collapsars or hypernovae[12] generated by the collapse of massive stars (see fig. 1.19). In order to power the emission of a long GRB, the hypernova progenitor must have an high angular speed which leads to the formation of an accretion torus during the collapse. Moreover, the progenitor star should have a low metallicity, in order to strip off its hydrogen envelope, so making possible the emersion of the jets from the surface. A small percentage of long bursts can be generated by massive black hole captures. The longest GRB (GRB110328A) was observed in 2011 and lasted for over two months. It was originated in the center of a small galaxy at redshift $z \approx 0.35$, and was interpreted as a white dwarf infalling and tidally disrupted in a supermassive black hole in the galaxy core.

Gravitational wave emission from gamma-ray bursts

The expected gravitational signal depends on the considered type of GRB. A short-GRB may be originated by the coalescence of a compact binary system composed of two neutron stars or by a black hole and a neutron star, therefore the related gravitational wave signal will be a chirp with amplitudes given by equations 1.114 and 1.115 during the inspiral phase, followed by a burts-type signal associated with the merger and eventually by the ringdown of the new-born black hole (see sec. 1.3.2).

SGR flares may be a source of quasi-periodic oscillations, with quadrupolar components in the $\sim 10-40\ Hz$ frequency range. It is also possible that non-radial oscillations, such as fluid (f), pressure (p) and purely spacetime (w) modes, would become excited by tectonic activity associated with a giant flare. These modes will then be damped by gravitational wave emission, resulting in the characteristic ring-down signal. In particular the f-mode will have a frequency which ranges between 1 and 3 kHz. Theoretical models of SGR indicates that the total energy associated with their gravitational wave emission should be $< 10^{39}\ J$.

[11] this mechanism also produce X-ray flares.

[12] i.e. a rare type of supernova explosion characterized by higher radiated energies compared to standard SNae

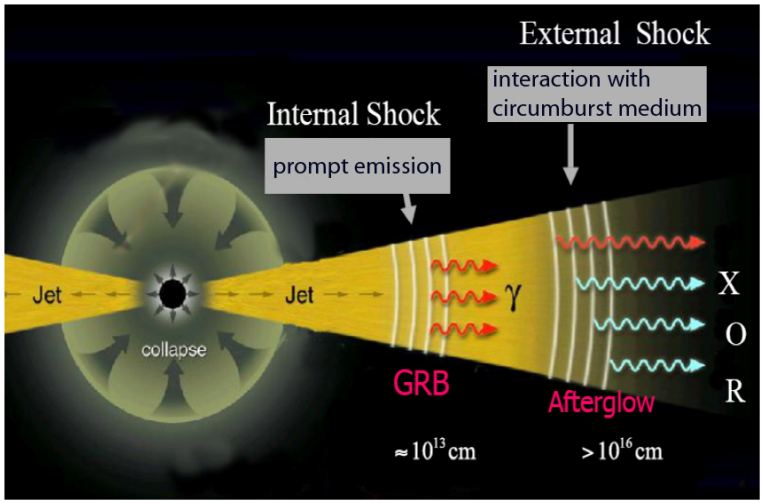

Figure 1.19: GBR from a stellar gravitational collapse. In order to explode as hypernova and power a long GRB, the progenitor star before the collapse must have 25 $M_\odot \geq M \leq 90\ M_\odot$, with an iron core mass 5 $M_\odot \geq M_{core} \leq 15\ M_\odot$

The gravitational wave emission from a long-GRB depends on the collapse and deflagration of massive stars, that is difficult to modelize. The bar or fragmentation instabilities of the disk formed during the collapse can emit inspiral-like chirps, as well as core instabilities. The material flows into the new-born black hole can also lead to its ring-down emission. An estimate of the expected gravitational wave amplitude is given by [26]:

$$h \sim 10^{-23} \left(\frac{E}{5 \times 10^{-2}\ M_\odot} \right)^{1/2} \left(\frac{1\ ms}{t} \right)^{1/2} \left(\frac{1\ kHz}{f} \right) \left(\frac{4.2\ Gpc}{r} \right) \tag{1.143}$$

where the energy E is given in equivalent solar masses, t is the duration time of the signal in ms, and the distance r is given in Gpc units. The eq. 1.143 can be written in terms of redshift z by substituting the last term with $(0.7/z)$.

1.4 Development of multimessenger astronomy

Many transient astronomical phenomena that we analyzed in section 1.3, such as supernovae, gamma-ray bursts and glitching pulsars, may produce bursts of gravitational waves which last from milliseconds (e.g. SNae) to several minutes or longer (e.g. NS instabilities). Detecting such waves, especially in coincidence with optical, X-ray, γ-ray or neutrinos could help to resolve decade-old problems in astronomy.

The first generation of large gravitational wave interferometric detectors (see chapter 2) have been successfully operating in the last years and are currently upgraded into second generation detectors in order to reach higher sensitivities, i.e. to observe a greater volume of the universe. Even if we are still looking forward to the first direct detection of gravitational radiation, a third generation of detectors

is already planned and will pave the way to the gravitational astronomy, which will be a powerful integration in the so-called multimessenger astronomy.

The simultaneous observation operated by a network of gravitational wave detectors will make possible to identify and localize event candidates on the sky, then the electromagnetic and/or neutrino follow-up will be able to confirm the astrophysical event and to produce complementary information about it in the other astronomic windows. In particular the synergy between neutrino and gravitational wave observatories is a very promising field, since both neutrinos and gravitational radiation interaction with matter is negligible, hence they can provide informations of the astrophysical sources and their emission processes otherwise inaccessible to the other windows of observation.

Since the gravitational wave data from interferometric detectors is not stationary, a search for gravitational signals conducted at times of observed electromagnetic events (the so-called external trigger strategy) increases confidence that the candidate signal is astrophysically produced, and not a spurious noise event. By constraining the gravitational wave search to a relatively short period (typically from tens to houndreds of seconds) in coincidence with observed electromagnetic events, such as GRBs, the background rejection is improved, and the detector sensitivity increased. In the past years, first generation detectors such as Virgo and LIGO (see chapter 2) developed another strategy for finding gravitational wave events in association with electromagnetic transients: during a period of joint data collection, directional information was sent to electromagnetic observatories (such as the Jodrell Bank radio Observatory and the interplanetary network of gamma ray satellites for SGRs and GRBs) soon after the identification of candidate events in their data. Moreover, a first attempt of coincident gravitational/neutrino detection was conduced with ANTARES [60].

We should remark that not only the detection but also the non-detection of gravitational waves can provide informations about the source characteristics (such as ellipticity upper limits of pulsar, see sec. 1.3.4) and position. For instance in 2007 a short GRB [61] was observed in a sky position coincident with the spiral arms of the Andromeda galaxy (M31), but in the coincident 180 s long time window around the GRB event time no plausible gravitational wave candidates were found in LIGO data. Considering that the most likely progenitor was a binary neutron star merging, this non-detection implies at $> 99\%$ confidence that the binary progenitor of that GRB was not located in M31[13], but simply on the same line-of-sight.

Even if we are only at the very beginning of gravitational astronomy, waiting for the first direct gravitational wave detection, the multimessenger astronomy era has already begun.

[13]another possibility is that the analyzed GRB was due to a SGR giant flare in M31.

Chapter 2

Interferometric detectors

We sow in sec. 1.2.3 that the passage of a gravitational wave produces a tidal effect on a system of test point-masses placed on a plane perpendicular to the wave propagation direction. In eq. 1.49 we found that this effect is proportional to the distance between the masses, and to the gravitational wave amplitude h, which in turn depends on the tiny factor G/c^4. Therefore it is evident that large-scale interferometry is the best experimental technique which can lead to a direct detection of the gravitational radiation. First generation detectors, such as Virgo [62] and LIGO [63], have demonstrated the feasibility of the interferometric gravitational wave detection, advanced detectors are under development and are expected to make the first direct detections, while third generation detectors are planned to be built and start operating within the next decade. In this chapter I will briefly discuss the direct interferometric detection of gravitational waves and I will make an overview of present and future interferometric detectors.

2.1 Principle of detection

An interferometric detector is based on the interference of two coherent beams of light along an optical path: the changes in their phase difference will directly measure the relative displacement of the reflective elements of the interferometer, which are the mirrors. This section deals with the Michelson configuration, which is the simplest interferometric optical layout, and it is widely used as the basic scheme of gravitational wave detectors.

2.1.1 Michelson interferometer

The simplest Michelson configuration consists of two mirrors M_1 and M_2 characterized by reflectivities r_1, r_2 and suspended at the end of two orthogonal vacuum tubes, which are called *arms* and intersect in coincidence with the beam-splitter mirror BS. The distance between BS and M_i will be the optical path L_i of the arm. When the input laser beam passes through the beam-splitter it is divided in two orthogonal beams, which reflect on the mirrors and recombine on the surface of the beam-splitter. Afterwards, the recombined beam reaches the photodetector at the output port of the interferometer. If the optical path of the two arms is

different, i.e. $L_1 \not\equiv L_2$, the two recombining beams will be out of phase, and their differential phase will be given by:

$$\Delta\Phi = (\Phi_1 - \Phi_2) = 2k\Delta L \tag{2.1}$$

where $k = 2\pi/\lambda$ is the wave vector of the laser beam of wavelength λ, and $\Delta L = (L_1 - L_2)$ is the length difference of the two arms. From eq. 2.1 it is clear how a passing gravitational wave producing a variation of ΔL will be seen as a change in the differential phase $\Delta\Phi$. This scheme is illustrated in fig. 2.1

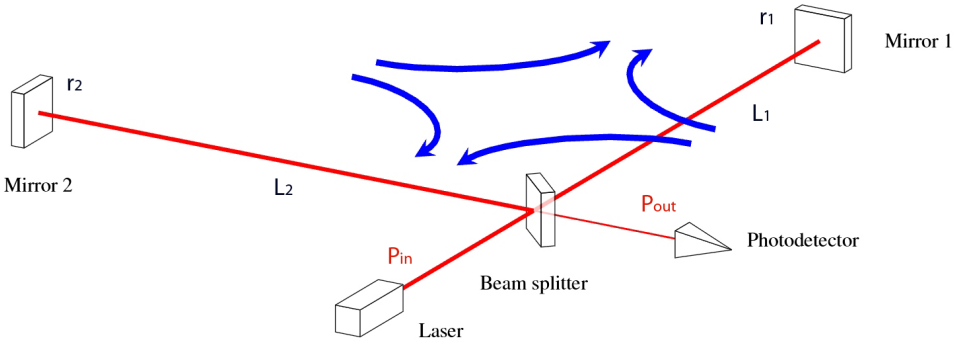

Figure 2.1: Layout of a simple Michelson interferometer, where the arms L_1 and L_2 are oriented as $\hat{x}$ and $\hat{y}$. The blue arrows indicate the tidal deformation produced by an incoming gravitational wave *plus*-polarized which propagates perpendicularly to the xy-plane of the interferometer.

2.1.2 Test masses

In order to be able to detect a gravitational wave, the mirrors of the interferometer must be in a *free-falling* condition, making them effective gravitational test masses. It is possible to fulfill this condition by suspending the mirrors from pendula, as demonstrated below.

If the two mirrors are placed on the plane xy and are spaced by the distance x_0^i, from eq. 1.52 we can derive the apparent acceleration produced by the passage of a gravitational wave with amplitude $h_{ij}(t)$ and propagating in the z direction:

$$\ddot{x}^i(t) = \frac{1}{2}\ddot{h}_{ij}(t)x_0^j \tag{2.2}$$

to which corresponds an apparent force along the x direction:

$$F_{gw} = m\ddot{x} = \frac{1}{2}mL\ddot{h} \tag{2.3}$$

where m is the mass of the mirror and having considered the length of the interferometer arm, i.e. $x = L$. If the mirror is suspended from a pendulum of length l, its equation of motion is:

$$m\delta\ddot{l} + \beta\delta\dot{l} + k\delta l = 0 \tag{2.4}$$

where β is the damping constant and $k = mg/l$. When the mirror is perturbed by the gravitational wave, it is affected by the force defined in eq. 2.3, and consequently the equation of motion 2.4 becomes:

$$m\delta\ddot{l} + \beta\delta\dot{l} + k\delta l = \frac{1}{2}mL\ddot{h} \tag{2.5}$$

The time-dependence of h and δl can be written explicitly as $h(t) = h_0 \exp[i\omega t]$ and $\delta l(t) = \delta l_0 \exp[i\omega t]$, where ω is the angular frequency of the monochromatic gravitational wave. Therefore the solution of eq. 2.5 is given by:

$$\delta l_0(\omega) = -\frac{1}{2}\frac{\omega^2 h_0 L}{(\omega_0^2 - \omega^2) + \frac{i\beta\omega}{m}} \tag{2.6}$$

where we introduced the resonant angular frequency of the pendulum: $\omega_0 = (k/m)^{1/2}$. It is evident that when $\omega \gg \omega_0$ eq. 2.6 becomes:

$$\delta l_0(\omega) \approx \frac{1}{2}h_0 L \tag{2.7}$$

2.1.3 Directional response

In sec. 2.1.2 we have shown that the suspended mirrors of an interferometer respond as free-falling test masses to the passage of a gravitational wave. However the geometry of the Michelson interferometer determines a directional response. Assuming that the interferometer lies in the xy plane, and its arms are long L and are aligned with the x and y directions, the response to a gravitational wave with an arbitrary polarization and arriving from an arbitrary direction is given by [64]:

$$\Delta L(t) = \frac{1}{2}h_+(t)L(1 + \cos^2\theta)\cos(2\phi) \tag{2.8}$$

$$\Delta L(t) = -h_\times(t)L\cos(\theta)\sin(2\phi) \tag{2.9}$$

where (θ, ϕ) indicates the propagation unit vector of the wave, being θ is the azimuthal angle and ϕ is the angle with the x axis in the xy plane. This directional response leads to the characteristic antenna pattern functions F_+ and $F_\times$ that are shown in fig. 2.2 [65].

2.1.4 DC & AC detection

The direct detection is based on the *static tuning* of the input laser, therefore the differential phase depends only on the length difference of the two arms. Let us consider the power incident on the beam-splitter P_{in}, we can derive the power P_{out} detected at the output port [66]:

$$P_{out} = P_{in}(r_{BS}t_{BS})^2(r_1^2 + r_2^2)(1 + C\cos\Delta\Phi) \tag{2.10}$$

where r_{bs} and t_{bs} respectively the reflectivity and the transmissivity of the beam-splitter, and C is the contrast given by:

$$C = \frac{2r_1 r_2}{r_1^2 + r_2^2} \tag{2.11}$$

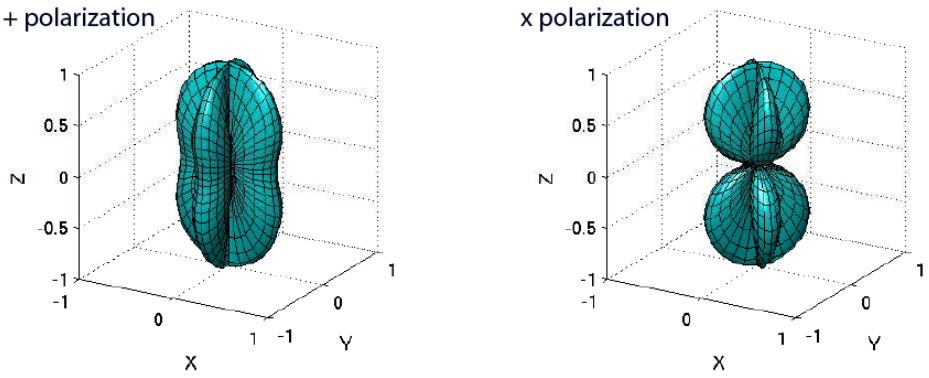

Figure 2.2: Antenna patterns for + and × polarizations in the long-wavelength approximation for a Michelson interferometer [65].

In the ideal case, the end mirrors of the interferometer are characterized by $r_i \sim 1$, with a contrast C very close to unity, and the beam-splitter mirror by $r_{bs}^2 = t_{bs}^2 = 1/2$. Therefore eq. 2.10 becomes:

$$P_{out} = \frac{P_{in}}{2}(1 + C\cos\Delta\Phi) \tag{2.12}$$

Let us analyze what happens to the signal when a *plus*-polarized gravitational wave propagates in the direction perpendicular to the plane of the interferometer[1]. The effect produced by the wave on a light ray traveling between two free-falling test masses is a change in the optical path, according to what we have seen in sec. 1.2.3. Hence, for a path oriented as the the x axis, at first order in strain amplitude h, from eq. 1.53 we can write:

$$dx = cdt\left[1 + \frac{1}{2}h(t)\right] \tag{2.13}$$

while on the path oriented as the the y axis we have:

$$dy = cdt\left[1 - \frac{1}{2}h(t)\right] \tag{2.14}$$

The gravitational wave amplitude $h(t)$ in eq. 2.13 and 2.14 can be written in terms of the time-indipendent amplitude h_+ and the time-varying component as follows:

$$h(t) = h_+ e^{i\omega(t-x/c)} \tag{2.15}$$

where $\omega = 2\pi f$ is the angular frequency of the monochromatic gravitational wave. The propagation of this wave can be described in terms of retarded time. Let us consider a light pulse emitted from a test mass at a given time, reflected by the other test mass at a distance $x = L$, and detected at the first mass at a certain

[1]the effect produced by a perpendicular propagating *cross*-polarized gravitational wave is similar to that of the *plus* polarization, but rotated by $\pi/4$ (see sec. 1.2.3).

time t_0. It can be calculated [64, 67] that the emission time of the light pulse depends on h_+ and ω, and is given by:

$$t_r = t_0 - \frac{2L}{c} \pm h_+ \frac{L}{c} \frac{\sin\left(\frac{\omega L}{c}\right)}{\left(\frac{\omega L}{c}\right)} \cos\left[\omega\left(t - \frac{L}{c}\right)\right] \tag{2.16}$$

where the $\pm$ sign indicates respectively the x and y directions, we replaced the complex exponential with its corresponding trigonometric function and we assumed the two arms of the same length L. In the case of two light pulses emitted from a test mass, placed in the origin of the interferometer plane xy, toward the other test masses at the end of the two arms, reflected back by them and detected in the origin, the time lag between the two detected pulses is given by the difference in the optical path due to the effect of the gravitational wave:

$$\Delta t_{gw} = h_+ \frac{2L}{c} \frac{\sin\left(\frac{\omega L}{c}\right)}{\left(\frac{\omega L}{c}\right)} \cos\left[\omega\left(t - \frac{L}{c}\right)\right] \tag{2.17}$$

Let us consider a laser with wavelength λ propagating in the two arms of the Michelson interferometer and detected back at the output port. If we multiply eq. 2.17 by $2\pi c/\lambda$ we obtain the corresponding differential phase shift due to the gravitational wave passage:

$$\Delta\Phi_{gw}(t) = \frac{2\pi c}{\lambda} h_+ \frac{2L}{c} \frac{\sin\left(\frac{\omega L}{c}\right)}{\left(\frac{\omega L}{c}\right)} \cos\left[\omega\left(t - \frac{L}{c}\right)\right] \tag{2.18}$$

where we note that the term $\sin(\omega L/c)/(\omega L/c)$ is close to unity for gravitational wave frequencies below some kHz. The effect produced by the additional dephasing is a variation of the power detected, which can be expressed considering the first term approximation of the gravitational perturbation as follows:

$$\Delta P_{out}(t) = \frac{P_{in}}{2} C \sin\left(\frac{\omega L}{c}\right) \Delta\Phi_{gw}(t) \tag{2.19}$$

and finally, considering eq. 2.12 and 2.19, we obtain the total power detected at the outport port:

$$P_{out}(t) = \frac{P_{in}}{2}\left[1 + C\cos(\Delta\Phi) + C\sin(\Delta\Phi)\Delta\Phi_{gw}(t)\right] \tag{2.20}$$

In the ideal case the detection of power fluctuation is not limited by any noise sources, therefore in order to achieve an optimal tuning of the interferometer we should maximize the sine function in eq. 2.20, which implies to obtain half of the maximum power in the output signal. In this condition the interferometer is locked on the *grey fringe*[2]. However the measure of P_{out} is limited by the shot noise, therefore in the DC detection the interferometer is tuned very close to the dark fringe (see sec. 2.2.2).

[2]it is indeed a condition halfway between the *dark fringe* and the *bright fringe*, which correspond respectively to the minimum and maximum power tuning.

The AC detection was widely used in first generation interferometric gravitational wave detectors, such as Virgo, and it is based on the phase-modulation of the input signal. Therefore the electric field of the injected laser beam, which originally is $E_{in}(t) = E_0 \exp[i\Omega_L t]$, becomes $E_{in}^m(t) = E_0 \exp[i\Omega_L t + m \sin(2\pi\Omega_m t)]$, where Ω_L and Ω_m are respectively the laser angular frequency and the electro-optical modulator driver frequency, while m is the modulation depth. The phase-modulation produces radio-frequency sidebands around the main carrier frequency, which can be observed even when the carrier frequency is tuned at destructive interference[3]. Afterwards, the signal arriving at the photodetector is demodulated and low-pass filtered, giving the output power P_{out}^m. The passage of a gravitational wave produces an additional dephasing of the two beams, equivalent to the deviation from the dark fringe condition, giving a linear response to the gravitational perturbation [68].

If the time taken by the light to travel along the optical path becomes comparable or greater than the gravitational wave period, the interferometer response function decreases since the effect produced by the wave is averaged over more than one period. Therefore, in an interferometer the length L of the arms defines a cutoff frequency in the detection bandwidth. To get an idea of such a frequency, in an interferometer with arm length L its order of magnitude is given by the following simple expression:

$$f_c \sim \frac{c}{L} \tag{2.21}$$

Therefore, in order to make the detector sensitive at lower frequencies we should increase the length of the arms. In order to estimate the order of magnitude of the effect produced by a gravitational wave on a Michelson interferometer, we can use the eq. 2.18. If we consider a wave with $h \sim 10^{-21}$ and $\omega \sim 100\ rad/s$, the laser wavelength $\lambda = 1\ \mu m$ and the arm length $L = 1\ km$, we obtain an angular response $\sim 10^{-12}\ rad$, which roughly corresponds to a arm length variation $\delta L \sim 10^{-18}\ m$. This effect can be increased by choosing an optical layout such that the effective length is $L_{eff} > L$.

2.1.5 Fabry-Perot cavities

In this section it has been shown that the effect produced by a gravitational wave on the test masses of an interferometer is proportional to the length of the arms and to the power of the input laser. However the maximum length for ground detectors is limited to a few km, while the input laser power is limited both by the *shot noise* (see sec. 2.2.2) and by the technical difficulties to build stable high-power lasers.

In order to increase the optical path and the power stored in the arms of length L, two input mirrors are added to the basic configuration of the arms of the interferometer, transforming them in resonant cavities, which are known as *Fabry-Perot* cavities (see fig. 2.3). The resonance condition is met when there is a constructive interference between the light transmitted through the input mirror and the light reflected back from the end mirror to the input mirror. In

[3]this is possible introducing the so-called *Schupp asymmetry* ΔL between the length of the two arms of the interferometer

this condition the power stored in the cavity, as well as the power transmitted, is maximum and it is proportional to F/π, which means that the photons are stored in the cavity for a time:

$$t_s = \frac{F}{\pi}\frac{L}{c} \tag{2.22}$$

that implies the introduction of a cutoff frequency proportional to the inverse of the storage time t_s. In eq. 2.22 we introduced the parameter F, that is called *finesse* and characterizes a Fabry-Perot cavity; it can be calculated as:

$$F = \frac{\pi(r_i r_e)^{1/2}}{1 - r_i r_e} \tag{2.23}$$

where r_i and r_e are the reflectivities of the mirrors of the cavity. For a fixed length of the cavity there can be different resonances varying the laser frequency, which are expressed by:

$$f_{res} = \left(n + \frac{1}{2}\right)\Delta f_{FSR} \tag{2.24}$$

where $\Delta f_{FSR} = c/2L$ is the *free spectral range*, i.e. the spacing between two successive resonances. While in a single-mirror arm of length L the phase-shift $\Delta\Phi$ due to a variation of the length ΔL is given by eq. 2.1, adopting the resonant cavity it is increased of a factor $2F/\pi$ and it is given by:

$$\Delta\Phi_{FP} = 2\frac{F}{\pi}\left(\frac{2\pi}{\lambda}\Delta L\right) = \frac{4F}{\lambda}\frac{1}{\sqrt{1 + \left(\frac{2FL\omega}{\pi c}\right)^2}} \tag{2.25}$$

where $\omega = 2\pi f$ is the angular frequency of the gravitational wave which caused the variation ΔL. From eq. 2.25 we can obtain the expression of $f_c \equiv \omega/2\pi$:

$$f_c = \frac{c}{4FL} \tag{2.26}$$

which is the cutoff frequency of the Fabry-Perot cavity. Therefore, the resonant cavity acts as a low-pass filter. From eq. 2.25 it is also evident that using a Fabry-Perot cavity is equivalent to have an arm of length $L_{eff} = (2F/\pi)L$, and we can define the Fabry-Perot gain: $G = 2F/\pi$. The power at the output port of a Fabry-Perot interferometer can be obtained by replacing $\Delta\Phi$ with $\Delta\Phi_{FP}$ in eq. 2.20.

2.1.6 Power recycling

When the interferometer is tuned at the dark fringe, almost all the injected power is reflected back to the laser, since the losses in the arms are negligible. Therefore, in order to reflect back the light into the interferometer, increasing the power circulating, a mirror is placed between the laser and the beam-splitter, creating the so-called *power recycling* cavity. The recycling gain G_{pr} due to such a cavity can be computed considering the Fabry-Perot-Michelson (FPM) interferometer (shown in fig. 2.3) as an equivalent mirror characterized by the reflectivity r_{FPM}[4].

[4]the reflectivity r_{FPM} is close to unity at the dark fringe tuning.

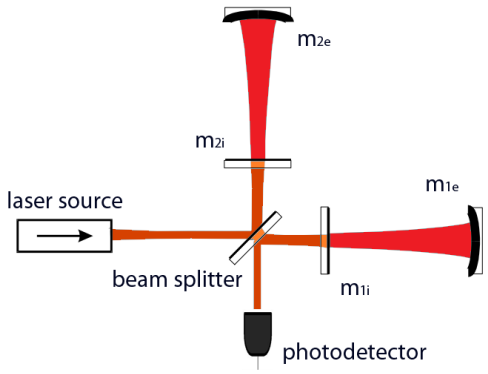

Figure 2.3: Layout of a Michelson interferometer with Fabry-Perot cavities.

In this way we can assume that the power recycling mirror and the FPM equivalent mirror define a Fabry-Perot cavity, therefore the recycling gain with respect to the input power is given by [67]:

$$G_{pr} = \left(\frac{t_{pr}}{1 - r_{pr} \cdot r_{FPM}} \right)^2 \tag{2.27}$$

where r_{pr} and t_{pr} are respectively the reflectivity and the transmissivity of the power recycling mirror. This gain factor is proportional to the inverse of the losses in the interferometer, hence it can be increased minimizing the mirror losses, such as light diffusion and absorption.

2.2 Noise sources

The sensitivity curve of an interferometric detector is delimited by the signal fluctuations produced by noise sources. They can be classified in different ways: with regard to their origin we can distinguish between *environmental* (e.g. seismic and Newtonian noises), *instrumental* (e.g. scattered light) and *fundamental* (e.g. quantum noises) noises; it is also possible to distinguish between *stationary* and *non-stationary* noises with regard to their stability in a given time range, or in *low-frequency* and *high-frequency* noises with regard to the frequency band in which they are dominant. In the low-frequency band the *seismic*, *Newtonian* and *thermal* noises are dominant, while at higher frequencies quantum noises becomes important. This is evident in the sensitivity curve of the initial Virgo detector, reported in fig. 2.4. In this section the main sources of noise will be briefly presented, in particular the low-frequency noise sources will be dealt with separately in chapters 3 and 4. Noise amplitudes are usually expressed by their spectral densities, such as the *equivalent spectral density*, and therefore calculated in terms of the strain $\tilde{h}$; for its definition see app. A.

2.2.1 Low frequency sources

The sensitivity of ground-based interferometric gravitational wave detectors in the low-frequency band ($1 - 100\ Hz$) is limited by three main contributions to the total noise, which are:

- **Seismic noise**, mainly below 10 Hz; see chapter 3;
- **Newtonian noise**, also called *gravity gradient noise*, mainly below 50 Hz, see chapter 3;
- **Thermal noise**, its *thermal pendulum* component is dominant in the range between 10 Hz and 50 Hz, while between 50 Hz and 100 Hz also its violin and mirror thermal components become important; see chapter 4.

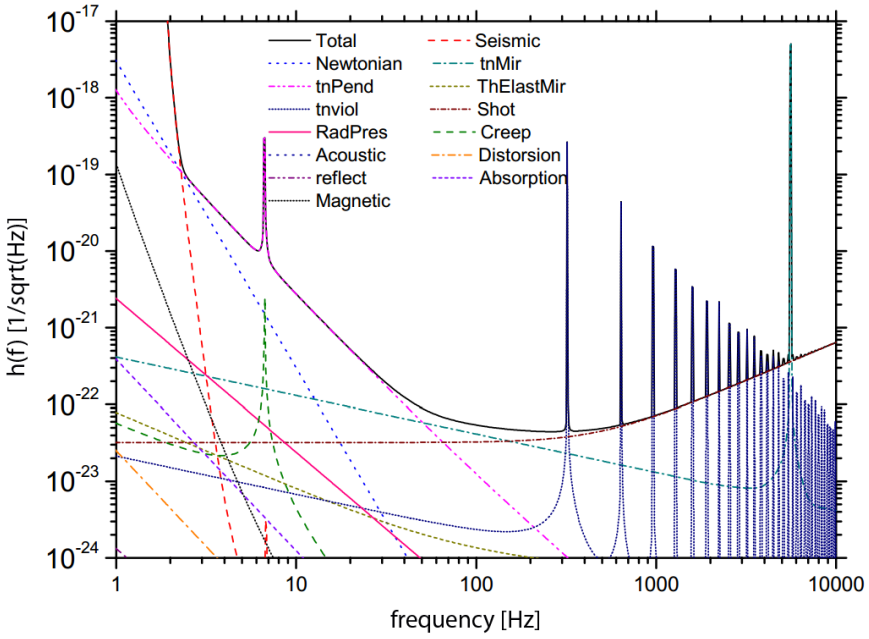

Figure 2.4: The sensitivity curve of the initial Virgo detector [69], defined by the main contributions to the total noise. For the details of these noise components see sec. 2.2.

2.2.2 Quantum noises

There are two fundamental sources of quantum-mechanical noise to be considered:

Shoot noise The power detection in a real interferometer will be limited by the quantum nature of the light: indeed the photons hit the detector with a Poisson distribution, resulting in a *shot noise* [68]. The amplitude spectral

density of this quantum noise is given by:

$$\tilde{S}_{SN} = \left(\frac{4\pi\hbar c P_{out}}{\lambda}\right)^{1/2} \tag{2.28}$$

where λ is the laser wavelength and P_{out} is the power hitting the photodetector at the output port of the interferometer. In eq. 2.28 we note that the spectral density does not not depend on the frequency f, therefore the shot noise is a white noise. In order to reduce this quantum noise, the Michelson interferometer must be tuned maximizing the signal to noise ratio (SNR), considering the amplitude spectral densities of the shot noise (eq. 2.28) and that of the power variation ΔP_{out} produced by a gravitational wave (from eq. 2.19):

$$SNR_P(f) = \frac{\tilde{S}_{\Delta P}}{\tilde{S}_{SN}} = \frac{1}{2}\left(\frac{\lambda P_{in}}{2\pi\hbar c}\right)^{1/2} \frac{C\sin\Delta\Phi}{(1+\cos\Delta\Phi)^{1/2}} \frac{2\pi L}{\lambda}\tilde{h}(f) \tag{2.29}$$

where the dephasing $\Delta\Phi$ for the interferometer in stationary condition is defined by eq. 2.1, λ is the wavelength of the laser, C is the contrast, L the length of the interferometer arm, P_{in} is the power injected in the interferometer and $\tilde{h}(f)$ is the spectral density of the gravitational signal. The maximum of eq. 2.29 is in correspondence with:

$$\cos\Delta\Phi = \frac{(1-C^2)^{1/2}-1}{C} \tag{2.30}$$

Considering that the contrast $C \sim 1$, it follows that the optimal tuning of the Michelson interferometer is close to the dark fringe condition, as said above in sec. 2.1.4. If we put $SNR_P = 1$ we obtain the equivalent spectral density (see app. A) of the shot noise:

$$\tilde{h}_{SN} = \frac{1}{L}\left(\frac{\lambda\hbar c}{4\pi P_{in}}\right)^{1/2} \tag{2.31}$$

A more accurate calculation for the FPM interferometer, considering Fabry-Perot and power recycling cavities, is given by [66, 69]:

$$\tilde{h}^{FPM}_{SN}(f) = \frac{1}{8FL}\left\{\frac{4\pi\hbar\lambda c}{\eta G_{pr} P_{in}}\left[1+\left(\frac{f}{f_c}\right)^2\right]\right\}^{1/2} \tag{2.32}$$

where η is the photodetector efficiency, F is the finesse of the Fabry-Perot cavities given by eq. 2.24, f_c is the cutoff frequency of the cavities given by eq. 2.26, and G_{pr} is the recycling gain factor given by eq. 2.27. It is evident from eq. 2.32 that this noise is limited by higher F, L and by higher circulating power $G_{pr}P_{in}$. Moreover, from eq. 2.32 we note that the shot noise becomes important at higher frequencies.

Radiation pressure This noise is produced by the momentum transfer from the incident electromagnetic radiation to the mirrors of the interferometer. The

radiation pressure is proportional to the intensity of the incident radiation, the increase of power obtained in a FPM interferometer causes also an higher radiation pressure. Taking into account the effect of the Fabry-Perot cavities, the equivalent spectral density of the radiation pressure noise can be obtained by [66, 69]:

$$\tilde{h}_{RP}^{FPM}(f) = \frac{4F}{mL}\left[\frac{\hbar G_{pr} P_{in}}{\pi^5 \lambda c}\cdot\frac{1}{f^4}\cdot\frac{1}{1+\left(\frac{f}{f_c}\right)^2}\right]^{1/2} \tag{2.33}$$

where m is the mirror mass. From eq. 2.33 it is evident that the radiation pressure noise is limited by decreasing F and $G_{pr}P_{in}$, that is the opposite of what is required to reduce the shot noise.

In order to reduce the overall quantum noise, a balance between shot noise and radiation pressure must be found. The optimal condition is obtained by equaling the spectral densities of shot noise and radiation pressure from eq. 2.32 and 2.33:

$$\tilde{h}_{SQL}(f) = \frac{1}{\pi L}\left(\frac{2\hbar}{m\eta^{1/2}}\right)^{1/2}\frac{1}{f} \tag{2.34}$$

The optimal condition found in eq. 2.34 is known as the Standard Quantum Limit. It is an fundamental limit to the sensitivity of an interferometer, and can be beaten only in a limited frequency range by means of squeezed light [70] and by adding a signal recycling mirror to the optical layout of the interferometer (as in advanced detectors, see 2.4.1).

2.2.3 Other sources of noise

In addition to those already mentioned in the previous subsections, there are other sources of noise which affect an interferometer, limiting its sensitivity.

Scattered light Due to small imperfections on the mirror surface and to residual gas molecules, some photons of the laser beam can scatter, bounce on the vibrating walls of the vacuum tube and eventually recombine with the laser beam, resulting in a phase noise. The equivalent spectral density in h is given by [71]:

$$\tilde{h}_{scl}(f) = K\frac{\lambda\tilde{x}(f)}{LR_t}\left(\frac{r}{\ln(1/r)}\right) \tag{2.35}$$

where K is a proportional constant, λ is the wavelength of the laser, $\tilde{x}(f)$ is the displacement spectral density[5], R_t is the tube radius, L is the length of the arm and r is the reflectivity. Considering the estimate $r \sim 0.99$ from eq. 2.35 the spectral density of this noise at 10 Hz is calculated to be [71]: $\tilde{h}_{scl}(10\ Hz) \approx 1.3\times10^{-23} Hz^{-1/2}$. Since it depends on the displacement spectral density $\tilde{x}(f)$, which is linked to the seismic and micro-seismic activity (see chapter 3), the scattered phase noise affects mostly the low frequencies.

[5] $\tilde{x}(f)$ is given by the RMS value along the several km of the tube.

A more precise computation of this kind of noise must take into account also the similar effect produced by the *backscattering* of the light, whose contribution, however, is calculated to be lower by at least two orders of magnitude [71]. The time-domain expression of $\tilde{h}(t)$ and the methods to measure it are discussed in [72, 73]. In order to reduce the scattered light in an interferometer, some baffles made of absorbing material are placed in the vacuum tubes, around the mirrors and optical benches.

Residual gas The residual gas inside the vacuum tubes of the interferometer can reduce its sensibility in different ways:

- residual molecules in the interferometer contributes to the thermal noise produced by the *viscous damping* of mechanical oscillators (e.g. the mirror suspensions), see chapter 4;
- the refractive index n depends on the residual gas pressure P_r as expressed by:
$$n = 1 + \epsilon_{H_2} \frac{P_r}{P_{atm}} \tag{2.36}$$
where $\epsilon_{H_2} = 1.2 \times 10^{-4}$ is related to the molecular hydrogen, which is the main component of the residual gas. Therefore fluctuations of the residual gas pressure produces fluctuations in the refractive index:
$$\Delta n = \epsilon_{H_2} \frac{\Delta P_r}{P_{atm}} = \epsilon_{H_2} \frac{\Delta N_r}{N_{atm}} \tag{2.37}$$
where N_i are the molecule densities. The fluctuations Δn causes a laser beam *phase noise*, that is given in equivalent spectral density by [69]:
$$\tilde{h}_{\Delta P} = \frac{\epsilon_{H_2}}{N_{atm}} \left(\pi^{1/2} \frac{W_b N_r}{\nu_{H_2} V_b} \right)^{1/2} \tag{2.38}$$
where W_b is the beam waist at the far mirror distance, $V_b = \pi W_b^2 L$ is the volume of the beam and ν_{H_2} is the velocity of H_2 molecules. Typically, the order of magnitude of this noise is $\tilde{h}_{\Delta P} \propto 10^{-26}$;
- vibrations of the external walls can be transmitted to the mirrors through the molecules of the residual gas, as shown in [74]. This mechanism causes the so-called low pressure acoustic noise, whose equivalent spectral density is given by:
$$\tilde{h}_{ac}(f) = \frac{k_b T R_m^2}{\pi^{-1/2} L P_r m f} \tilde{x}(f) \tag{2.39}$$
where k_b is the Boltzman constant, T is the temperature, R_m and m are respectively the radius and the mass of the mirror and $\tilde{x}(f)$ is the seismic noise spectral density (see chapter 3). Typically, in a ground-based interferometric detector $\tilde{h}_{ac}(f) \propto 10^{-24}/f^3$.

In order to lower the noises produced by the residual gas under the typical levels of quantum noises, the hydrogen partial pressure must be at least $P_{H_2} \leq 10^{-9}\ mbar$.

Creep The metallic components of the mirror suspensions are subject to mechanical stress and, subsequently, they undergo a anelastic relaxation in which the energy stored in the deformations of the crystal structure is released. This effect is a sort of mechanical shot-noise and is called *creep* [75]. The creep affects metallic wires as well as blade springs, and its effect is driven by two parameters: the creep event size q_s and the creep rate λ_s. Its contribution in the case of metallic wires can be estimated by experimental measurements which give the terms $\lambda_s q_s^{1/2}$, with typical values $q_s \sim 10^{-15}$ and $\lambda_s \sim 20$. The wire creep equivalent spectral density in h is given by [69]:

$$\tilde{h}_{creep}(f) = \frac{\theta_0 \lambda_s q_s^{1/2}}{2L} \frac{1}{2\pi f} m\omega_v^2 |H_v(2\pi f)| \tag{2.40}$$

where θ_0 is the horizontal-to-vertical coupling angle, H_v and ω_v are respectively the force-to-displacement transfer function for the vertical mode oscillation and the related angular frequency, m is the mirror mass and L the length of the interferometer arm. In order to minimize the creep noise, suitable metal alloys which minimize λ_s and q_s must be chosen.

Hysteresis of polycrystalline metals In the low-frequency band the dissipations caused by the viscosity become negligible, but conversely static hysteresis becomes important in the metallic components of the mechanical oscillators, giving rise to a noise proportional to $1/f$. These effects are produced by internal microscopic dynamics of polycrystalline metals used in blades and flexible joints of oscillators: the hysteresis can be considered an effect of spatial disorder in crystalline materials caused by impurities, gaps and linear defects called dislocations. When the dissipation in a metal goes from being dominated by the motion of a single dislocation, characterized by a viscous-like effect, to the collective motion of many dislocations, it manifest itself as an avalanche described by a statistic of self-organized criticality which can propagate throughout the metal component [76]. The reorganization of the dislocation network removes part of the elasticity from the system, resulting in a variation of the Young modulus from the nominal value. This effect is not important at high frequencies, because for $f \gg 1$ the avalanches do not have the time to propagate and grow. In the first generations of interferometric gravitational wave detectors this effect is negligible in their typical sensitivity band, but this low-frequency instability might become significant in the third generation of detectors which are expected to operate at lower frequencies (see sec. 2.5). A possible solution to avoid this noise source is to use amorphous metals (also known as *glassy* metals) which are dislocation-free, or ceramic materials, whose dislocations are blocked by polar bonds; however it must be taken into account that the motion of dislocations in the material reduces its fragility, consequently the use of materials in which such motion is hindered will inevitably lead to an increase of the fragility of the mechanical components.

Control noises Control loops used to maintain the interferometer in its operating point may reintroduce or amplify the system noises. Below 50 Hz longitudinal and angular controls of the mirror can be sources of noise, caused by

non-optimal filters or noisy error signals; at frequencies $> 50\ Hz$ magnet-coil actuators can give rise to noise caused by DAC and/or eddy currents; at kHz frequencies the control loop of the laser stabilization can be affected by fluctuations in the laser frequency.

Electromagnetic noises These noises are generated by the coupling between the electromagnetic fields of electrical components and the detector output through some electromagnetic pickup, and by the coupling of the magnets used in the position control of the mirror suspension. In particular the magnetic noise caused by the actuator magnets is coupled with the seismic amplitude spectral density, i.e. $\tilde{h}_{mag} \propto \tilde{x}$, through diamagnetic coupling and eddy currents.

Transverse electromagnetic modes The wavefront of the laser beam used in interferometers is composed of the sum of different transverse modes with respect to the direction of propagation of the light. The fundamental mode is called TEM_{00} and is characterized by a Gaussian intensity profile, while the other modes are describable by means of Hermite polynomial functions (see fig. 2.5). The diffraction effects caused by the optics in the interferometer produce a phase shift that is different for each mode of the electromagnetic field, resulting in the instability of the cavities. Furthermore, the convolution of these modes with the vibration modes of the mirror is different from that produced by the fundamental mode. In order to avoid these effects and to select only the fundamental mode TEM_{00}, optical filters are added to the basic configuration of an interferometric gravitational wave detector, between the laser source and the interferometer, and between the output port of the interferometer and the acquisition optical bench. They are constituted of triangular cavities called respectively input mode cleaner and output mode cleaner (see sec. 2.3.1).

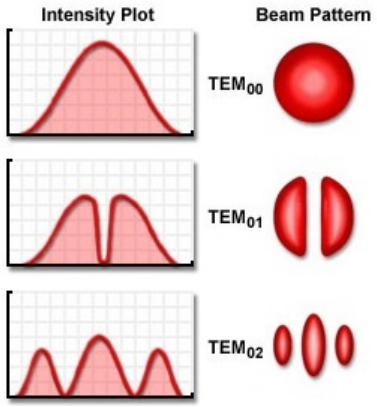

Figure 2.5: Transverse electromagnetic modes of a laser beam; the first three modes TEM_{00}, TEM_{01} and TEM_{02} are represented; the TEM_{10} and TEM_{20} patterns can be obtained from the rotation of the represented modes by $\pi/2$; TEM_{ij} can be obtained by the mix of these modes.

2.3 First generation detectors

In the past years a first generation of large ground-based interferometric gravitational wave detectors has been active, composed of the detectors:

- **Virgo**, a FPM interferometer with 3 km long arms, located at the European Gravitational Observatory in Cascina, Italy. It is described with some detail in sec. 2.3.1;
- **LIGO**, consisting of three FPM interferometers sited in two observatories in USA (a 4 km long FPM interferometer at the Livingstone observatory in Louisiana and 4 km + 2 km long FPM interferometers at the Hanford observatory in Washington);
- **GEO600**, a FPM interferometer with 600 m long arms, located at Sarstedt, Germany;
- **TAMA300**, a FPMI interferometer with 300 m long arms, located at the Mitaka campus of NAOJ, Japan.

Coincidence observations performed by the detector network allowed cross - correlation analysis of the detected signals and improved the antenna pattern resulting from the global array of detectors, as shown later in fig. 2.19 for the advanced detector network. After a first phase of operations, the two main detectors Virgo and LIGO were upgraded to the improved-performance configurations: Virgo+ (see sec. 2.3.1) and Enhanced LIGO. The sensitivity curves for these initial detectors, and those for next generations detectors, are shown in fig. 2.6.

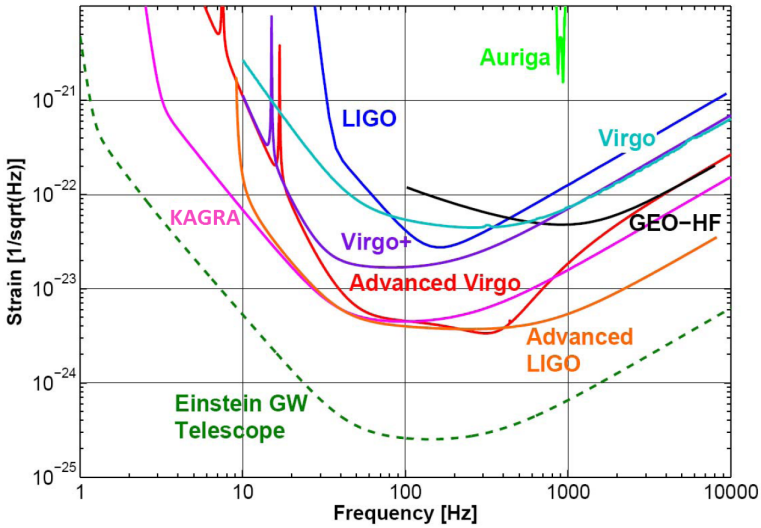

Figure 2.6: The sensitivity curves of initial and enhanced (Virgo/Virgo+, LIGO, GEO HF), second generation (advanced Virgo and LIGO, KAGRA) and third generation (Einstein Telescope) detectors. For comparison it is plotted also the narrow sensitivity band of a resonant bar detector (AURIGA).

2.3.1 Virgo

Virgo represents the classic example of first generation gravitational wave interferometric detector. It is a power-recycling FPM interferometer with 3 km long arms (see fig. 2.7) and its mirrors are suspended to seismic attenuators, making them gravitational test masses as shown in sec.2.1.2. The interferometer pipes are kept in ultra-high vacuum regime, with partial pressures: $P_{H_2} = 10^{-9}\ mbar$ for the molecular hydrogen, $P_{hc} = 10^{-14}\ mbar$ for the hydrocarbons and $P_i = 10^{-10}\ mbar$ for other gases. The construction of Virgo was founded by INFN and CNRS and ended in 2003. In its initial configuration it was commissioned and operated till 2010, performing two long science runs (see table 2.1) and many weekend science runs. In 2010 it was upgraded to the enhanced configuration called Virgo+, performing two other long science runs till the end of 2011. The interferometer is currently being upgraded to the advanced configuration (see sec. 2.4.1).

Science Run	Start Time	End Time
VSR1	$2007/05/18^{th}$ 21:00 UTC	$2007/10/01^{st}$ 05:00 UTC
VSR2	$2009/07/07^{th}$ 21:00 UTC	$2010/01/08^{th}$ 22:00 UTC
VSR3	$2010/08/10^{th}$ 21:00 UTC	$2010/10/20^{th}$ 05:00 UTC
VSR4	$2011/07/03^{rd}$ 21:00 UTC	$2011/09/03^{rd}$ 05:00 UTC

Table 2.1: Virgo and Virgo+ long science runs.

Figure 2.7: Aerial view of the Virgo detector and EGO (European Gravitational Observatory) facilities.

Optical layout

The optical layout of the Virgo detector is represented in fig. 2.8. The two arms are 3 km long Fabry-Perot cavities characterized by a finesse $F = 50$, which correspond to an effective length $L_{eff} \approx 95\ km$. These two cavities are oriented in the north and west directions and delimited by their input and end mirrors, usually indicated as WI-WE and NI-NE. The power recycling mirror (PR) is placed 6 m before the beam-splitter (BS), forming a cavity characterized by a recycling gain $G_{pr} \approx 50$. The input mirrors are placed approximately 6 m after the beam-splitter, with a Schnupp asymmetry $\Delta L = L_W - L_N \approx 0.88\ m$ (see sec. 2.1.4). The laser beams transmitted and reflected by the mirrors are measured by single and quadrant photodiodes, respectively for the longitudinal and angular control.

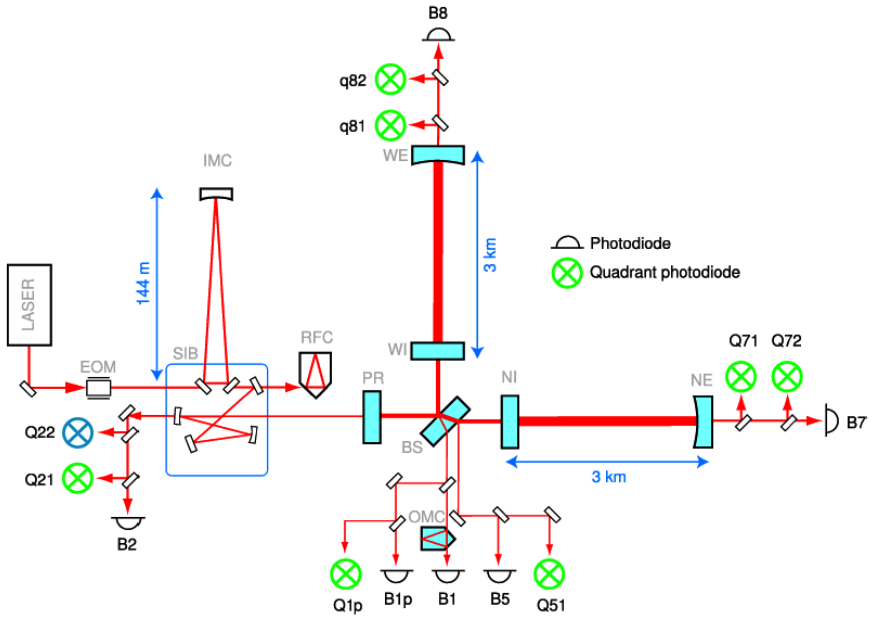

Figure 2.8: Optical layout of initial Virgo. The west and north input/end mirrors are indicated by WI/WE and NI/NE, the beam-splitter by BS, the power recycling by PR, the input and output mode cleaner by IMC and OMC, the suspended injection bench by SIB, the reference frequency cavity by RFC, the electro-optic modulators by EOM. The laser beams are indicated by B as follows: B7 and B8 are transmitted through the north and west end mirrors; B2 is reflected by the PR; B5 is reflected by the secondary surface of the BS and used as an indicator of the power recycling; finally B1 is the dark fringe signal reflected by the BS.

Injection system

The laser beam injected in the interferometer is generated by two laser sources: the high-power Nd:TVO_4 (slave laser) stabilized by the high-stability solid-state Nd:YAG (master laser). The resulting laser beam is characterized by a wavelength $\lambda = 1064\ nm$, and by a power of 20 W. The stabilized beam is modulated in

phase by two electro-optic modulators (EOM in fig. 2.8) at three radio-frequencies $(6, 8, 22\ MHz)$ in order to obtain an AC detection configuration (see sec. 2.1.4) [68]. Subsequently, the modulated beam pointing is controlled by the piezo-electric actuated mirrors of the beam monitoring system, and sent to the suspended injection optical bench (SIB in fig. 2.8) in a vacuum chamber. The SIB hosts the output mirrors of the *input mode cleaner* (IMC in fig. 2.8), a 144 m long triangular cavity characterized by a finesse $F_{IMC} = 10^3$. Since the IMC is a resonant cavity, it is a first order low-pass filter for the laser power and frequency fluctuations, with a cut-off frequency which can be calculated from eq. 2.26 as $f_{IMC} \sim 500\ Hz$. Moreover, the IMC suppresses the transverse modes different from the fundamental Gaussian TEM_{00} mode (see *transverse electromagnetic modes* in sec. 2.2.3). From the SIB the main beam is injected toward the power recycling mirror, while a small part of the beam is sent to the *reference frequency cavity* (RFC in fig. 2.8), a 30 cm long cavity used for the laser stabilization system.

Detection system

The laser beams from the interferometer output, which typically have a power between few μW and 100 mW, are measured by single or quadrant photodetectors. In particular the dark fringe signal (B1 in fig. 2.8) is focused by a telescope to the *output mode cleaner* (OMC in fig. 2.8), which is a 2.5 cm long resonant cavity with finesse $F = 50$, kept in resonance condition by controlling its temperature. In analogy with the IMC, also the OMC suppresses the transverse electromagnetic modes higher than the fundamental one which might be caused by misalignment in the interferometer. From the OMC the output beam is sent to the external detection bench, which is kept in acoustic insulation and hosts the photodetectors and the CCD control cameras. The output signal is converted by dedicated ADC boards, processed through digital filters, such as the anti-aliasing filter, and finally converted in a format suitable for the data acquisition system.

Suspension system

In the low-frequency band the seismic noise is the main limitation to the sensitivity of the interferometer (see fig. 2.4 and chapter 3), appearing as a displacement noise in the six (translational and rotational) degrees of freedom of the test masses, which are coupled among them since the terrestrial curvature produces a $\alpha \sim 3 \times 10^{-4}\ rad$ angle between the perpendicular lines of the mirrors. In order to suppress such a noise, the mirrors and the main optical elements of the interferometer are suspended from a seismic low-pass filter called **superattenuator**, providing a seismic noise reduction of a factor 10^{12} at $f = 10\ Hz$. It is composed of a three-legs inverted pendulum and a subsequent chain of vertical filters (see fig. 2.9), and can be modeled as a chain of seven pendula for every mirror[6]. The superattenuator of Virgo is characterized by a resonant frequency $f_r \sim 0.5\ Hz$, therefore it keeps the suspended test masses in a free-falling condition at frequencies higher than f_r (see sec. 2.1.2). Moreover it allows the actuation control of the mirror alignment

[6] the IMC mirror, injection and detection benches are suspended by a smaller filter composed by an inverted pendulum and two vertical filters

by means of coil-magnet pairs. The inverted pendulum forms the pre-insulator element of the superattenuator, acting as a second order low-pass filter. The attenuation factor $\mathcal{A}$ of the vertical motion in y_0 produced by this pendulum on the suspended mass m in y is given by:

$$\mathcal{A} = \frac{y}{y_0} = f_0^2 \left[(f_0^2 - f^2)^2 + \frac{f_0^2 f^2}{Q^2} \right]^{-1/2} \tag{2.41}$$

where Q is the quality factor (see sec. 4.2.1) of the inverted pendulum and f_0 is its resonant frequency, given as function of pendulum length l by [77]:

$$f_0 = \frac{1}{2\pi} \left(\frac{k}{m} - \frac{g}{l} \right)^{1/2} \tag{2.42}$$

The resonant frequency f_0 shown in eq. 2.42 depends on k, which is the elastic constant of the three flexible joint of the inverted pendulum legs. Using the typical numbers of the Virgo superattenuator, the resonant frequency obtained is $f_0 \approx 30\ mHz$, which roughly corresponds to the resonance of a standard pendulum with $l = 280\ m$. The following seismic insulator is a chain of six cylindrical mechanical

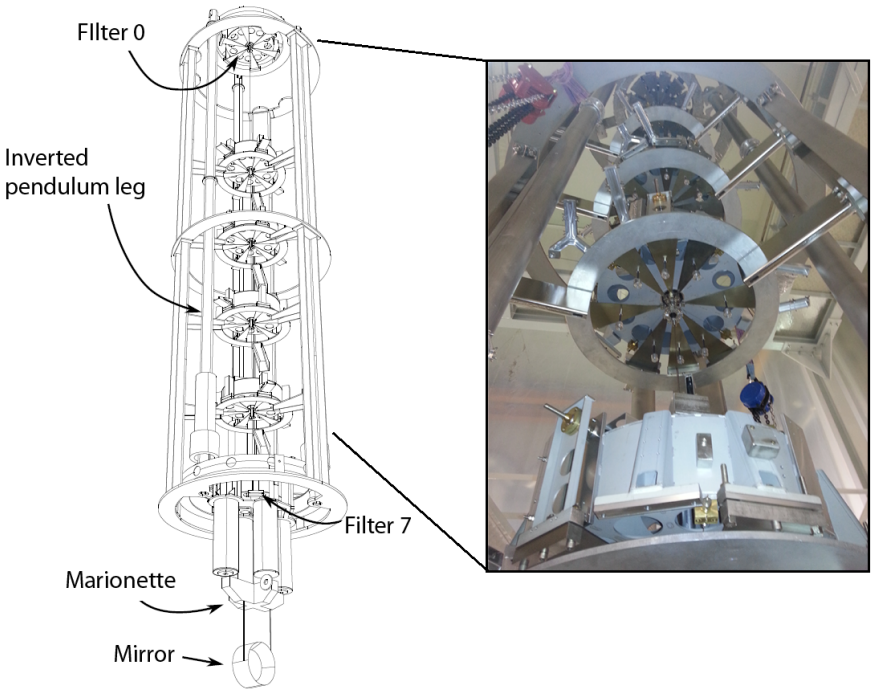

Figure 2.9: *left*: scheme of the superattenuator of the initial Virgo, composed by the inverted pendulum and the $\sim 8\ m$ high vertical filter chain, from filter 0 to filter 7 (so called for historical reasons); *right*: superattenuator of the NE mirror, picture taken during upgrade operations in 2013.

filters (see fig. 2.10) connected to the top-stage of the inverted pendulum by steel wires. In such a N-stage pendulum the horizontal displacement of the suspension

point, at a frequency higher than its normal modes, is transmitted to the last stage with an attenuation proportional to f^{-2N} (see eq. 3.13). Each vertical filter has a mass $m_{vf} \sim 100\ kg$ and is suspended from its barycenter. In the chain, two consecutive filters are connected together by means of maraging steel-made triangular blades characterized by a resonant frequency $f_0 \sim 1.5\ Hz$; the number of blades (up to a maximum of 12) depends on the suspended load of each filter. These blades at rest have a transverse shape with a constant curvature, while when they are loaded it becomes horizontal. The equivalent pendulum resonant frequency of these vertical filters is lowered by means of magnetic anti-springs, composed of repellent magnet pairs, with parallel faces at distance d and free to move in the vertical y direction. The vertical component of the repulsive force is consequently given by:

$$F_{m\perp} = F_m \sin\alpha \approx F_m \frac{\Delta y}{d} \tag{2.43}$$

where α is the angle between the perpendicular central axis of the two magnets. When they are aligned $\alpha = 0$ and the perpendicular repulsive force is zero. Instead, when they slide of Δy forming a certain angle α, $F_{m\perp}$ in the small-angle approximation (i.e. for $\Delta y \ll d$) is given by the last term of eq. 2.43. Therefore, this configuration is equivalent to a spring with a negative elastic constant, which lower the resonant frequency of the oscillator. The vertical filters are characterized by an high moment of inertia in order to reduce the torsional motion around the vertical axis. Furthermore, the suspension wires are fixed at the minimum possible distance in order to lower their torsional frequency, which is $f_t \sim 1\ Hz$. The overall seismic suppression obtained by the superattenuator of Virgo is shown in fig. 2.11. The whole suspension is hosted in a tower, whose upper environment is

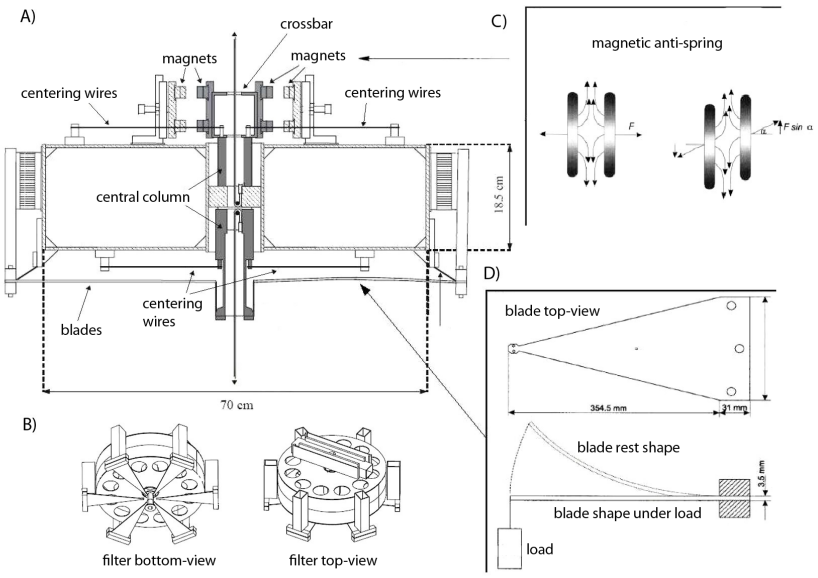

Figure 2.10: Vertical filter of the superattenuator of Virgo [77]; *A)* transversal section of the filter; *B)* prospective view of the filter; *C)* magnetic anti-spring detail; *D)* triangular blades of the filter at rest and under load.

kept in vacuum regime at $P \approx 10^{-6}\ mbar$, since the outgassing of the mechanical parts represent a limit for the vacuum system. The lower part of the tower hosts the payload, i.e. the last stage of suspension, the mirror and its reaction mass, which are kept in ultra-high vacuum regime. The two vacuum environments of the tower are separated and the last stage of suspension is connected to last vertical filter of the superattenuator, called filter 7, by a maraging steel wire through a low-conductance hole.

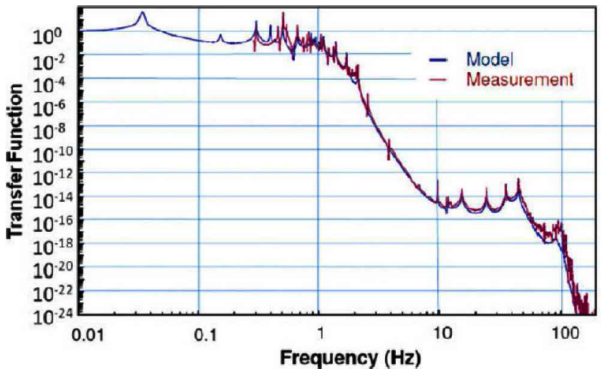

Figure 2.11: Vertical transfer function of the Virgo superattenuator extrapolated by measurements using the stage-by-stage technique (red curve) compared to the analytical model (blue curve). The experimental TF must be multiplied by the input seismic noise at the ground level in order to obtain the residual mirror displacement along the beam, considering a vertical-to-horizontal coupling of 10^{-2} [78].

Payload

The payload of initial Virgo (see fig. 2.12) is composed of the last stage of the suspension, the mirror and its reaction mass, in a branched configuration. It has been designed [79] in such a way to have mechanical resonant frequencies as high as possible, in order to avoid spurious thermal noise contributions to the output signal of the interferometer. Moreover, it allows the actuation of the mirror, controlling its longitudinal displacement (along the direction of the laser beam z) and torsional (θ_x, θ_y and θ_z) modes of oscillation with magnet-coil pairs.

The first element of the payload, suspended with a maraging steel wire by the filter 7, is the **marionette**. This element is made of amagnetic metal alloy and has an anvil-like shape with a mass $m_{mario} \approx 108\ kg$. Its torsional and translational modes respect to the "legs" of filter 7 (the lower long cylindrical elements in fig. 2.9) are controlled by magnet-coil pairs, respectively placed on the marionette orthogonal arms and on the filter 7. Moreover, inside the marionette a stepper motor is connected to a mobile mass that can be used to adjust its alignment. Four concentric C85-steel wires are clamped and suspended from the marionette, surrounding the semi-cylindrical lower surfaces of the mirror[7] and of its reaction mass, resulting in four equivalent wires for each suspended element.

[7] these wires were later substituted by the monolithic suspension of the mirror in Virgo+.

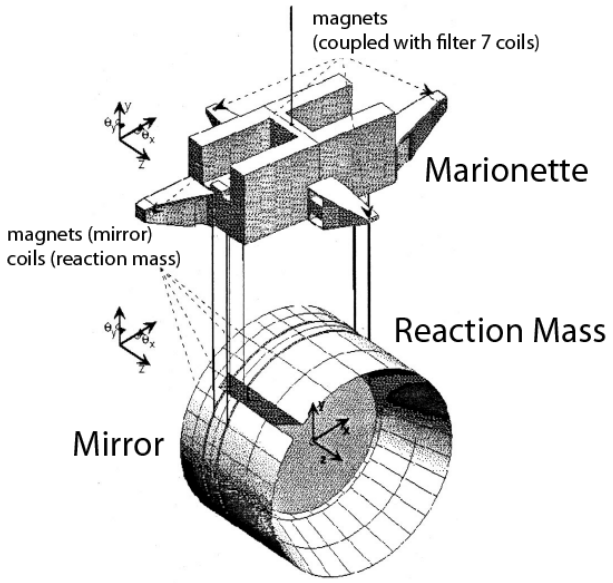

Figure 2.12: Schematic view of the payload of initial Virgo [79]. The standard frame of reference used to describe the motion of the suspended and optical elements in the interferometer are indicated in the figure.

The **reaction mass** (also called *reference mass*) is an hollow cylinder made of 6063 aluminum alloy for a mass of $m_{rm} \approx 60\ kg$. It is used to apply a direct actuation on the mirror: four coils are fixed on this mass in coincidence with four magnets fixed on the mirror. Moreover, it acts as a safety structure for the mirror itself. On the edge of the reaction mass four ceramic markers are placed in order to allow the control system to do a first coarse alignment of the mirror.

The **mirrors** are cylinders made of suprasil (i.e. fused silica, SiO_2), with a diameter $d \approx 35\ cm$ and mass $m_{mir} \approx 20\ kg$, except for the beam-splitter mirror which is smaller ($d \approx 23\ cm$ and $m_{bs} \approx 5\ kg$, shown in fig. 2.13). On the suprasil bulk of the mirrors several coating layers are deposited, with alternate low and high refractive indices. The surface of the input mirrors are flat, while that of the end mirrors has a concave shape with radii of curvature $r_{NE} \approx 3580\ m$ and $r_{NE} \approx 3601\ m$, in order to keep the stability of the 3 km long Fabry-Perot cavities.

Control system

The controls and operations needed to keep the interferometer in operating conditions is known as the *locking* of the interferometer. In Virgo this system must control the relative displacement of the mirrors with a precision of $10^{-12}\ m$. The locking of the interferometer is achieved extracting the error signals of the mirror position (and therefore of distances), and setting feedback filters which act on the electromagetic actuators of the various stages. In particular, the control system is subdivided in two levels: the **local control** and the **global control**.

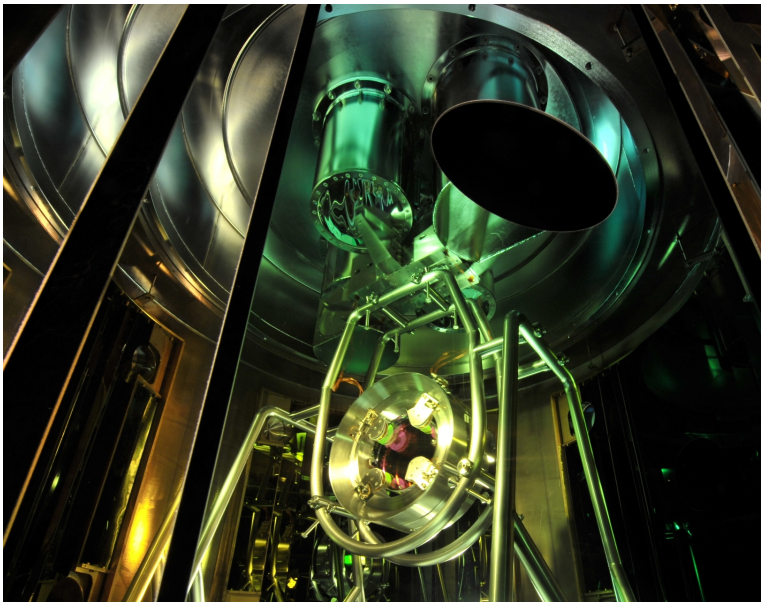

Figure 2.13: The beam-splitter payload of initial Virgo, suspended in its tower. Picture taken just before the unmounting on 2012 during the upgrade operations to Advanced Virgo.

Local control The local control depends on the error signals produced by relative and inertial sensors, such as optical levers, accelerometers and displacement sensors. The active control of each suspension is divided into three parts:

- *inverted pendulum*, controlled at the level of the filter 0 by the inertial damping system, dedicated to very low and low frequency actuation. In the upper part of the filter 0 three accelerometers and three LVDT (i.e. linear variable displacement transformer) are fixed and used to determine the absolute position of the stage of the suspension (see fig. 2.14). The output signals of these sensors are digitalized via analog-to-digital converters (ADC) processed and combined via digital-signal processor (DSP). LVDT sensors are used for frequencies $< 50 - 100\ mHz$, while accelerometers are considered for higher frequencies, up to 4 Hz. Finally, their processed signals are used to obtain the necessary corrections to the translational and rotational modes of the suspension, translated into corresponding electric signals by digital-to-analog (DAC) boards and sent to the electromagnetic actuators, i.e. to the coils of the three magnet-coil pairs of the inverted pendulum;
- *vertical filter*, their length is controlled by single LVDT sensors, and from the sum of all the displacement signals of the various stages is realized the vertical position control of the suspended payload;
- *payload*, at this level the angular and longitudinal motions are controlled by the magnet-coils actuators fixed to marionette-filter 7 and mirror-recoil mass. The longitudinal and angular positions of the payload elements are obtained by the error signals of position sensing devices

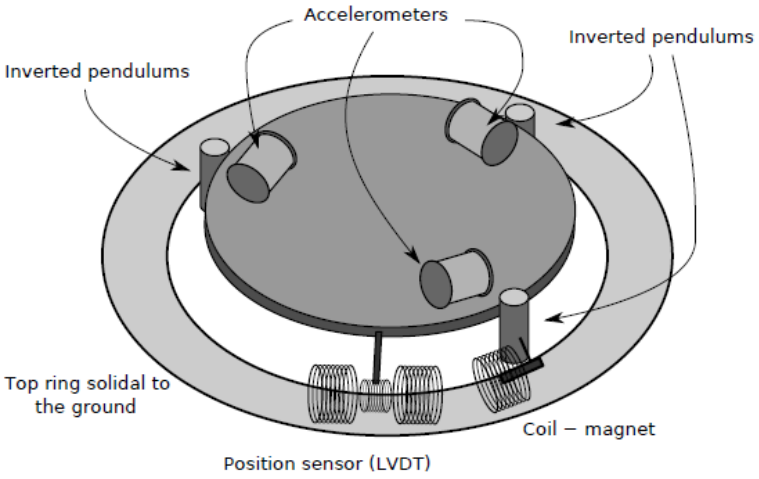

Figure 2.14: Schematic view of the top of the superattenuator, with the relative displacement sensors (LVDT, only one of them shown) and the accelerometers. The top outer ring is solidal to the ground, while the central structure is the top stage of the inverted pendulum, with its legs indicated.

(PSDs), which are optical levers (low-power red diode lasers and quadrant photodiodes) that measure the mirror position and that of the marionette, taking advantage of a small mirror anchored to it. In the case of oscillation motions too large for the dynamic range of the PSDs, the position of the mirror is reconstructed using a CCD camera pointed at four diffusive markers fixed to the mirror. As for the inertial damping system, the digitalized error signals are processed by a dedicated DSP in order to generate the necessary correction signals to be sent to the electromagnetic actuators of the payload. The intermediate frequency corrections are sent to the actuators of the marionette, while the high frequency corrections are obtained acting on the electromagnetic actuators of the mirror-recoil mass.

The local control can provide a mirror position accuracy at the order of $\sim 1\mu rad$, which is not enough to keep the interferometer in the working condition with the necessary resonance conditions. Moreover, except for the accelerometers, the position sensing is related to the ground reference, and therefore it is affected by the seismic activity and by temperature drifts.

Global control The global control provide the fine locking of the detector keeping it in the resonance conditions by using the error signals coming from the photodiodes of the interferometer, generating the necessary correction signals and sending them to the local control at the level of the payload via optical links, in order to control the length of the cavities. The error signals from single photodiodes are used for the longitudinal control of the mirrors, while those from quadrant photodiodes are used for their angular control. In particular, since the laser is modulated, the resonance conditions of fundamental TEM_{00}, higher modes and sidebands are kept by this control.

Virgo+

In 2010 the initial Virgo detector was enhanced to the so-called Virgo+ configuration. The main modifications were:

- **Monolithic payload.** In the initial Virgo configuration the mirrors were suspended by means of two loops of C85 steel wires. In order to reduce the thermal noise contribution due to this kind of suspension, the steel wire loops were substituted by fused silica (SiO_2) fibers[8], made up and assembled in Virgo laboratories and attached to the mirrors by means of silica ears silicate-bonded on the lateral flat sides of the mirrors (see fig. 2.15). In this way the mirror, the suspension wires and their clamps can be considered as a monolithic bloc of fused silica. This configuration provide many advantages, such as smaller loss angle than steel and lower thermoelastic dissipations [80, 81], for a breaking stress limit $P_{BSL} \sim 10^9\ Pa$ comparable to that of steel wires; however fused silica fibers are also characterized by some disadvantages, such as the fragility in case of cracks and defects, and aging due to environmental pollution.

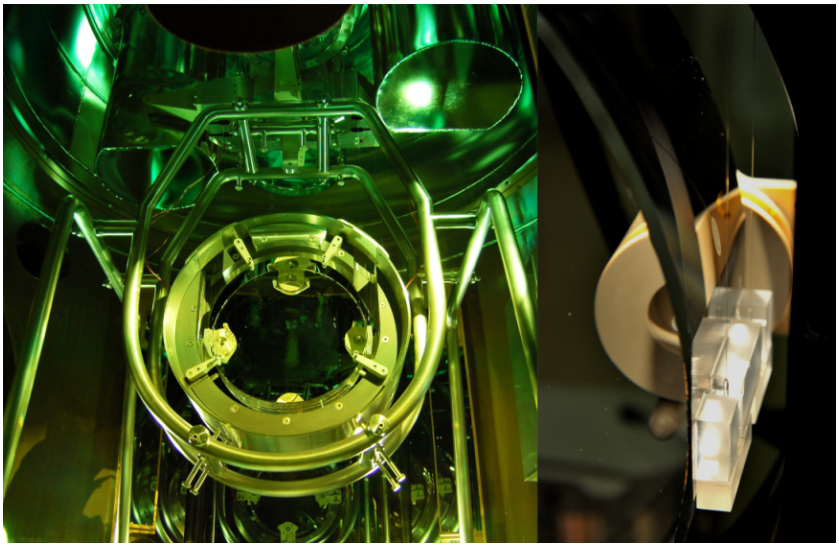

Figure 2.15: *left*: The monolithic payload of Virgo+ suspended in the West Input tower; *right*: detail of the fused silica fibers with thier anchors silicate-bonded to the silica ear on the lateral surface of the mirror.

- **New mirrors.** New suprasil end and input mirrors were installed. A difference in the radius of curvature (RoC) was noticed in the end mirrors, therefore it was necessary to add a new system to the configuration: the *Central Heating RoC Correction* (CHRoCC) [82]. It corrects the RoC sending a beam heating pattern to the mirrors from dedicated black-body-emitters, obtaining a thermal expansion of the fused silica substrate which adjust the curvature of the end mirror. This system was installed before the VSR4.

[8] fused silica fibers were originally developed by GEO, and later adopted by eLIGO and Virgo+.

- **Laser injection upgrade.** The laser power at the input port was enhanced to 25 W by means of a new laser amplifier;

- **Thermal compensation.** A part of the optical power stored in the Fabry-Perot cavities is absorbed by the high reflective coating of the mirrors, generating a temperature gradient inside the substrate. This absorption leads to thermo-optic and thermo-elastic effects on the test masses, such as the thermal lensing and the deformation of the profile of the reflective surface (see sec. 4.4.2). In particular the thermal lensing affected the power recycling cavity, degrading the performances of the interferometer. To contrast this kind of effects a thermal compensation system was installed, consisting in an additional and independent CO_2 laser which provide a heating pattern of the input mirrors, in order to reduce such deformations.

- **Input mode cleaner upgrade.** The input mode cleaner end-mirror was replaced by an heavier one.

Sensitivity curves and horizon distance

The sensitivity curves, such as those shown above in fig. 2.6 and 2.4, are calculated by considering the different sources of noise in the interferometer depending on the frequency, i.e. indicate the minimum detectable intensity of a gravitational wave, usually in units of equivalent spectral density $\tilde{h}$ (see app. A). They are computed using dedicated codes such as GWINC, developed within the LIGO collaboration and therefore modified for Virgo [83]. In fig. 2.16 and 2.17 there are reported the experimental best strain sensitivity curves until 2010 for Virgo and LIGO.

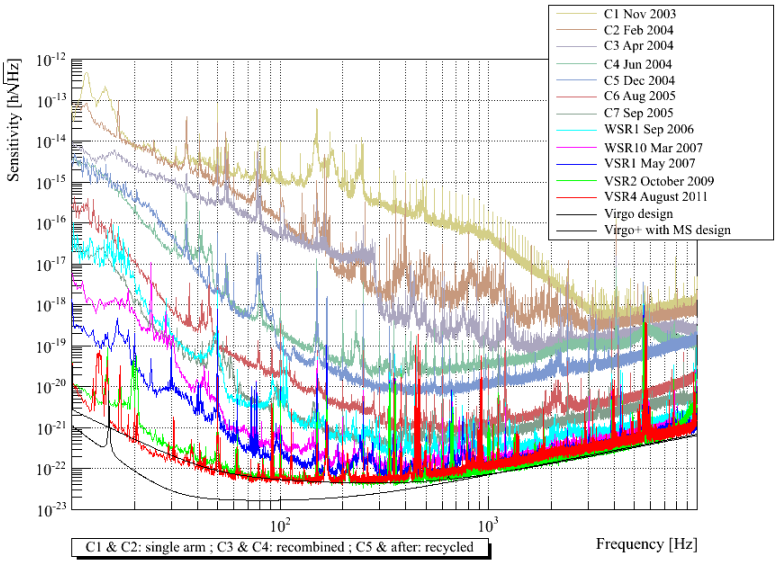

Figure 2.16: The best strain sensitivity curves from the Virgo commissioning, weekend and long science runs, compared to the initial and enhanced design sensitivities.

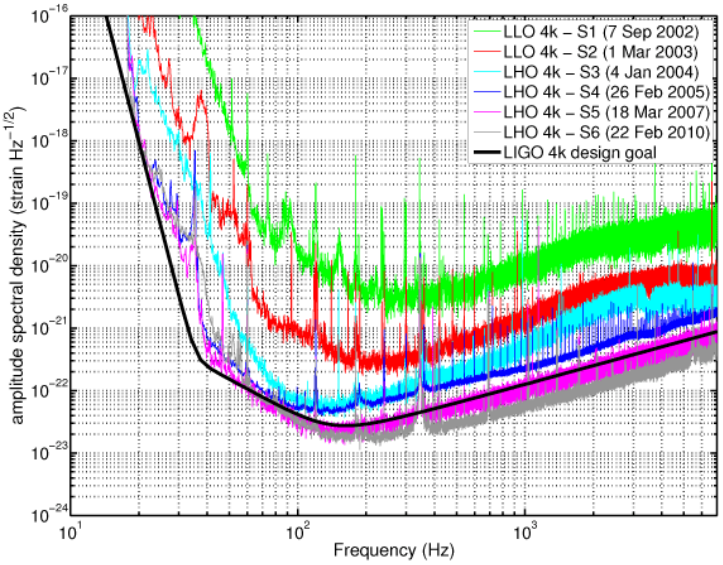

Figure 2.17: The best strain sensitivity curves from the LIGO science runs S1 to S6 [84].

A quantity indicative of the sensitivity of the detector is the **horizon distance**. It is the maximum range out to which the interferometer can detect a coalescence of two neutron stars with mass $M = 1.4\ M_\odot$ that are optimally oriented and located[9] at a signal-to-noise ratio $SNR = 8$. When it is considered the average over all the sky locations and source orientations, it is defined *average horizon* and it is proportional to the equation [85]:

$$D_h \propto \left(\frac{5\mathcal{M}^{5/3}\Theta^2}{96\pi^{4/3}\rho_0^2} \int_{f_{low}}^{f_{high}} \frac{f^{-7/3}}{S_h(f)} df \right)^{1/2} \tag{2.44}$$

where S_h is the power spectral density of h, $\rho_0 = 8$ is the minimum signal-to-noise ratio required for the detection, $\Theta = 1.77$ si a parameter accounting for the averaging over the binary positions and orientations, and $\mathcal{M}$ is the chirp mass as defined in eq. 1.111. The average horizon distance for Virgo is calculated on-line during the observations and is expressed in Mpc by the equation [86]:

$$D_h^V = 10^{-20} \left(\int_{40\ Hz}^{2300\ Hz} \frac{f^{-7/3}}{S_h(f)} df \right)^{1/2} \ Mpc \tag{2.45}$$

The increase of the horizon distance, and then of the observable universe, depends on the sensitivity of the detector. Referring to fig. 2.16, the horizon distances for the weekend runs WSR1 and WSR10 were respectively $D_h^{WSR1} \approx 8 \times 10^6\ ly$ and $D_h^{WSR10} \approx 10^7\ ly$, to be compared with the distance of the Andromeda galaxy $D_{M31} \approx 2.5 \times 10^6\ ly$, and was improved to $D_h^{VSR1} = 1.5 \times 10^7\ ly$ during the long science run VSR1, to be compared to the distance of the Virgo cluster of galaxies $D_{VC} \approx 5.4 \times 10^7\ ly$ (see fig. 2.18).

[9] the optimal orientation and localization is when the orbital plane is perpendicular to the line-of-sight and parallel to the detector plane, maximizing the antenna pattern.

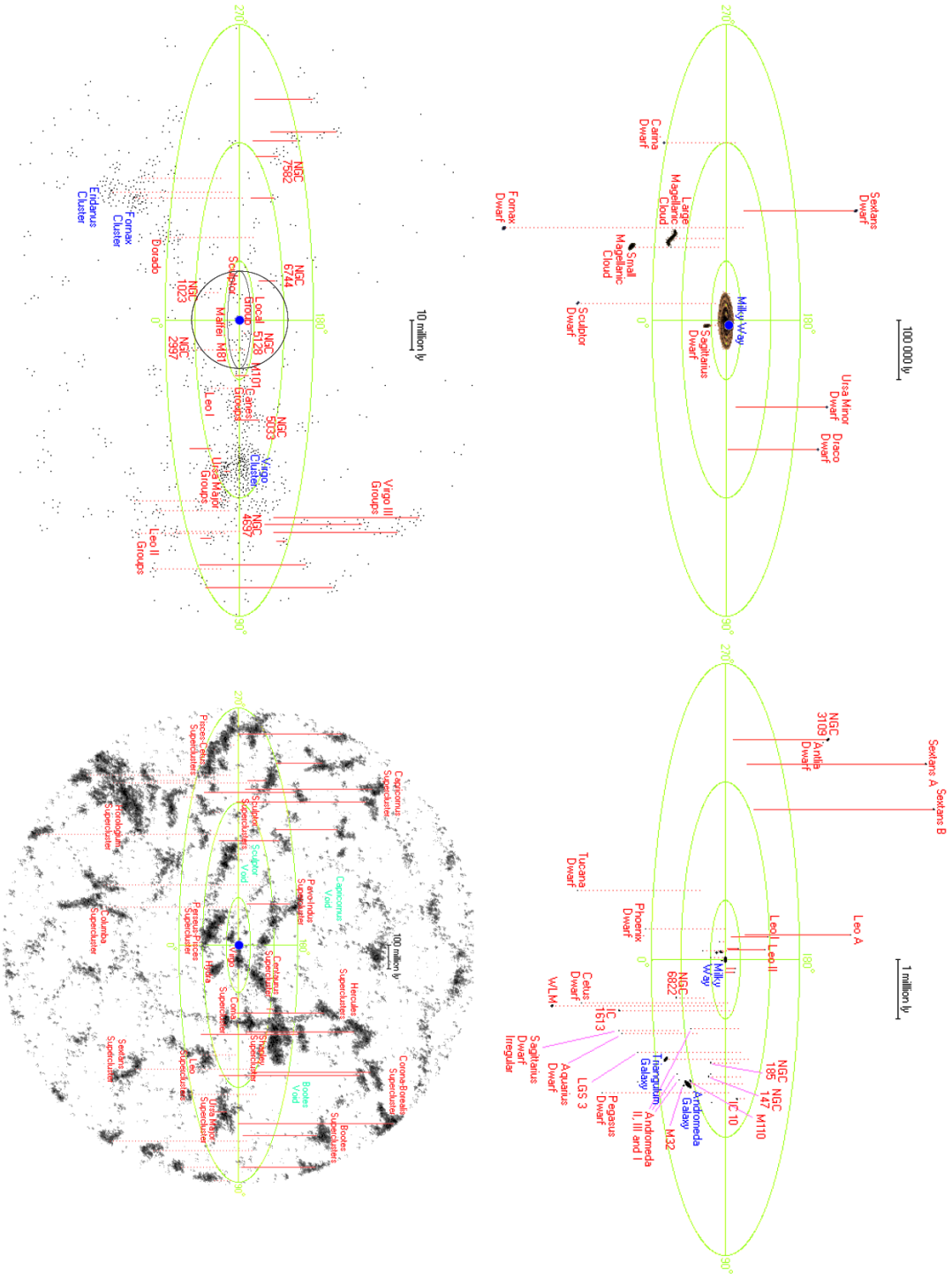

Figure 2.18: Galaxies and clusters of galaxies in the local universe; from top-left to down-right the horizon is equal to 10^5, 10^6, 10^7 and 10^8 ly ($1\ ly \approx 0.307\ pc$).

2.4 Advanced detectors

The second generation of interferometric detector is currently under construction. The two main first generation detectors Virgo and LIGO are being upgraded to their Advanced design, which it is expected to be completed in 2014. They will form the core of the advanced global network of detectors that will be enhanced by the addition of the Japanese underground and cryogenic detector KAGRA (by 2017, see sec. 2.4.2), improving the resultant antenna pattern for coincidence observations (see fig. 2.19). A further improvement to the second generation network of detector will be given by the addition of the upgraded GEO-HF (which can be competitive in the high frequency range) and of a new detector built from the possible moving of the H2 LIGO interferometer to another location which can improve the overall antenna pattern (e.g. the proposed IndIGO project).

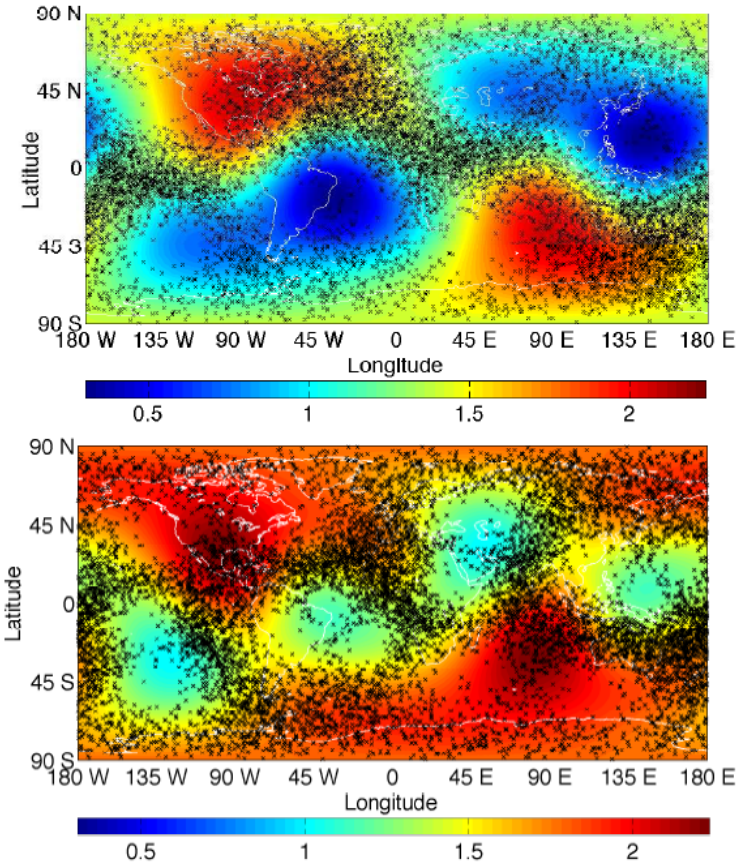

Figure 2.19: *up*: Antenna power pattern for the network of advanced generation interferometers Advanced Virgo and the two Advanced LIGO, considering both the polarization, i.e. $\sum_k (F_{+,k} + F_{\times,k})$; *down*: the same antenna pattern calculated for the network composed of Advanced Virgo, Advanced LIGO and KAGRA. Points indicates the possible detections depending on the sky location [87].

The second generation of interferometers will be characterized by a sensitivity ten times better than that of first generation, corresponding to an observable volume of the universe 10^3 times larger, expanding the horizon distance from $D_h \sim 12\ Mpc$ up to $D_h \sim 140\ Mpc$ for a BNS coalescence, and to $D_h^{BBH} \sim 1\ Gpc$ for the coalescences of a 30 $M_\odot$ - BBH (see fig. 2.18 and 2.20). Consequently the expected detection rates will increase: $\dot{N}_{NS-NS} = 0.02\ yr^{-1} \rightarrow \dot{N}_{NS-NS} = 40\ yr^{-1}$, from initial to advanced Virgo-LIGO network [7]. The most important technological improvements leading to the advanced detectors increased sensitivity are:

- the monolithic suspension of mirrors with silica fibers, already tested in the enhanced first generation detectors. It reduces the thermal noise;
- the increase of the input laser power in order to reduce the shot noise in the high frequency range. Since the adoption of high power laser would also increase the radiation pressure noise (as shown in sec. 2.2.2) and the thermal lensing (see sec. 4.4.2), it will be necessary to adopt:
  - heavier mirrors, since the radiation pressure is proportional to m^{-1};
  - a thermal compensation system, which corrects the profile of the mirror;
- new high-reflectivity coatings, characterized by reduced dissipation and absorption;
- a signal recycling mirror which allows the tuning of the detector bandwidth, in order to increase the sensitivity in a given frequency range, optimizing the sensitivity for a given kind of expected astrophysical source;
- the improvement of the seismic attenuator is necessary in Advanced LIGO; in Virgo the SuperAttenuator already meets the requirements for the advanced design.

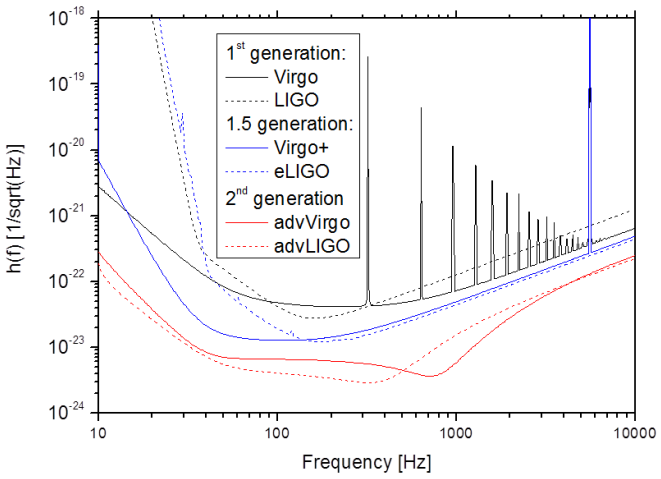

Figure 2.20: Sensitivity curves of Virgo and LIGO for their initial, enhanced and second generation phases.

2.4.1 Advanced Virgo

The upgraded design of the Virgo interferometer, leading to the increase of its sensitivity (see fig. 2.23), is widely described in the recently issued Technical Design Report [78]. The optical scheme is currently being modified by adding a tunable signal recycling cavity (see fig. 2.22) and increasing to 443 the finesse of the Fabry-Perot cavities. Moreover, the detection strategy will change from the AC (heterodyne) to the DC scheme (see sec. 2.1.4), in order to reduce some technical noises. Other infrastructure improvements will reduce the environmental noise and enhance the vacuum system performances.

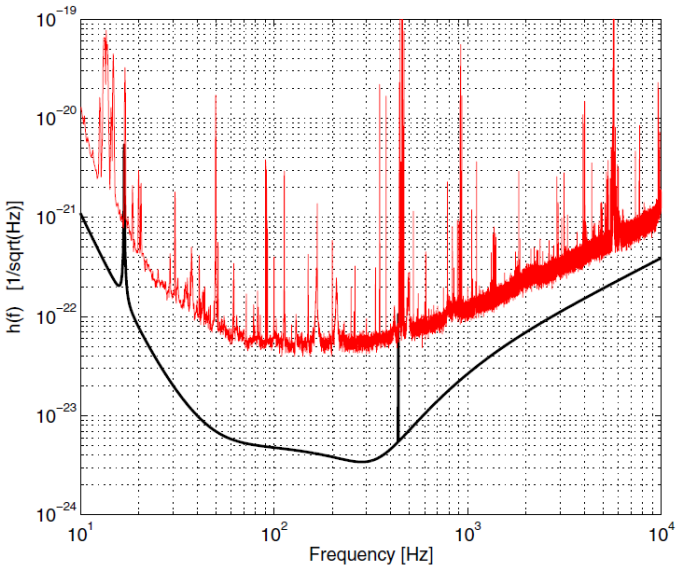

Figure 2.21: Sensitivity curve expected from Advanced Virgo (black line) compared to the best sensitivity reached by Virgo+ during the science run VSR4 [88].

Laser and injection system upgrades

The laser power will be increased in order to have 125 W at the input port of the interferometer, i.e. after the IMC, whose optics will be improved. Therefore, taking into account the losses of the injection system, the laser source must provide at least 175 W. In order to obtain such a power, two 100 W fiber rod amplifier[10] will be used, as shown in fig. 2.22. The injection system is completed by electro-optic modulators and Faraday insulators compatible with the high power laser.

Suspension upgrade

The superattenuators of initial Virgo already provide a seismic insulation compliant with that required for the Advanced design. Nonetheless there will be some upgrades to improve the insulation during bad weather conditions, such as:

[10] the prototype of this system is currently being tested.

- new monolithic inverted pendulum legs, characterized by higher resonant frequency which will allow to expand the bandwidth of the inertial damping system (see *control system* in sec. 2.3.1);

- piezoelectric actuators will be added to the inverted pendulum stage, in order to perform the tilt-control.

Moreover, the benches which host all the photodiodes to be used in science mode will be seismically isolated by dedicated suspensions.

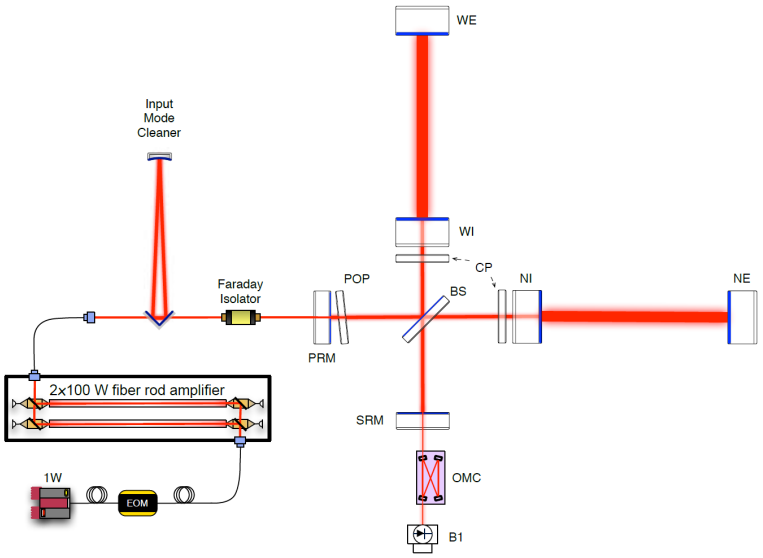

Figure 2.22: Advanced Virgo optical scheme. The detector will be a dual-recycled interferometer thanks to the signal recycling mirror (SRM); in the scheme are indicated also the compensation plates (CP), the pickoff plate (POP) and the new laser injection, with its proper electro-optic modulators (EOM) and the Faraday insulator developed for the new high power laser system [78].

Payload upgrade

The payloads underwent a substantial re-design. The last stage of the suspension will no longer be branched, by removing the mirror recoil mass, substituted by a new designed *caged* payload: in the new payloads the filter 7 will support not only the coils for the actuation of the marionette, but also those acting on the mirror, through the so called *Actuator Cage*, which will serve also as a safety structure for the mirror during the operations (see fig. 2.23). The mirrors will be suspended by means of fused silica fibers, in a monolithic suspension scheme similar to that successfully used in Virgo+.

Mirrors In order to reduce the radiation pressure noise, mirrors will be heavier ($m = 42\ kg$): keeping the same diameter of initial Virgo (35 cm), but with doubled thickness (20 cm). Moreover, in order to limit the scattering losses, the flatness of the reflective surface will be increased ($< 0.5\ nm$) through

a better polishing and by using corrective coating techniques. The coating will be based on optimized multilayer and Tantala-doped Titanium for the high-refractive index layers.

Baffles Since about 100 W of the 125 W injected power in the interferometer will be lost mainly by scattering around the mirrors and towards the pipes, causing a phase noise, new diaphragm baffles will be installed, either suspended around the mirrors (see fig. 2.23) or ground connected inside the vacuum pipes.

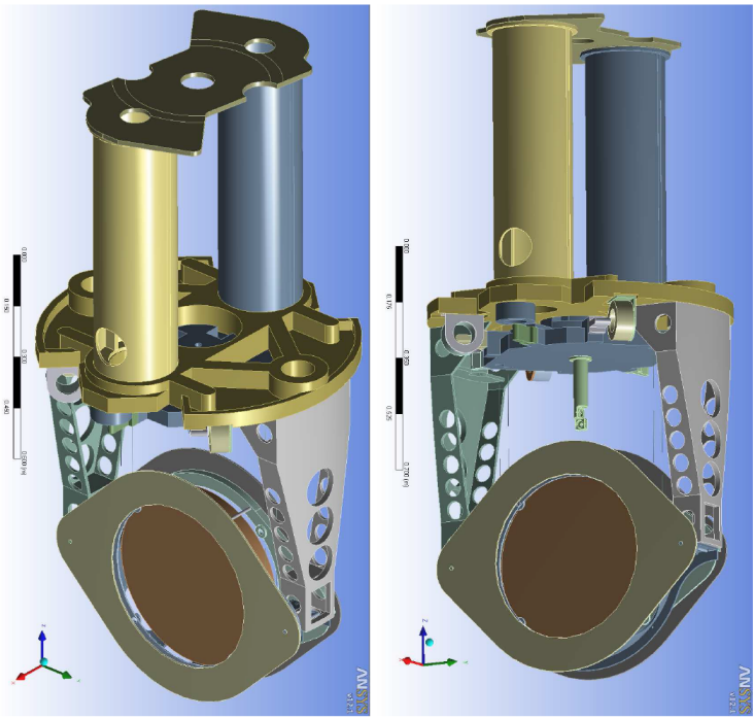

Figure 2.23: Design of the beam splitter payload of Advanced Virgo [78]. The Actuation Cage is connected to the the filter 7 (its two legs are clearly visible) and acts on the new marionette (at the end of the legs) and on the mirror (bottom part of the cage). The payload is completed by the baffles. Test masses payloads will be characterized by a similar design; in the input payloads a compensation plate will be added to the structure.

Thermal compensation system

The thermal compensation system (TCS) is dedicated to the reduction of the thermal effects produced on the mirrors, which would degrade the detector sensitivity. These effects can be geometrical distortions (due to thermal expansion coefficient) or purely optical distortions (due to the temperature-dependence of the refraction index). Advanced Virgo will use a higher power laser that combined with the higher finesse of the Fabry-Perot cavities results in a circulating power of $\sim 800\ kW$: such a high power will produce an absorption in the reflective coatings

of the order of $\sim 0.5\ W$, which causes a change in the radius of curvature of the test masses via thermoelastic deformation. This effect can be controlled by means of a shielded ring heater placed around each mirror. The laser absorption in the input masses causes the heating of their center, locally changing the refraction index and then perturbing the optical path as would do a spurious lens in the interferometer. In Virgo+ this effect was corrected by a CO_2 laser beam in annulus shape on the mirror obtained by an axicon. In the Advanced design this scheme will be followed with a slight modification: indeed the corrective laser cannot act directly on the mirror, because its amplitude noise would spoil the detector sensitivity, therefore the new TCS will be designed to heat an additional plate, called *compensation plate*, with a double-axicon pattern CO_2 laser. The compensation plate is a transmissive optic with the same diameter of the mirror and a thickness of 35 mm, placed in front of the mirror in the related payload. The above mentioned strategies in the TCS will cope only with deformations with a cylindrical symmetry, though non-axisymmetric deformations can be also relevant, causing aberrations in the marginally stable recycling cavities [78]. To cope with such deformations a corrective scanning laser [89] will be added to the system. The TCS sensing will be performed by phase cameras and Hartmann sensors [90].

Detection upgrade

In Advanced Virgo will be adopted the DC detection scheme in order to reduce some technical noises, such as the radio-frequency noise, which limits the detector sensitivity in the AC scheme. The seismic and acoustic noises will be reduced placing all the photodiodes used in science mode on suspended benches and keeping them in vacuum condition. Moreover, a new output mode cleaner will be installed in order to meet the requirements on the sidebands filtering.

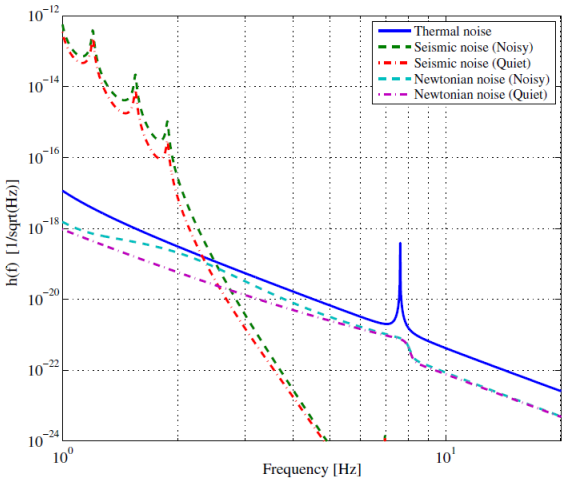

Figure 2.24: The dominant low frequency noises expected in surface-based and room-temperature second generation detectors such as Advanced Virgo [88]; suspension thermal noise and seismic/Newtonian noises during quiet/noisy days are plotted.

2.4.2 KAGRA

KAGRA [91] (the former LCGT) is a second generation interferometric gravitational wave detector under construction in the Kamioka mine (Gifu prefecture, Japan). It is the evolution of CLIO [92], the co-located 100 m-long first prototype of a cryogenic interferometer. In many aspects KAGRA will be a precursor of third generation detectors: indeed the entire detector is located in an underground infrastructure, and its test masses will be cooled down to 20 K. These features will ensure the reduction of the seismic/Newtonian and thermal noises, which represents a limit to the low-frequency sensitivity for the other Advanced detectors, as shown in fig. 2.24. The optical design is based on a power recycling (with gain $G_{pr} = 10$) Michelson interferometer with 3 km-long Fabry-Perot cavities (with finesse $F = 1550$), in resonant-sideband extraction configuration [93] with a laser power[11] at the input port of $50 - 80\ W$; the schematic view of KAGRA is reported in fig. 2.25. The development of the detector is planned in two phases:

1. **iKAGRA**. The initial configuration of the detector, operated at room temperature, is expected to be ready to start the observations in 2015, using 10 kg silica test masses provided by LIGO;

2. **bKAGRA**. The cryogenic configuration is expected to be completed in $2017 - 2018$. The test masses will be 23 kg sapphire test masses, cooled down to 20 K in dedicated cryostat vacuum chambers with two radiation shields at 8 K and 80 K. In this final configuration the horizon distance for BNS inspirals will be $240 - 280\ Mpc$, with an expected detection rate of $\dot{N} \sim 6 - 10\ yr^{-1}$.

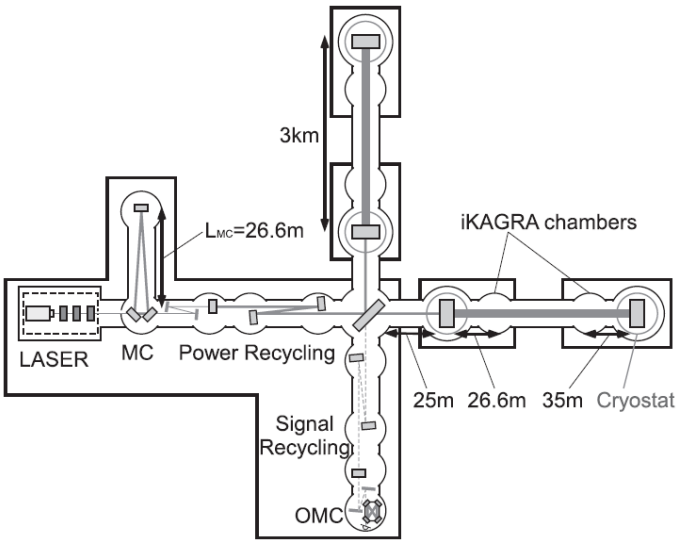

Figure 2.25: Schematic view (not to scale) of the KAGRA detector in its final configuration [91].

[11] the input power must be chosen taking into account the absorption in sapphire test masses.

Underground suspensions

The core optics and the test masses will be suspended from two kinds of suspension: type-A and type-B, shown in fig. 2.26. Type-A suspension will be installed in two caverns placed one above the other: the legs of the inverted pendulums will be installed on the floor of the top cavern, four geometric anti-spring (GAS) filters will be placed in the shaft which connects the two caverns, and a triple pendulum suspension will be placed in the lower cavern for the cryogenic test mass suspension. The type-B suspension is designed to suspend the beam-splitter and the recycling mirrrors; it will be similar but shorter compared to type-A, and it will be hosted in a single cavern. Although the type-A suspension will be characterized by more filters than type-B, the residual seismic noise will be similar for both, since type-A attenuation will be limited by the cryo-cooler and heat-link vibrational noise.

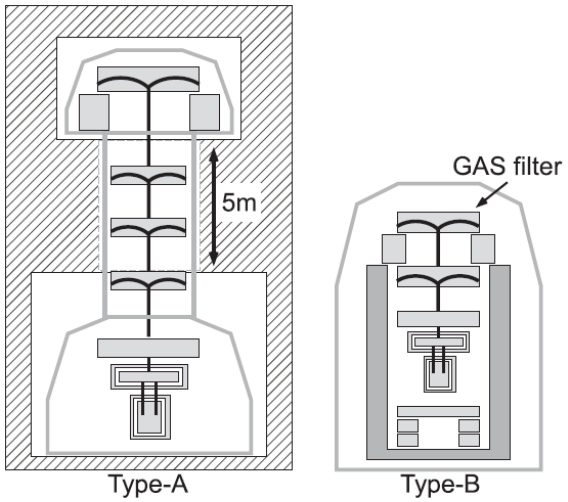

Figure 2.26: The two types of suspension used in KAGRA [91]. In type-A the upper cavern hosts the inverted pendulum and the top of the three-stage vertical filter chain, while the lower cavern hosts the triple pendulum suspension of the cryogenic test mass; the type-B vertical filter chain is shorter.

Cryogenic payloads

The payload of KAGRA is composed of three stages (see fig. 2.27): the upper stage is the so called suspension *platform*, the median stage is the *intermediate mass*, and the last stage, which is in turn composed of the mirror and its recoil mass. The mirror substrate must be characterized by an high thermal conductivity: in KAGRA the sapphire (Al_2O_3) has been chosen for mirrors and suspension fibers, and has been already cooled in CLIO, demonstrating the reduction of the mirror thermal noise. However sapphire is described by a three-axial crystal, giving rise to birefringence[12], so it must be re-shaped in order to be used as a mirror. The

[12]a material is affected by birefringence when the refractive index depends on the polarization and propagation direction of light; this optical property is responsible for the phenomenon of double refraction.

payload will be located inside a cryostat vacuum chamber (see fig. 2.27) with outer (80 K) and inner (8 K) radiation shields connected respectively to the first and second stages of four pulse-tube cryo-coolers (PTC) by means of flexible heat links. The suspension platform of the payload will be connected to the inner radiation and to the lower intermediate mass shield through pure aluminum heat links. Finally, the heat absorbed in the mirror will be transferred to the intermediate mass through the suspension fibers, and then through the heat links of the upper stages.

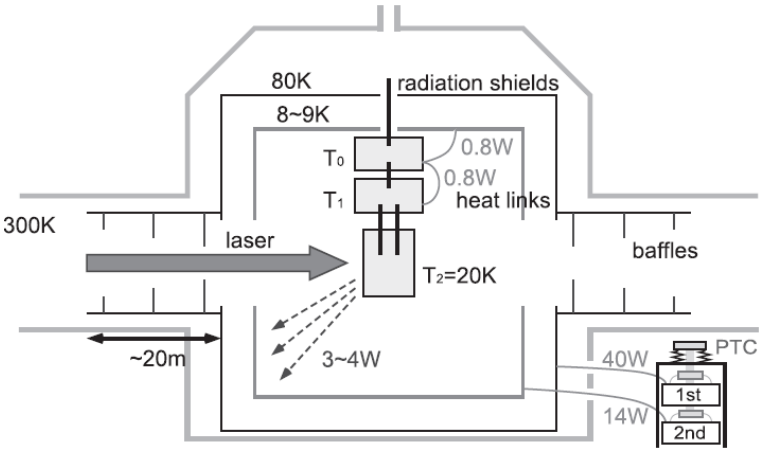

Figure 2.27: Schematic view of the cryogenic payload of KAGRA inside the cryostat vacuum chamber [91].

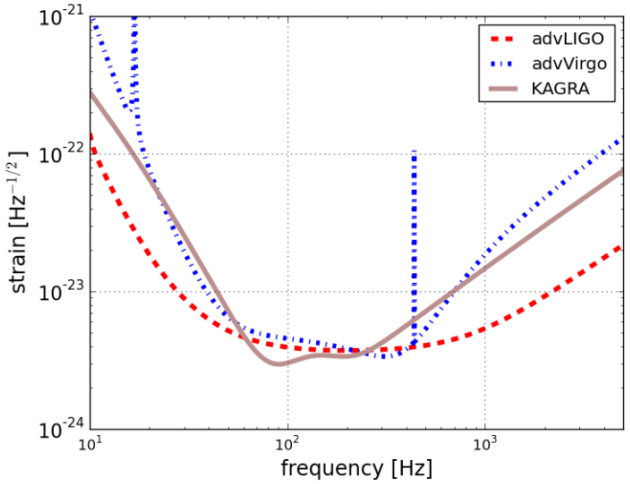

Figure 2.28: Sensitivity curve expected from KAGRA (continuous line) compared to those of Advanced Virgo and LIGO (dotted lines).

2.5 Third generation detectors

First generation detectors demonstrated the effectiveness of the working principle of the interferometric gravitational wave detection by approaching their design sensitivity, while second generation detectors will reach a sensitivity that is expected to guarantee the first direct detections of gravitational waves within the first year of observations, as shown in the detection rates reported in sec. 2.4. However the expected signal-to-noise ratio for these first detections will be too low to allow precise astronomical studies of gravitational wave sources and for complementing optical and x-ray observations. In order to start the "era of gravitational wave astronomy", third generation detectors with new infrastructures will be necessary, improving the sensitivity over a wide band of frequency, especially in the low-frequency range.

2.5.1 The Einstein Telescope

The Einstein Telescope (ET) will be the European third generation gravitational wave observatory, and its design study [26], founded by the European Commission, was recently issued. Its construction is planned to start before the 2020. The project aims to reach a sensitivity at least ten times better than that of advanced detectors (see fig. 2.6), expanding the horizon distance of a factor 10^6 compared to that of first generation detectors such as Virgo. Moreover, the detector is designed for the optimization of the observations, and in order to host several detectors which will evolve for decades. Indeed, ET will consist of three nested detectors, each in turn composed of two interferometers in *xylophone* configuration. In this configuration one interferometer will be dedicated to the detection of low-frequency components (ET-LF) of the gravitational wave signal ($1 - 30\ Hz$) by adopting cryogenic payloads, while the other (ET-HF) will be dedicated to the high-frequency components, using a high laser power and frequency-dependent squeezed light technologies. Each interferometer will be dual-recycled FPM, with a length of 10 km. ET will be located underground at a depth of $100 - 200\ m$, in order to suppress the seismic and Newtonian noises. An artistic representation of the observatory is show in fig. 2.29. ET specifications are reported in app. C.

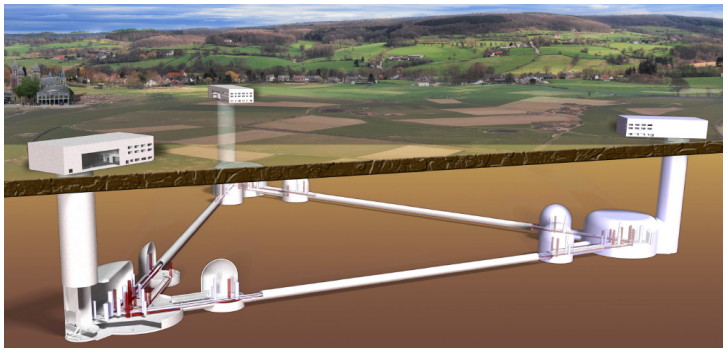

Figure 2.29: Artist's view (not to scale) of the Einstein Telescope underground infrastructure [26].

Detector layout

In the first phase of its development, ET will consist of one detector in xylophone configuration (the "red" detector in fig. 2.30), in turn composed of two interferometers with 10 km-long arms: a cryogenic low-frequency dual-recycled FPM and an high laser power ($\sim 1\ kW$) high-frequency dual-recycled FPM. Eventually, in its final stage of construction, the observatory will consist of three nested detector (the overall configuration of fig. 2.30). In contrast to the traditional L-shaped ge-

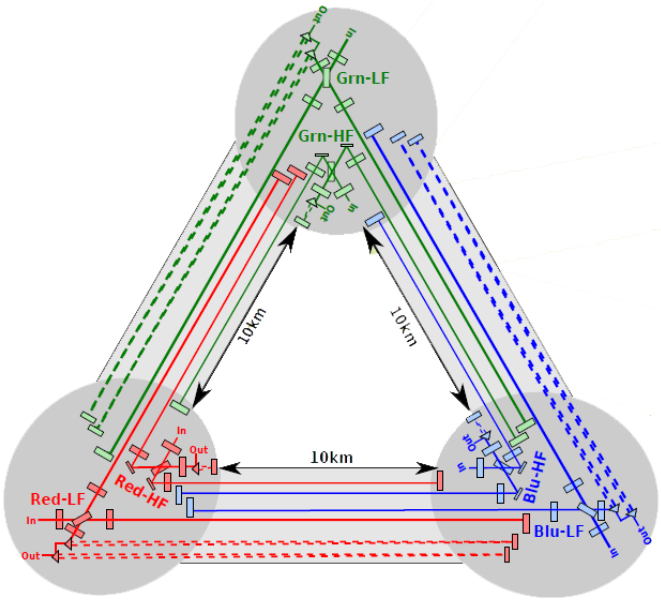

Figure 2.30: The xylophone configuration (not to scale) of the Einstein Telescope. In the first phase it will consist of one detector composed of two interferometers (indicated in red); in the final stage of construction it will consist of all the three detectors represented in the scheme. Each side of the triangle is 10 km long [26].

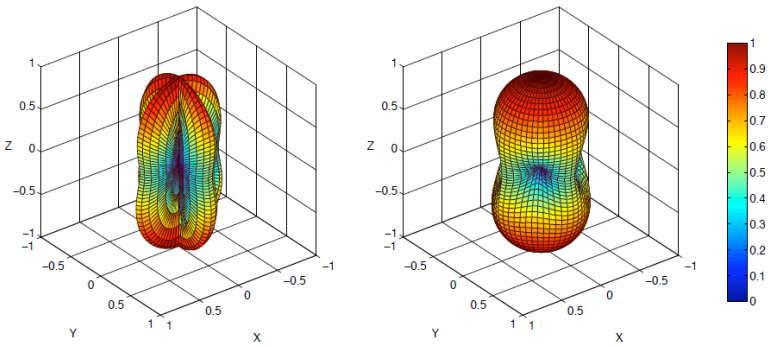

Figure 2.31: The antenna pattern of a L-shaped interferometer compared to that of the xylophone configuration adopted for ET [26].

ometry widely used in the first and advanced generations detectors, the xylophone configuration is equally sensitive to both the polarizations of gravitational waves. Indeed, the resulting antenna pattern is more isotropic than that of L-shaped interferometers (see fig. 2.31). The schemes of the Low-Frequency (LF) and High-Frequency (HF) interferometers which form a single detector are reported in fig. 2.32. The HF interferometer will operate at room temperature in the frequency range between 30 Hz and 10 kHz, using fused silica mirrors with a diameter and mass respectively equal to $d \approx 60\ cm$ and $m \approx 200\ kg$, with a laser power stored in the cavities of about 3 MW. The LF interferometer will operate in the frequency range between 1 Hz and 30 Hz adopting cryogenic payloads cooled down to 10 K: in this case the test masses will be silicon (Si) mirrors with a diameter $d \approx 40\ cm$ and a mass of the same order of that used in the HF interferometer; the cryogenic optics will be made of sapphire and silicon. In both interferometers the higher mass of the mirrors will lower the radiation pressure noise, allowing higher power and larger sized beam spots on the mirror surfaces. The Standard Quantum Limit (SQL, see sec. 2.2.2) determines the lower limit of the quantum noise that cannot be reached for all the frequencies simultaneously in a classic interferometer: in order to beat the SQL in ET, non-classical light (the so-called *squeezed light*) with correlations between the phase and the amplitude quadratures will be used. In the shot noise dominated frequency range the squeezed light will lower the phase fluctuations at the cost of the amplitude fluctuations in comparison to classical laser light in the interferometer cavities. In the low-frequency radiation pressure dominated range the fluctuations in the amplitude quadrature are lowered by reflecting squeezed light in a filter cavity. Thermal noise and thermal lensing will be suppressed by the use of non-Gaussian laser beam profiles in addition to the corrective systems already implemented in Advanced detectors.

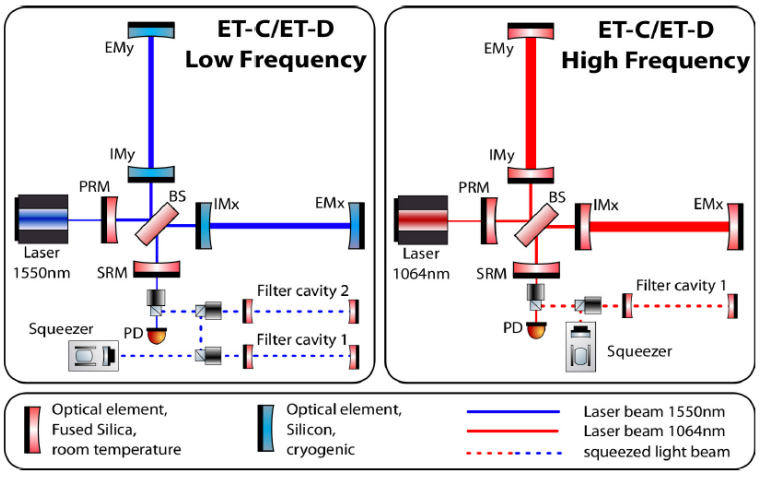

Figure 2.32: The optical scheme of Low-Frequency and High-Frequency interferometers composing each detector of ET [26].

Underground infrastructure

The underground infrastructure (see fig. 2.29) is motivated by the suppression of natural and anthropogenically-generated seismicity and by the Newtonian (also known as gravity gradient) noise, which is generated by gravity field fluctuations and couples directly to the test masses, short-circuiting the vibration isolators (see chapter 3). Therefore an extensive study of seismic environmental and anthropogenic noises in various locations will lead to the site selection for ET in the next years. The local geography and geology of the chosen site will determine what kind of access to the observatory (vertical shafts or horizontal/inclined tunnels) and excavation method will be adopted. Several meters large vertical shafts will be present in every corner station and in the middle of the arms, delimited by a surface building. The corner stations, containing the components of the three detectors, will be hosted in cylindrical caverns with a diameter of about 65 m, divided in two levels: the top level cavern host the main suspension and vacuum systems, while the basement level is devoted to the clean rooms and to allow the underneath access to the suspended components of the interferometers. A total of 17 suspension towers will be present in every corner station and will host the suspension of multiple payloads (of different interferometers). Satellite and smaller caverns will be needed to host the input test masses suspension towers. Finally, the cryogenic equipments of the LF interferometers will be installed in the main and satellite caverns. The arms of the detectors will be hosted in tunnels with a diameter $d = 5.5\ m$ and 10 km long (except for those connecting the satellite caverns which will be 300 m long). In the final stage of construction, every main interferometer arm tunnel will host six vacuum pipes (four for the HF and LF interferometers and two for filter cavities) and all the service connections of the underground and cryogenic infrastructures.

Suspension system

The suspensions system will be based on the superattenuator (SA) design already used in Virgo over 10 years activity: a N-stage pendulum supported by an inverted pendulum (IP) composed of an elastic three-leg structure. The SA designed for Virgo with six vertical filters is already compliant with the HF interferometer requirements, while the LF interferometer will require a better attenuation in the low-frequency range (below 3 Hz). In order to meet the requirements of the LF interferometer, the SA of ET will be 17 m high, assuming $N = 6$ vertical magnetic anti-spring filters equally spaced and tuned with a vertical cut-off frequency around 300 mHz. The cryogenic last stage of suspension of the LF interferometer will be suspended in the lower part of the SA vacuum tower.

Cryogenic payload

In ET a Virgo-like last stage of suspension of mirrors will be used, consisting in the marionette, the recoil mass and the mirror. The payload will operate at cryogenic temperature, being cooled down with two possible techniques:

- with pulse-tube (PT) cryocoolers, whose vibrations must be suppressed by

means of passive and active actuation, such as studied in the Vibration-Free cryostat [94];

- with cryogenic fluids in the form of liquid helium and liquid nitrogen which can be used to cool down the cryostats of the payloads: the refrigerator systems can be installed on the surface building, while the cryogenic fluids are sent to the underground cryostat by long transfer lines, as already did in other large-scale experiments such as LHC at CERN.

A *cold box* will be connected to marionette via heat-links[13], keeping the mirror at cryogenic temperature. It can be either the cold head of a PT cryo-refrigerator or a simple liquid helium container in the case of a cryoplant based on cryogenic fluids. In order to damp the vibrations associated to the cooling system, the cold box will be installed on the top of a cryo-compatible attenuator chain (see fig. 2.33) hosted in an ancillary cryostat, close to the payload suspension tower. The whole payload will be hosted in the lower part of the vacuum tower hosting the 17 m-long SA: this tower basement will be a cryostat with two radiation shields. Moreover, in order to reduce the thermal radiation from the beam duct into the cold mirror, cryotraps will be installed along the vacuum tubes and appropriate low-emissivity coatings will be deposed on their inner walls.

Since fused silica has a very small thermal conductivity at low temperatures, the mirrors and the main optics of the LF interferometer will be made of crystalline materials (silicon and sapphire) as said above, since these crystals have a large thermal conductivity in the low temperature range. As in advanced detectors, the mirrors will be monolithically suspended with fibers of the same material.

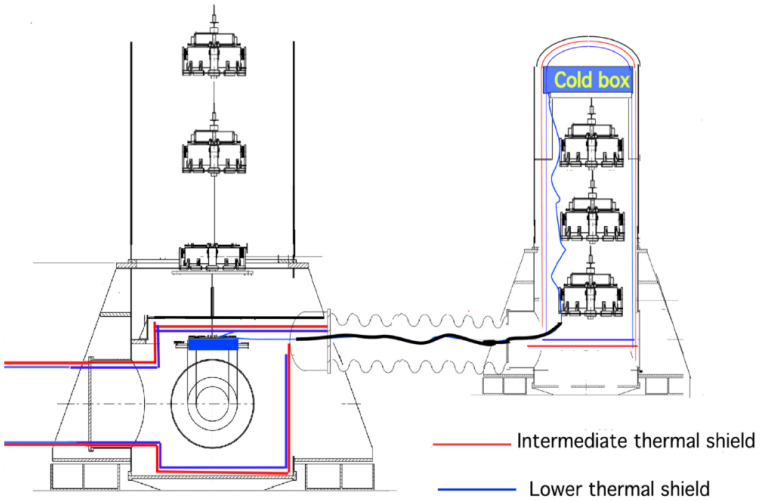

Figure 2.33: Scheme of the cryogenic payload and cryo-links in ET [26].

The local control of the payload components will be similar to that of first and second generation of gravitational wave interferometric detectors. The actuation can be realized by mean of coil-magnet actuators (as in initial and advanced Virgo)

[13]the heat-links can be realized adopting a suitable design in order to suppress the residual vibrations generated by the cold box, as already did in KAGRA [95].

or alternatively with electrostatic actuators based on polarized capacitances (as in GEO600). However, sensing devices suitable for cryogenic operations of the local control loop have to be developed. In chapter 6 of this thesis I will present an inertial sensor developed for this task.

2.6 Space-borne interferometers

In order to explore the very low-frequency range below 1 Hz, where a large number of potential gravitational wave sources are expected to emit, such as extremely massive coalescences, galactic binaries and stochastic/cosmological sources, it will be necessary to build an interferometer of million km baseline. Clearly, such a large interferometer is unimaginable on Earth; moreover, the Newtonian noise will be a fundamental limit below 1 Hz for ground and underground detectors. For these reasons the space-borne interferometer feasibility was studied in the last decades, resulting in the proposal of **LISA** (Laser Interferometer Space Antenna) joint ESA-NASA space mission [96]. It will consist of a constellation of three spacecrafts, hosting the test masses and placed in a heliocentric orbit at $d \approx 1$ $A.U.$ in xylophone configuration: each side of the resulting triangle will be 5×10^6 km long, inclined by $\pi/3$ with respect to the ecliptic and following the Earth by about $\pi/9$ (see fig. 2.34). LISA is expected to reach a strain sensitivity of the order of

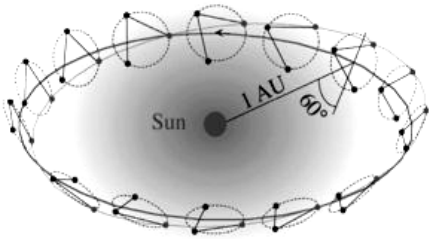

Figure 2.34: Schematic representation of LISA constellation yearly heliocentric orbit (not to scale), following the Earth by about $\pi/9$; the interferometer arms are 5×10^6 km long.

10^{-20} $Hz^{-1/2}$ in a frequency window which ranges from 3×10^{-5} Hz to 0.1 Hz. The detection scheme will be different from ground-based interferometers: due to the large distance between test masses, the phase difference will be measured not by recombining the laser transmitted and reflected between the two spacecrafts, but by combining the incident light with a local oscillator phase-locked to a common clock [96]. The launch of the main space mission is foreseen after 2020, while the feasibility test mission, called LISA Pathfinder, is planned to be launched in 2014 by ESA. Other LISA-like space missions have been proposed so far in order to explore the very low-frequency primordial gravitational waves, such as DECIGO and BBO [97].

Part II

Low Frequency noise

Chapter 3

Seismic and Newtonian Noises

At low frequencies the seismic and Newtonian noises are fundamental limits to the sensitivity of a ground-based gravitational wave interferometric detector (see fig. 2.24). They are generated by geological, meteorological and anthropic processes. As shown in chapter 2 dealing with the first and next generations of detectors, these sources of noise can be limited by means of two complementary approaches:

1. underground infrastructures, such as for KAGRA (sec. 2.4.2) and ET (sec. 2.5.1).

2. suitable seismic attenuators composed of long pendula chains (such as the SA of Virgo, see sec. 2.3.1) and/or active actuators (such as in the mirror suspension of LIGO);

In this chapter I will discuss the main features of the seismic and Newtonian noises, and the strategies necessary to suppress them, especially in third generation interferometric detectors.

3.1 Seismic noise

Unlike transient seismic signals, which are coherent[1], since they are radiated by localized sources and have a finite duration, the background seismic noise, generated either by natural sources or human activities, can be described as a quasi-stationary stochastic process. Seismic daily variations due to anthropic and natural sources occur usually below 10 Hz:

- at very low frequency ($f < 1\ Hz$) the main contribution comes from oceanic and sea-generated microseisms (see sec. 3.1.3) related to large-scale meteorological conditions, and therefore it is generated by non-local sources, usually characterized by a rather high coherence[2] ($> 70\%$) [98];

- around 1 Hz local meteorological conditions (such as local wind and rain) dominates;

[1] coherent signals have small phase shifts and identical time dependence and polarization, and therefore they can interfere constructively.

[2] here we define the degree of coherence as the ratio between the auto-correlation and the cross-correlation of the signal.

- at higher frequencies ($f > 1\ Hz$) the noise produced by anthropic activities (cultural noise, see sec. 3.1.2) becomes dominant and is characterized by low coherence ($> 30\%$).

The correlation radius r_c is defined as the longest distance between two seismic sensors for which the recorded noise in a certain spectral range remains correlated. It depends on the composition of the medium in which the seismic noise propagates: usually the correlation radius increases with depth, from the surface (where the unconsolidated sedimentary materials results in smaller r_c) to the underground hard rocks (where r_c is larger). The correlation radius is also frequency dependent: for the very low-frequency seismic noise ($< 1\ Hz$), such as oceanic microseisms, it may be several km, while for higher frequencies it drops to few meters or even less. The amplitude spectral density of the displacement produced by the seismic noise can be expressed to a first approximation by the empirical law:

$$\tilde{x}_s(f) \approx \frac{10^{-7}}{f^2} \frac{m}{\sqrt{Hz}} \tag{3.1}$$

However, the seismic measurements in frequency domain are usually presented in terms of acceleration power spectral densities (PSD, see app. A), thus in units of frequency-dependent squared acceleration: $(m/s^2)^2/Hz$. In fig. 3.1 it is reported the background seismic noise PSD in the $10^{-5} - 50\ Hz$ frequency range, measured by Peterson [99] from a worldwide network composed of 75 stations (in surface and underground) during several years. The resulting plots combined give rise to the so-called *new high noise model* (NHNM) and *new low noise model* (NLNM) represented by the the upper and lower bound envelopes of the cumulative compilation of ground acceleration PSD measured during noisy and quiet periods.

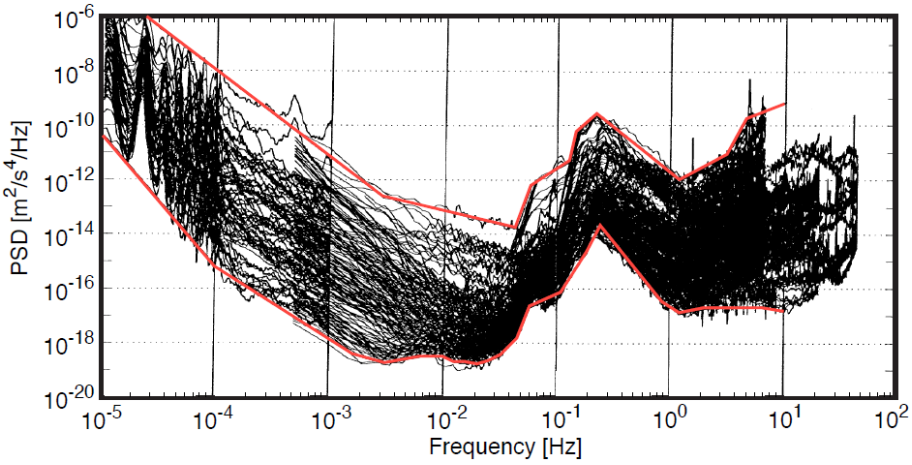

Figure 3.1: The high and low noise models (NLNM and NHNM, upper and lower red lines) obtained by Peterson [99] from the seismic spectra (black lines) measured in a worldwide network of surface and underground stations.

3.1.1 Seismic waves

The seismic activity [100] can be subdivided according to the two main types of seismic waves (see fig. 3.2):

Body waves propagate through the interior strata of the Earth. They are characterized by smaller amplitudes and shorter wavelengths (i.e. higher frequencies) than surface waves, traveling at higher speeds.

- **Primary waves**, also known as pressure waves, or simply *P-waves*, are described by a longitudinal particle motion along the direction of propagation of the wave: they push and pull the medium (rock or fluid) they move through, similarly to sound waves in air. Therefore, P-waves are compressional waves. They are the fastest type of seismic waves: the propagation velocity is given by:

$$v_P = \sqrt{\frac{\mathcal{B} + \frac{4}{3}\mu}{\rho}} \tag{3.2}$$

  where $\mathcal{B}$ and μ are respectively the bulk and shear moduli, and ρ is the density of the medium through which the wave propagates. In the superficial layers of the Earth's crust, the typical speed of P-waves is $v_P^{sup} \sim 500 - 2000\ m/s$, while in the deeper layers, where the rocks are more consolidated and homogeneous, the velocity is higher: $v_P^{deep} \sim 5000 - 8000\ m/s$.

- **Secondary waves**, also known as shear waves, or simply *S-waves*,are described by a transversal particle motion with respect to the propagation direction of the wave. Since fluids do not support shear stresses, S-waves can travel only through a solid medium, at a speed slower than that of P-waves:

$$v_S = \sqrt{\frac{\mu}{\rho}} = v_P \sqrt{\frac{1-2\nu}{2-2\nu}} \approx \frac{v_P}{2} \tag{3.3}$$

  where $\nu = \frac{1}{2}\frac{3\mathcal{B}-2\mu}{3\mathcal{B}+\mu}$ is the Poisson's ratio. The typical speed of S-waves in the upper layers of the Earth's crust is $v_S^{sup} \sim 250 - 700\ m/s$, while in the deeper layers is $v_S^{deep} \sim 1500 - 4000\ m/s$.

The wavelengths of the P- and S- waves are defined as $\lambda_{P,S} = v_{P,S}/f$; neglecting the coupling effects, the amplitudes of these waves are attenuated by a factor $\exp(-\pi r/Q\lambda_{P,S})$, where r is the distance between the source and the sensor, and Q is the quality factor ($Q_P \sim 2Q_S$). Therefore, we can define the attenuation length:

$$\mathcal{L}_{P,S} = \frac{Q_{P,S}\lambda_{P,S}}{\pi} \tag{3.4}$$

Using the typical values of seismic P- and S- waves in eq. 3.4, it follows that seismic waves produced on the surface by local meteorologic or anthropic sources are usually attenuated within few kilometers, while vibration modes produced in deep and homogeneous rocks are attenuated over longer distances.

Surface waves are produced by the interaction of P-waves and/or S-waves, propagating and being confined in the upper layers of the crust. Surface waves are characterized by lower frequencies and larger amplitudes than those of body waves.

- **Love waves** are horizontally-polarized S-waves (SH-waves), with an associated particle motion described by a transversal oscillation with respect to the propagation direction of the wave. Since they are not composed of any P-wave component, Love waves do not imply compressions in the medium through which they propagate. Their amplitude decreases exponentially with depth, but only as $r^{-1/2}$ with the distance traveled r. Love waves propagates at a speed of about 90% v_S.

- **Rayleigh waves** propagates as ripples similarly to the waves on the surface of water, with an associate particle motion described by a retrograde rolling. Rayleigh waves are produced by the superposition of vertically-polarized S-waves (SV-waves) and P-waves, so that they produce compressions in the medium they move through. Rayleigh waves couple with the horizontal discontinuity of the crustal layers, even with that between the surface and the atmosphere. It is possible to distinguish between the fundamental Rayleigh mode (RF-) and those produced by the resonances in the geological strata (RS- or RP- depending on the main components, SV- or P-, forming the resonant waves). A particular type of large-amplitude (i.e. low-frequency) Rayleigh waves are the so-called *Stonely-waves* [101], which propagates along the solid-fluid boundaries, such as in vertical shafts or boreholes, being an important source of coherent noise. Stonely-waves amplitude decreases exponentially with the distance from the shaft. In general, Rayleigh waves travel at a lower speed than that of P- and S-waves: their horizontal propagation velocity v_R expressed in units of v_S is a purely function of the Poisson's ratio ν. If we define the dimensionless variable $\chi = v_R/v_S$ with the condition $0 < \chi < 1$, the Rayleigh wave velocity comes from the real root of the equation [102]:

$$\chi^6 - 8\chi^4 + 8\left(\frac{2-\nu}{1-\nu}\right)\chi^2 - \frac{8}{1-\nu} = 0 \tag{3.5}$$

  The eq. 3.5 describes the harmonic Rayleigh waves propagating far from the source. Indeed, the excitation of the medium they move through results in a combination of all the different body and surface waves. The amplitude of Rayleigh waves decays exponentially and is negligible at a depth of a few Rayleigh wavelengths ($\lambda_R = 0.92\, v_S/f$).

As waves propagate through the medium, their amplitudes decreases due to two factors: the geometrical and the material damping. The first is a result of energy spreading over an increasing area; the frequency-dependent material damping involves the energy lost due to friction through the medium. Seismic wave

attenuation for homogeneous media can be described by the equation [103]:

$$A_2 = A_1 \left(\frac{r_1}{r_2} \right)^n e^{-\pi \eta f (r_2 - r_1)/v_i} \tag{3.6}$$

where A_1 and A_2 indicate the wave amplitudes at the distances r_1 and r_2 from the source, n and η represents respectively the geometric damping coefficient and the loss factor related to the material damping, f is the frequency and v_i is the propagation velocity of the wave. The geometric damping can be calculated analytically by assessing the type of wave involved and the source type. It is $n = 1/2$ for radial surface waves, while radial body waves decay with $n = 1$.

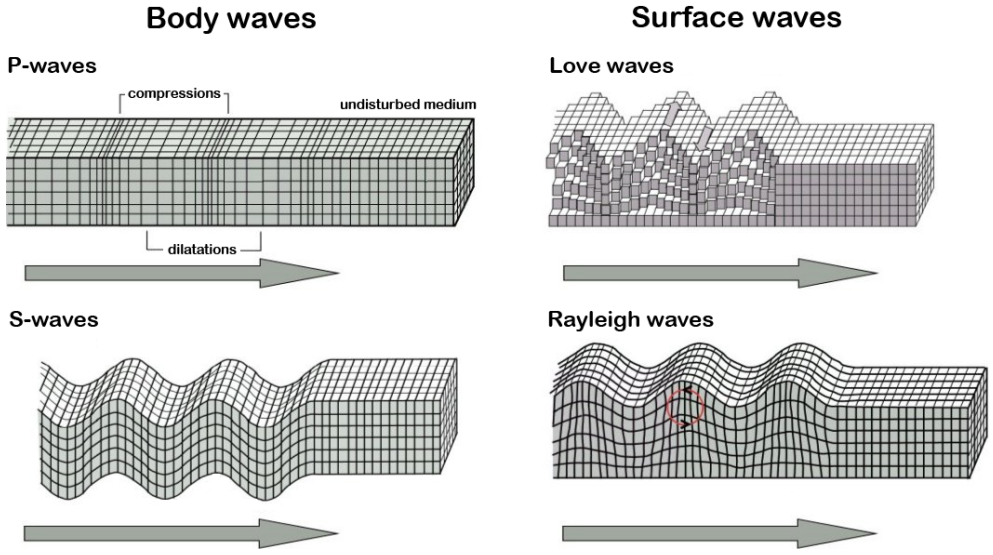

Figure 3.2: Main types of seismic waves, propagating as indicated by the arrows; *left*: body waves, subdivided in primary (P-) and secondary (S-) waves; *right*: surface waves, subdivided in Love and Rayleigh waves.

3.1.2 Short-period seismic noise

The short-period noise ranges from about 1 Hz to $\sim$ 50 Hz and can be generated by meteorological phenomena, such as the wind friction over rough terrain, trees/vegetation and man-made objects swinging or vibrating. However, the dominant part of the short-period seismic noise comes from anthropic activities and machines (e.g. rotating machinery, road/rail traffic, etc.). The contributions from these sources, which can be stationary as well as moving, produce a superposition to a quite complex random field. Since the short-period noise has a surface-wave character [98], the horizontal propagation velocity of this seismic noise is frequency dependent, resulting close to the shear-wave velocity in the superficial crustal layers ($v_s \sim 2.5 - 3.5$ km/s in hard rocks and $\sim 300 - 650$ m/s in unconsolidated sedimentary layers). Moreover, the surface-wave nature of the short-period seismic noise explains the exponential decay of the noise amplitude with depth (see sec. 3.1.5), which is not the case of body waves. Since the penetration depth of surface

waves is proportional to their wavelength, the seismic noise at higher frequencies attenuates more rapidly with depth. The wind-generated seismic noise becomes noticeable for wind speeds higher than $3-4\ km/s$, destroying the coherence below $15\ Hz$ [104]. The amplitude increase of such a noise is apparently non-linear and may reach underground depth down to several hundred meters for wind speeds $v_s > 8\ km/s$. However, the wind-generated seismic noise is usually much higher on surface, being exponentially reduced with depth.

Cultural noise

The cultural noise, also called anthropogenic noise, can be distinguished from the natural microseismic noise for its diurnal variability (day/night pattern), related to human activities. Moreover, it depends on many local factors: e.g. the "road" noise depends on the road structure and materials, traffic density and vehicle type/speed. As reported in [105], at the LIGO Hanford Observatory, in the $1-50\ Hz$ frequency span, the peaks are around $4-12\ Hz$ and it is produced by vehicular traffic. A correlation between the seismic noise at Virgo interferometer and the "road" noise in a 4 km-far major high-way overpass was found by [106] with a peak around $3\ Hz$. The diurnal pattern of the cultural noise was recognized even in seismic data from seismometers placed in boreholes at several depths down to $\sim 1950\ m$ [107]. The only way to reduce such an environmental noise is to build the detector in a site far away from major urban sites in a low population density area.

3.1.3 Microseisms

Below 1 Hz microseismic peaks related to the activity of oceans and seas are a prominent feature that can be observed in fig. 3.1 around $7 \times 10^{-2}\ Hz$ and $\sim 0.2\ Hz$. These two value ranges correspond to two possible schemes of generation of the oceanic microseism (see fig. 3.3) [98]:

1. Primary (and smaller) oceanic microseisms with a period of $14 \pm 2\ s$, are generated only in shallow waters next to coastal regions. The wave energy is converted directly into seismic energy either through vertical pressure variations or by the impact of the waves (with a typical frequency of $\sim 0.06 - 0.1\ Hz$) on the shores. The correlation between this microseismic peak and the swell at the beaches was known starting from the data sets studied by [108];

2. Secondary (and dominant) oceanic microseismic peak with a period around $6\ s$, generated by the superposition of ocean swell waves[3] of equal period traveling in opposite direction, and therefore generating standing waves of half the period [110]. Non-linear second-order pressure perturbations are produced by these standing waves and propagate with negligible attenuation to the ocean bottom where they are converted into seismic waves. This phenomenon can take place off-shore and in the far deep ocean: in the first

[3]wind waves are generated at high frequencies and evolve into swell as soon as the waves separate from the wind that generated them [109]. Swell is stabilized by nonlinear processes and eventually acquires its typical oscillation period around $14 - 16\ s$.

case, the forward-propagating waves, generated by a low-pressure area, superpose with those with the same frequency inward-propagating after being reflected by the coast line; in the latter case, waves from two sides superpose after being generated by two separate perturbations. The seismic waves, produced in the ocean bottom crust by the standing wave-induced pressure perturbations, are composed mainly by Rayleigh waves.

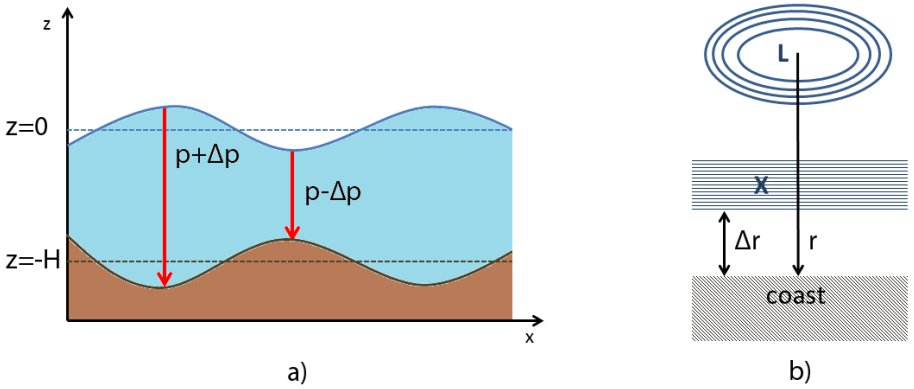

Figure 3.3: Illustration of the two main schemes of generation of ocean and sea microseism: a) the primary microseism is generated by the pressure variations on the ocean bottom crust and on the shores; b) the secondary and dominant microseisms is generated by the interference of the waves propagating from the low-pressure area L with those with the same frequency being reflected by the coast line: standing waves with half the period of ocean waves develop in the interference area X and propagate through the ocean bottom crust, where they are converted into seismic waves.

Similar microseismic noise peaks may be generated in shallower seas and even lakes, usually characterized by shorter periods ($2 - 4$ s). Moreover, the coastal geometry produces local interference patterns, which can be characteristic of a certain geographical place, e.g. in a bay of channel where typical resonances can be noticed. Therefore, in the acceleration PSD it is possible to observe multiple microseismic peaks in the very-low frequency range. Oceanic and sea microseismic surface-waves are characterized by a low attenuation, hence they can be observed hundreds of km in inland sites. Since they are produced in relatively localized areas, the microseismic signals have a coherent portion around the peaks. Therefore, in principle, an array of seismic sensors can be able to localize the source locations of microseismic peaks. In several studies [111, 112, 113] it has been shown that the ocean-bottom (and even in deep seas) microseismic spectrum has a similar shape of that measured in continental sites, but with a greater amplitude, which increases at higher frequencies. Moreover, the correlation of these spectra with known storm systems was noticed. Finally, at lower frequencies ($10^{-2} - 10^{-3}$ Hz) it is obseved the microseismic contribution due to the so-called infragravity waves, produced by subharmonics through non-linear processes from wind waves and swell.

3.1.4 Long-period seismic noise

In the long-period period band ($t > 10\ s$) which corresponds to very low-frequencies ($f < 0.1\ Hz$) the atmospheric pressure field variability generates a background seismic noise due to the elastic response of the ground to these fluctuations. This effect, produced by barometric pressure fluctuations [114, 115], occurs both in vertical and horizontal directions, but it is mainly noticeable in the horizontal displacements related to the ground tilt, which couples with gravity. Indeed, horizontal seismometers are usually based on horizontal pendula, therefore thy are also extremely sensitive tilt-meters: a small tilt of θ radians would produce an apparent translational acceleration in m/s^2 given by [99]:

$$\ddot{x} \approx g_0 \theta \tag{3.7}$$

where g_0 is the local acceleration of gravity. A method which can be used in order to extract the real translational ground acceleration from the output of an horizontal floating-mass based seismometer is to subtract the tilt-generated translational acceleration by means of a parallel tilt-meter. The long-period noise generated by pressure fluctuations is unavoidable, however it decreases with depth: in underground environments surface deformations are attenuated while the barometric pressure and temperature are more stable than in surface locations.

Earth tide

At very low-frequency the surface of Earth experiences large external forces due to the gravitational interaction with the Moon and Sun with a typical semi-diurnal/diurnal modulation: the effect consists in the rise and fall of the surface with an amplitude up to $\sim 0.5\ m$ with respect to the center of the Earth. This phenomenon is particularly evident in fig. 3.1 at a frequency of $f_{tide} = 2.3 \times 10^{-5}\ Hz$. However, at such a low frequency, well below the minimum detectable frequency even in third generation detectors ($f_{tide} \ll 1\ Hz$), the test masses of a ground based interferometer move coherently, thus the Earth tide does not involve a substantial limitation to the detector sensitivity. Moreover, since it is related to the orbital motions of the Earth and Moon, the produced effect can be predicted. An additional contribution to the Earth body tide comes from the ocean tidal loading[4], which causes the rising and falling of the adjacent ground, especially in coastal areas. This "side effect" can be of the same order of magnitude of that related to the body tide of the Earth. Another purely-structural side effect, to be considered in the construction of underground observatories, is the erosion of tunnels and caverns produced by the tide-generated physical stresses, resulting in the fragmentation of loose rocks[5].

[4] ocean tides are produced by resonance interactions between water movements, tidal forces and Earth rotation, and therefore are characterized by amplitudes and periods quite different from those of "purely" Earth body tides.

[5] other causes of loose rocks are the temperature fluctuations and oxidation processes.

3.1.5 Seismic noise suppression

As said at the beginning of this chapter, the seismic can be reduced in two ways: building the detector into underground infrastructure, and suspending the interferometer test masses and optics from pendulums chains, which act as seismic filters. The first choice is related to the behavior of the seismic waves in deep crustal layers, where propagation velocities are higher and the surface waves are damped; the second choice is based on the mechanic filters that were already used in first generation interferometric detectors.

Depth dependence

The seismic noise, generated by the superposition of several seismic waves produced either by natural or anthropic sources, is attenuated exponentially in underground environment. In particular, the attenuation is important for surface waves (Love and Rayleigh waves), which are significantly attenuated in more homogeneous and consolidated underground crustal layers. The amplitude spectral density $\tilde{x}_{seism}(f, z)$ associated to the seismic noise at depth $z = d$, with respect to that at the ground level $z = 0$, is given by:

$$\tilde{x}_{seism}(f, z = d) \approx \tilde{x}_{seism}(f, z = 0)e^{-4d/\lambda} \tag{3.8}$$

where λ is the wavelength of the considered seismic wave. This attenuation is the first advantage for a detector built into an underground site.

Mechanical filter

The seismic noise at the detector site (see fig. 3.4) affects the test masses of the interferometer, but can be mechanically filtered by a chain of pendulums. In fact, neglecting external forces and dissipative effects, the equation of motion for a mass m, suspended from a l-long pendulum at the point x_0, is given by:

$$m\ddot{x} + k(x - x_0) = 0 \tag{3.9}$$

where $k = mg/l$ is the restoring force of the pendulum. When a seismic wave of frequency f perturbs the suspension point $x_0 = x_0(f)$, the horizontal oscillation transfered to the suspended mass in x can be obtained considering the horizontal transfer function $\mathcal{T}^H(f)$:

$$\mathcal{T}^H(f) \equiv \frac{x(f)}{x_0(f)} = \frac{f_0^2}{f_0^2 - f^2} \tag{3.10}$$

where f_0 is the resonant frequency of the pendulum. When $f \gg f_0$, eq. 3.10 becomes:

$$\mathcal{T}^H(f) \approx -\frac{f_0^2}{f^2} \tag{3.11}$$

Therefore the pendulum suspension acts like a mechanical low-pass filter. When we consider a chain of N harmonic oscillators, each with its proper resonant frequency

f_i, the overall transfer function is given by the product of the transfer functions associated to each oscillator:

$$\mathcal{T}^H(f) \equiv \frac{x(f)}{x_0(f)} = \prod_{i=1}^{N} \mathcal{T}_i^H(f) = \prod_{i=1}^{N} \frac{f_i^2}{f_i^2 - f^2} \tag{3.12}$$

Also in this case, for frequencies higher than resonances, i.e. for $f \gg f_i$, the chain of N harmonic oscillators is a mechanical low-pass filter:

$$\mathcal{T}^H(f) \equiv \frac{x(f)}{x_0(f)} \approx (-1)^N \frac{1}{f^{2N}} \prod_{i=1}^{N} f_i^2 \tag{3.13}$$

Therefore, the seismic attenuation provided by a chain of N harmonic oscillators is proportional to the factor f^{-2N}. Hence, an higher number N of stages would improve the overall seismic isolation, while lower resonant frequencies of the suspension stages would extend to the low-frequencies the attenuation. The suppression of vertical oscillations can be obtained by a similar calculation, considering a chain of springs, e.g. the blade springs in the Superattenuator of Virgo (see the related subsection in sec. 2.3.1), where also the inverted pendulum attenuation $\mathcal{A}$ (see eq. 2.41) contributes to the overall seismic suppression.

In addition to the passive filter provided by the mechanical suspension, the residual seismic noise can be actively suppressed by means of electromagnetic and electrostatic actuators, driven by suitable position sensors in a control feedback loop.

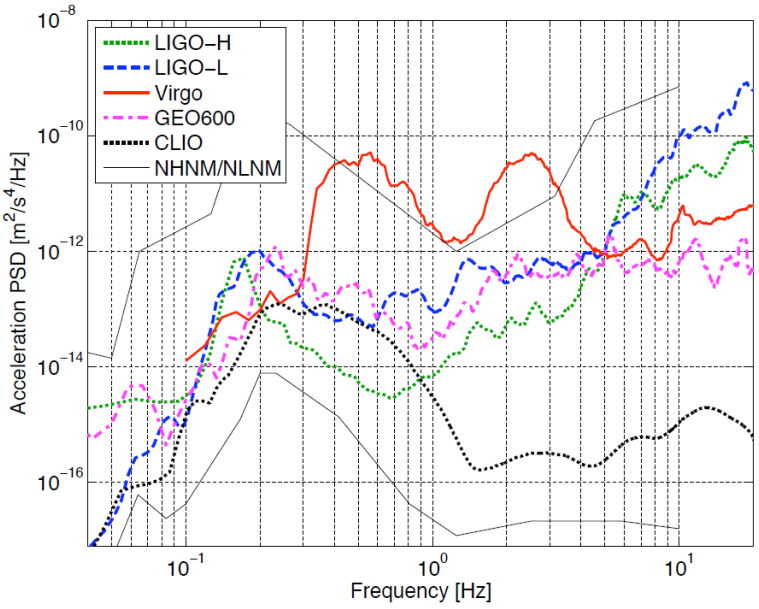

Figure 3.4: The seismic acceleration PSD measured at the sites of ground-based gravitational wave detectors (LIGO, Virgo, GEO600) compared to that of CLIO (which was the prototype of KAGRA) in the underground site of Kamioka. The Peterson low and high noise models are reported in the plot [26].

3.2 Newtonian noise

Local density fluctuations of rock, water and atmosphere, and those produced by the anthropic activities, cause variations of the local gravitational acceleration vector $\vec{g}_0$: this source of noise known as *gravity gradient* or Newtonian noise (NN). The effect produced on the interferometer test masses is indistinguishable from that produced by a gravitational wave [116]. Moreover, fluctuating gravitational fields directly couple to the test masses themselves, short-circuiting all the attenuator stages of a seismic mechanical filter. Because of this feature, NN will be the main sensitivity limit for future interferometric gravitational wave detectors in the low-frequency range. Although density fluctuations of superficial bodies of water and those related to the atmosphere (due to temperature and barometric pressure fluctuations which generate internal dynamical processes) are a primary source of NN, the main mechanism responsible for the generation of fluctuating gravity gradients is the seismic activity. In particular, as shown above in sec. 3.1.1, seismic body P-waves and surface Rayleigh waves produce alternating compressions and dilatations, resulting in local density fluctuations of the crustal rocks.

3.2.1 Analytical model

In a first approximation, the effect produced by the seismic-induced NN to the test mass of an interferometric detector can be described through the transfer function defined by [117]:

$$\mathcal{T}_{NN}(\omega) = \frac{\tilde{x}_{NN}(\omega)}{\tilde{A}(\omega)} \tag{3.14}$$

where $\tilde{A}(\omega)$ is the ASD (see app. A) of the ground oscillation induced by the seismic noise, and $\tilde{x}_{NN}(\omega) \equiv \tilde{h}_{NN}(\omega)L$ is the ASD of the oscillation transmitted through the NN to the test mass, considering a L-long arm of the interferometer. The oscillation at the ground level $\tilde{A}(\omega)$ is the RMS value of the oscillations along the three spatial dimensions:

$$\tilde{A}(\omega) = \sqrt{\frac{[\tilde{X}(\omega)]^2 + [\tilde{Y}(\omega)]^2 + [\tilde{Z}(\omega)]^2}{3}} \tag{3.15}$$

In order to calculate the form of $\mathcal{T}_{NN}(\omega)$, we consider a coherently fluctuating massive region $M(t)$, adjacent to the interferometer: the time-dependent fluctuations $\Delta M(t) = M(t) - \langle M(t) \rangle$ due to the seismic activity gravitationally induces a varying acceleration $\vec{a}_{NN}(t)$ on the test mass (see fig. 3.5). The resulting gravitational force experienced by the test mass m is given by:

$$\vec{F}_{NN}(t) \equiv m\vec{a}_{NN}(t) = m\frac{G\Delta M(t)}{r^3}\hat{r} \tag{3.16}$$

Let us consider the projection along the x-direction of $\vec{a}_{NN}(t)$ from eq. 3.16, in the frequency domain it becomes:

$$a_{NN\,x}(\omega) = \frac{G\Delta M(\omega)}{r^2}\cos\theta \tag{3.17}$$

Since the interferometer test mass is suspended from a pendulum, we can describe it as an oscillator with resonant frequency $\omega_0 = 2\pi f_0$ and damping time τ. Hence, considering that the acceleration in the oscillator can be written as $a = \omega^2 x$, we can rewrite eq. 3.17, expressing the magnitude:

$$\left[(\omega^2 - \omega_0^2)^2 + \frac{\omega^2}{\tau^2}\right] |x(\omega)|^2 = G^2 |\Delta M(\omega)|^2 \frac{\cos^2\theta}{r^4} \tag{3.18}$$

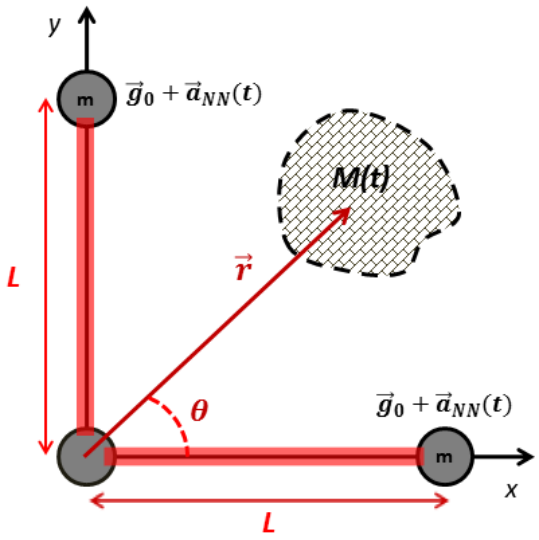

Figure 3.5: A simple scheme of Newtonian noise generation in an interferometric detector: the coherently fluctuating mass region $M(t)$ induces a varying gravitational acceleration $\vec{g}_0 + \vec{a}_{NN}(t)$ on the test masses m of a simple Michelson interferometer with L-long arms.

So far we took into account only a single coherently fluctuating region of mass $M(t)$; in order to extend the calculation to several coherently fluctuating masses, we need to consider a coherence radius r_c of the same order of half the wavelength of superficial seismic Rayleigh waves $\lambda_R = v_R/f$. Moreover, another assumption is needed: mass fluctuations in different coherent regions must be uncorrelated and independent, so that we can add in quadrature the gravitational forces generated by the fluctuating masses. The last assumption is verified in a typical ground-based several kilometers-long interferometer, for which $\lambda_R \ll L$. Therefore, considering the planar approximation, the total contribution comes from the summation of $\cos^2/r^4$ over the coherent regions, which can be written as the integral over θ and r [116, 117]:

$$\sum \frac{\cos^2\theta}{r^4} \approx \frac{1}{\lambda_R} \int_{r_{min}}^{\infty} \int_0^{2\pi} \frac{\cos^2\theta}{r^4} d\theta dr \tag{3.19}$$

Generally, the integral summation above would be divergent since the local gravitational fluctuations, associated to small radii $r \ll 1$, are dominant. In order to ensure the convergence of eq. 3.19, we start the integration from the cutoff radius

$r_{min} = \lambda_R/4$. Hence, from eq. 3.19 we obtain:

$$\sum \frac{\cos^2\theta}{r^4} \approx \frac{64\pi}{3\lambda_R^4} = \frac{4\omega^4}{3\pi^3 v_P^4} \tag{3.20}$$

where, expressing the last term, we considered $\lambda_R = 2\pi v_R/\omega$. By substituting the eq. 3.20 in eq. 3.18, we find:

$$\left[(\omega^2 - \omega_0^2)^2 + \frac{\omega^2}{\tau^2}\right] |x(\omega)|^2 = \frac{4G^2\omega^4}{3\pi^3 v_R^4} |\Delta M(\omega)|^2 \tag{3.21}$$

The mass fluctuation $|\Delta M(\omega)|$ can be expressed as a function of the oscillation of a point on the surface around its equilibrium position $\Delta X(\omega)$, produced by the passing seismic Rayleigh wave:

$$|\Delta M(\omega)|^2 = \frac{\pi\rho^2\lambda_R^4}{16} |\Delta X(\omega)|^2 = \frac{\pi^5 v_R^4 \rho^2}{\omega^4} |\Delta X(\omega)|^2 \tag{3.22}$$

where ρ is the local density of the soil of the coherent fluctuating mass region. By substituting the eq. 3.22 into eq. 3.21, considering the displacement $|x(\omega)|$ as the differential displacement between the test masses $|\Delta x(\omega)|$, and taking into account the contributes from each test mass added in quadrature, we obtain the relation between $|\Delta x(\omega)|$ and the ground oscillation $|\Delta X(\omega)|$:

$$\left[(\omega^2 - \omega_0^2)^2 + \frac{\omega^2}{\tau^2}\right] |\Delta x(\omega)|^2 = \frac{16\pi^2 G^2 \rho^2}{3} |\Delta X(\omega)|^2 \tag{3.23}$$

Since $|\Delta x(\omega)| \equiv \tilde{x}_{NN}(\omega)$ and $|\Delta X(\omega)| \equiv \tilde{A}(\omega)$, following the definition of eq. 3.14, the NN transfer function is expressed by the square root of the ratio between $|\Delta x(\omega)|$ and $|\Delta X(\omega)|$ from eq. 3.23:

$$\mathcal{T}_{NN}(\omega) = \frac{4\pi G\rho}{\sqrt{3(\omega^2 - \omega_0^2)^2 + \frac{\omega^2}{\tau^2}}} \tag{3.24}$$

Considering that the angular frequency of a seismic wave is defined as $\omega \equiv 2\pi f$, for frequencies $f > f_0$ and damping time $\tau \sim 10^8\ s$, eq. 3.24 becomes:

$$\mathcal{T}_{NN}(f) \approx \frac{G\rho}{\pi f^2} \beta(f) \tag{3.25}$$

where $\beta(f)$ is a dimensionless parameter called *reduced transfer function* [116]. In our calculation we found $\beta(f) = 1/\sqrt{3}$: this constant value arises from the cutoff radius $r_c = \lambda_R/4$ we have introduced, having described the soil around the test masses as a grid of masses λ_R-sized, fluctuating randomly and independently of each other due to an isotropic distribution of passing seismic Rayleigh waves. Hence, the expression of the NN transfer function in eq. 3.25 allows us to make a rough estimate of the relation between the seismic amplitude spectral density $\tilde{x}_{seism}(f) = \tilde{A}(f)$ and the NN amplitude spectral density $\tilde{x}_{NN}(f)$ at the ground

level: assuming the average soil/superficial rock density value $\rho \approx 2 \times 10^3\ kg/m^3$, by combining the equations 3.25 and 3.14 we obtain:

$$\tilde{x}_{NN}(f) \approx \frac{2.46 \times 10^{-8}}{(f^2/Hz^2)} \tilde{x}_{seism}(f) \tag{3.26}$$

Since the NN noise depends on the seismic activity, as shown in eq. 3.26, and the main contribution to fluctuating gravity gradients comes from the seismic compressional waves, which have a larger amplitude on surface (e.g. Rayleigh waves), we deduce that NN noise is attenuated in underground sites, where also the cultural seismic noise produced by human activities and that generated by atmospheric/water fluctuations are reduced by the distance from their sources. A depth-dependent analytical model is described in the next subsection.

3.2.2 Depth-dependent model

The equivalent spectral density related to the seismically-generated Newtonian noise, acting on an interferometric detector, can be calculated from an analytical model which takes into account the depth-dependence of the NN. Let us describe the distribution of masses around the test mass with the mass density function $\rho(\vec{x}, t)$, then the acceleration induced on the test mass placed in $\vec{y}$ is given by:

$$\vec{a}_{NN}(\vec{y}, t) = G \int_V \rho(\vec{x}, t) \frac{\vec{x} - \vec{y}}{|\vec{x} - \vec{y}|^3} dV_x \tag{3.27}$$

where we are considering the integration within the volume V. Assuming the medium around the test mass as an elastic solid, its density variations, due the the seismic-generated oscillation, induce a fluctuation in the eq. 3.27, respecting the mass conservation:

$$\dot{\rho} + \nabla \cdot \vec{J}_m = 0 \tag{3.28}$$

where we introduced the mass density current defined by:

$$\vec{J}_m = \rho_0(\vec{x}) \dot{\vec{\xi}}(\vec{x}, t) \tag{3.29}$$

being ρ_0 and $\vec{\xi}$ respectively the density of the medium in static condition and the displacement from the static condition at a given point. By combining the equations 3.28 and 3.29 in eq. 3.27, we obtain in the frequency domain:

$$\vec{a}_{NN}(\vec{y}, \omega) = G \int_V \nabla \cdot [\rho_0(\vec{x}) \vec{\xi}(\vec{x}, \omega)] \frac{\vec{x} - \vec{y}}{|\vec{x} - \vec{y}|^3} dV_x \tag{3.30}$$

In eq. 3.30 we can find two different effects by expanding the derivative expression: the term proportional to $\rho_0(\vec{x}) \nabla \cdot \vec{\xi}(\vec{x}, \omega)$ describes the fluctuations of the local density related to the compression of the medium, while the term $\vec{\xi}(\vec{x}, \omega) \cdot \nabla \rho_0(\vec{x})$ describes the movement of density inhomogeneities, like those at the surface boundary. In order to calculate the connection between the NN and the seismic measurements around the test mass in an interferometric detector, a depth-dependent generalization of the model described in sec. 3.2.1 can be developed starting from

Eq. 3.30: the details of this calculation can be found in ref. [118]. In this model, the seismic motion is decomposed in normal modes of oscillation, which can be considered as oscillators coupled to unknown stochastic forces. The measurements of quantities related to seismic fluctuations (e.g. the power spectra of horizontal and vertical displacement, or the correlation matrix elements of the displacement between different points) can give the information about the excitation of these oscillators, obtaining the estimate of the strain equivalent spectral density $\tilde{h}_{NN}(f)$ produced by the NN acting on the test masses of a third generation detector. The model is based on some assumptions:

1. the mirrors of the interferometer are placed in underground cavities, whose effect can be neglected at low frequencies (i.e. for large seismic wavelength), surrounded by an homogeneous medium with density ρ_0, characterized by the longitudinal and transversal speeds of sound v_L and v_T;

2. the surface fluctuations, associated to surface Rayleigh waves, are dominant with respect to bulk fluctuations. Both contributions are exponentially damped by depth (see eq. 3.8) over a typical scale of λ_R;

3. damping effects are negligible, so that each mode is excited only at is resonant frequency.

The equivalent spectral density of the seismically-generated NN, in an interferometer with L-long arms at depth z, is therefore calculated by [118]:

$$\tilde{h}_{NN}(\omega) = \frac{4\pi G\rho_0}{\sqrt{2}L\omega^2}\mathcal{D}(K,z)[\mathcal{G}(KL)]^{1/2} \times \tilde{x}^{vv}_{seism}(\omega) \tag{3.31}$$

where $K = K(\omega)$ is the wave number and $\tilde{x}^{vv}_{seism}(\omega)$ is the vertical spectral density of the surface motion. The real function $\mathcal{G}(KL)$ in eq. 3.31 is called *geometrical suppression factor* and describes the coherence between gravitational accelerations of different test masses: it goes to zero for $\omega \to 0$, because for $\lambda_R \gg L$ each mirror experience the same acceleration, i.e. the resonant cavities of the interferometer do not fluctuate[6]; in the low-frequency range of interest, we can consider $\mathcal{G}(KL) \sim 1$. Finally, the depth-dependence of eq. 3.31 is given by the *attenuation factor* $\mathcal{D}(K,z)$, defined by:

$$\mathcal{D}(K,z) = \left(\frac{2(\beta_T^2+1)e^{\beta_L Kz} - (1+2\beta_L+\beta_T^2)e^{Kz}}{\beta_L(\beta_T^2-1)}\right) \tag{3.32}$$

where β_T and β_L are the dimensionless functions:

$$\beta_T = \sqrt{\frac{1-\chi^2}{\chi^2}} \tag{3.33}$$

$$\beta_L = \sqrt{\frac{1-\chi^2(v_T^2/v_L^2)}{\chi^2}} \tag{3.34}$$

[6]this effect is analogous to that related to the cut-off frequency on gravitational waves caused by the arm length of the interferometric detector, see eq. 2.21.

being χ the real root of eq. 3.5, with the condition $0 \ll \chi \ll 1$. Setting $z = 0$ and substituting eq. 3.32 in eq. 3.31, given $\mathcal{G}(KL) \sim 1$ and taking into account that $\tilde{h} = \tilde{x}/L$, we can compare the resulting expression with that given by eq. 3.25, finding a good agreement. The attenuation factor $\mathcal{D}(K, z)$ is plotted in fig. 3.6 as a function of depth z for several frequencies[7]. The calculated curves give the NN contribution equal to zero at given depth and frequency, but it is a consequence of the simplified analytical model adopted, in particular with the assumption (3), i.e. taking into account in the NN only the oscillation modes at their resonant frequency $\omega = K v_T \chi$. In a more realistic estimate of the NN also the soil quality factor Q and the coherence effects must be taken into account.

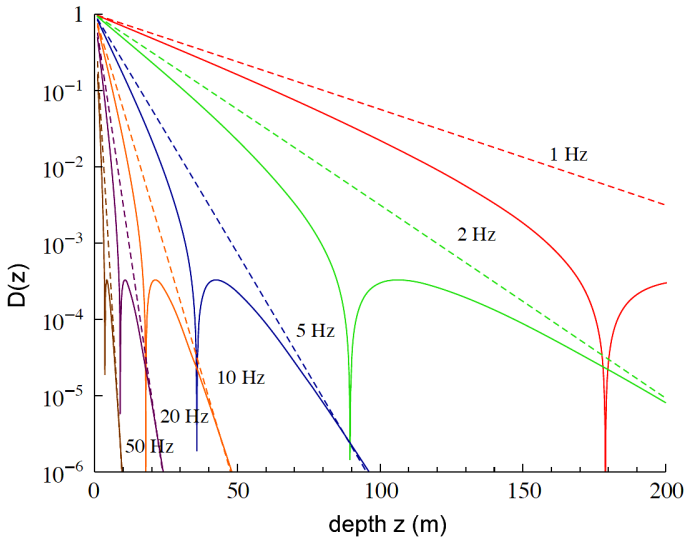

Figure 3.6: The Newtonian noise attenuation factor $\mathcal{D}(K, z)$ of eq. 3.32, as a function of the depth z, plotted for several low frequencies with different colors: red for 1 Hz, green for 2 Hz, blue for 5 Hz, orange for 10 Hz, purple for 20Hz, and brown for 50 Hz [26, 118]. The longitudinal and transversal speeds of sound are assumed to be $v_T = 220\ m/s$ and $v_L = 440\ m/s$ (continuous curves) or $v_L = 880\ m/s$ (dashed curves). The zero values are artifacts of the simplified model, appearing when the two exponentially damped factors of eq. 3.32 cancel each other; the decay constant depends on the dominant between these two factors.

3.2.3 Noise subtraction

Seismically induced NN is characterized by an amplitude spectral density several orders of magnitude lower than that of the seismic noise, as shown in eq. 3.26. Although it is always possible to filter the seismic component, even by many orders of magnitude, either mechanically or actively, this is not true for the Newtonian component, since the gravity gradients couple directly to the test masses themselves, making such a noise the main limitation to the sensitivity at the lowest frequencies. Therefore, it is necessary to develop suitable techniques which allow

[7] since $K = K(\omega)$, also the attenuation factor depends on the frequency.

to subtract the NN signal from the overall output signal of the interferometer, being known the "progenitor" seismic displacement time-series from an extensive network of sensors.

Subtraction scheme

The strategy of NN subtraction, reported here and developed by [118], is based on the exploitation of the correlation between NN and the seismic displacement at several points, monitored continuously by an array of seismometers. Let us assume that the measured displacements are statistically stationary, then the time series acquired by the i-th sensor will be composed of the displacement signal s_i and the proper instrumental noise σ_i, i.e. $X_i = s_i + \sigma_i$. The overall output signal Y from the interferometer can be expressed as the sum of a component H uncorrelated to the seismic motion, and that which takes into account the seismically induced NN, indicated by N: therefore we can write the output as $Y = H + N$. The subtracted time series Y_s will be constructed in order to meet an optimization criterion, under the assumptions that the seismic time series X_i are uncorrelated with the gravitational wave signal in Y and the noise is Gaussian [26]. Hence, appropriate linear and time-invariant filters will be applied to each X_i signal and, subsequently, the filtered signal will be subtracted from the interferometer output Y. Let us write the linear combination of the time series from the interferometer and the sensor array outputs:

$$Y_s(\omega) = Y(\omega) + \int d\omega' \sum_i \alpha_i(\omega, \omega') X_i(\omega') \tag{3.35}$$

where the Y_s is the subtracted signal which minimizes the power spectrum at each frequency, being $\alpha_i(\omega)$ the minimization variables, i.e. the linear filters that must be applied to the output signals of the seismic sensors before adding them to the interferometer output Y. The power spectrum of Y_s is related to the following correlation [118]:

$$\begin{aligned} \langle Y_s(\omega)^* Y_s(\omega') \rangle &= \langle Y(\omega)^* Y(\omega') \rangle \\ &+ \int d\omega'' \sum_i \alpha_i(\omega, \omega'')^* \langle X_i(\omega'')^* Y(\omega') \rangle \\ &+ \int d\omega'' d\omega''' \sum_{i,j} \alpha_i(\omega, \omega'')^* \alpha_j(\omega', \omega''') \langle X_i(\omega'')^* X_j(\omega''') \rangle \\ &+ \alpha_i(\omega', \omega'') \langle Y(\omega)^* X_i(\omega'') \rangle \end{aligned} \tag{3.36}$$

Where with the indices i,j we indicate the i-th and j-th element of the sensor array. By minimizing the previous eq. 3.36 with respect to $\alpha_k(\omega', \omega'')^*$ we find a set of linear integral equations for the optimal filters:

$$\langle X_k(\omega'')^* Y(\omega') \rangle + \sum_j \int d\omega'' \langle X_k(\omega'')^* X_j(\omega''') \rangle \alpha_j(\omega', \omega''') = 0 \tag{3.37}$$

The expression of the α_j variables can be obtained by the inverse of the kernel $K_kj(\omega,\omega') \equiv \langle X_k(\omega)^* X_j(\omega')\rangle$, and is formally given by:

$$\alpha_i(\omega',\omega) = -\sum_k \int d\omega'' K^{-1}_{ik}(\omega,\omega'')\,\langle X_k(\omega'')^* Y(\omega')\rangle \tag{3.38}$$

If the noise is stationary, we can find the following expression:

$$\langle X_i(\omega)^* Y(\omega')\rangle = 2\pi\delta(\omega-\omega')C_{SN\,i}(\omega) \tag{3.39}$$

where $C_{SN}(\omega)$ is the vector whose i-th component is the cross correlation between the i-th output and the NN. We can now define the relation between the outputs of the seismic sensors of the array in a similar way:

$$\langle X_i(\omega)^* X_j(\omega')\rangle = 2\pi\delta(\omega-\omega')[C_{SS\,ij}(\omega) + C_{\Sigma\Sigma\,ij}(\omega)] \tag{3.40}$$

where the i-th and j-th entry of the array C_{SS} represents the cross correlation between the seismic noise measured by the i-th and j-th seismic sensors, while the same entry of the array $C_{\Sigma\Sigma}$ is the correlation between their intrinsic noises. The last term we need to define is the first element of the second member in eq. 3.36. It can be written as the decomposition of the interferometer power spectrum in a NN contribution $C_{NN}(\omega)$, plus those which is uncorrelated with it, indicated by C_{HH}:

$$\langle Y(\omega)^* Y(\omega')\rangle = 2\pi\delta(\omega-\omega')[C_{NN}(\omega) + C_{HH}(\omega)] \tag{3.41}$$

By combining the previous relations in eq. 3.36 and 3.38 we obtain the expression for the optimal filters [118]:

$$\alpha_i(\omega,\omega') = -\delta(\omega-\omega')[C_{SS}(\omega) + C_{\Sigma\Sigma}(\omega)]^{-1}_{ij}[C_{SN}(\omega)]_j \tag{3.42}$$

The $\alpha_i(\omega,\omega')$ defined by eq. 3.42 are time-invariant in the stationary case we considered. Finally, we can define the amplitude efficiency $\epsilon(\omega)$ of the NN subtraction as the ratio between the power spectra of the subtracted signal $S_{Y_s}(\omega)$ and that of the unprocessed output signal $S_Y(\omega)$:

$$1-\epsilon(\omega) = \left(\frac{S_{Y_s}(\omega)}{S_Y(\omega)}\right)^{1/2} = \left(1 - \frac{C^+_{SN}(\omega)[C_{SS}(\omega) + C_{\Sigma\Sigma}(\omega)]^{-1}C_{SN}(\omega)}{C_{NN}(\omega)}\right)^{1/2} \tag{3.43}$$

The square of eq. 3.43 gives the ratio between the power spectra of the NN contained in the subtracted and original interferometer output signal. From the last expression we can deduce the three conditions needed to achieve a good NN subtraction efficiency:

1. $C_{SN}(\omega)$ must be as large as possible, i.e. all the seismic sensor must be coupled to the NN as much as possible;

2. the intrinsic noise of the i-th sensor, described by its power spectra $[C_{SS}]_{ii}$, must be small;

3. the correlation between the displacements measured by different sensors, described by C_{SS}, must also be small.

While the correlation C_{SS} between seismic sensors can be measured easily, the same is not true for the C_{NN}, so that there is no hope to test the described subtraction procedure without building a NN sensitive detector. However, it is possible to estimate the eq. 3.43 by means of a theoretical model, as follows [118].

Parameters estimate

Let us consider a single test mass, surrounded by an infinite medium, and suppose that each sensor can monitor the mass density fluctuation at its position. The i-th sensor will be affected by the intrinsic noise $\sigma_i(\omega)$, but without correlations between $\tilde{\sigma}_i$ and $\tilde{\sigma}_j$ when $i \neq j$. The mass density fluctuations can be thought as a Gaussian stochastic field, described by an exponential cross correlation function:

$$\langle \tilde{\rho}(\omega, \vec{x})^* \tilde{\rho}(\omega', \vec{x}') \rangle = 2\pi\Gamma^2(\omega)\delta(\omega - \omega') \exp\left(-\frac{|\vec{x} - \vec{x}'|}{\xi(\omega)}\right) \tag{3.44}$$

where $\xi(\omega)$ is the frequency-dependent correlation length, Γ is a parameter related to the quality factor Q of the considered medium, and $\rho(\omega, \vec{x})$ is the frequency-dependent mass density at a given point. The quantities necessary to make an estimate of eq. 3.43 are consequently:

$$C_{SS\,ij}(\omega) + C_{\Sigma\Sigma\,ij}(\omega) = \Gamma^2(\omega)\exp(-|\vec{u}_i - \vec{u}_j|) + \sigma^2(\omega)\delta_{ij} \tag{3.45}$$

$$C_{SN\,i}(\omega) = 4\pi\xi G\Gamma^2(\omega)\cos\theta_i \Phi(u_i) \tag{3.46}$$

$$C_{NN}(\omega) = \frac{16}{3}\pi^2\xi^2 G^2\Gamma^2(\omega) \tag{3.47}$$

where $\vec{u}_i = \xi^{-1}\vec{r}_i$ is the position of the i-th sensor given in units of the correlation length ξ, θ_i is the angle between the acceleration $\vec{a}_{NN}$ and r_i, and the function $\Phi(u)$ is given by:

$$\Phi(u) = \frac{1}{u^2}\left[2 - e^{-u}(2 + 2u + u^2)\right] \tag{3.48}$$

Therefore, from this model we obtain the explicit expression of eq. 3.43:

$$1 - \epsilon = \sqrt{1 - 3\left(e^{-|\vec{u}_i - \vec{u}_j|} + \frac{\sigma^2}{\Gamma^2}\delta_{ij}\right)\Phi(u_i)\Phi(u_j)\cos\theta_i\cos\theta_j} \tag{3.49}$$

The previous eq. 3.49 can be used to find the optimal positions and orientations of the seismic sensors in the array devoted to the NN subtraction scheme [26]. In the simplest case of two sensors, the optimal positions are along the direction of $\vec{a}_{NN}$, placed at a distance $d \approx 1.28\ \xi$ from the test mass; the $\cos\theta$ factor is maximized along the axis, while the function $\Phi(u)$ has a maximum at $u \sim 1.45$, therefore in this optimal case we find $1 - \epsilon \sim 0.9$. Starting from this configuration it is possible to add other sensors, finding the optimal relative positions, as shown in ref. [118]. We should remark some particular features deduced by the model described above:

1. the separation between the seismic sensors must be optimized in agreement with the correlation length ξ of the contributions to the NN that must be subtracted, which depends on the frequency band where the subtraction scheme is applied;

2. the NN subtraction procedure improves with the number of the sensors; obviously, in a practical implementation of this procedure, positioning possibilities of the sensors in the detector site will be limited, so that the optimization of the sensor positions will be not a trivial problem.

The environmental NN subtraction technique is an important issue for third generation interferometric gravitational wave detectors, which is still under investigation. While a simple model like that described above can be adequate in some scenarios, we will need more complex models and FEM analyses in order to develop an efficient subtraction scheme, especially in those geological scenarios where the loss of coherence described by the scale ξ is less relevant. Moreover, since the coherence length is generally a function of the frequency, i.e. $\xi \equiv \xi(f)$, it follows that the NN subtraction scheme will be optimal only in a given frequency range.

Active NN subtraction schemes have been already proposed for LIGO and Virgo [119, 120], based on seismometers which monitor the seismic noise sources in order to find the NN transfer function and the optimal linear filters. However the impulsive and periodic sources related to the anthropic activities and to the infrastructures of the detector will be a main concern for third generation interferometers: even in an underground site the placement of electricity generators, pumps and cryocoolers will be carefully investigated in order to minimize the anthropogenically generated seismic gravity gradients.

Chapter 4

Thermal Noise

The thermal noise is a fundamental limit to the interferometric detector sensitivity in a band that ranges from the low frequencies to some hundreds Hz. As the definition suggests, it is strictly related to the temperature, and affects the mechanical parts of the test mass suspension and the the mirror itself. Indeed, the variables (e.g. the displacement) which describes a physical system, assumed as free-evolving in thermodynamical equilibrium, undergo spontaneous fluctuations at a given temperature T. This fact was firstly noticed in 1827 by Brown [121] during his observations of particles in suspension, and was consequently known as *Brownian motion*. Einstein, in one of his famous "annus mirabilis" papers of 1905 [122, 123], described physically the process as driven by thermally-generated molecular random collisions, which can be dealt with statistical mechanics. About twenty years later, Nyquist and Johnson found that in electric conductors also the voltage fluctuations are proportional to $\sqrt{k_B T}$ [124], where k_B is the Boltzmann constant, resulting in the so called Johnson noise. The generalization of this relation to any dissipative system led to the formulation of the Fluctuation-Dissipation theorem [125], which allows to calculate the displacement fluctuations due to the thermal noise in a physical system.

In the first section of this chapter I will outline the Fluctuation-Dissipation theorem, subsequently I will introduce the ideal case of a damped harmonic oscillator, and the real case of dissipative mechanical systems, such as the test mass suspensions and the mirrors of an interferometric gravitational wave detector. Finally, I will conclude with the the cryogenic suppression of the thermal noise in the mechanical and optical components.

4.1 Fluctuation - Dissipation theorem

The displacement fluctuations of a particle in thermodynamic equilibrium with its environment, at a given temperature T, are caused by the thermally-induced Brownian motion. These fluctuations are related to dissipative mechanisms which cause an irreversible loss of energy among the various degrees of freedom of the system. Let us consider a stochastic force $F(t)$ which perturbs the dissipative system from its equilibrium state: the observed fluctuations are the response of the system to the perturbation. The existence of spontaneous fluctuating forces

coupled to irreversible processes and the amplitude of the so-induced fluctuations can be predicted by means of the *Fluctuation-Dissipation theorem* [125, 126, 127]: if the dissipative system is linear, i.e. the power dissipation is quadratic in the magnitude of the perturbation, the theorem establishes a relation between appropriate generalized forces and a generalized impedance $Z(\omega)$, that is defined as the proportionality constant between the power and the square of the perturbation. Denoting with $\langle \xi^2 \rangle$ the mean square fluctuation in a given frequency interval, which is determined by the range of integration, the theorem states that:

$$\langle \xi^2 \rangle = \frac{2k_B T}{\pi} \int d\omega Y(\omega) \omega^{-2} \tag{4.1}$$

where $Y(\omega) = 1/Z(\omega)$ is the generalized admittance. The result expressed by eq. 4.1, can be written in terms of the mean square fluctuation of an equivalent generalized force, function of the real part of the generalized impedance $Z(\omega)$:

$$\langle \delta F^2 \rangle = \frac{2k_B T}{\pi} \int d\omega \mathcal{R}e[Z(\omega)] \tag{4.2}$$

We can derive the expressions of the fluctuation power spectra of a variable X due to the thermal noise as follows: let us start considering an unidimensional linear dissipative system, assumed to be in thermodynamical equilibrium. If $X(t)$ is the response of the system to the external perturbation force $F(t)$, the generalized impedance of the system is defined as:

$$Z(\omega) = \frac{\mathcal{F}\{F(t)\}(\omega)}{\mathcal{F}\{\dot{X}(t)\}(\omega)} \equiv \frac{\mathcal{F}\{F(t)\}(\omega)}{i\omega \mathcal{F}\{X(t)\}(\omega)} \tag{4.3}$$

where with $\mathcal{F}\{f(t)\}$ we indicate the Fourier transform of $f(t)$. From eq. 4.3 we can derive the expression of the transfer function $\mathcal{T}(\omega)$ of the system in terms of the generalized impedance:

$$\mathcal{T}(\omega) = \frac{\mathcal{F}\{X(t)\}(\omega)}{\mathcal{F}\{F(t)\}(\omega)} \equiv \frac{1}{i\omega Z(\omega)} \tag{4.4}$$

Using the fluctuation-dissipation theorem expressed in eq. 4.1, we can write the PSD of the thermal noise for the physical quantity $X(\omega)$ in terms of the transfer function $\mathcal{T}(\omega)$, that in turn is a function of the impedance $Z(\omega)$ (i.e. the inverse of the admittance, $Y^{-1}(\omega)$), obtaining:

$$S_X(\omega) = -\frac{4k_B T}{\omega} \mathcal{I}m[\mathcal{T}(\omega)] \tag{4.5}$$

where $\mathcal{I}m[\mathcal{T}(\omega)]$ is the imaginary part of the transfer function expressed by eq. 4.4. From the previous equations we can also derive the PSD of the stochastic force $F(t)$, that is given by:

$$S_F(\omega) = 4k_B T \mathcal{R}e[Z(\omega)] \tag{4.6}$$

The dissipation of the system is taken into account by the transfer function $\mathcal{T}(\omega)$, related to the generalized impedance by eq. 4.4. Moreover, the power spectra of thermal fluctuations (eq. 4.5) and perturbation force (eq. 4.6) directly depends

on the temperature T of the environment in thermodynamic equilibrium with the system.

We can extend this results to a n-dimensional system [128], characterized by n response variables X_i and perturbed by n generalized forces F_i. In this case the generalized impedance of the system is expressed by the $n \times n$ matrix $Z_{ij}(\omega)$, therefore also the transfer function must be in the form of a matrix with the same dimensions: $\mathcal{T}_{ij}(\omega)$. The energy is dissipated among all the degrees of freedom, so that we can write the generalization of eq. 4.3 as follows:

$$\mathcal{F}\{F_i(t)\}(\omega) = Z_{ij}\mathcal{F}\{\dot{X}_j(t)\}(\omega) \tag{4.7}$$

and therefore, from eq. 4.4, we find:

$$\mathcal{F}\{X_i(t)\}(\omega) = \mathcal{T}_{ij}\mathcal{F}\{F_j(t)\}(\omega) \tag{4.8}$$

From the fluctuation-dissipation theorem we obtain the cross-spectral density (CSD) of the fluctuations (see app. A):

$$S_{X_iX_j}(\omega) = -\frac{4k_BT}{\omega}\mathcal{I}m[\mathcal{T}_{ij}(\omega)] \tag{4.9}$$

Therefore, the PSD of X_i in the unidimensional case (eq. 4.5) is the special case of eq. 4.9 with $i = j$.

4.2 Damped harmonic oscillator

In the previous section we found that the PSD of the thermal noise can be expressed as a function of the imaginary part of the transfer function (see eq. 4.5 and 4.9). Therefore, in order to make an estimate of the thermal noise limiting the detector sensitivity, we have to calculate the form of the transfer function associated to the physical systems which we are considering (e.g. the mechanical suspension and the mirror). The simplest model to consider is the unidimensional harmonic oscillator with mass m and resonant frequency ω_0 which undergoes an external generalized force $F(t)$. In the ideal case there are not losses and the equation of motion is given by:

$$m\ddot{x}(t) + m\omega_0^2 x(t) = F(t) \tag{4.10}$$

where $m\omega_0^2 = k$ is the elastic spring constant. With a Fourier transformation of eq. 4.10 we can write the equation of motion in the frequency domain:

$$m(\omega_0^2 - \omega^2)\mathcal{F}\{x(t)\}(\omega) = \mathcal{F}\{F(t)\}(\omega) \tag{4.11}$$

By combining eq. 4.11 with eq. 4.4 we obtain the transfer function of the ideal harmonic oscillator, that is:

$$\mathcal{T}_{ideal}(\omega) = \frac{1}{m(\omega_0^2 - \omega^2)} \tag{4.12}$$

The fluctuation-dissipation states that the PSD of thermal fluctuations is a function of the imaginary part of the transfer function (see eq. 4.5), but $\mathcal{T}_{ideal}(\omega)$

expressed in eq. 4.12 is a real function, so that we obtain a null thermal noise PSD in the above-described harmonic oscillator: this is not surprising, because in the ideal case there are not dissipations. This is evident also from the divergence of eq. 4.12 when $\omega \to \omega_0$. Conversely, a real physical harmonic oscillator is damped by dissipative processes [129], which can be subdivided in *viscous* and *intrinsic* dissipations (see sec. 4.2.2 and 4.2.3 respectively). By introducing the damping coefficient β, we can rewrite the equation of motion 4.10 for the damped harmonic oscillator as follows:

$$m\ddot{x}(t) + \beta\dot{x}(t) + m\omega_0^2 x(t) = F(t) \tag{4.13}$$

and in frequency domain it becomes:

$$m(\omega_0^2 - \omega^2 + i\frac{\omega\beta}{m})\mathcal{F}\{x(t)\}(\omega) = \mathcal{F}\{F(t)\}(\omega) \tag{4.14}$$

so that the transfer function $\mathcal{T}(\omega)$, given by the ratio between $\mathcal{F}\{x(t)\}(\omega)$ and $\mathcal{F}\{F(t)\}(\omega)$, is composed in general by an imaginary part, resulting in a non-null thermal noise PSD and finite values of the resonance peaks.

4.2.1 Loss angle and Quality factor

In order to describe the dissipations in a damped harmonic oscillator, it is useful to introduce two parameters [130]:

Loss angle indicated with $\phi(f)$, it is related to the ratio between the mechanical energy lost per oscillation cycle $\Delta E_{mec}(f)$ and the total mechanical energy stored in the oscillator $E_{mec}(f)$:

$$\frac{\Delta E_{mec}(f)}{E_{mec}(f)} = 2\pi\phi(f), \quad \text{for} \quad \phi(f) \ll 1 \tag{4.15}$$

If the damping coefficient β varies slowly with the angular frequency, we can write it as a function of the loss angle:

$$\beta \equiv \frac{\phi(\omega)m\omega_0^2}{\omega} \tag{4.16}$$

By substituting eq. 4.16 into eq. 4.14, we rewrite the equation of motion as:

$$m[\omega_0^2(1 + i\phi(\omega)) - \omega^2]\mathcal{F}\{x(t)\}(\omega) = \mathcal{F}\{F(t)\}(\omega) \tag{4.17}$$

In eq. 4.17 we note that the loss angle represents the imaginary part of the elastic spring constant k:

$$k \equiv m\omega_0^2 \to m\omega_0^2(1 + i\phi(\omega)) \tag{4.18}$$

The elasticity of a material is expressed by the Young's modulus $\mathcal{E}(\omega)$, which is defined as the ratio between the tensile stress $\sigma(\omega)$, a force per unit area, and the tensile strain $\epsilon(\omega) \equiv \Delta\xi(\omega)/\xi_0$ along a given axis:

$$\mathcal{E}(\omega) = \frac{\sigma(\omega)}{\epsilon(\omega)} \tag{4.19}$$

In eq. 4.18 we found that the damping is described by an imaginary component of the elastic constant, therefore we have also to consider the complex form of the Young's modulus, writing it as a function of the loss angle ϕ:

$$\mathcal{E}(\omega) = \mathcal{R}e[\mathcal{E}(\omega)] + \mathcal{I}m[\mathcal{E}(\omega)] = |\mathcal{E}|e^{i\phi(\omega)} \tag{4.20}$$

In the harmonic oscillator the frequency-dependent tensile strain is given by:

$$\epsilon(\omega) = \epsilon_0 e^{i\omega t} \tag{4.21}$$

so that, combining eq. 4.21 and 4.20 with eq. 4.19, we obtain the expression of the tensile stress during the oscillations:

$$\sigma(\omega) = \sigma_0 e^{i\omega t} = |\mathcal{E}|\epsilon_0 e^{i(\omega t+\phi)} \tag{4.22}$$

Therefore, the loss angle ϕ represents the phase lag between the excitation (i.e. the tensile stress) and the system response (i.e. the tensile strain) of the damped harmonic oscillator.

Taking into account several dissipation processes, we note that the overall energy loss is given by the addition of the energy losses in each dissipative process. Therefore, from the definition 4.15, we find that the overall loss angle $\phi_{tot}(\omega)$ must be defined as the sum of the loss angles $\phi_i(\omega)$ related to each dissipation acting in the system:

$$\phi_{tot}(\omega) = \sum_i \phi_i(\omega) \tag{4.23}$$

Quality factor or Q-factor, is a dimensionless parameter related to the ratio between the total mechanical energy stored in the oscillator and the energy dissipated per cycle: higher Q values means lower energy dissipations. The quality factor is strictly related to the loss angle, and it is defined by:

$$Q(\omega) = \frac{\omega}{\omega_0 \phi(\omega)} \tag{4.24}$$

At the resonant frequency $\omega = \omega_0$, the relation 4.24 becomes:

$$Q(\omega_0) = \frac{1}{\phi(\omega_0)} \tag{4.25}$$

From eq. 4.17 we note that the transfer function of the damped harmonic oscillator (eq. 4.4) depends on the loss angle $\phi(\omega)$, therefore also the thermal noise PSD (eq. 4.5) will be a function of $\phi(\omega)$. However, the measurement of the the loss angle over a wide frequency span is not trivial, so that its estimate is usually obtained by eq. 4.25, at the resonant frequency of the system, by measuring the Q-factor from the following relations:

- when the characteristic time τ_0 of the oscillation amplitude decay is large, i.e. for $\tau_0 \gg 1$, the Q-factor at the resonance is given by:

$$Q(\omega_0) = \pi\tau_0 \left(\frac{\omega_0}{2\pi}\right) \tag{4.26}$$

- otherwise, when the decay time is short, i.e. for $\tau_0 \ll 1$, the Q-factor can be esimated by:
$$Q(\omega_0) = \frac{\omega_0}{\Delta\omega_0} \tag{4.27}$$
where $\Delta\omega_0$ is the full width at half maximum (FWHM) at the resonance peak.

4.2.2 Viscous dissipations

The viscous dissipation causes a damping proportional to the velocity $\dot{x}$ and described by the damping coefficient β. The equation of motion of the viscously damped harmonic oscillator is that of eq. 4.13 (in the time domain) and eq. 4.14 (in the frequency domain). By combining the last one with eq. 4.4 we immediately find the transfer function of the system:

$$\mathcal{T}_{vis}(\omega) = \frac{1}{m(\omega_0^2 - \omega^2) + i\frac{\omega\beta}{m}} \tag{4.28}$$

therefore, the imaginary part of eq. 4.28 is:

$$\mathcal{I}m[\mathcal{T}_{vis}(\omega)] = \frac{-\omega\beta}{m\left[(\omega_0^2 - \omega^2)^2 + \frac{\omega^2\beta^2}{m}\right]} \tag{4.29}$$

By substituting eq. 4.29 in eq. 4.5 we find the expression of the thermal noise PSD:

$$S_{vis}(\omega) = \frac{4k_BT\omega_0}{m\left[(\omega^2 - \omega_0^2)^2 + \frac{\omega_0^2\omega^2}{Q_{vis}^2(\omega_0)}\right]}\frac{1}{Q_{vis}(\omega_0)} \tag{4.30}$$

where we used the quality factor at the resonant frequency, defined in terms of β and ω_0:

$$Q_{vis}(\omega_0) = \frac{m\omega_0}{\beta} \tag{4.31}$$

Now we can derive the approximate expressions of eq. 4.30 below and above the resonant frequency ω_0, shown in fig. 4.1:

$$S_{vis}(\omega) \approx \begin{cases} \frac{4k_BT}{m\omega_0^3}\frac{1}{Q_{vis}(\omega_0)} = \text{const} & \text{if } \omega \ll \omega_0 \\ \\ \frac{4k_BT\omega_0}{m}\frac{1}{Q_{vis}(\omega_0)}\frac{1}{\omega^4} & \text{if } \omega \gg \omega_0 \end{cases} \tag{4.32}$$

Air damping

The canonical example of viscous dissipation is the air damping due to the momentum transfer between the oscillator and the residual gas molecules in vacuum regime. The thermal velocity of the molecules is $v_{th} \propto \sqrt{k_BT/m_{gas}}$, therefore their mean free path is usually larger than the typical dimensions of the mechanical oscillator. In this case the damping coefficient is given by [66]:

$$\beta = \frac{P_{gas}m_{gas}Av_{th}}{4k_BT} \tag{4.33}$$

where P_{gas} is the residual pressure, m_{gas} the mass of the gas molecules and A is the cross section of the mechanical oscillator. Therefore, we can write the loss angle associated to the air damping from eq. 4.16, substituting β with eq. 4.33, obtaining:

$$\phi_{gas} = \frac{P_{gas} m_{gas} A v_{th}}{4 k_B T m \omega_0^2} \omega \tag{4.34}$$

In the simple case of a vibrating wire, eq. 4.34 can be expressed as function of the wire mass density ρ_w and radius r [131]:

$$\phi_{gas}^{w} = \frac{P_{gas} m_{gas} v_{th}}{4 k_B T \rho_w r \omega_0^2} \omega \equiv \frac{\rho_{gas} v_{th}}{4 \rho_w r \omega_0^2} \omega \tag{4.35}$$

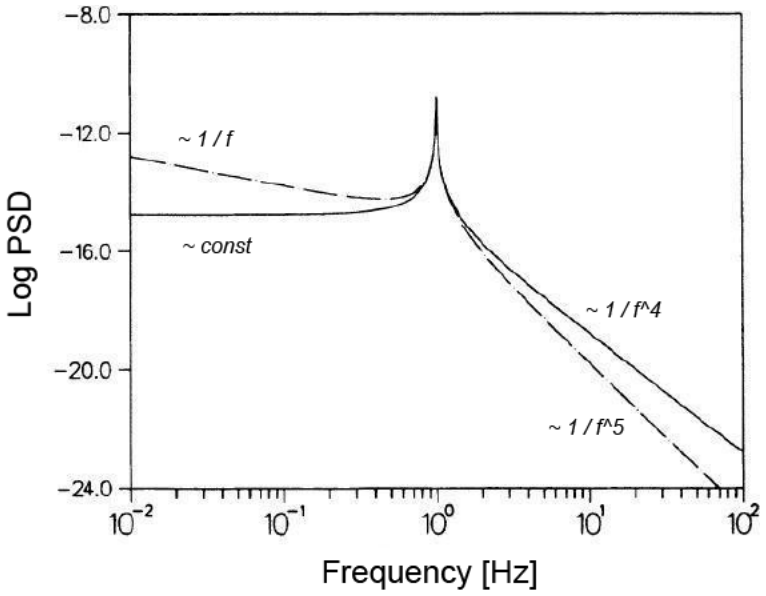

Figure 4.1: Thermal noise power spectral densities of an harmonic oscillator with viscous damping (solid line) or intrinsic damping (dotted line); the frequency dependence of the curves is given by equations 4.32 and 4.39; the PSD shown in figure have been calculated for an oscillator with mass $10^{-3}\ kg$, resonant frequency $f_0 = 1\ Hz$ and $Q = 100$ [129].

4.2.3 Intrinsic dissipations

Intrinsic dissipations, due to the microscopic and mechanical structures of the oscillator, are described by an imaginary part in the elastic constant (see eq. 4.18) which depends on the loss angle $\phi(\omega)$. As said above, this parameter represents the phase lag in the response of the elastic system (see eq. 4.22). From the equation of motion 4.17 we can derive the transfer function depending on ϕ:

$$\mathcal{T}_{int}(\omega) = \frac{1}{m\left[(\omega_0^2 - \omega^2) + i\omega_0^2 \phi(\omega)\right]} \tag{4.36}$$

and then from its imaginary part:

$$\mathcal{I}m[\mathcal{T}_{int}(\omega)] = \frac{-\omega_0^2\phi(\omega)}{m\left[(\omega_0^2-\omega^2)^2+\omega_0^4\phi^2(\omega)\right]} \tag{4.37}$$

substituted into eq. 4.5, we obtain the expression of the thermal noise PSD:

$$S_{int}(\omega) = \frac{4k_BT\omega_0^2}{m\omega[(\omega^2-\omega_0^2)^2+\omega_0^4\phi^2(\omega)]}\phi(\omega) \tag{4.38}$$

Usually, the loss angle of metal materials is almost constant in a wide frequency range below $10^4\ Hz$, so that we can take $\phi(\omega) \approx \phi(\omega_0)$ and derive the approximate expressions of eq. 4.38 below and above the resonant frequency ω_0, that are shown in fig. 4.1:

$$S_{int}(\omega) \approx \begin{cases} \frac{4k_BT\phi(\omega_0)}{m\omega_0^2}\frac{1}{\omega} & \text{if } \omega \ll \omega_0 \\ \\ \frac{4k_BT\omega_0^2\phi(\omega_0)}{m}\frac{1}{\omega^5} & \text{if } \omega \gg \omega_0 \end{cases} \tag{4.39}$$

The loss angle $\phi(\omega)$, which is needed to make an estimate of the thermal noise PSD of eq. 4.38, are calculated for the several dissipation mechanisms in the next subsections.

Structural and superficial losses

The structural and superficial losses are related to the configuration and relative displacement of the molecules that compose the mechanical system, therefore they depend on inhomogeneities and defects in the microscopic spatial and superficial structures. Vibrations and reconfigurations in the microscopic structure, such as those induced by the elastic deformations or by the dislocation motions in polycrystalline metals (see the relative paragraph in sec. 2.2.3 and ref. [76]), give rise to energy dissipations proportional to the volume (structural loss, $\Delta E_{str} \propto V$) or to the surface (superficial loss, $\Delta E_{sur} \propto S$) of the mechanical oscillator. From eq. 4.23 we can write the total loss angle at a given frequency f as:

$$\phi_{tot} = \frac{1}{2\pi}\frac{\Delta E_{str}+\Delta E_{sur}}{E_{tot}} \tag{4.40}$$

where E_{tot} is the total energy stored in the mechanical oscillator. The ratio between the superficial and structural energy loss is proportional to the ratio between the surface and the volume:

$$\frac{\Delta E_{sur}}{\Delta E_{str}} = \eta x_d \frac{S}{V} \tag{4.41}$$

where η is dimensionless coefficient which depends on the geometry and the relative elastic strain between the surface and the bulk, while x_d is the *dissipation depth* which takes into account the dissipation in the superficial layer with respect to that of the structure, and depends on the geometric depth ξ and on the loss angles ϕ_{str} and ϕ_{sur}:

$$x_d = \frac{1}{\phi_{str}}\int_0^h d\xi\phi_{sur}(\xi) \tag{4.42}$$

where h is the thickness of the superficial layer. If the superficial dissipation does not depend on the geometrical depth[1], the eq. 4.42 reduces to $x_d = h\phi_{sur}/\phi_{str}$. Since the total energy stored in the elastic oscillator is mainly composed of structural energy, i.e. $E_{tot} \approx E_{str}$, by defining the structural loss angle as $\phi_{str} \equiv \Delta E_{str}/2\pi E_{str}$ and combining eq. 4.40 with 4.41, we find:

$$\phi_{tot} \approx \frac{1}{2\pi}\left(\frac{\Delta E_{str}}{E_{str}} + \eta x_d \frac{S}{V}\frac{\Delta E_{str}}{E_{str}}\right) \approx \phi_{str}\left(1 + \eta x_d \frac{S}{V}\right) \tag{4.43}$$

Thermoelastic losses

In the materials with a non-negligible thermal dilatation coefficient α, the temperature variation ∂T is coupled to the volumetric dilatation ∂V:

$$\frac{\partial V}{V} = \alpha \partial T \tag{4.44}$$

therefore, for $\alpha > 0$, a local volumetric dilatation causes a local cooling of the body, conversely a local contraction increases the local temperature (see fig. 4.2). During the elastic oscillations, the system is periodically stretched and compressed, so that they give rise to heat flows between the parts which undergo heating and cooling, in order to restore the thermal equilibrium. The irreversible heat flows which is driven by the temperature gradient dissipates vibrational energy. The time-scale τ necessary to reach the equilibrium is given by [132, 133]:

$$\tau = \frac{c_V r^2}{4.32\pi D} \tag{4.45}$$

where c_V is the volumetric heat capacity, r is the typical distance scale of the heat flux and D is the thermal diffusion coefficient, which in turn depends on the thermal conductivity:

$$D = \kappa/c_V \tag{4.46}$$

The thermoelastic loss angle depends on the above defined parameters and on the Young's modulus $\mathcal{E}$, and is given by [132, 133]:

$$\phi_{thermoel}(\omega) = \frac{\mathcal{E}\alpha^2 T}{c_V}\frac{\omega\tau}{1+\omega^2\tau^2} \tag{4.47}$$

Eq. 4.47 depends on ω and has a maximum at the frequency $\omega_\tau = 2\pi/\tau$, which is defined thermoelastic peak. If the system oscillates at frequencies below ω_τ, i.e. with a period $t \gg \tau$, the process is almost isothermal; otherwise, if the oscillation frequency is $\omega \gg \omega_\tau$, the system does not have enough time to relax and to reach the equilibrium, so that the process is almost adiabatic. Therefore, the maximum thermoelastic dissipation occurs at frequencies around the peak ω_τ. To reduce the sensibility limitation related to this dissipation, the mechanical structure of the detector must be designed in order to put the thermoelastic peak as far as possible from the detection band.

This thermoelastic dissipation is particularly important in systems with a small section, such as vibrating wires, whose total loss angle can be approximated with the sum of structural and thermoelastic loss angles.

[1] this condition is true if loss angle and Young's modulus does not vary with the geometrical depth

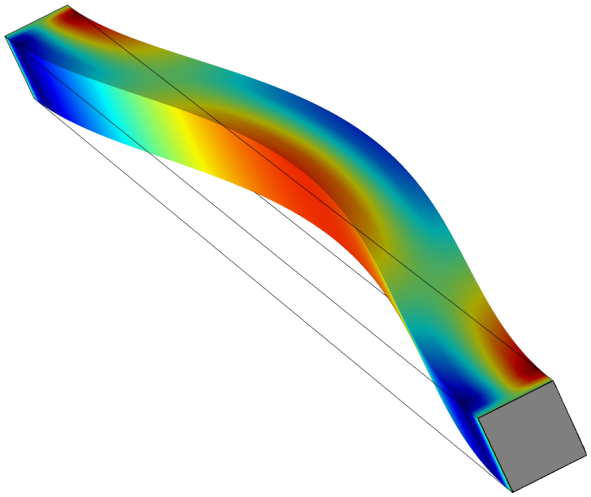

Figure 4.2: Temperature variation due to local dilatations and compressions in a bar from a FEM simulation. Dilatations cause local coolings (in blue), compressions result in local heating (in red). The so-generate temperature gradient drive irreversible thermal flows, resulting in the thermoelastic energy loss.

Recoil losses

An ideal mechanic oscillator is fixed to a frame with a mass $M \to \infty$ and an infinitely rigid structure, so that its inertia can be considered as infinite. In the real case, the frame mass has a finite value m_1 and must be considered as another coupled oscillator, so that the frame recoil motion dissipate vibrational energy [129]. Such a system is described by the coupled oscillator shown in fig. 4.3, where m_1 and m_2 are respectively the frame and the oscillator mass, connected each to the other, and with the ground by two springs, with proper damping coefficients.

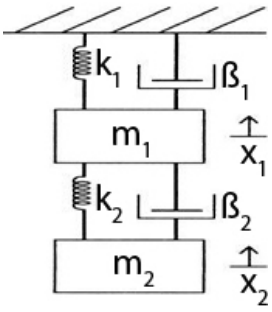

Figure 4.3: The simple model of two coupled oscillator describes the recoil energy losses.

The equation of motion of the coupled oscillator with damping is:

$$\begin{cases} m_1\ddot{x}_1(t) = -k_1x_1(t) - \beta_1\dot{x}_1(t) - k_2[x_1(t) - x_2(t)] - \beta_2[\dot{x}_1(t) - \dot{x}_2(t)] \\ m_2\ddot{x}_2(t) = -k_2[x_2(t) - x_1(t)] - \beta_2[\dot{x}_2(t) - \dot{x}_1(t)] \end{cases} \tag{4.48}$$

that becomes in the frequency domain:

$$\begin{cases} \mathcal{F}\{x_1(t)\}(\omega)\left[m_1\left(\omega^2-\omega_1^2-\frac{i\beta_1}{m_1}\omega\right)-m_2\left(\omega_2^2-\frac{i\beta_2}{m_2}\omega\right)\right]+ \\ \qquad\qquad +\mathcal{F}\{x_2(t)\}(\omega)\left[m_2\left(\omega_2^2+\frac{i\beta_2}{m_2}\omega\right)\right]=0 \\ \mathcal{F}\{x_1(t)\}(\omega)\left[m_2\left(\omega_2^2+\frac{i\beta_2}{m_2}\omega\right)\right]+ \\ \qquad\qquad +\mathcal{F}\{x_2(t)\}(\omega)\left[m_2\left(\omega^2-\omega_2^2-\frac{i\beta_2}{m_2}\omega\right)\right]=0 \end{cases} \tag{4.49}$$

where ω_1 and ω_2 are the resonant frequencies of the two uncoupled oscillators. The damping effect can be described as the imaginary part of the elastic constant $k_{1,2}$, obtained by the substitution of eq. 4.16 into eq. 4.49:

$$\begin{cases} k_1 = m_1\omega_1^2(1+i\phi_1) \\ k_2 = m_2\omega_2^2(1+i\phi_2) \end{cases} \tag{4.50}$$

The solutions of eq. 4.49 are two coupled oscillation modes which depends on the resonant frequencies of the uncoupled oscillators:

$$\omega_{+,-} = \sqrt{\frac{[\omega_2^2(1+\mu)+\omega_1^2] \pm \sqrt{[\omega_2^2(1+\mu)+\omega_1^2]^2-4\omega_1^2\omega_2^2}}{2}} \tag{4.51}$$

where $\mu = m_1/m_2$. If the resonant frequencies of the two coupled oscillators is the same, i.e. for $\omega_1 = \omega_2 = \omega_0$, eq. 4.51 becomes:

$$\omega_{+,-} = \omega_0\sqrt{\frac{2+\mu \pm \sqrt{\mu^2+4\mu}}{2}} \tag{4.52}$$

If an impulsive external force F acts on m_1 at $t = 0$, the displacement of the two oscillators will be in the form of:

$$\begin{cases} x_1 = A[\sin(\omega_+ t) + sin(\omega_- t)] = A\sin(\omega_0 t)\cos(\omega_b t) \\ x_2 = A[\sin(\omega_+ t) + sin(\omega_- t)] = \frac{A}{\mu}\cos(\omega_0 t)\sin(\omega_b t) \end{cases} \tag{4.53}$$

where A is the amplitude of the oscillation and ω_b is the beat frequency, defined as:

$$\omega_b = \frac{\omega_+ - \omega_-}{2} \tag{4.54}$$

If $\omega_1 = \omega_2$, from eq. 4.53 we note that the two oscillators are characterized by a motion in antiphase, and the energy is transferred between the two bodies at the beat frequency ω_b. We are interested in the case of a recoiling frame mass greater than the coupled oscillator, i.e. for $m_1 \gg m_2$ and $\phi_1 \gg \phi_2$. In such a configuration, introducing the external force $F(\omega)$ in the second equation of 4.49, it is possible to obtain the recoil-dissipation transfer function for the lighter body m_2 [129], which leads to the total loss angle associated to the recoil dissipation:

$$\phi_{2,rec} = \phi_2 + \phi_1\mu\frac{\omega_1\omega_2^3}{(\omega_1^2-\omega_2^2)^2} \tag{4.55}$$

From eq. 4.55 we note that the effect is small only if $\mu \ll 1$, that is not our case; moreover, the recoil damping is most important when the resonant frequency of the frame is close to that of the lighter oscillator. Thermal noise peaks of this coupled oscillator system are represented in fig. 4.4.

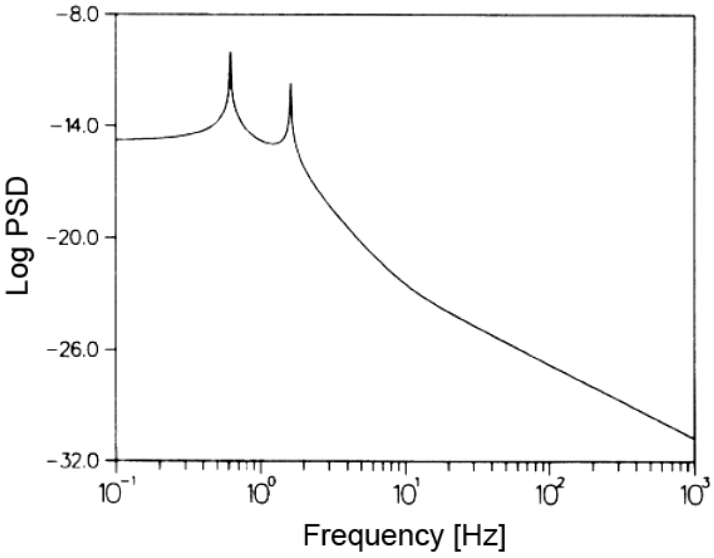

Figure 4.4: Thermal noise power spectral densities for the coupled oscillator described by eq. 4.48, in the special case of $m_1 = m_2 = 1\ g$ [129].

4.3 Thermal noise in a mechanical suspension

In an interferometric detector, the thermal noise acts on the position of each test mass and is caused by the thermal fluctuations of the mechanical suspension. Each stage of the suspension introduces a component of the overall thermal noise, as shown in the following subsections.

4.3.1 Pendulum oscillations

The last stage of the suspension is described by a pendulum, whose horizontal elastic-like restoring force is given by the gravitational field, which is clearly not dissipative. This choice allows to reduce the thermal noise acting on the test mass, which reduces to that of the suspension wires (or fibers). Therefore, in such a system, the equation of motion is:

$$m\ddot{x}(t) = [k_{grav} - k_{el}(1 + i\phi_p)]x(t) \tag{4.56}$$

where the gravitational constant is given by $k_{grav} = mg/l$, being m and l the mass and the length of the pendulum, while the elastic spring constant k_{el} is composed of an imaginary part, which depends on the loss angle ϕ_p. In the small-angle

approximation $x(t) \approx \theta(t)$, therefore we can rewrite the equation of motion in the frequency domain when an external force $F(\omega)$ acts on the system:

$$\theta(\omega)[k_{grav} + k_{el}(1 + i\phi_p) - \omega^2] = \frac{F}{l} \tag{4.57}$$

Since the gravitational "spring" is free of loss, the mechanical loss is the fraction $2\pi\phi(\omega)$ per cycle of the mechanical energy that is stored in the suspension wire [129]. Therefore, the relation between the pendulum loss angle and that of the wire is given by:

$$\phi_p = \phi_w \frac{E_{el}}{E_{grav} + E_{el}} \approx \phi_w \frac{E_{el}}{E_{grav}} = D_p \phi_w \tag{4.58}$$

where E_{el} and E_{grav} are respectively the energy stored in the flexing wire and in the gravitational field, ϕ_w is the loss angle associated to the internal loss of the wire, while D_p is definited as the *pendulum dilution factor*. Since usually $E_{grav} \gg E_{el} \rightarrow D_p \ll 1$, we note that the pendulum can have a loss angle much smaller than that relative to the material of which it is made. The factor D_p can be also written in terms of elastic constant, so that:

$$D_p = \frac{E_{el}}{E_{grav}} = \frac{k_{el}}{k_{grav}} \tag{4.59}$$

If we consider a pendulum suspended by n wires, the overall elastic spring constant is defined by:

$$k_{el} = \frac{n\sqrt{\top \mathcal{E} I}}{2l^2} \tag{4.60}$$

where $\top$ is the tension in each wire, $\mathcal{E}$ is the Young's modulus and I the moment of inertia of the wire cross section. By combining eq. 4.59 with eq. 4.60 and taking into account the gravitational constant k_{grav}, we obtain:

$$D_p = \frac{n\sqrt{\top \mathcal{E} I}}{2mgl} \tag{4.61}$$

that we can substitute in eq. 4.58 finding:

$$\phi_p(\omega) = \phi_w(\omega) \frac{n\sqrt{\top \mathcal{E} I}}{2mgl} \tag{4.62}$$

By substituting the loss angle of 4.62 in eq. 4.38 we obtain the PSD of the pendulum thermal noise:

$$S_p(\omega) = \frac{4k_B T \omega_p^2}{m\omega[(\omega^2 - \omega_p^2)^2 + \omega_p^4 \phi_p^2(\omega)]} \phi_p(\omega) \tag{4.63}$$

where ω_p is given by:

$$\omega_p^2 = \left(\frac{k_{el}}{m} + \frac{g}{l} \right) \tag{4.64}$$

However, in a more realistic estimate of the pendulum thermal noise we must include in ϕ_w the superficial loss angle ϕ_{sur}, and the recoil dissipations, so that $\phi_p \rightarrow D_p(\phi_{str} + \phi_{sur} + \phi_{thermael}) + \phi_{rec}$. The resulting strain equivalent spectral density of pendulum thermal noise in the L-long arm of the interferometer can be obtained by eq. A.7 and A.8, finding:

$$\tilde{h}_p(\omega) = \frac{2}{L} \sqrt{S_p(\omega)} \tag{4.65}$$

Residual gas limit

As shown in eq. 4.25, the Q-factor of the pendulum at the resonance is given by ϕ_p^{-1}. However, the viscous damping produced by the residual molecules of gas[2] (see sec. 4.2.2) can limit the quality factor reachable by the system, that is [69]:

$$Q_{limit} = 4\frac{m}{\pi r^2}\frac{\omega_p}{P}\sqrt{\frac{\pi k_b T}{8\mu_{H_2}}} \tag{4.66}$$

where m and r are the mass and radius of the oscillating test mass, ω_P is given by eq. 4.64, P is the residual pressure and μ_{H_2} is the molecular mass of hydrogen.

Tilt and rotational modes

There are two other pendulum oscillations that must be taken into account: the tilt mode around the horizontal axis perpendicular to the optic axis, and the rotational mode around the vertical axis. The expression of the thermal noise in the appropriate coordinates is similar to that of eq. 4.63 but, since $\theta \ll 1$, the coupling with the laser beam direction is very small.

4.3.2 Vertical oscillations

Due to the radius of curvature $R_\oplus$ of the Earth, gravitational acceleration vectors form an angle $2\theta_0 \approx 2\arcsin(L/2R_\oplus)$ in coincidence of the test masses suspended at the ends of the L-long arm of the interferometric detector. For this reason, the vertical fluctuation of the suspension chain is coupled to the displacement along the horizontal direction, which is that of the laser beam.

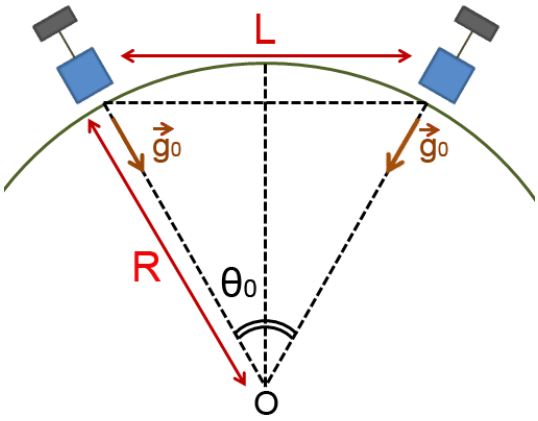

Figure 4.5: The vertical displacement of the test mass suspension is coupled by an angle θ_0 with the horizontal displacement measured by the interferometer due to the curvature radius $R_\oplus$ of Earth (not to scale).

[2] usually the residual gas is mainly composed of molecular hydrogen H_2.

By considering the suspension as a vertical oscillator with the loss angle $\phi_v = \phi_{str} + \phi_{sur} + \phi_{thermoel}$, the thermal noise along this direction is given by eq. 4.38:

$$S_v^y(\omega) = \frac{4k_B T\omega_v^2}{m\omega[(\omega^2 - \omega_v^2)^2 + \omega_v^4\phi_v^2(\omega)]}\phi_v(\omega) \tag{4.67}$$

where ω_v is the vertical resonant frequency, given by:

$$\omega_v^2 = \frac{k_v}{m} = \frac{\mathcal{E}S}{ml} \tag{4.68}$$

being m the mass of the test mass, k_v the vertical elastic spring constant, $\mathcal{E}$ the Young's modulus, S and l respectively the section and the length of the suspension wire. The amount of vertical thermal noise coupled in the horizontal direction is given by:

$$S_v^x(\omega) = \theta_0 S_v^y(\omega) \tag{4.69}$$

From eq. A.7 and A.8 we can write the strain equivalent spectral density of the coupled vertical thermal noise in the L-long arm of the interferometer as follows:

$$\tilde{h}_v(\omega) = \frac{2\theta_0}{L}\sqrt{S_v^y(\omega)} \tag{4.70}$$

4.3.3 Violin-modes

In a real mechanic suspension, the wires are not ideal massless springs but extended bodies, which vibrate in the transversal direction: since the two ends of the wires are fixed, these vibrations can be described as standing waves in a string between two fixed points, so that they are defined *violin-modes* (see fig. 4.6).

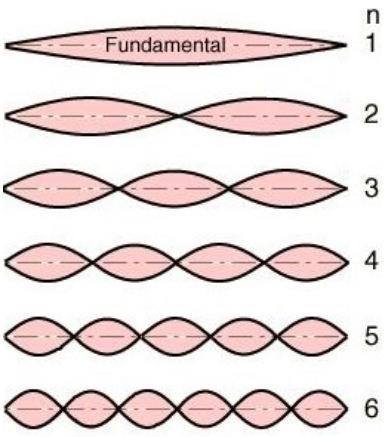

Figure 4.6: Standing waves in a string are a good representation of the vibrational violin-modes. The fundamental mode $n = 1$ and the first five overtones are shown.

For frequencies $\omega \gg \omega_p$, the thermal noise produced by these vibration modes is dominant with respect to that of pendulum mode and, although violion-modes are weakly coupled to the horizontal direction in the interferometer, their resonant frequencies are usually inside the detection bandwidth, at some hundreds Hz. The

expansion theorem [129] allows the decomposition of the overall vibration motion in normal modes, since their off-resonance contribution is negligible: by considering the wire as an unidimensional system along x, with length l and linear mass density $\rho_l(x)$, there are $\varphi_n(x)$ transversal vibration modes, given the normalization condition:

$$\int_0^l \rho_l(x)\varphi_m(x)\varphi_n(x)dx = \delta_{mn} \tag{4.71}$$

so that the displacement $y(x,t)$ is given by the superposition:

$$y(x,t) = \sum_{n=1}^{\infty} \varphi_n(x)\xi_n(t) \tag{4.72}$$

where $\xi_n(t)$ are the generalized coordinates of the n-th mode. Let us define the generalized force $G_n(t)$ associated to that mode in terms of the force density $f(x,t)$:

$$G_n(t) = \int_0^l f(x,t)\varphi_n(x)dx \tag{4.73}$$

Now we can write the equation of motion in terms of generalized coordinates and forces:

$$\ddot{\xi}(t) + \omega_n^2\xi_n(t) = G_n(t) \tag{4.74}$$

A force $F(t)$, applied at the end of the wire in $x = l$, can be written by means of eq. 4.73 as follows:

$$G_n(t) = F(t)\varphi_n(l) \tag{4.75}$$

Therefore, from eq. 4.74, taken in the frequency domain and including the damping term, we find:

$$\xi_n(\omega) = \frac{F(\omega)\varphi_n(l)}{\omega_n^2 - \omega^2 + i\phi_n(\omega)\omega_n^2} \tag{4.76}$$

The resonant frequency ω_n of the n-th mode, when the wire undergoes a tension $\top$, is given by [134]:

$$\omega_n = \frac{\pi n}{l}\sqrt{\frac{\top}{\rho_l}}\left[1 + \frac{2}{k_e l} + \frac{1}{2}\frac{n^2\pi^2}{k_e^2 l^2}\right] \tag{4.77}$$

where $k_e \equiv k_e(\omega_n)$ is the elastic flexural stiffness, which depends on the Young's modulus $\mathcal{E}$ and on the moment of inertia of the wire cross section I:

$$k_e(\omega_n) = \sqrt{\frac{\top + \sqrt{\top^2 + 4\mathcal{E}I\rho_l\omega_n^2}}{2\mathcal{E}I}} \tag{4.78}$$

while the loss angle of the n-th mode, appearing in eq. 4.76, is defined by:

$$\phi_n(\omega) = \phi_w(\omega)\frac{2}{k_e l}\left(1 + \frac{n^2\pi^2}{2k_e l}\right) \tag{4.79}$$

where $\phi_w(\omega)$ is the loss angle associated to the dissipation processes in the wire, i.e. $\phi_w(\omega) = \phi_{str}(\omega) + \phi_{sur}(\omega) + \phi_{thermoel}(\omega)$. As for the loss angle of the fundamental

mode of pendulum (see eq. 4.58), the violin-mode loss is a small fraction of that of the wire material itself. By substituting eq. 4.76 into eq. 4.72, at $x = l$ we obtain:

$$y(l,\omega) = \sum_{n=1}^{\infty} \frac{F(\omega)\varphi_n^2(l)}{\omega_n^2 - \omega^2 + i\phi_n(\omega)\omega_n^2} \tag{4.80}$$

therefore, the transfer function is:

$$\mathcal{T}(\omega) = \sum_{n=1}^{\infty} \frac{\varphi_n^2(l)}{\omega_n^2 - \omega^2 + i\phi_n(\omega)\omega_n^2} \tag{4.81}$$

and substituting the previous eq. 4.81 into eq. 4.5 we find the PSD of thermal noise associated to the internal oscillations of the extended system:

$$S_{con}(\omega) = 4k_B T \sum_{n=1}^{\infty} \frac{\varphi_n^2(l)\omega_n^2}{\omega[(\omega_n^2 - \omega^2)^2 + \phi_n^2(\omega)\omega_n^4]}\phi_n(\omega) \tag{4.82}$$

If we consider the pendulum wire as a continuous system with uniform mass density ρ_l and a point mass m attached at $x = l$, the normalization condition of eq. 4.71 becomes:

$$\rho_l \int_0^l \varphi_n^2(x)dx + m\varphi_n^2(l) = 1 \tag{4.83}$$

while the eigenfunction $\varphi_n^2(x)$ in $x = l$ is:

$$\varphi_n^2(l) = \frac{2\rho_l l}{\pi^2 m^2}\frac{1}{n^2} \tag{4.84}$$

By substituting the previous relation 4.84 in eq. 4.82, we find the thermal noise of violin-modes:

$$S_{viol}(\omega) = \frac{8k_B T\rho_l l}{\pi^2 m^2} \sum_{n=1}^{\infty} \frac{1}{n^2} \frac{\omega_n^2}{\omega[(\omega_n^2 - \omega^2)^2 + \phi_n^2(\omega)\omega_n^4]}\phi_n(\omega) \tag{4.85}$$

where ω_n and ϕ_n are given by eq. 4.77 and 4.79. In an ideal wire the stiffness is negligible, so that, taking the tension $\top = mg$, we can rewrite ω_n as follows:

$$\omega_n = \frac{\pi n}{l}\sqrt{\frac{mg}{\rho_l}} \tag{4.86}$$

that substituted in eq. 4.85 gives:

$$S_{viol}^{ideal}(\omega) = \frac{8k_B T\rho_l^2 l^3}{\pi^4 m^3 g}\frac{1}{\omega}\sum_{n=1}^{\infty}\frac{\phi_n(\omega)}{n^4} \tag{4.87}$$

Since test masses in the interferometer are suspended by means of N wires or fibers, the overall thermal noise due to violin-modes is given by eq. 4.85 multiplied by N:

$$S_{viol}^{tot}(\omega) = N \times S_{viol}(\omega) \tag{4.88}$$

where usually $N = 4$. From eq. A.7 and A.8 we find the strain equivalent spectral density of violin-modes thermal noise in the L-long arm of the interferometer:

$$\tilde{h}_{viol}(\omega)\frac{2}{L}\sqrt{S_{viol}^{tot}(\omega)} \tag{4.89}$$

4.4 Thermal noise in a mirror

Internal vibrational modes of the bulk of the test mass (see sec. 4.4.1) define the mirror thermal noise which limits the detector sensitivity. Other temperature-dependent noise sources in the mirror are the shape deformation due to the so-called thermal lensing (see sec. 4.4.2), and the thermodynamical fluctuations in the bulk and in the coating [135].

4.4.1 Bulk-modes

The normal modes of a cylindrical body, assumed to have an aspect ratio ~ 1, are characterized by a rather complicated shape. Such a system can be treated with an unidimensional approach by weighting each mode by a factor that describes the mean motion of the central part of the frontal surface of the body along the optic axis [129]. If we assume that the optical axis is aligned with the center of mass of the cylinder, we can use the expansion theorem as we did in sec. 4.3.3, in order to separate n modes of vibration. The eigenfunctions $\varphi_n(x)$ of the modal expansion can be defined by the mirror mass m as follows:

$$\varphi_n^2 \approx \frac{2}{m_n^e} \tag{4.90}$$

where m_n^e is the effective mass of the n-th normal mode of vibration. The thermal noise PSD can be found similarly to the calculation of sec. 4.3.3; since the resonant frequency of the n-th bulk mode ω_n is usually larger than frequencies of the detection band, we can write the PSD with in the following approximation [129]:

$$S_{bulk} \approx \frac{8k_BT}{\omega} \sum_{n=1}^{\infty} \frac{\phi_n(\omega)}{m_n^e \omega_n^2} \tag{4.91}$$

The strain equivalent spectral density can be obtained as usual from eq. A.7 and A.8, taking into account the n-th mode that has the maximum amplitude.

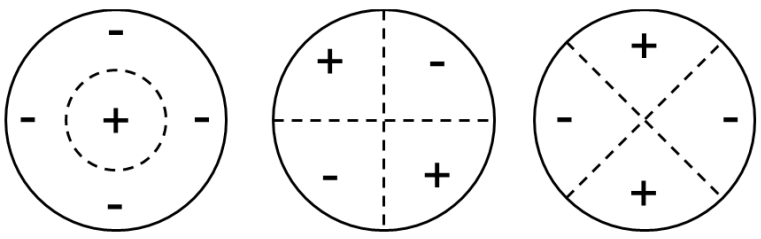

Figure 4.7: Schematic representation of the most important bulk modes of the test mass, seen on the frontal surface. From left: fundamental "drum mode", "butterfly + mode" and "butterfly × mode".

4.4.2 Thermal distortions

Part of the laser beam power circulating in the Fabry-Perot cavity of the interferometer is absorbed either by the coating or by the substrate of the mirror, in correspondence with, and according to the shape of the laser spot. The thermal heating on the test mass, produced by this absorption, distorts the mirror profile and, in turn, the wavefront of the reflected laser beam, producing a *geometric distortion* (or thermoelastic deformation) of the reflective surface. Moreover, the thermal gradient generated through the coating and substrate results in a gradient of the refractive index n dependent on the temperature: the so-produced change in the optical path is defined *thermal lensing* effect. Both the distortions can be described with the schematic model [136] represented in fig. 4.8.

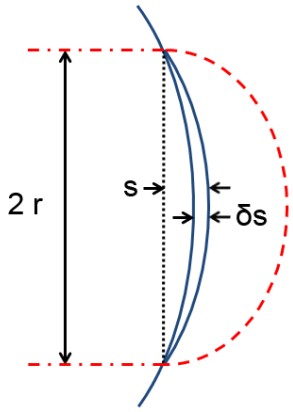

Figure 4.8: Geometric distortion of the mirror curvature due to the heating caused by the laser, resulting in the thermal lensing effect.

Geometric distortion

Let us consider a mirror with curvature radius R, suspended and kept in vacuum condition. If an orthogonally incident laser beam, with a spot radius r, heats the surface of the test mass, the ratio between the heat dissipated by radiation and that removed through conduction $\mathcal{R}$ is:

$$\mathcal{R} \approx 4\sigma T^3 \epsilon \frac{r}{\kappa} \tag{4.92}$$

where σ is the radiation constant of the body, ϵ the emissivity coefficient, r the beam radius and κ the thermal conductivity of the substrate material. In the substrate material the dominant mechanism is the conduction, so that the ratio $\mathcal{R}$ is usually $\sim 10^{-1}$. The power absorbed in the hemisphere corresponding to the laser beam spot, where the temperature gradient is maximum, is given by:

$$P_a = \kappa A \nabla T \approx 2\pi r^2 \kappa \frac{\delta T}{r} \tag{4.93}$$

where $A = 2\pi r^2$ is the area through which the heat flows and δT is the temperature drop across the hemisphere. The heating due to the power absorption causes a

variation of the sagitta s, which is geometrically defined as:

$$s \approx \frac{r^2}{2R} \tag{4.94}$$

and a change of δs through thermal expansion:

$$\delta s \approx \frac{1}{2}\alpha r \delta T \tag{4.95}$$

where α is the thermal expansion coefficient. By combining eq. 4.95 and 4.93 we find:

$$\delta s \approx \frac{1}{4\pi}\frac{\alpha}{\kappa}P_a \tag{4.96}$$

From eq. 4.96 it is clear that a crucial parameter of the substrate material is the ratio α/κ, that is reported in table 4.1 at room temperature for the typical materials used in the interferometers: fused silica, sapphire and silicon. Note that both α and κ depends on the temperature T, as it is clear in fig. 4.9 in the case of a silicon sample.

Material	α/κ ($\times 10^{-8} m/W$) at room temperature
Fused silica	$\sim$ 33
Sapphire	$\sim$ 28
Silicon	$\sim$ 1.67

Table 4.1: The ratio between thermal expansion and thermal conductivity coefficients at room temperature for the materials used for the mirrors of interferometric detectors [136].

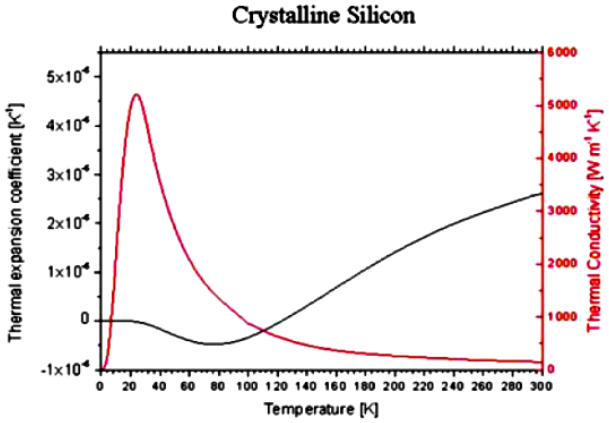

Figure 4.9: Thermal conductivity $\kappa(T)$ and thermal expansion coefficient $\alpha(T)$ of a crystalline sample of silicon, depending on the temperature T.

Thermal lensing

The refractive index n is usually temperature-dependent, so that the temperature gradient in the heated volume of substrate and coating acts as a spurious lens, deforming the wavefront and changing the optical path (see fig. 4.11). This change, calculated similarly to that in eq. 4.96, corresponds to the equivalent sagitta variation:

$$\delta s \approx \frac{1}{2}\beta r \delta T \approx \frac{1}{4\pi}\frac{\beta}{\kappa}P_a \tag{4.97}$$

where $\beta = \partial n/\partial T$ is the temperature-dependence of the refractive index n. Eq. 4.97 corresponds to eq. 4.96 with $\beta \to \alpha$, so that we can directly compare the two effects. Since the values of β are usually greater than α (see the reported values of β/κ in tab. 4.2), the thermal lensing effect in coating and in substrate is dominant with respect to the geometric distortion. We note that also this effect depends on the temperature, since $\kappa = \kappa(T)$: in fig. 4.10 the temperature-dependent thermal conductivity of fused silica, sapphire and silicon are compared.

Material	β/κ ($\times 10^{-7} m/W$) at room temperature
Fused silica	~ 300
Sapphire	~ 6
Silicon	~ 3.5

Table 4.2: The ratio between the temperature-dependence of refractive index $\beta = \partial n/\partial T$ and thermal conductivity coefficient at room temperature for the materials used for the mirrors of interferometric detectors [136, 137].

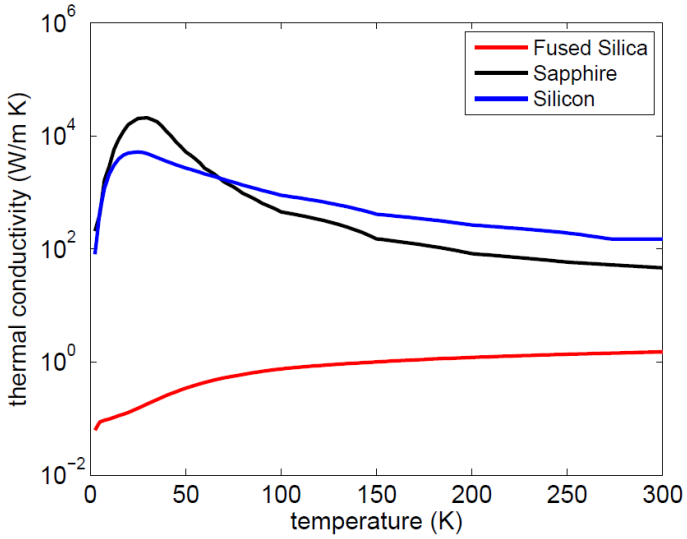

Figure 4.10: Temperature-dependent thermal conductivity $\kappa(T)$ of fused silica, sapphire and silicon [26].

In eq. 4.96 and 4.97 we note that the optical path variation produced by the laser heating on the mirror is proportional to the power absorbed P_a. Therefore, geometric deformation and thermal lensing, if not corrected, introduce a theoretical limit to the maximum circulating power in the cavity:

$$P_{max} = \frac{4\pi\kappa(T)}{\beta} \frac{\delta s}{1.3\mathcal{A}_{sub} d + 0.5\mathcal{A}_{coat} N_{eff}} \tag{4.98}$$

where $\mathcal{A}_{sub}$ and $\mathcal{A}_{coat}$ are respectively the absorption per unit length of the substrate and that per unit reflection of the coating, d is the thickness of the mirror and $N_{eff} = 2F/\pi$ the number of effective reflections, obtained from the finesse F of the Fabry-Perot cavity. Moreover, from eq. 4.96 and 4.97 we note that laser power fluctuations induce a component of noise in the optical direction [69]. Although the distortion effects can be corrected by means of compensative heating (e.g. the thermal compensation system in Virgo, see sec. 2.3.1), a complementary method to reduce such distortions is the cooling of the test masses, made of suitable materials, since the thermal conductivity depends on T.

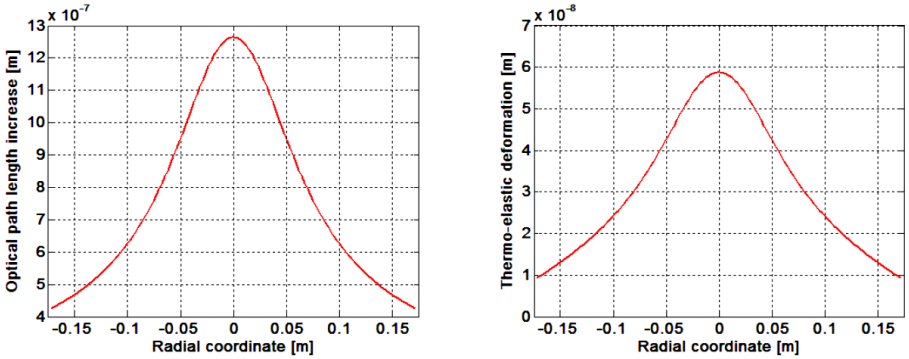

Figure 4.11: The optical path length change due to thermal lensing (left panel) and geometric distortion (right) produced by the laser power absorption in substrate and coating of test masses. These values have been computed for Advanced Virgo (see sec. 2.4.1 and ref. [78]).

4.5 Thermal noise suppression

All the dissipation processes analyzed in this chapter directly depends on the temperature T, so that the amplitude spectral density of the overall noise produced by thermal dissipations is:

$$\tilde{x}^{tot}_{ther} \propto \sqrt{T} \tag{4.99}$$

Moreover, also thermal distortions, such as the thermoelastic deformation and the thermal lensing, which depends on the thermal conductivity $\kappa(T)$, are temperature-dependent. Therefore, an effective reduction of thermal noise can be achieved by means of a **cryogenic payload** in future interferometer detectors, as already done with the prototype interferometer CLIO [92], tested on the Virgo-like cryogenic

payload prototype [138], and planned in KAGRA (see sec. 2.4.2 and ref. [91]) and in ET (sec. 2.5.1 and ref. [26]). The best candidate materials for cryogenic payloads are sapphire and silicon, whose low α and high κ at low temperatures reduce the thermal effects and speed-up the cooling process.

The cryogenic system must be able to extract tens of mW of heat from the mirror during the working steady state, taking also into account the additional heating produced by the high power laser circulating in the cavities of the interferometer. As shown in sec. 2.5, two main strategies have been considered so far: closed-loop pulse-tube cryocoolers and cryogenic fluids, such as liquid helium. In fig. 6.1 it is shown a simple scheme of the cryogenic payload during interferometer operations, when a fraction of the laser power is absorbed by the mirror ($\dot{Q}_{las}$), subsequently flows through the monolithic suspension fibers and is extracted by the refrigerating system in the upper stages of the payload; in the represented configuration, the mirror reaction mass acts also as a thermal shield, since there are not extra thermal inputs on it.

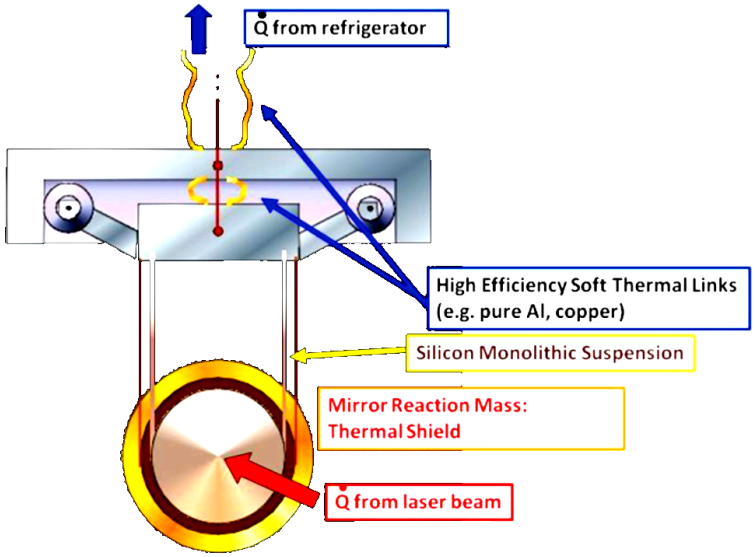

Figure 4.12: The conceptual scheme of a cryogenic last stage of suspension for test masses [26].

At the thermal equilibrium the power extracted by the cryocooler is equal to that absorbed by the mirror, i.e. $\dot{Q}_{abs} = \dot{Q}_{cooler}$, so that the heat flows through the suspension fibers (or wires), and is removed by the heat links (made in Al/Cu) connected to the refrigerator. In this condition, given the environmental temperature T_{env}, the mirror reaches the equilibrium temperature T_{mir}, that is given by:

$$\tilde{Q}_{abs} = \frac{4a}{l}\langle\kappa_i\rangle(T_{env} - T_{mir}) = \frac{1}{Z_{th}}\Delta T \tag{4.100}$$

where a and l are the section and the length of suspension fibers (or wires), Z_{th} is the thermal impedance and κ_i is the average value of the thermal conductivity, defined as follows:

$$\langle\kappa_i\rangle = \frac{1}{\Delta T}\int_{T_{env}}^{T_{mir}} \kappa_i(T)dT \tag{4.101}$$

However the cryocooling of test masses is not a trivial implementation, since the introduction of cryostats surrounding the vacuum chambers requires an adequate design; moreover the additional vibrations that such a system produces must be taken into account. This argument will be treated experimentally in chapter 6.

Part III

Experimental Activity

Chapter 5

Characterization of an underground site for ET

For a third generation underground interferometer capable of precise astronomical studies of gravitational wave sources, such as the Einstein Telescope (ET), the critical frequency region is in the range of $0.1 - 10\ Hz$, where the seismic noise is variable mainly due to microseismic and anthropogenic activities. Therefore, it is important to select a site location which is, at the same time, characterized by a low microseismic noise and far from human activities. As shown in chapter 3, below $1\ Hz$ the seismic noise is strictly correlated to the oceanic (or sea) dynamics and to weather conditions, while for $f > 1\ Hz$ the noise floor is nearly flat in remote sites (as clear in the NLNM curve of fig. 3.1), corresponding to a displacement spectrum with f^{-2} frequency-dependence after a double integration. Among the theoretical and experimental activities to be performed for the construction of ET, the seismic characterization of potential sites plays a key role. In previous years, a first short-period characterization was made across Europe, identifying four potential sites, as reported in the ET conceptual design study [26]. Long-period measurements and microseismic studies are the next step toward the final site selection.

In this chapter I introduce the motivations of the search for an underground site in Sardinia and the local geological features. After that, I present my experimental work on the characterization of the Sos Enattos former mine, from the construction of a seismic underground array to the long-period data analysis. In particular, I wanted to study the seismic noise stability over a long period of almost one year, and the correlation of the microseismic activity with the sea activity and local weather conditions. The results of this work are very promising and suggest further detailed studies of the site, which can be an ideal location for the construction of ET.

5.1 Motivation for an underground site in Sardinia

Sardinia is a seismically quiet island, the second largest in the Mediterrenean sea. Unlike the Italian mainland, where is placed the gravitational wave interferometer Virgo, Sardinia lies entirely in the Eurasian tectonic plate, far from active fault lines, so that it is characterized by a noticeable geological stability (see fig. 5.1). Moreover, the population density of the island is low compared to other regions of Europe (see fig. 5.3), resulting in a reduced day/night cultural noise PSD ratio, while the mean wind speed is not too high with respect to other European locations (see fig. 5.4). For the reasons outlined above, Sardinia appears an ideal location in Europe for an interferometer of third generation.

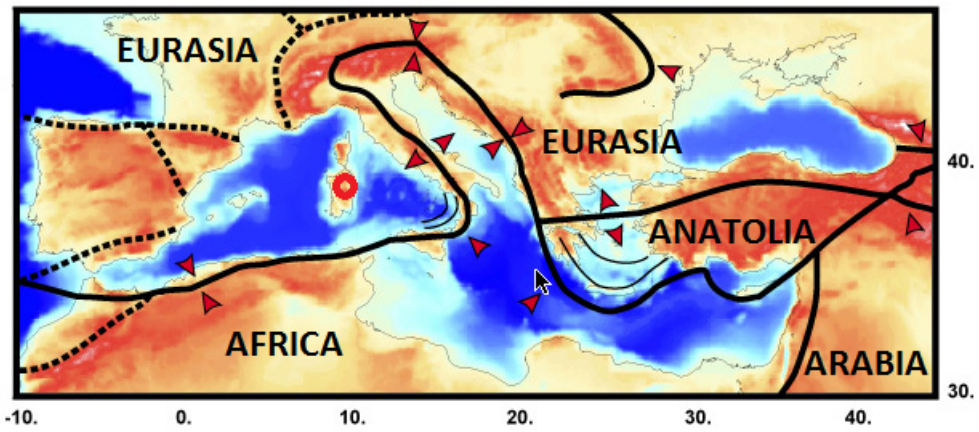

Figure 5.1: Tectonic plates and main fault lines in the southern Europe. The red arrows indicate the tectonic movements, while the red circle shows the position of the Sos Enattos site in the island of Sardinia, placed into the Eurasian plate.

Figure 5.2: Position of Sos Enattos underground site (yellow pointer) in the north-west Sardinia.

Initially, the search for a suitable underground site was focused in the basaltic zone in the west area of the island, but the requirement to locate the experimental site in a zone not too far from a modern motorway, plus the possibility to rely on previous geological studies, moved the search toward the oriental zone of Sardinia, that is the most ancient part of the island (see sec. 5.2 and fig. 5.6), and then the most geologically stable. In that area a promising underground site was found in Sos Enattos (see fig. 5.2), a former mine which appears to be compliant with the low seismic background requirements of a third generation gravitational wave interferometer. The detailed map of the site is reported in fig. 5.5, where a circle of radius $r = 10\ km$ indicates the possible excavation area for the Einstein Telescope.

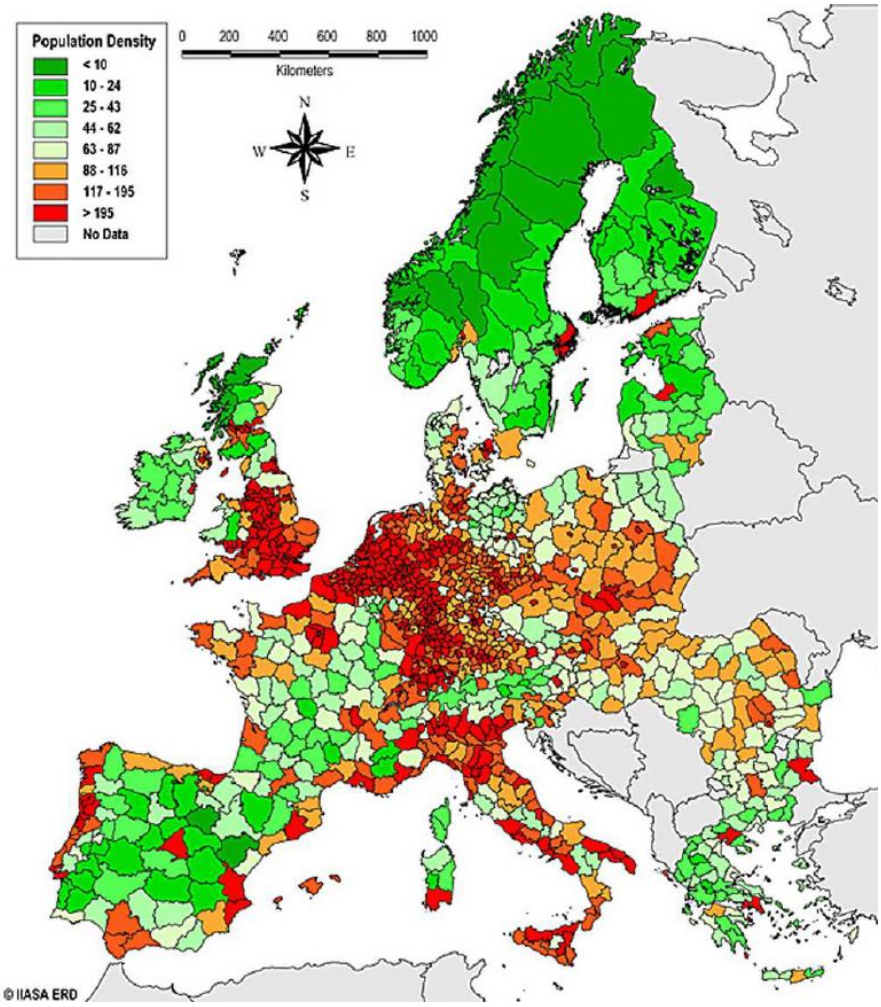

Figure 5.3: Density of population in Europe from the REGIO database of Eurostat [26]; low densities result in reduced cultural noise in the $1-10\ Hz$ frequency band.

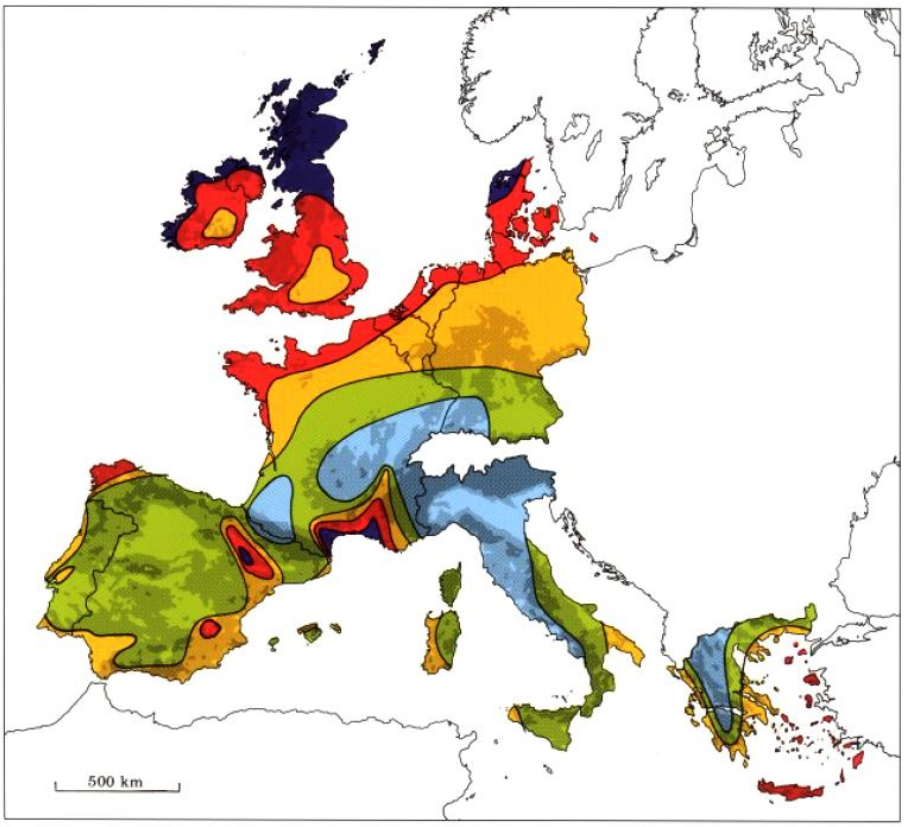

Wind resources[1] at 50 metres above ground level for five different topographic conditions

	Sheltered terrain[2]		Open plain[3]		At a sea coast[4]		Open sea[5]		Hills and ridges[6]	
	$m\,s^{-1}$	Wm^{-2}	$m\,s^{-1}$	Wm^{-2}	$m\,s^{-1}$	Wm^{-2}	$m\,s^{-1}$	Wm^{-2}	$m\,s^{-1}$	Wm^{-2}
	> 6.0	> 250	> 7.5	> 500	> 8.5	> 700	> 9.0	> 800	> 11.5	> 1800
	5.0-6.0	150-250	6.5-7.5	300-500	7.0-8.5	400-700	8.0-9.0	600-800	10.0-11.5	1200-1800
	4.5-5.0	100-150	5.5-6.5	200-300	6.0-7.0	250-400	7.0-8.0	400-600	8.5-10.0	700-1200
	3.5-4.5	50-100	4.5-5.5	100-200	5.0-6.0	150-250	5.5-7.0	200-400	7.0- 8.5	400- 700
	< 3.5	< 50	< 4.5	< 100	< 5.0	< 150	< 5.5	< 200	< 7.0	< 400

Figure 5.4: European wind resources based on data collected for the European Wind Atlas [26, 139].

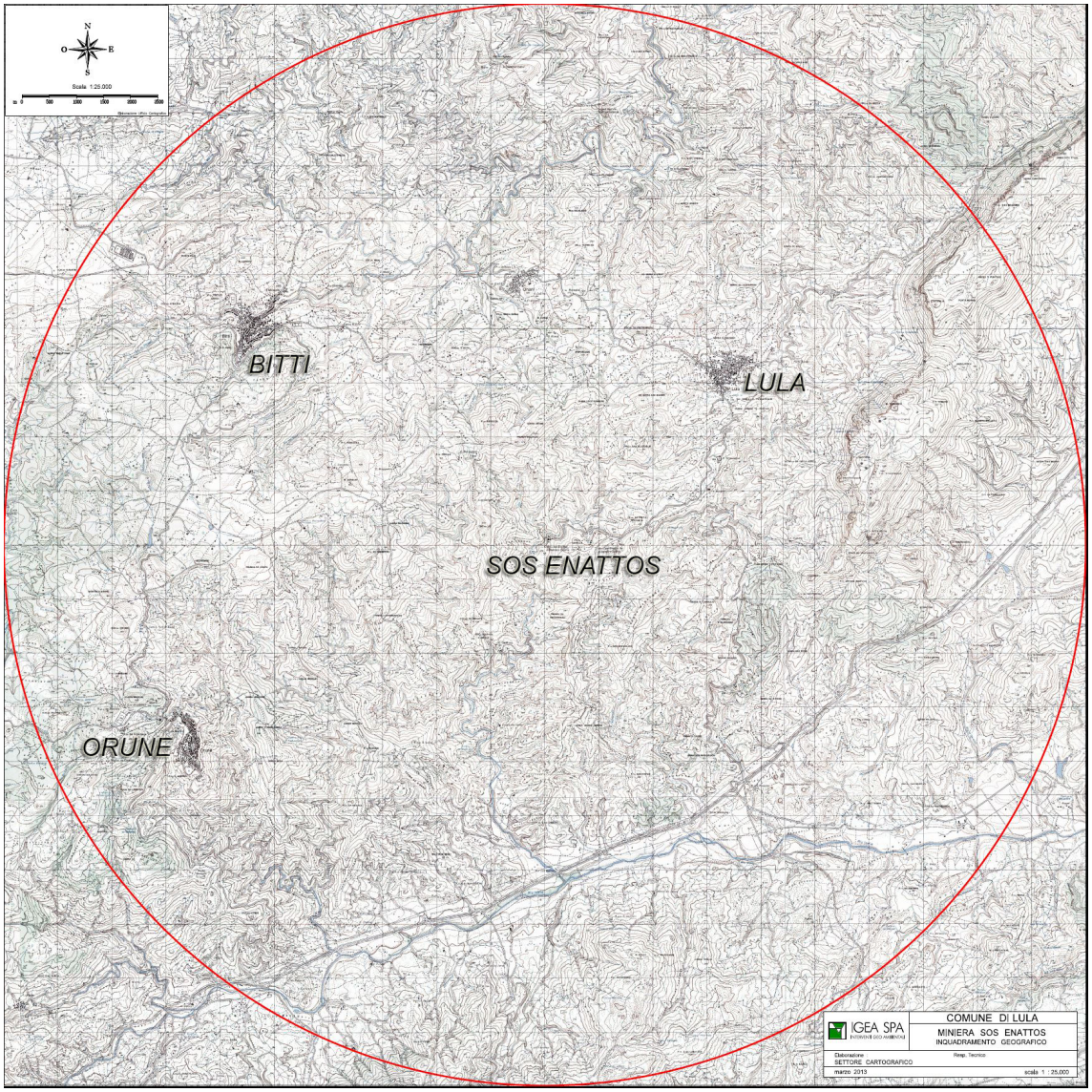

Figure 5.5: Detailed map of the Sos Enattos area; main villages near the former mine are indicated. The site is accessible through the SS 131 d.c.n. highway. A red circle, centered on the mine entrance and with a radius of $r = 10\ km$, indicates the possible excavation area for the Einstein Telescope. Courtesy of IGEA S.p.A.

5.2 The geology of Sardinia and of the Sos Enattos mine

Sardinia is a region seismically quiet located in the European tectonic plate, far from the edge of many fault lines. The island is constituted by an ancient continental landmass (the *Sardinia-Corsica block*), isolated and partially dismembered from its Alpine orogeny, which explains its low seismic activity. It is largely formed by rocks of the Paleozoic era or, to be more precise, dating back to the Cambric and Silurian eras[1]. During the Carboniferous period the corrugation of the earth provoked the rising of great magmata land masses hence the intrusion of granite. The solidification of the magma formed the foundations of the island and, furthermore, it was the transformation of the fragmented rock of a complex of scissions of clay, quartz, porphyry and others that cloaked the underlying granite. During the geological phase of Alpine orogeny, quakes devastated the land, causing the fragmentation of the Paleozoic and Mesozoic crusts in various areas. A series of fractures formed tectonic fissures that divided the island longitudinally into two unequal parts; one oriental, mountainous and continuous, the other occidental divided into smaller parts by minor fissures. From the quaternary deposits, the canal that separated the oriental and occidental parts of the island was filled, forming fields. During the quaternary period Sardinia became similar in its aspect to what we see today with only minor changes occurring in more recent times. The island is classically divided into two geological domains, the *Sardinia Alpina* and the *Sardinia Hercynian* (i.e. Sardinia of the *Paleozoic era*):

- Sardinia Alpina occupies the western half of the island with the exception of the north-west (NW) and south-west (SW) extremities, characterized by the massive outcrops of Paleozoic and Nura-Sulcis Iglesiente. Tertiary volcanic and sedimentary rocks have accumulated in two main structures: the *Oligomiocene Rift* in the regions of Sassari and Marmilla and the *Graben Plio-Quaternary* in the Campidano region.

- The Hercynian Sardinia, as well as in two massive outcrops just mentioned, extends in the eastern half of the island. It consists of Paleozoic metamorphic rocks with Hercynian deformation and a large intrusive complex of coal with a variable composition.

The central-eastern sector of the region is characterized by a rugged morphology in particular in the zone dominated by carbonate rocks. The Albo mountain stretched for about fifteen miles to the north-east (NE), and has peaks over 1000 m. It is bordered on the south-east (SE) from the valley of Siniscola and to the west by a plateau of the Manno river. In the northerly direction, blocks degrade and show a stark contrast between the morphological rounded shapes developed in the metamorphism and those of granite, which are most rugged. In the east-south-east of the valley of Siniscola, the aspect of the landscape is hilly with sharp contrast between the forms of granitoids and metamorphic ones.

[1] the Sardinian basement, formed in the Paleozoic era, is one of the oldest geological formations of the central and southern Europe.

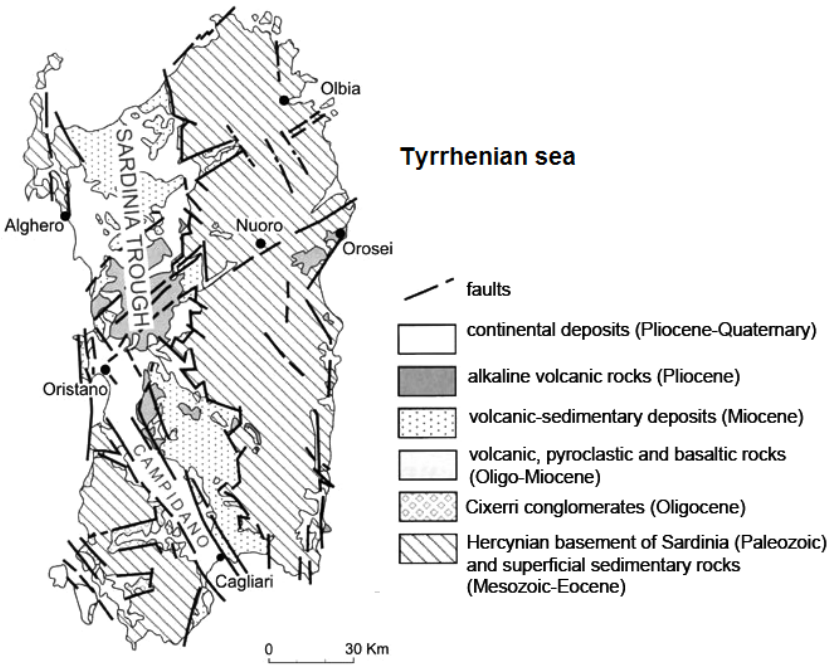

Figure 5.6: Geological map of Sardinia. The Hercynian basement, formed during the Paleozoic era, is the oldest part of the island.

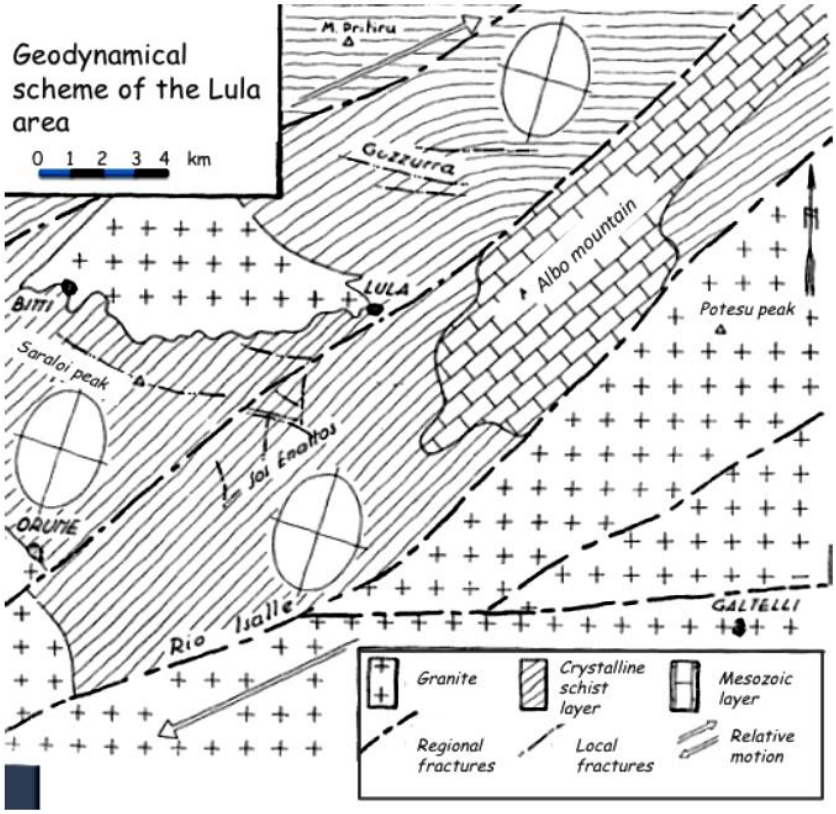

Figure 5.7: Geodynamical scheme of the land around Sos Enattos former mine.

The Sos Enattos mine is located in this area, $\sim 40\ km$ far from the city of Nuoro, in the municipality of the Lula village; it easily accessible via the motor way connecting the Bitti village to the *131bis* highway of Sardinia (see fig. 5.5). The area of Sos Enattos is hosted by Paleozoic metamorphic terrains, which are part of the broader *inclined roof* within the Hercynian granites of Sardinia. At the south edge of the area, this *roof* is covered by deposits of a carbonate platform due to a series of tectonic events at lower pressures during the Tertiary age. The tectonic transposition caused a significant homogenization of the original lithological types and a full distribution of each fossil, so that it is difficult to reconstruct the original stratigraphic sequence. However, the age of the crystalline-schist layer is definitely pre-Hercynian. This layer shows an uniform behavior with respect to mechanical stress, while the carbonaceous phyllite, are more plastic of the other formations. In other words, we observe a bending of the carbonaceous layers and the absence of fractures. The existing few fractures have been studied with great attention because sometime they are filled with minerals that can be exploited by the mining industry. Their location and characteristics are also interesting in our study because their spatial distribution influences the seismic wave propagation and reflection. The location of the fractures in the Lula territory is reported in figure 5.7.

Around Monte Albo territory there are few old mines[2] and one of them is Sos Enattos. This mine of schist rocks composed of sphalerite ([Zn,Fe]S) and galena (PbS), was exploited to extract lead and zinc. The mine history starts in 1864 and the end of its exploitation is dated 1996. The mine age (more than 100 years) is a guarantee for the stability over long terms also in presence of long caverns in a deep underground environment. The site is managed by the I.G.E.A. s.p.a. company, which guarantee the safety access to the mine.

Finally, we note that the Sos Enattos area is characterized by a very low anthropic activity: in general the population density in the Albo mountain area is low and in the Lula's territory goes up to 10 $habitants/km^2$, a factor ~ 7 lower than the mean value for Sardinia[3].

[2]Sardinia has also an old mining history started probably around the 6th millennium BC with the mining of obsidian exported to Southern France and Northern Italy. After the Italian unification in 1861 lead and silver, by then the most extracted minerals on the island, were added to a third one, zinc. The quality of the mineral was very high: while in the rest of the world the average silver revenue for $100kg$ of lead was swaying around $200 - 300\ gr$, in the Sardinia mine an average of $1\ kg$ for $100\ kg$ was achieved. Today, this *silver* era is far. The mining activity is going through an harsh crisis, which seems to be irreversible for all the mines in Sardinia. Many other mines are closed and the Geomineral Park of Sardinia, founded in 1989, and supported by UNESCO, today preserves the ancient mines and the ex mining villages that are become examples of industrial archeology.

[3]The mean population density of the 28 nations of European Union is 116 $habitants/km^2$.

5.3 The experimental set-up

There are two main access of the Sos Enattos mine (see fig. 5.8), both of them are located well above the sea level (a.s.l.). The first access is a vertical pit equipped with a lift, the second one is a long tunnel (called *rampa Tupeddu*) used for transporting by car, in the past the workers with their mine tools, at present tourists and scientists with their instrumentation.

Figure 5.8: The two main access of the Sos Enattos mine: on the left the tunnel *rampa Tupeddu*, on the right the vertical shaft.

The tunnel entrance is at +338 m a.s.l.; near this point the weather station Vantage Pro II[4] was installed (see fig. 5.9). It includes a rain collector, an anemometer for measuring the velocity and the direction of the wind, and the sensors of the atmospheric pressure and temperature. Temperature and humidity sensors are enclosed in a radiation shield to protect against solar and other sources of radiated and reflected heat, improving accuracy. The meteorological data is acquired by a monitoring station set-up inside a container at ground level.

Figure 5.9: *Left*: the weather station installed next to the tunnel entrance; *right*: the meteorological data-acquisition system set-up into the ground-level station. This station is connected to the underground seismic stations by means of optical fiber links.

In the mine there are two seismic stations distributed along the access tunnel of the mine. Both of them are connected by 1.3 km-long optical fiber link to the tunnel entrance, where the meteorological station is located.

[4]it is a commercial weather station made by the US company Davis.

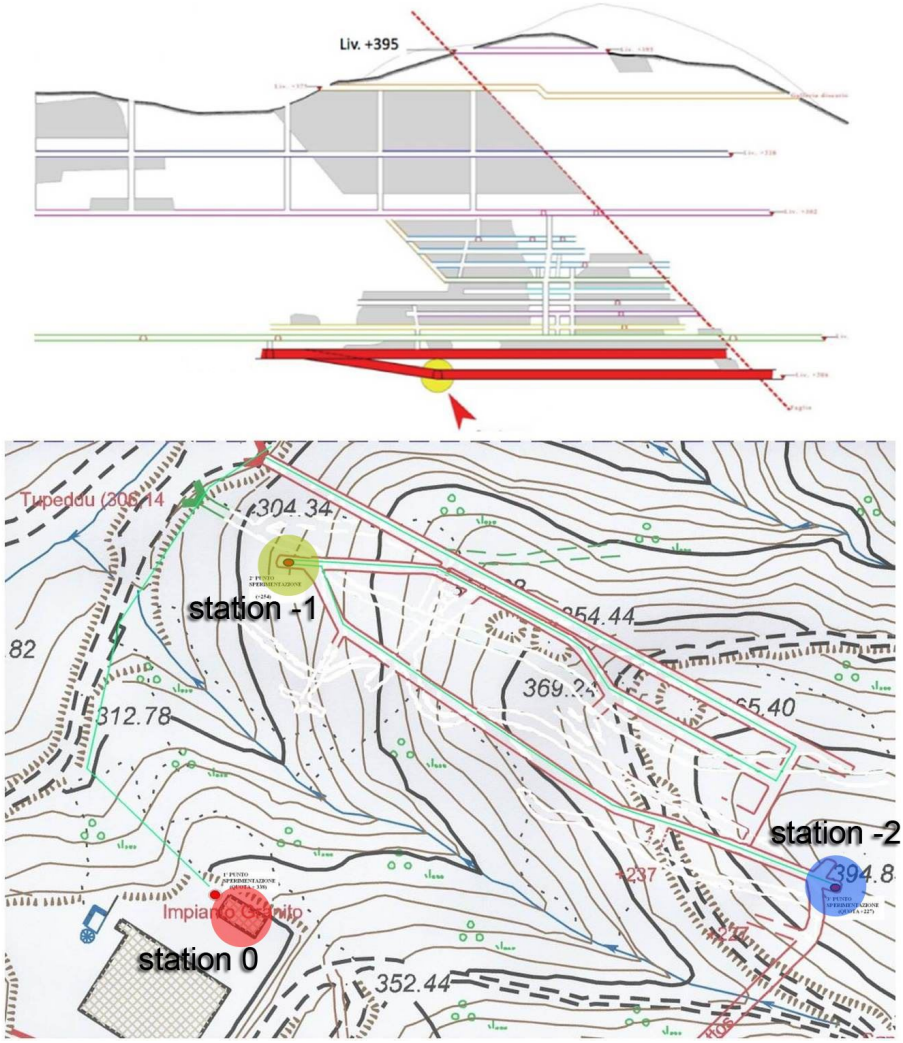

Figure 5.10: On the top: the vertical cross-section of the mine, showing the location of the deeper seismic station (red arrow/yellow spot); below: the locations of the ground (red circle) and underground (yellow and blue circles) seismic stations on the mine map.

The first underground seismic station (*station -1*, fig. 5.11) is located at +254 m a.s.l. and 800 m far from the entrance of the mine tunnel. A polyurethane wall protects the station from the acoustic disturbances and limits the small thermal drift observed in the mine[5]. This location is equipped with horizontal seismometers built at the university of Salerno [140]. This kind of sensor is a horizontal folded pendulum, carved from a monolithic block of the Aluminium Alloy 7075-T6, that can be configured as accelerometer (in a configuration with an applied feed-back force) or, when no feed-back is applied, as a seismometer with a large band at low-frequency ($10^{-7} - 10\ Hz$). In the Sos Enattos mine the sensors are operated

Figure 5.11: The underground station -1. The horizontal seismometers built at the university of Salerno [140] are placed on a plinth cemented to the bedrock, and enclosed into insulation boxes (one opened in the left, the other closed in the right).

as seismometers in open feed-back loop and are equipped with laser optical lever readout achieving a sensitivity of ($2 \times 10^{-11}\ m/\sqrt{Hz}$) in the frequency range $0.01 - 10\ Hz$, a value few order of magnitude lower than the quiets seismic location [141]. They are set in an enclosed box to limit the thermal drift and acoustic coupling.

The deeper seismic station is located at +227 m a.s.l. and 1100 m far from the tunnel entrance (see fig. 5.10). I selected one of the caves along the tunnel access and there I built a wall doublet, made of polyurethane and mineral-wool layers, in order to insulate the cave entrance to the tunnel access (see fig. 5.12). In the inner part of the cave I anchored to the mine bedrock a granite plinth using a concrete mix with sand and fine grit. In this way the contact between the ground and the plinth was increased and it provides a near-level surface for installing the seismometer.

[5]The thermal excursion in one year of observation is $\pm 1\ ^{\circ}C$.

Figure 5.12: Insulation and instrumentation of station -2 in Sos Enattos, from top-left to bottom-right: a) the granite plinth, leveled and cemented on the bedrock; b) the cave before the insulation; c) the first insulation wall, made of polyurethane and mineral-wool layers; d) the second insulation wall, also made of polyurethane; e) the outer room between the two insulation walls, before the installation of the DAQ and power instrumentation; f) installation of seismometer Trillium 240 (indicated by the circle), placed on the plinth, inside the inner room: the sensor is enclosed in a thermal shield plus an external insulation box.

Here the sensor is a tri-axial seismometer Trillium 240 by *Nanometrics Inc.* (see app. B). The instrument is shielded from air currents and temperature fluctuations by covering it with a thermal shield. In addition, the system is enclosed in a second box made of wood with the inner walls padded with 5 *cm* polystyrene slabs.
The sensor cable exits the seismometer enclosure at the base of the instrument: it runs loosely from the inner to the outer chamber of the cave preventing the vibrations from being transmitted along the cable. In the outer chamber of the cave I placed the data acquisition system *Taurus*, made by Nanometrics Inc., that collects and store the data in the local memory. The *Taurus* is connected to the local network via an Ethernet-optical fiber link switch, so that it is possible to monitor the data acquisition process and retrieve the collected data on the computer located in the surface station. In order to avoid power surges and to ensure a stabilized[6] power supply to the instrumentation, I installed a buffer battery, connected in parallel to a DC generator through inductive filters.

The Trillium 240 has a symmetric triaxial arrangement of the sensing elements. The use of three identical axis elements ensures the same frequency response for vertical and horizontal outputs, it guarantees true orthogonality of the three outputs and a minor dependence of its response to rapid changes in temperature. The orthogonal outputs are elaborated to extract the information related to the cardinal directions. On the mounting surface of the sensor a North-South line is traced and the seismometer is aligned with the marked direction. Thus, the x-output of the seismometer is proportional to the East-West displacement of the ground, while y is related to the North-South direction and z to the vertical movement. The input-ouput transfer function of each channel has a frequency response flat from few mHz to 5 Hz and it rolls off at 40 $dB/decade$ below the lower corner frequency. The acceleration power spectral density (PSD) of the Trillium 240 intrinsic noise is shown in figure 5.14, where it is compared to the Peterson's new low-noise and high-noise models (NLNM and NHNM) [99]. The noise floor shown is the typical level of instrument self-noise given a proper installation. The comparison ensures that the Trillium 240 is a sensor suitable for monitoring microseismic noise below the NLMN limit in a wide interval of the frequency bandwidth of the instrument.

Each seismic station is equipped with an environmental monitoring system. The pressure, humidity and temperature sensors provide digital and fully calibrated output, which allows for easy integration in a data acquisition system without the need for additional calibration. They are characterized by an excellent long term stability and makes them ideal for our long term sensing application.

5.4 Environmental measurements

During the operation of the first generation of gravitational wave detectors it was noted that the meteorological status of the site influences the detector performance. In particular, in presence of bad weather the root mean square (R.M.S.)

[6] power surges may introduce a non-negligible component of electric noise in the sensor output.

Figure 5.13: The data acquisition system Taurus (on the left), in a temporary setup next to the seismometer Trillium 240 (placed into the external insulation box, on the right side), during the sensor installation.

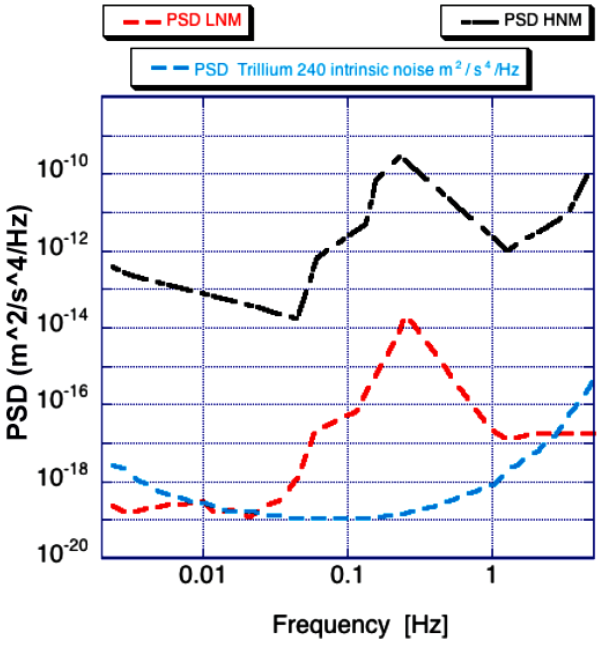

Figure 5.14: Typical curve of the intrinsic noise spectrum of the Trillium 240 seismometer (blue dotted line) compared to the Peterson's [99] NLNM and NHNM models (red and black dotted lines). On the vertical axis is reported the acceleration noise spectrum measured in $m^2/s^4/Hz$.

value of seismic motion in the frequency band below the mirror suspension cut-off increases. As a consequence, the dynamics of the feed-back control loop of the mirror suspension is limited and the interferometer unlocks more often, reducing the detector duty cycle. This behavior is observed mainly during windy days and it is partially due to the random stress applied by the wind to the buildings hosting the interferometer mirrors. In an underground laboratory this effect should be reduced but, since the requirement of new interferometer is to achieve a displacement sensitivity an order of magnitude higher than that of the advanced detectors, we still need to verify how the seismic noise can be affected by the weather change. For this reason, we monitored continuously the weather variables at the mine entrance.

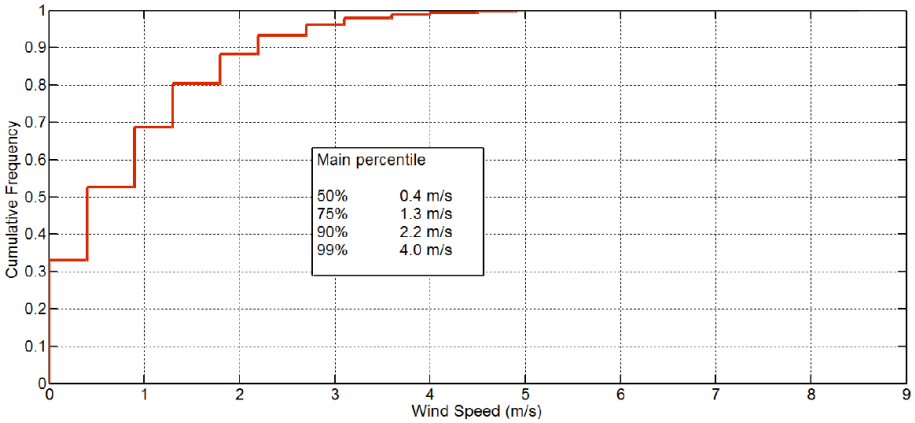

Figure 5.15: Cumulative distribution of the wind velocity based on data taken during one year of measurements.

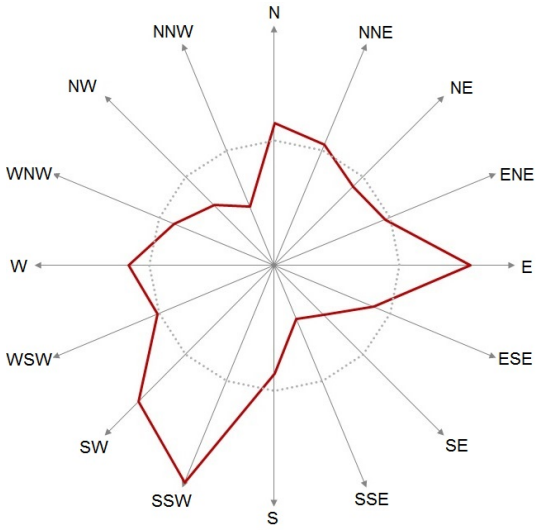

Figure 5.16: Polar representation of the wind direction based on data taken during one year of measurements. The hypothetical isotropic distribution is represented by the gray circle.

The weather in Sos Enattos is rather stable: as an example in figure 5.15 we show the cumulative distribution of the wind velocity monitored in one year of observation (2012-2013). The plot shows that for the 50% of the time the wind is in practice absent (the wind velocity is below 0.5 m/s) and for the 99% the site is hit just by a light or a moderate wind, increasing up to a velocity of 4 m/s (a moderate breeze).

In fig. 5.16 I report the polar representation of the wind direction based on the same data of the previous plot. Here it is evident the effect due to the local orography, in particular to the Albo mountain, the 20 km long barrier extended in the NE-SW direction (135° - 315° respect to the N direction)[7].

As I will show in the next section, the meteorological status of the sea is an other important element to be considered in connection with the seismic activity of the mine site. The most common measuring devices of the sea status are based on the record of both vertical and horizontal accelerations of a floating buoy and pressure in the water columns. Then, satellite observation are routinely used today, based mainly on techniques as altimetry and synthetic aperture radar imagery. Moreover, since the late 1950s numerical wave models have been developed, it is also possible to infer the spectral decomposition of the sea state and the propagation direction of each wave component. The surface of the sea is discretized in a grid made of points, which are separated by 100 km for a global scale prevision, but these may be only a few meters apart near the coasts. *Nettuno* [142] is the wind-wave forecasting system with the highest resolution currently operating in the Mediterranean sea (7 km for the wind and $4 - 5$ km for the waves). It is based on the regional (WAM) and nearshore (SWAN) wave models [143, 144]. It allows to describe with great accuracy the evolution and breakdown of the fields along the coasts in a broad frequency spectrum. The model has been calibrated and validated using data taken in-situ and using the *EnviSat Radar Altimeter* observations both in the Mediterranean sea [145] and Atlantic ocean [146].

At each of these points the program manages the evolution of the energy of all the spectral components. *Nettuno* uses 36 directions and 30 wave frequencies between $0.05 - 0.793$ Hz. This means that at each point of the sea we are dealing with 36 times 30 variables that have to be evolved.

On the base of a formal agreement between the university of Rome "Sapienza" and the Weather National Center of the Italian Air Force (CNMCA), we have access to the several output values, updated each three hours by the *Nettuno* model. The list of the available variables is reported in the table 5.1.

These data are collected in four different point of the Tyrrhenian sea: two of them are near the oriental cost of the Sardinia, while the others are ~ 10 km far from it (see figure 5.17 and table 5.2). The related data format is described at the end of app. B.

[7]Near the entrance the access tunnel is oriented NNW, i.e. 332° respect to the north direction

Significant height of combined wind waves and swell [m]
Mean wave direction $[deg]$
Mean value of the wave frequency $[Hz]$
Wind speed $[ms^{-1}]$ (10 m space resolution)
Wind direction $[deg]$ (10 m space resolution)
Wave frequency of the highest peak in one-dimensional spectrum $[Hz]$
Coefficient of drag with waves
Mean sea level u component of wind $[ms^{-1}]$
Mean sea level v component of wind $[ms^{-1}]$

Table 5.1: List of the variables derived by the *Nettuno* model provided by CNMA.

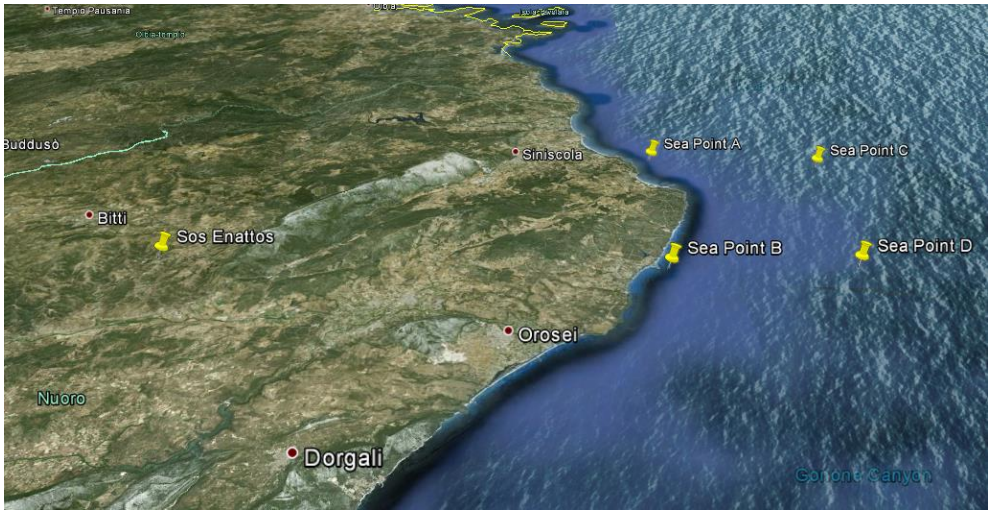

Figure 5.17: Map of the Sardinia cost near the mine site. On the map I marked the location of Sos Enattos and the four points to infer the meteorological status of the sea.

Point	Coordinates (latitude and longitude)	Depth [m]	Distance [m] (from Sos Enattos)
A	$40°32'60.00''N$ $9°48'00.00''E$	< 10	31308
B	$40°27'00.00''N$ $9°48'00.00''E$	< 10	29112
C	$40°32'60.00''N$ $9°56'60.00''E$	155	43416
D	$40°27'00.00''N$ $9°56'60.00''E$	134	41840

Table 5.2: The four points chosen to monitor the sea status: position, sea depth and distance from Sos Enattos (*Rampa Tupeddu* tunnel entrance).

5.5 Seismic measurements

In order to demonstrate immediately the potential gain in sensitivity for a gravitational waveinterferometer built in Sos Enattos, I show in fig. 5.18 the overlap of two curves: the first one is the displacement noise spectrum measured near the north building of the Virgo interferometer during a day of good meteorological condition [147]. The second curve is one of the typical displacement noise spectrum measured by the Trillium 240[8] located in the deepest station of the Sos Enattos mine. Note that at the frequency of 1 Hz the noise reduction is a factor ~ 200; at higher frequencies the Sos Enattos seismic noise continue to decrease roughly as the square of the frequency inverse, and the noise reduction increases. This first result complies with the ET-LF requirement of $5 \times 10^{-9}\ m/f^2$ and is two orders of magnitude better than that of ET-HF (see app. C). In fig. 5.19 is shown the comparison between the seismic spectra measured in the two underground stations during a very stormy day, when the contribution due to superficial Rayleigh waves is higher, in order to evaluate the differences at the two depths. Despite the high microseismic noise, also in this case the seismic level at 1 Hz corresponds to a displacement $< 10^{-8}\ m/\sqrt{Hz}$; the two spectra are very similar since the difference in depth is less than 30 m, therefore in this case the depth-attenuation is not so evident.

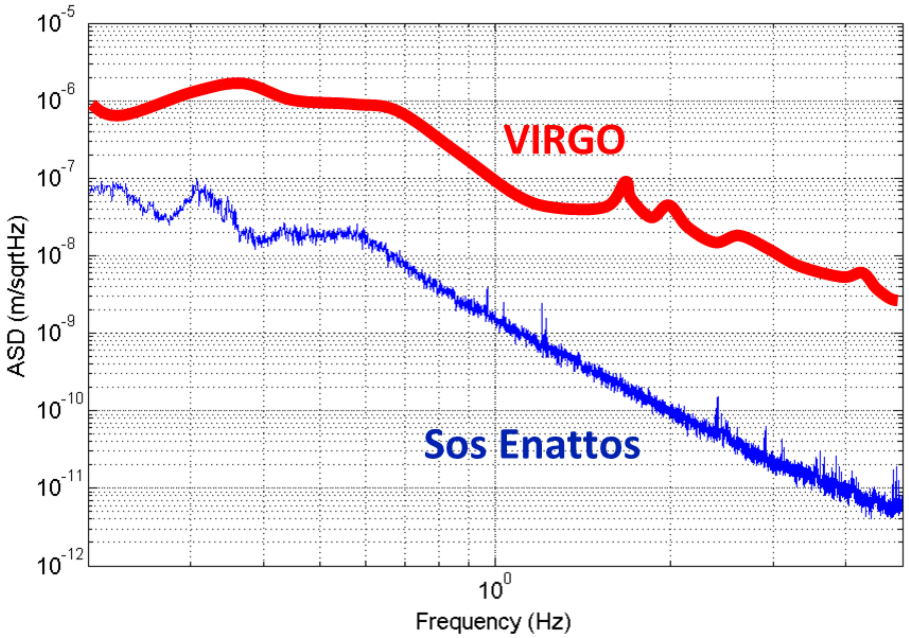

Figure 5.18: Typical displacement noise spectra measured in the Sos Enattos mine compared to that measured near the North building of the Virgo interferometer in a day with optimal meteorologic condition.

Although the gain in the noise reduction around $f = 1\ Hz$ is satisfactory, it is not sufficient to qualify the Sos Enattos site for a new gravitational wave

[8]data elaboration for the Trillium 240 seismometer is discussed in app. B

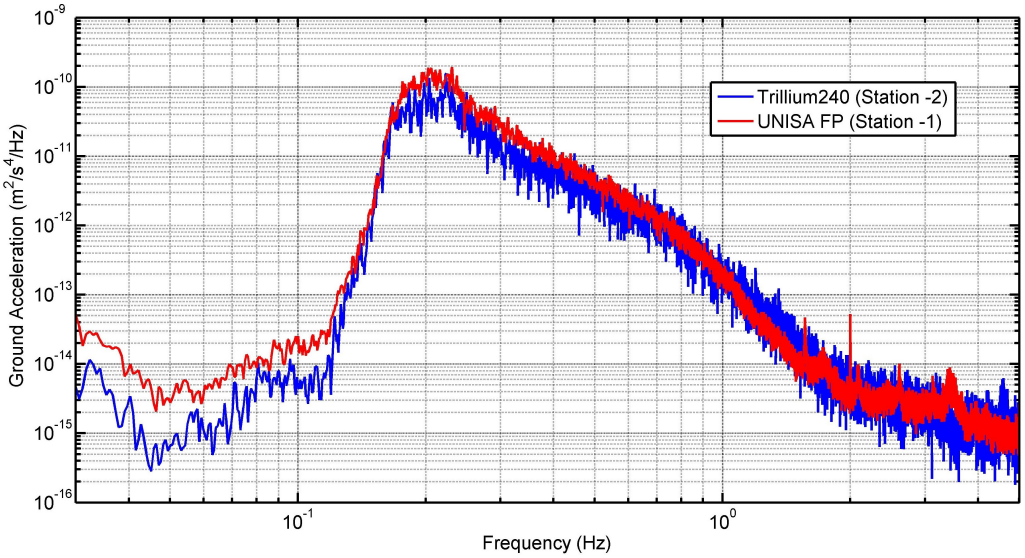

Figure 5.19: The power spectral density of the acceleration (averaged over few hours) measured in the Sos Enattos mine during a very stormy day at the station -1 (with the seismometer developed by the University of Salerno [140]) compared to that measured at the station -2 with the Trillium 240 seismometer. The difference in depth between the two stations is $< 30\ m$, therefore the attenuation is not so evident. During this measurement the two sensors had not a common timing. Courtesy of F. Acernese.

underground detector installation. As stated before, we need to assess the level of non-stationarity of the spectrum. In particular we have to monitor the part of the spectrum below 1 Hz. This band is the major contribution to the R.M.S. motion of the test mass, which must be kept in position by the feed-back control of the interferometer: a high R.M.S. value is a limiting factor of the feedback dynamics. In fig. 5.20 I show the power spectral density of the acceleration measured in the deepest station of the Sos Enattos mine in the suitable frequency range of the Trillium 240[9]: the shape of the spectrum is similar to that obtained by Peterson in the NLNM model [99] and the three directional components are similar, except for few peaks. We can subdivide the spectrum in two regions:

- between 0.03 and 0.17 Hz there are clustered peaks of the power spectrum. In this frequency range, the noise classified as *microseismic* is due to non-local causes, and generally it depends on large-scale meteorological conditions[10].

[9] i.e. in the frequency range where the intrinsic noise of the Trillium 240 is lower than the Peterson's NLNM (see fig. 5.14).

[10] At lower frequencies, out of the Trillium 240 bandwidth, the Earth ground experiences the large external forces due to the gravitational attractions of the Moon and Sun (see sec. 3.1.4). The tidal motion has amplitudes of about 0.5 m with respect to the center of the Earth, but it occurs in a frequency range of 10^{-5} Hz and determines a quasi-coherent movement of the interferometer test masses. The quadrupolar gravitational wave signal will be detected at much higher frequencies and the residual tidal effect due to the tide anisotropy is easy compensated by a feed-forward system [148].

- Above 0.17 Hz a broad band resulting from the envelop of several broad peaks is present. During the long period of the monitoring process I observed that this part of the spectrum shows a non-stationary behavior correlated to the change of the meteorological and sea conditions.

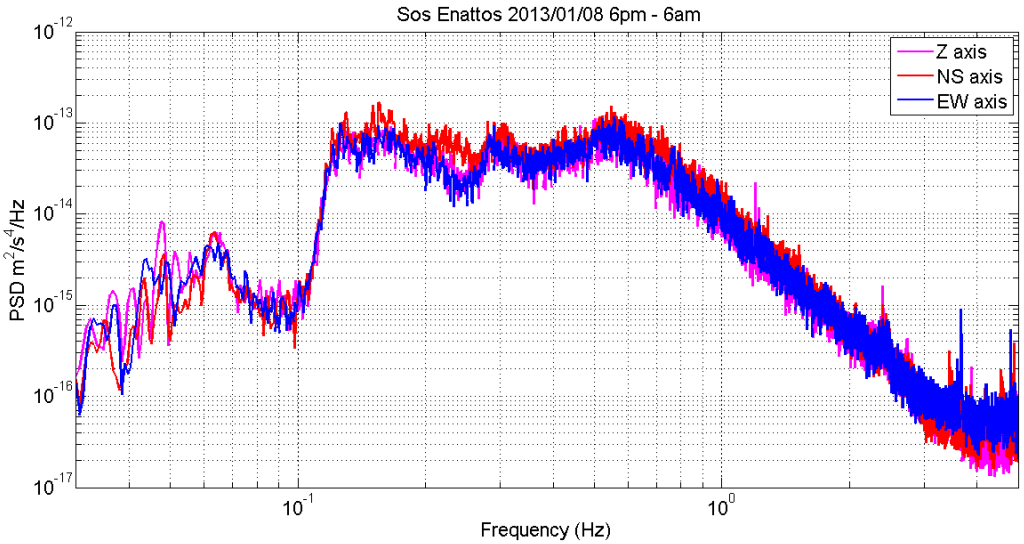

Figure 5.20: The power spectral density of the acceleration measured in the Sos Enattos mine during a day of good weather: Z (purple line) is the vertical component, NS (red line) is the component along the North-South direction and EW (blue line) is the component along the East-West direction.

During stormy days the microseismic broad band grows up almost two order of magnitudes as it is shown in the fig. 5.21. However, in the frequency range above 1 Hz, i.e. in the detection bandwidth of third generation gravitational wave detectors, the change of PSD value is just a factor two (see fig. 5.22). In fact, in this frequency range and above we expect that the micro-tremor noise is related mainly to the *anthropogenic* activity (cultural noise).

5.5.1 Peaks identification

The primary oceanic microseismic peak, produced by pressure variations and wave impacts on the continental shores, is expected to be generated at $f_p^{oc} \approx 7{\times}10^{-2}\ Hz$, while the oceanic secondary peak, related to the stationary wave generated by the interference of reflected oceanic waves, appears at $f_s^{oc} = 2 \times f_p^{oc}$, i.e. at about 0.14 Hz (see sec. 3.1.3). In a continental site, at a significant distance from inland seas, the oceanic secondary peak is clearly distinguishable in a typical low frequency spectrum [149]. The situation is more complicated at Sos Enattos mine, which is located on an island, roughly 30 km from the eastern shoreline: in this case the oceanic secondary peak is enveloped into a more complex spectral structure composed of the envelope of primary and secondary microseismic peaks generated by the Tyrrhenian sea, and to a lesser extent, by other sectors of Mediterranean

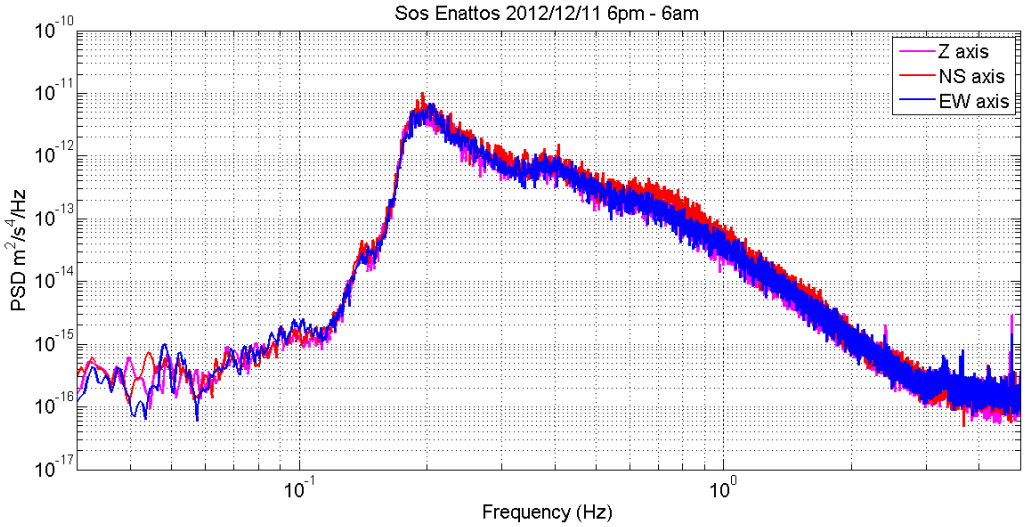

Figure 5.21: The power spectral density of the acceleration measured in the Sos Enattos mine during a stormy day: Z (purple line) is the vertical component, NS (red line) is the component along the North-South direction and EW (blue line) is the component along the East-West direction.

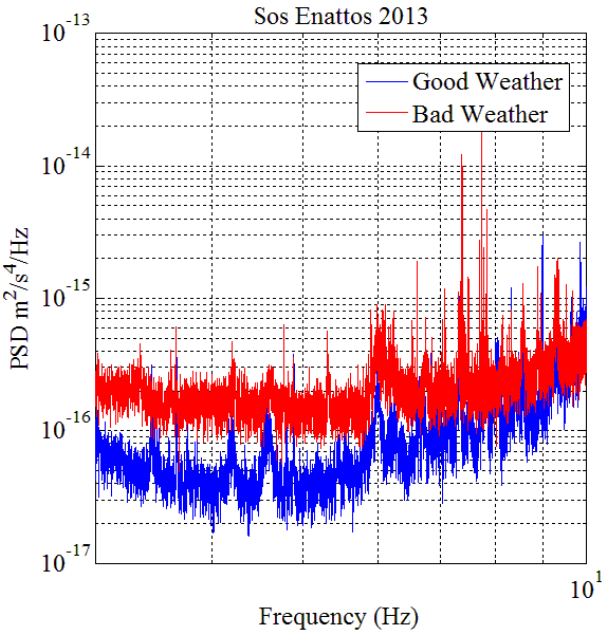

Figure 5.22: Power spectrum of the acceleration noise, measured in the deepest station of Sos Enattos, within the detection bandwidth $(3 - 10\ Hz)$ of a third generation gravitational wave interferometer. The spectra taken in good and bad weather conditions are compared.

sea[11] (see sec. 5.5.3). In order to identify the sea-generated peaks, I compared the frequencies obtained by the *Nettuno* model (see tab. 5.2), provided by CNMA, with those observed in the microseismic envelope. However, since this part of the spectrum varies significantly day by day, or to be more precise, with a time scale of the order of few hours, the identification must be performed on a case by case basis. I show in fig. 5.23, 5.24 and 5.25 three examples of the microseismic envelope generated by the sea. Usually the stationary wave-produced secondary peak of the sea is dominant, but sometimes the primary sea peak, produced by pressure variations of the water columns and by the impact of the wind-generated waves and swell on the island shore, results to be of the same order of magnitude of the secondary peak. Moreover, at higher frequencies a tertiary peak is observed in some cases, maybe produced by the stationary wave in another sector of the sea or by a local resonant mechanism. As a general reference, I list in tab. 5.3 the main microseismic peaks resulting from the analysis of the spectra acquired in Sos Enattos from July 2012 to June 2013. The correlation between the microseismic power amplitude and the wind-generated waves is analyzed in sec. 5.5.3.

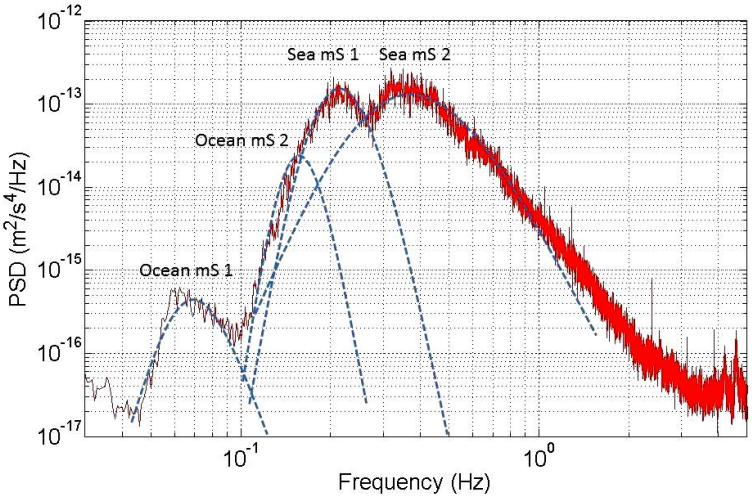

Figure 5.23: The microseismic envelope in the power spectrum of the acceleration noise measured in the deepest station of Sos Enattos, in good weather condition. The positions of the main oceanic and sea-generated peaks are indicated. In this case the primary and secondary peaks from produced by the sea have a similar amplitude and hide the secondary peak from the ocean.

5.5.2 Local weather effects

Apparently the noise increase in the frequency range $0.1 - 1\ Hz$ seems to be correlated to the local wind velocity and to the lowering of the atmospheric pressure. The effect is more evident if we focus our analysis on the data taken at the end of autumn, a period of time characterized by unstable weather condition. In fig. 5.26

[11] the northern and western shorelines are at $\sim 80\ km$ from Sos Enattos, while the southern coast is $\sim 140\ km$ far.

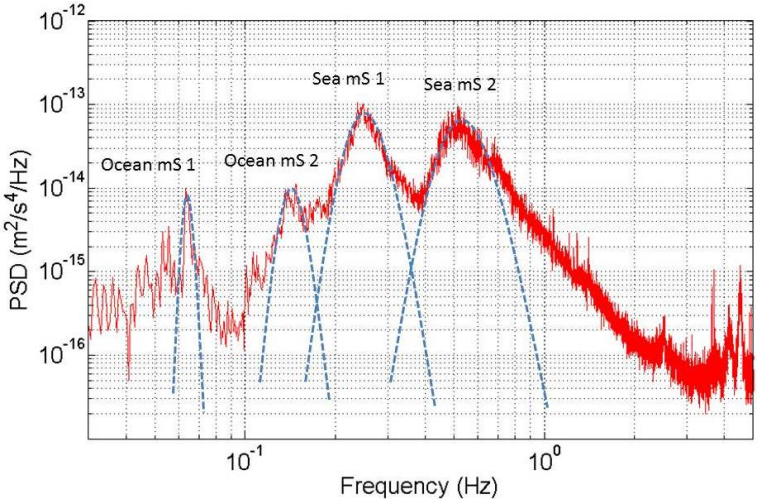

Figure 5.24: The microseismic envelope in the power spectrum of the acceleration noise measured in the deepest station of Sos Enattos, in bad weather condition. The positions of the main oceanic and sea-generated peaks are indicated. In this case all the primary and secondary peaks from the oceans and the Mediterranean sea are clearly distinguishable.

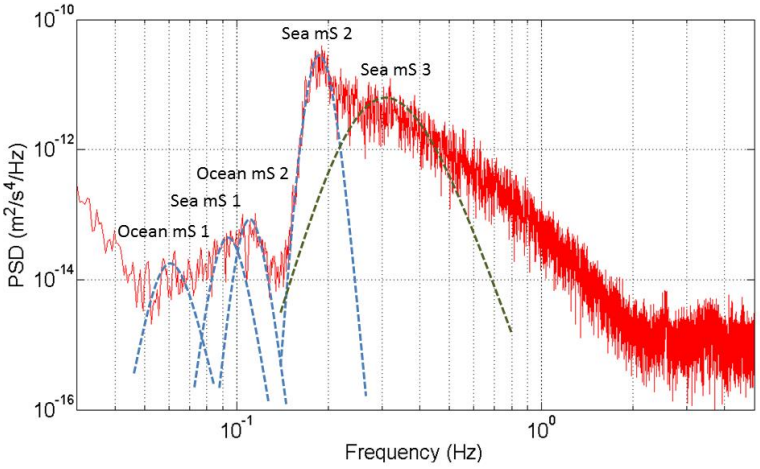

Figure 5.25: The microseismic envelope in the power spectrum of the acceleration noise measured in the deepest station of Sos Enattos, in bad weather condition. The positions of the main oceanic and sea-generated peaks are indicated. In this case the sea-generated primary peak frequency is very close to that of the oceanic secondary peak, while the sea-generated secondary peak is dominant. At higher frequency a tertiary peak appears, related to another sector of the sea or to a local resonance.

Peak	Source	Mechanism	Frequency [Hz]
Primary	Oceans	Pressure variations, wave impact on shores	$6 - 9 \times 10^{-2}$
Secondary	Oceans	standing wave	$0.12 - 0.20$
Primary	Tyrrhenian sea	Pressure variations, wave impact on shores	0.08-0.23
Secondary	Tyrrhenian sea	standing wave	$0.16 - 0.46$
Tertiary	Mediterranean (?)	standing wave or local resonance	$0.27 - 0.63$

Table 5.3: Main microseismic peaks observed in Sos Enattos. A tertiary peak appears sometimes, maybe produced by standing waves in another sector of Mediterranean sea. The microseismic amplitude is discussed in sec. 5.5.3.

I show the history plot of the wind vector velocity measured at the mine entrance versus time and the corresponding acceleration noise in the mine integrated in the frequency range $0.1 - 3\ Hz$. An analogue plot is shown in the fig. 5.27 for the atmospheric pressure.

In order to clarify if the wind is the direct cause of the seismic noise increase in the deep mine, I selected three days of observation. The corresponding history plots of this time period are shown in the figures 5.28 and 5.29. In the first plot the wind velocity increase is delayed with respect of the seismic noise. However, in the same plot we note the presence of a wind velocity peak at the time $t_w = 12\ h$, which could be interpreted as a precursor of the systematic worsening of the meteorological condition. The precursor peak appears nearly 6 hours before the seismic noise increase. In the second plot 5.29, the pressure drop anticipates the seismic noise increase of nearly 10 hours and it seems to be correlated with the $12 - 13\ h$ peak of the wind velocity spectrum, the precursor of the weather worsening.

The delays of several hours rule out a direct relation between the wind stress on the rocks of the hill hosting the mine and the seismic noise. In the following subsection, analyzing the spectral content of both the seismic noise and the offshore waves, I show that the observed effect is related to the status of the sea on the oriental coast of Sardinia.

5.5.3 Sea influence on the microseism

The height of combined wind-generated waves and swell is one of the parameters derived by the *Nettuno* model provided by CNMA (see tab. 5.1), and can be used as a quantitative measure of the sea status. In fig. 5.30 I show the history plot of the sea wave height, measured in the four points listed in tab. 5.2, versus the corresponding acceleration noise in the deepest station of the mine integrated in the frequency range $0.1 - 3\ Hz$, for a period of about one month.
In the history plot I used synchronized data, i.e. a zero time delay. This fact is justified by the distance between the coast and Sos Enattos mine (see table 5.2)

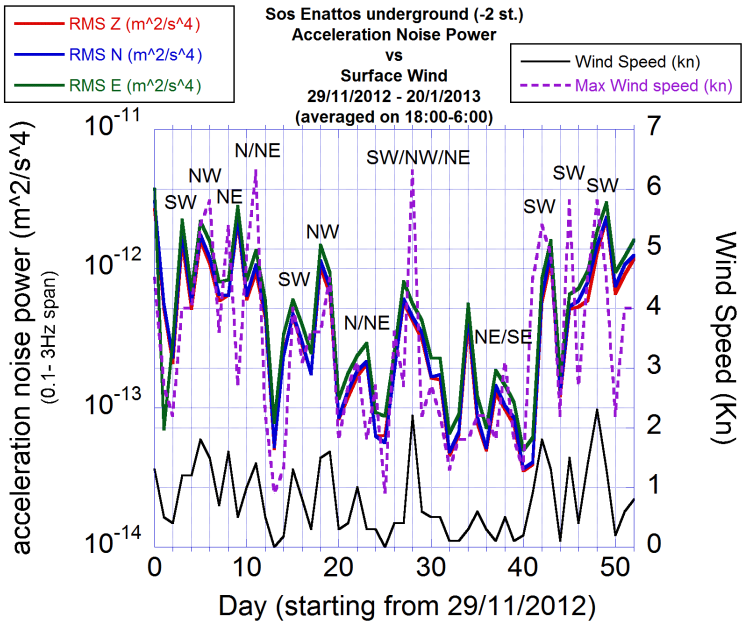

Figure 5.26: Average and maximum wind speed (in knots) measured at the mine entrance versus time and the corresponding spectral acceleration noise in the mine integrated in the frequency range $0.1 - 3\ Hz$. The direction of wind gusts is indicated.

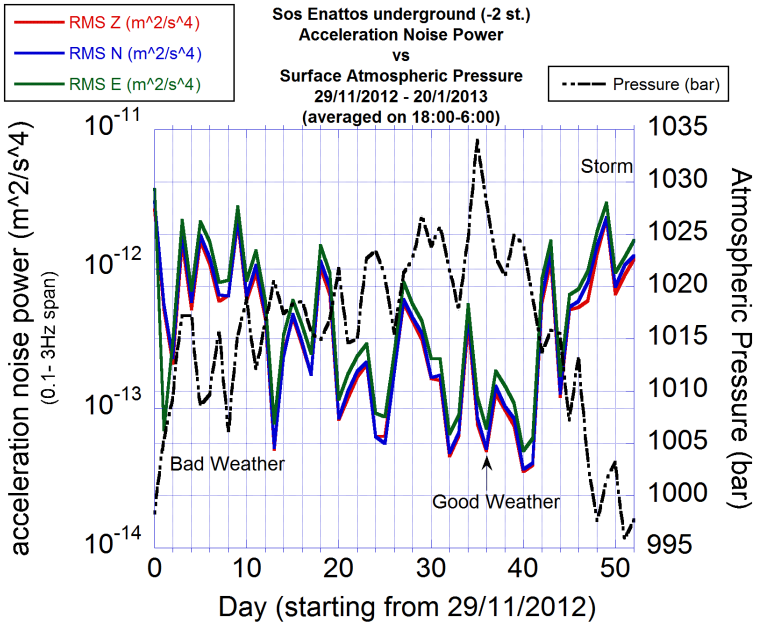

Figure 5.27: Atmospheric pressure measured at the mine entrance versus time and the corresponding spectral acceleration noise in the mine integrated in the frequency range $0.1 - 3\ Hz$.

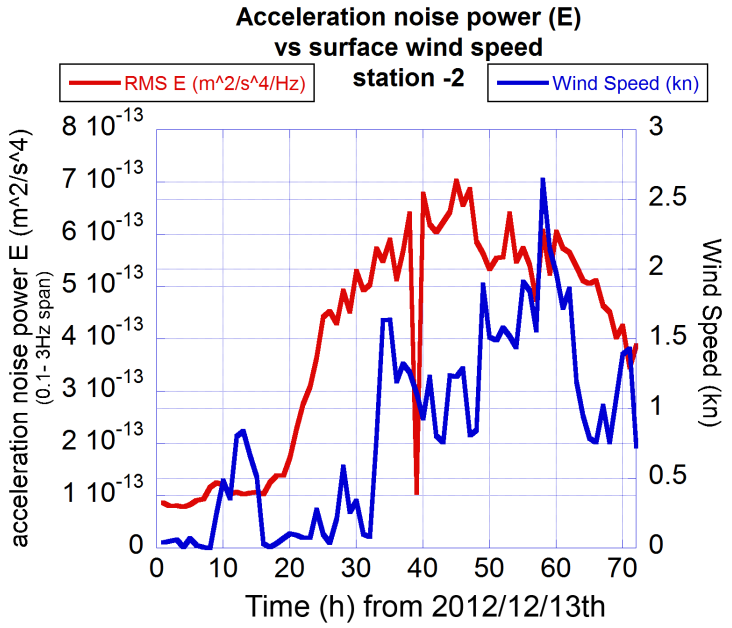

Figure 5.28: Wind speed measured at the mine entrance versus time and the corresponding spectral acceleration noise in the mine integrated in the frequency range $0.1 - 3\ Hz$. Data acquired from $2012/12/13^{th}$.

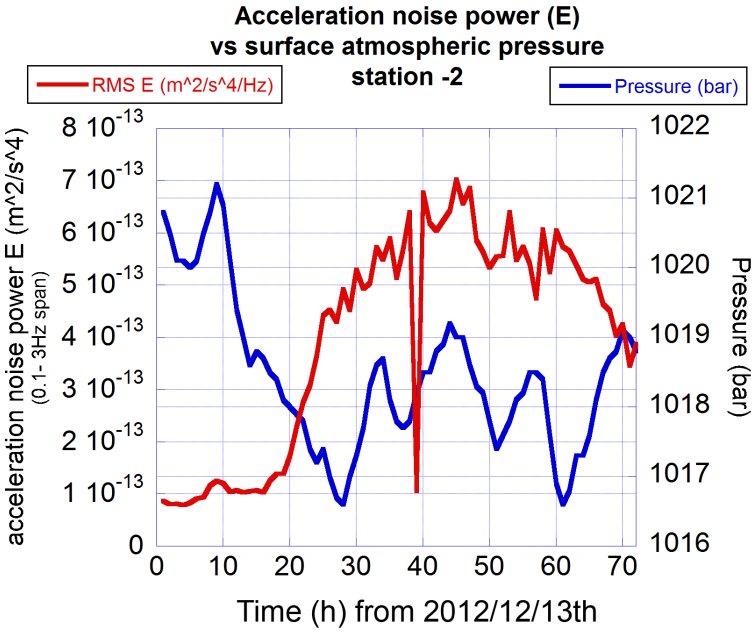

Figure 5.29: Atmospheric pressure measured at the mine entrance versus time and the corresponding spectral acceleration noise in the mine integrated in the frequency range $0.1 - 3\ Hz$. Data acquired from $2012/12/13^{th}$.

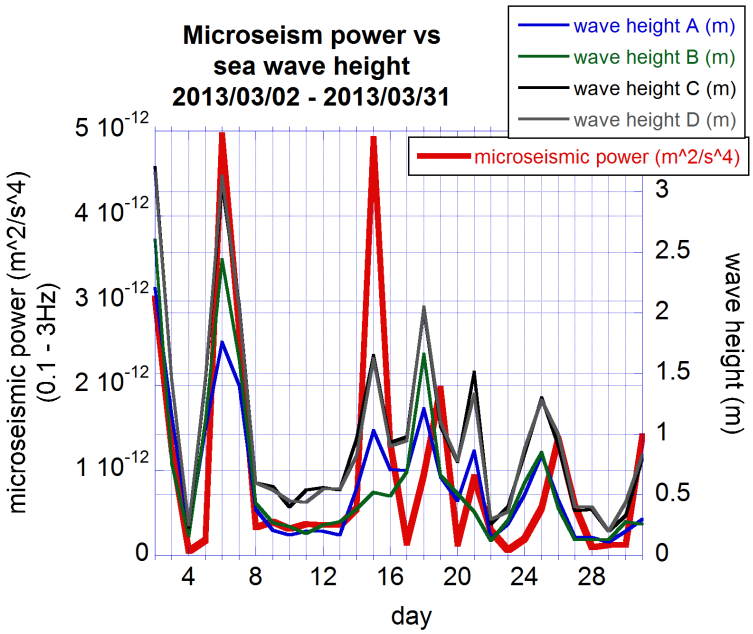

Figure 5.30: The height of combined wind-generated waves and swell (measured at the four points listed in tab. 5.2) versus time and the corresponding spectral acceleration noise in the mine integrated in the frequency range $0.1 - 3\ Hz$. Data acquired from $2013/03/02^{th}$.

and by the geology of this region of Sardinia. In fact, the propagation time of the seismic perturbation from the sea to the mine is expected to be of the order of tens of seconds, a time delay too short to be appreciated in the considered data, seen the sampling rate of the *Nettuno* output variables and the averaging over 12 h of the seismic spectra.

The correlation between the sea waves and the microseism is evident for the peaks at $t = 6,\ 15,\ 21,\ 31\ d$, and for the plateau between $t = 8\ d$ and $t = 13\ d$, while the microseismic increase seems to be delayed at $t = 9\ d$ and $t = 26\ d$: in this case the noise peak may be driven by the oceanic secondary peak, related to a large-scale worsening of the ocean status. Moreover, the microseism result to be better correlated with the wave height at the points C and D, i.e. at the off-shore points.

In fig. 5.31 I compared the microseismic noise power with the height of combined wind-generated waves and swell in the four sea points considered in this study, in the same time interval of fig. 5.28 and 5.29, where the microseismic activity was compared to local weather parameters. In this case, the correlation is evident, and the microseismic increase (or decrease) appears in coincidence with the increase (or decrease) of the sea wave motion.

In sec. 5.5.1 I showed that two oceanic microseismic peaks and the sea-generated primary peak (with the related tails) overlap in the low frequency range $\sim 0.08 - 0.20\ Hz$, so that in general it is not easy to distinguish between the two contributions to the microseismic noise. However, a rough separation can be performed by integrating the acceleration spectral noise between 0.06 Hz and 0.18 Hz, when we

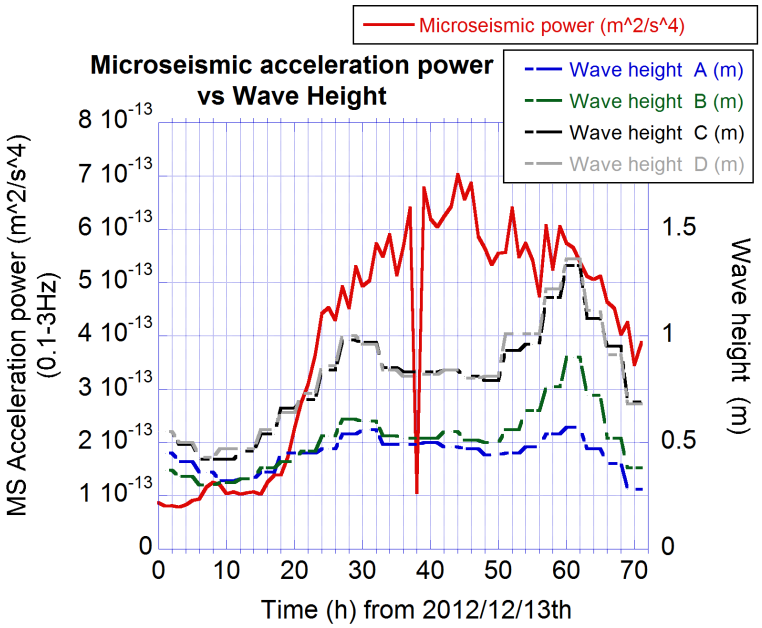

Figure 5.31: The height of combined wind-generated waves and swell (measured at the four points listed in tab. 5.2) versus time and the corresponding spectral acceleration noise in the mine integrated in the frequency range $0.1 - 3\ Hz$. Data acquired from $2012/12/13^{th}$.

consider the oceanic effect, and between 0.18 Hz and 2 Hz for the sea contribution. In fig. 5.32 I show the above-defined acceleration spectral noises compared to the sea wave height in the two off-shore points (C and D in tab. 5.2) for a period of about seven days. In this case the seismic spectra are calculated every 3 h, at the same sampling frequency of the *Nettuno* model's output, therefore the coincidence must be considered within $\Delta t \sim 3\ h$ since the spectra are averaged over that period. However, the relation between the sea waves and the sea-generated microseismic amplitude it is clear; the peak at $t \sim 110\ h$ shows the influence of the ocean activity to the overall acceleration spectral noise, in addition to the contribute directly due to the waves of the local sea.

Frequency correlation

In fig. 5.33 I show the correlation plot of the frequency value of the maximum peak in the shallow-water wave spectrum, provided by the *Nettuno* model, and the frequency of the primary peak in the seismic spectrum measured at the same time in the mine. In this analysis I considered the same data sample of fig. 5.32, taking the values corresponding to wave heights $0.3\ m > h > 1.7\ m$ for which the primary sea generated peak was distinguishable[12]: in fact the peaks generated by

[12]as shown in sec. 5.5.1, usually the dominant peak is the secondary sea-generated. Since the primary peak is not always clearly distinguishable, also because of the superposition with the the oceanic peaks, the sea-generated primary microseismic frequency can be alternatively deduced taking into account half the frequency of the dominant secondary peak.

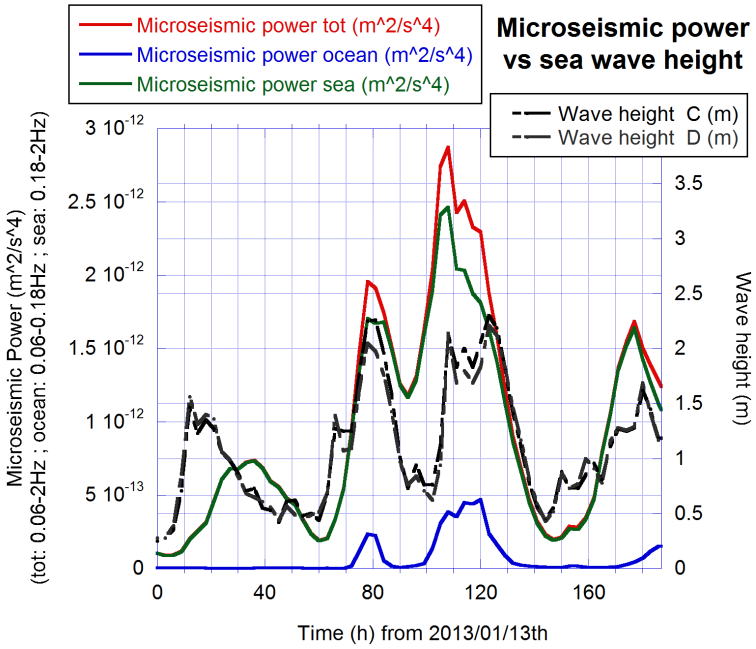

Figure 5.32: The height of combined wind-generated waves and swell (measured at the off-shore points C and D, see tab. 5.2) versus time and the corresponding spectral acceleration noises in the mine integrated in the frequency ranges $0.06 - 0.18\ Hz$, $0.18 - 2\ Hz$ and $0.06 - 2\ Hz$. Data acquired from $2013/01/13^{th}$.

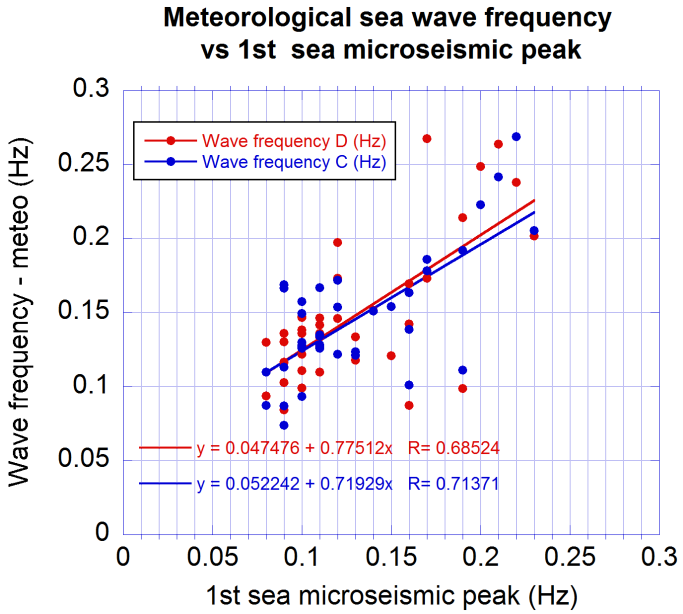

Figure 5.33: Correlation plot of the frequency of the maximum peak on the sea wave spectrum, calculated by the *Nettuno* model in sea points C and D (see tab. 5.2), versus the frequency of the primary sea-generated peak on the seismic spectra measured in the Sos Enattos mine. The linear fit and correlation R are indicated. Data acquired from $2013/01/13^{th}$ to $2013/01/21^{st}$.

wind waves with $h < 0.3\ m$ in the considered sea points can be hidden by peaks produced by higher waves in other sectors of the Mediterranean sea, while for $h > 1.7\ m$ the frequency of the secondary peak decreases approaching the oceanic spectral structures, and it can be difficult to distinguish the single peak in the spectral envelope. With the correlation coefficients $R \approx 0.71$ (sea point C) and $R \approx 0.68$ (sea point D) the t-test reject the null-hypothesis, with the two-tailed probabilities $p = 8 \times 10^{-5}$ and $p = 3 \times 10^{-4}$ associated to the correlation absence.

The correlation between the trends of the microseismic activity (i.e. the band-integrated microseismic noise) and the Tyrrhenian sea wave height, together with the frequency-based identification of the sea peaks (see sec. 5.5.1) and the frequency correlation between the primary sea-generated microseismic peak and its meteorological value provided by the *Nettuno* model, indicate the close link of cause and effect between the local microseismic variations and the sea status: meteorological forces, such as wind and air pressure, produce wind-generated waves, which transform into swell, transferring their energy to the continental crust as seismic waves through the primary and secondary mechanisms (see sec. 3.1.3).

5.5.4 Comparison with a deep underground site

In fig. 5.34 I show a comparison between a typical displacement spectrum taken in the deepest station of Sos Enattos, at a depth[13] of $\sim 111\ m$, and the average displacement spectrum that I measured in the deep underground site of Homestake, South Dakota - USA, at a depth of $\sim 1250\ m$, in July 2009 [149].
In the frequency region between $0.03\ Hz$ and the oceanic secondary peak ($0.12 - 0.20\ Hz$), Sos Enattos is at most one order of magnitude above the noise level of Homestake; between $0.2\ Hz$ and $\sim 1\ Hz$ the sea-generated microseisms cause a greater deviation (however less than two orders of magnitude), but from $f = 2\ Hz$ Sos Enattos shows a comparable and even smaller seismicity than Homestake.

5.5.5 Anthropic contribution

The seismic noise produced by anthropic activities can be observed in the ratio between the the acceleration noise PSD measured in the day and that measured in night hours. I selected 30 days and nights from the seismic data measured in May 2013 and I calculated the ratio between the spectra taken during the daytime and nighttime. In fig. 5.35 I show the ratio between the averaged 12 h daytime spectra with the related 12 h nighttime spectra in the $0.2 - 5\ Hz$ band: the increase of the floor level due to the anthropic noise mostly affects the analyzed band above $1\ Hz$, however the average level of the ratio is below 15.

5.5.6 Long-period stationarity

The microseismic stability of the site can be analyzed through a three-dimensional plot of the acceleration power spectrum versus time, as I show in the 12 h-long spectrogram of fig. 5.36.

[13]here I considered the depth from the entrance level, however the rock thickness above the station is slightly greater, since the tunnel was excavated into a mountain.

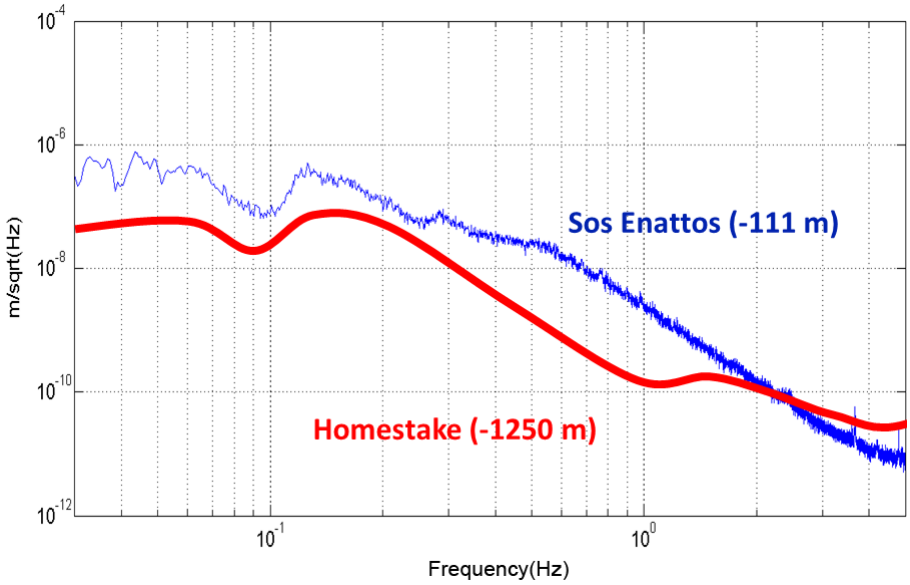

Figure 5.34: Comparison between displacement spectra taken at Sos Enattos ($\sim -111\ m$) and in the deep underground site of Homestake ($\sim -1250\ m$) in July 2009 [149].

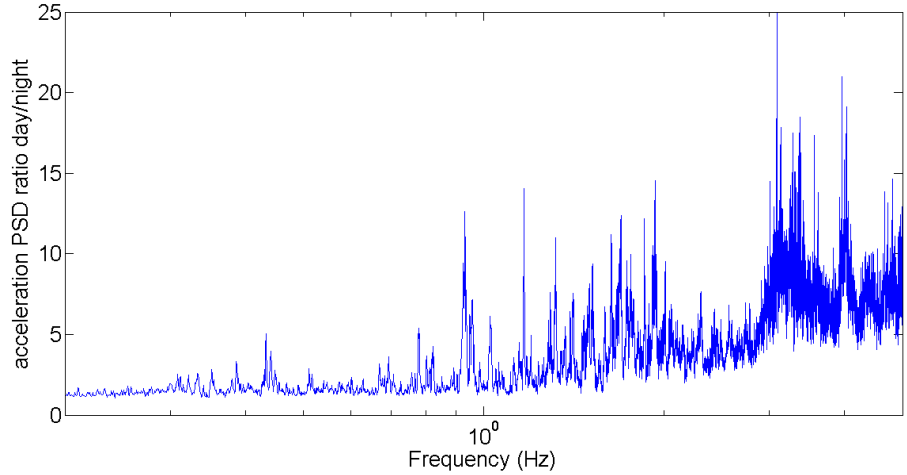

Figure 5.35: The ratio between 12 h-averaged day and night seismic noise PSDs at Sos Enattos, obtained from the data measured on May 2013; the floor level increase due to the anthropic noise mostly affects the analyzed band above $\sim 1\ Hz$.

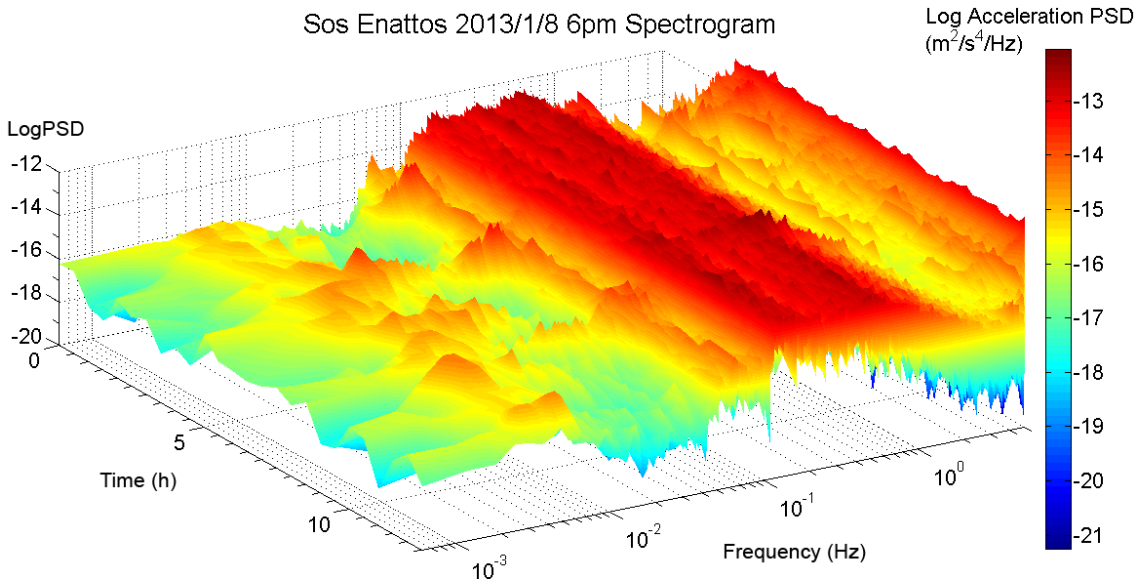

Figure 5.36: Ensemble of the power spectral densities of the acceleration noise measured in Sos Enattos in a day of winter over a period of 12 h.

The long-period seismic monitoring of Sos Enattos mine is summarized in the spectrogram of fig. 5.37. Here I present spectra taken during the long observation period, lasting from July 2012 to July 2013, in function of the time. The spectrogram is subdivided in six intervals of continuous data.
In this plot it is rather evident that the two frequency intervals $0.02 - 0.05\ Hz$ and $0.1 - 1.0\ Hz$ are the most affected by a non stationary behavior. However, the variations of the noise level also during the stormy days are not so high to violate the feed-back requirement of the mirror control system of a third generation interferometer. I also note that, above 1 Hz, i.e. within the detection band of the interferometric detector, the noise level does not vary significantly, even with bad (local and large-scale) weather conditions.

The environmental underground conditions were stable during the whole year of data acquisition: the temperature in the sensor (inner) room was $T = 19.0 \pm 0.5°C$, in the instrumentation (outer) room was $T = 24 \pm 1.5°C$, while the humidity in both was stable at $\sim 94\%$. The daily temperature variations are within $\Delta T < 0.1°C$.

The geological stability of the region, the low micro-tremor noise registered in the mine, due to the absence of industrial activities in the vicinity, and in general the whole profile of the PSD acceleration spectrum, that is even lower than the NLNM curve of Peterson [99] in a large frequency range, lead to the conclusion that the Sos Enattos former mine is a strong candidate for the construction of a third generation of gravitational wave interferometer.

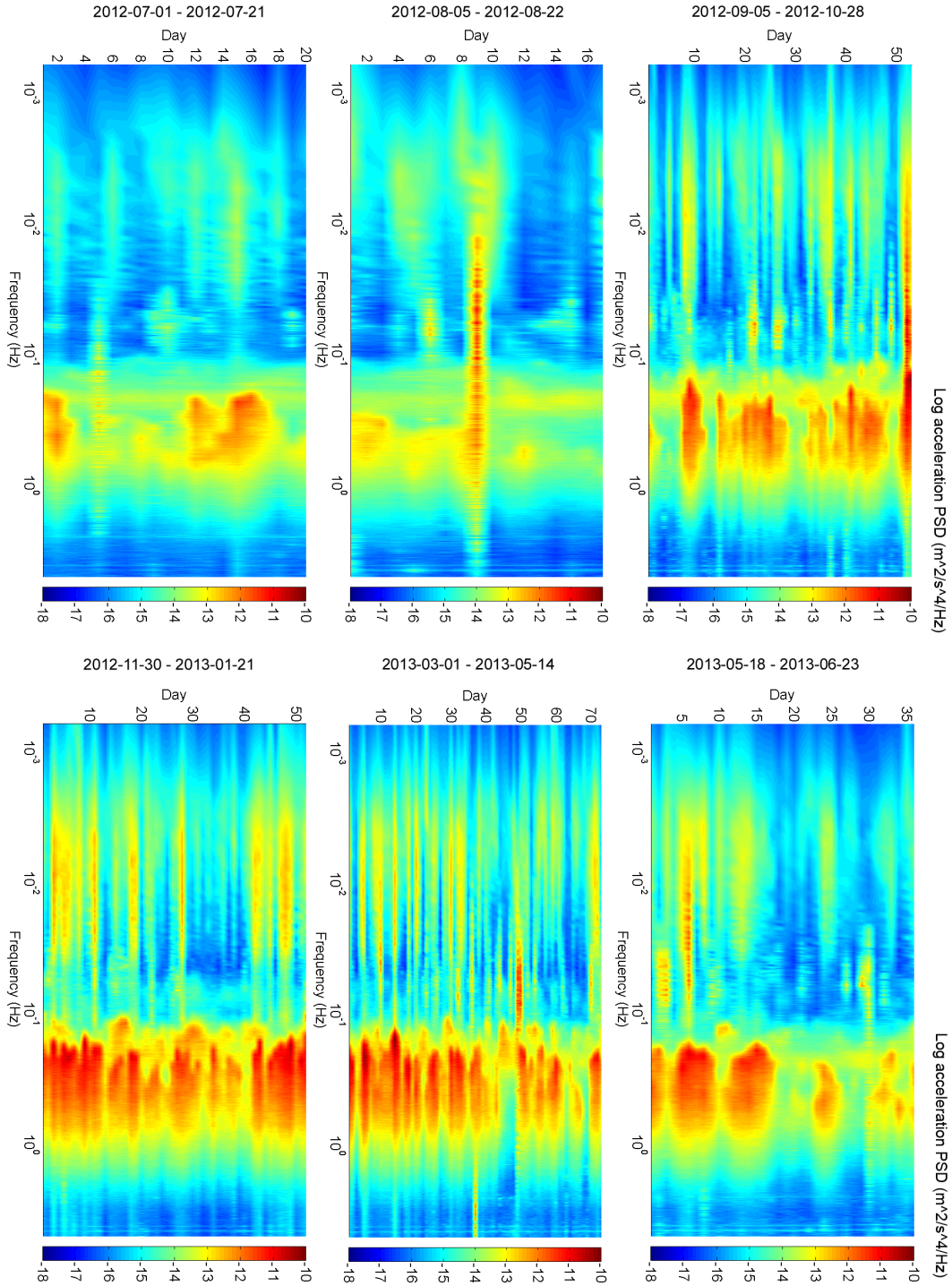

Figure 5.37: Ensemble of the power spectral densities of the acceleration noise measured in Sos Enattos during the whole observation period, between July 2012 and July 2013.

Chapter 6

Development of a cryogenic accelerometer

In third generation gravitational wave detectors the vacuum chamber hosting the test masses will be replaced by large cryostats and dedicated sensing devices, suitable for low temperature operations, will be adopted in order to set up an adequate closed-loop local control. In particular, the main concern is the noise generated by the cryocoolers and transmitted to the cryogenic mirror, either through the mechanical structure (e.g. via the heat-links) or through scattered light. On the other hand, the test mass must keep an inertial state during operations, but relative displacement sensors, such as optical levers, may be not sufficient for the control at low frequencies, since they are non-inertial devices. Therefore, cryo-compatible inertial sensors, such as accelerometers, will be a complementary and suitable choice.

In this chapter I report my experimental work on the development, test and calibration of a vertical accelerometer, capable of operating at cryogenic temperatures [150]. This prototype is derived from the classical scheme of the sensor used in previous years as sensing device for the inertial damping of vertical modes in the Virgo interferometer suspensions (see sec. 2.3.1). In this scheme, the vertical acceleration signal is provided by feedback voltage used to lock the position of an internal floating mass. Thermal contractions of mechanical parts are an important issue during the cooling of such a kind of device, and the calibration check at low temperature, in absence of commercial sensor working in parallel, plays a crucial role.

In the first section of this chapter I summarize the context in which my experimental activity takes place, i.e. the local control of cryogenic payloads. Subsequently, I introduce the vertical accelerometer, dealing with its development, test and calibration at 20 K. In the last section, I report about the installation of the device into the cryostats #2 and #3 of KAGRA detector (see sec. 2.4.2), where the accelerometer was tested down to 8 K and provided a measurement of the vibration modes of their inner radiation shields, deducing their impact on the detector sensitivity curve.

6.1 Cryogenic payload local control

The cryogenic payload local control system must be designed in order to slow-down and align the suspended mirrors of the interferometer, driving their dynamics within the linear range of automatic position control. Since the third generation of interferometric detectors will operate at lower frequencies than past and advanced detectors (i.e. from $\sim 2\ Hz$), an adequate sensing at the level of the cryostats and of the suspension must be developed. In particular, pulse-tube (PT) cryocoolers will introduce a significant amount of vibrational noise, through heat-links or ground-recoil due to the presence of compressors, since their operative frequency and the related harmonics lye in the detection band.

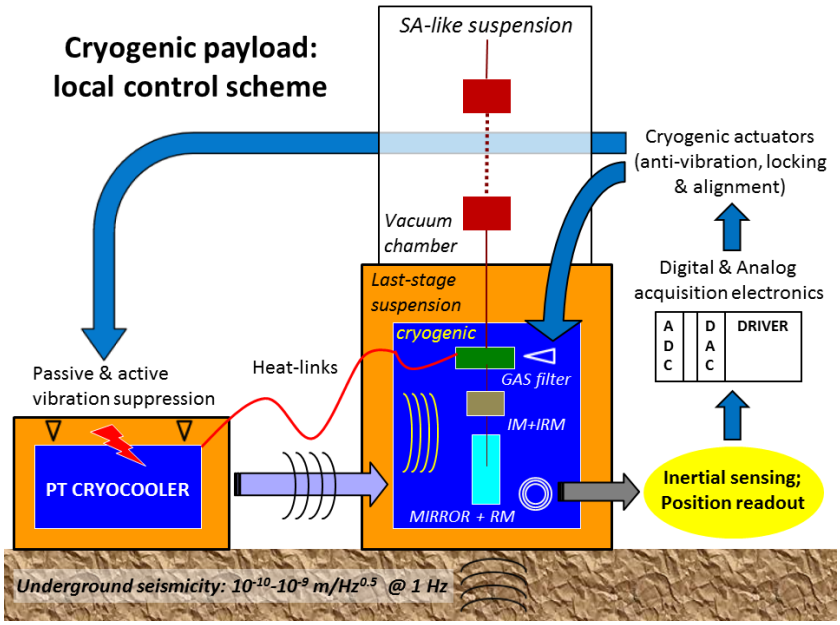

Figure 6.1: Conceptual scheme of local control for the cryogenic payload in third generation interferometric detectors.

6.1.1 Low-frequency vibration suppression

Low-frequency noise will be produced by the gas pulse flowing in the cold head of PT-cryocoolers, with a fundamental harmonic at $\sim 1\ Hz$, which would be directly injected in a suspension. This noise can be suppressed by adopting two complementary solutions:

- a suitable design of the refrigerator system, in order to achieve a passive suppression by means of ad-hoc suspension filter chains for the PT-cryocooler cold head and heat-links;

- an active suppression of the PT-cryocooler injected noise, which will require both cryogenic position readout devices and actuators.

6.1.2 Vibration-free cryostat

The active suppression strategy is already used in the vibration-free cryostat (VFC, [94]), developed some years ago in order to reduce the vibrations produced by the PT-cryocooler cold head on the heat-links of a cryogenic detector. The refrigerator chosen for this system is a two-stage *Sumitomo SR052A*, characterized by a throttle valve which is separated, by means of a pipe link, from the main body of the cold head, whose fundamental harmonic is at $f_0^{PT} \sim 1\ Hz$. The scheme of the VFC is reported in fig. 6.2. The basic concept of the system is to cancel the PT-cryocooler vibrations by directly acting on it by means of three piezo-electric stacks set at room temperature outside the cryostat vacuum. The actuators are loaded by the upper platform, placed on dampers, on which the PT-cryocooler cold head is clamped. This stage is connected to the cryostat by means of a soft bellow, designed in order to mechanically decouple the cold head from the cryostat. The control feedback loop is actually based on optical bundle fiber which monitor the cold head vibration: the error signal is acquired by a dedicated ADC board and then elaborated by a LabVIEW[151]-based code which drives the piezo-electric actuation through DAC and amplification boards. Inside the cryostat a Cu thermal shield (*insulation chamber*) is hung to the upper flange by means of three steel (C85 alloy, $\varnothing = 0.4\ mm$) wires, and is thermally connected to the 40 K first stage of the cryocooler by Cu soft heat-links shaped as jellyfish. Inside the thermal shield, an Al vacuum chamber (*inner chamber*) is hung in cascade to the Cu shield flange, and thermally connected to the 4 K cryocooler's second stage by other jellyfish-like flexible Cu heat-links.

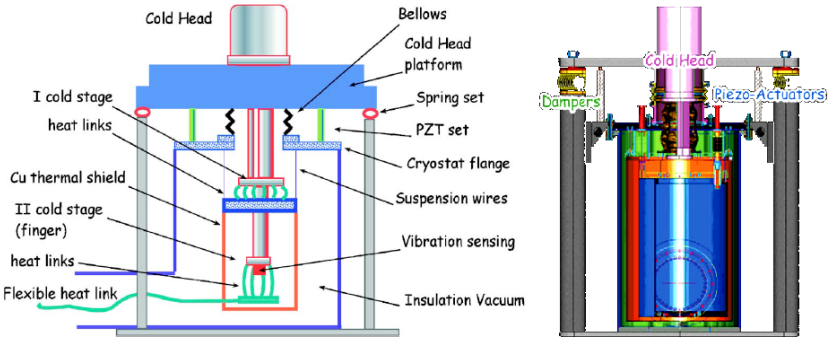

Figure 6.2: Simplified scheme of the vibration-free cryostat. Active noise suppression is provided by three piezo-electric actuators operating in a close feedback loop driven by the displacement sensing actually based on optical bundle fibers [94].

In the actual configuration of the VFC, only the vertical degree of freedom is controlled, with an effective attenuation of the order of 3×10^{-3}. A further improvement is expected by controlling the horizontal degree of freedom, reducing the recoil effects on the overall structure, including the position sensing of the cold head, by means of an inertial cryo-compatible accelerometer. The last point was the initial motivation for the development of the device presented in the next section, since reliable high-sensitivity cryogenic accelerometers suitable for control purposes in the low frequency range $(0.3 - 3\ Hz)$ are not commercially available.

6.2 The cryogenic vertical accelerometer

The development of low-frequency sensors for positioning control and damping, suitable for cryogenic gravitational wave detectors is a leading task. They play, indeed, a crucial role both at the level of the interface between the seismic isolation system and the mirror suspension and inside the cryostat monitoring the mechanical noise injected by the cryocoolers. In fact, the suspension design and control strategy cannot be directly ported from ground-based room-temperature detectors to underground cryogenic detectors, mainly due to the two following reasons:

1. there is a separation between the suspension and cryostat so that the suspension design is to that extent constrained;

2. the performance demand to the seismic isolation system is certainly lower in an underground detector (see sec. 3.1.5) and, in order to adequately exploit such an advantage, the requirements to the environmental quietness are severe.

High-sensitivity cryogenic vertical accelerometers suitable for control purposes in the low frequency range ($0.3 - 3\ Hz$) are not easily available on the market. Therefore, driven by the aim of equipping the vibration-free cryostat (see sec. 6.1.2 and [94]) with an inertial sensor suitable for rejecting the technical noise injected by the cryocooler, I worked on the development of a high-sensitivity vertical accelerometer that works at cryogenic temperatures [150]. It can be integrated within a control system as well as in other fields requiring cryogenic operation compliant with high accuracy mechanical control. The device is an inertial sensor based upon a floating mass, whose displacement is measured by a positioning sensor (LVDT) that provides error signal suitable for in-loop operation, whose correction signal is proportional to the acceleration.

6.2.1 Development

The vertical cryogenic accelerometer prototype is derived from the design of the vertical and horizontal accelerometers used in previous years within the feedback control of the superattenuator inverted pendulum for the Virgo interferometer (see fig. 6.3 and sec. 2.3.1). This kind of sensor was originally designed by INFN - Pisa Group [152] and proved to be high vacuum (HV) compatible, to be effectively used to measure typical seismic noise at ground level and was adopted as standard device used for the Virgo suspensions [153] Active Mode Damping (AMD), along the vertical degree of freedom, in the bandwidth $50\ mHz - 5\ Hz$, with a sensitivity of $\sim 7 \times 10^{-10} m/s^2/\sqrt{Hz}$. For an identical purpose a similar device had been implemented for horizontal degrees of freedom too. This kind of accelerometer can be considered an inertial sensor because it is based on an oscillating mass suspended by means of a low frequency spring system, operating in a closed-loop feedback.

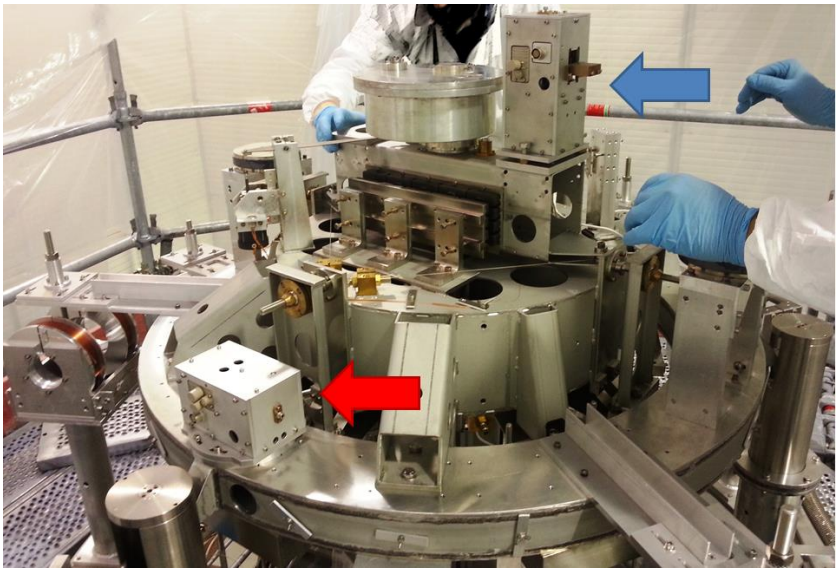

Figure 6.3: The room-temperature and high vacuum compatible vertical (blue arrow) and horizontal (red arrow) accelerometers fixed to the top stage of the inverted pendulum in the superattenuator of Virgo (NE tower, picture taken during the Advanced Virgo upgrade operations, 2013).

6.2.2 Principle of Operation

As shown in [152], the accelerometer can be thought as a spring loaded by the mass m, with resonant frequency at $\omega_0/2\pi$ and mechanical quality factor Q (see sec. 4.2.1). If $x(t)$ and $x_0(t)$ are the coordinates of the mass and that of the spring ground and $F_{fb}(t)$ is the feedback force applied to the mass, the equation of motion in the frequency domain is:

$$\frac{F_{fb}(\omega)}{m} = -\omega^2 x(\omega) + i\frac{\omega\omega_0}{Q}[x(\omega) - x_0(\omega)] + \omega_0^2[x(\omega) - x_0(\omega)] \tag{6.1}$$

The proportionality factor between the feedback force and the displacement of the mass with respect to the external support is defined as the feedback filter transfer function $\mathcal{T}_{fb}(\omega)$, given as force per unit displacement:

$$\mathcal{T}_{fb}(\omega) = \frac{F_{fb}(\omega)}{x(\omega) - x_0(\omega)} \tag{6.2}$$

Let $\mathcal{T}_s$ be the spring transfer function, given as displacement per unit force:

$$\mathcal{T}_s(\omega) = \frac{1}{m}\frac{1}{\omega_0^2 - \omega^2 + i\frac{\omega\omega_0}{Q}} \tag{6.3}$$

therefore, the open loop gain is defined as follows:

$$G_l(\omega) = |\mathcal{T}_s(\omega)\mathcal{T}_{fb}(\omega)| \tag{6.4}$$

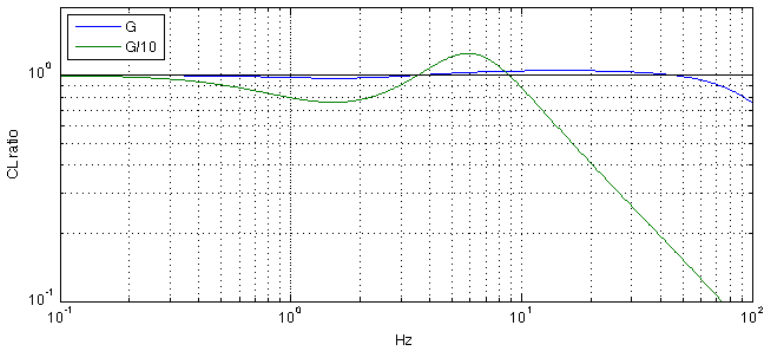

Figure 6.4: Closed-loop ratio in eq. 6.5 in practical cases. The typical response of the accelerometer is proportional to the acceleration until a given frequency cut-off. In specific conditions the gain might set below the nominal operation value and inter-calibration with another sensor is needed to flatten the response to acceleration sensing.

Considering the previous equations, the feedback force can be written in terms of transfer functions as follows:

$$F_{fb}(\omega) = [-m\omega^2 x_0(\omega)]\frac{G_l(\omega)}{1+G_l(\omega)} \tag{6.5}$$

If the open loop gain is large (i.e. $G_l(\omega) \gg 1$) eq. 6.5 becomes:

$$F_{fb}(\omega) \approx -m\omega^2 x_0(\omega) \tag{6.6}$$

Therefore, eq. 6.6 and 6.5 state that ground acceleration can be measured by the measurement of the feedback force $F_{fb}(\omega)$, given an appropriate calibration. However eq. 6.6 is valid only when the open loop gain is high: if this condition cannot be assumed (e.g. if the expected vibrations are too large, an high gain may saturate the signal), an appropriate point-by-point calibration over the considered frequency range is required, as shown in sec. 6.3. I followed this procedure, since I opted for low gain operation during the tests of KAGRA cryostat (see sec. 6.4) for sake of safeness, given the industrial environment, affected by large sudden disturbances, and the major request of avoiding a-priori any possible impact on cryogenic validation tests through Joule heating from the sensor coil.

6.2.3 Mechanical scheme

The accelerometer case is made of Al alloy (*anticorodal* class 6000). The cylindrical floating mass, made of W75Cu25 alloy and having a total load of $m = 0.45\ kg$, is suspended to the vertical wall of the case by two $CuBe_3$ blades 100 μm thick. The blades ensure the unidimensional movement of the floating mass, whose gravity is balanced by a C85 steel spring set at about 35°, according to the LaCoste configuration adopted for low-frequency compact vertical seismometers [154]. The spring orientation and, as a consequence, its elongation at rest can be adjusted by softening the spring stiffness along the vertical direction. Through the same mechanism the spring resonant frequency can be easily tuned around 3 Hz. Since

a large thermal drift of the floating mass suspension vertical position is expected, the resonance was set at an higher value: $f_r = 3.55 \pm 0.15\ Hz$. The vertical displacement of the suspended mass is measured by an inductive device (see sec. 6.2.5) and its position is re-adjusted to the equilibrium point (i.e. the position signal is driven to zero) by a feedback loop using a voltage-force transducer consisting of a coil fixed to the mass and a magnet rigidly connected to the external structure (i.e. to the accelerometer case). The sensor output signal consists in the voltage across the feedback coil, which is proportional to the the feedback force $F_{fb}(\omega)$, and therefore is a measure of the ground acceleration, as shown above in eq. 6.5 and 6.6. In fig. 6.5 the basic mechanical scheme and an internal view of the accelerometer are shown.

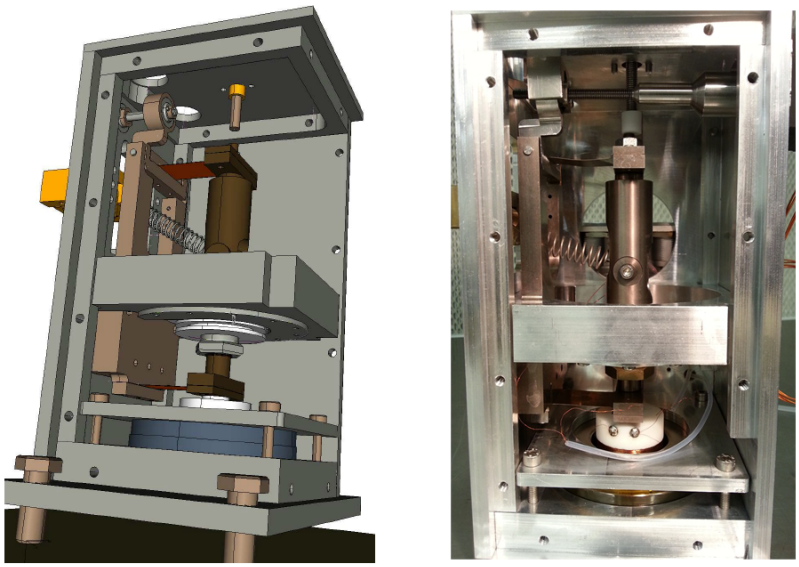

Figure 6.5: 3D technical drawing (left panel) and internal view (right panel) of the cryogenic vertical accelerometer. On the upper part of the right side picture it is visible the stepper motor screw acting on the spring blade. The external box has dimensions $104 \times 98 \times 183.5\ mm$.

6.2.4 Set point adjustment

Thermal contractions of the accelerometer parts results in a temperature-dependent drift of the floating mass rest position by several *mm* with respect to the mechanical range of the displacement sensor (LVDT, *Linear Variable Differential Transformer*) that is 1 *mm* only. If not properly compensated, this effect makes such a sensor unusable at low temperatures since both the mechanical range of the oscillation and the dynamic of the error signal saturate during the cooling-down. In order to check the behavior of the contraction during the thermal cycle I track it keeping the operation set point over the cooling-down. The automatization of this process can be, in principle, easily implemented. The accelerometer is equipped

with a stepper motor that acts on a clamp of the upper blade nested into a fork that tilts it by means of an axial screwing. I slightly modified this tilting scheme by making it more compact and reliable due the extensive use of that regulation required by the cryogenic use. In order to follow the axis of screwing, the stepper motor is fixed on a plate which can be tilted with respect to the side plate of the accelerometer. The selected stepper motor (model *UHV C14.1* produced by AML for Ultra High Vacuum environment, see fig. 6.6) was designed by the manufacturer to be used in cryogenic environment down to $T = 77\ K$, but in our tests and measurements have proved to be reliable even down to $T = 8\ K$, the typical temperature of the test mass in third generation gravitational wave detectors.

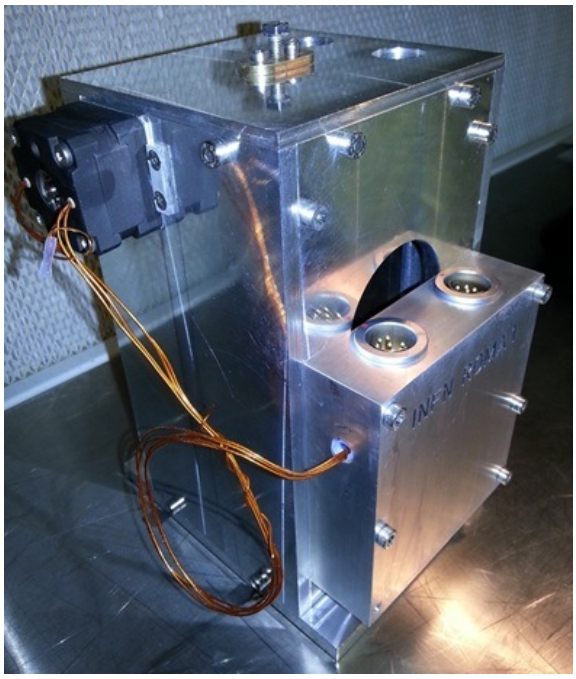

Figure 6.6: External view of the cryogenic accelerometer. On the left plate it is visible the UHV C12.1 stepper motor; the frontal case hosts the LVDT board, the diode thermometer and the two I/O *Fischer*-connectors.

6.2.5 Position sensing

The displacement sensor used in the cryogenic accelerometer is an air-core LVDT inductive position sensor [155] (see fig. 6.7), which consists of three coaxial coils: two antiparallel external coils are rigidly connected to the oscillating mass, while the primary central coil is fixed to the external structure (see fig. 6.8). The primary circuit connected to the central coil is driven at 53 kHz and induces on the secondary circuit connected between the two external coils a voltage difference proportional to the relative displacement. This kind of sensor ensures a low signal degradation in the transmission through relatively long cables, allowing to place the electronics outside the cryostat in the environment at room temperature. The voltage of the sinusoidal signal on the LVDT primary coil influences the gain of

the system; during the cryogenic tests I set it at 2 V since, given the priority of the cryogenic performance and its validation, I intended to reduce as much as possible the Joule heating in pass-through cables and through the primary coil during the cooling phase. The voltage on the primary coil (and therefore the system gain and bandwidth) can be increased to 10 V: in this case the response to acceleration would have been just proportional to the acceleration without any inter-calibration. Moreover, it must be remarked that choosing higher primary voltage would reduce the intrinsic noise of the sensor (see sec. 6.3.4).

6.2.6 Electronics

An electric board is fixed to the cryogenic accelerometer case into a shielding box (see fig. 6.6), made of the same Al alloy (*anticorodal* class 6000) and hosting the basic circuital connections of LVDT and feedback coils, whose electric parameters are shown in tab. 6.1. The capacitive component of the LVDT secondary circuit is a 1.6 nF capacitor, while its resistor divider consists of a $0 - 100\ \Omega$ trimmer connected to the on-board circuit. I placed that trimmer outside of the cryostat, so that the electric balance of the LVDT read-out is possible at any time. In fact, once adjusted at room temperature, the balancing of the real part of the impedance does not drift significantly, but as soon as the cooling-down process starts and the mechanical set-point is recovered through the stepper motor, one needs to trimmer the resistive unbalancing to zero in order to keep a balanced read-out. Thus, it is always possible to reach the fine tuning of the sensor compensating the residual offset signal on the LVDT secondary circuit during the cooling. Then, as the final temperature is reached and stable, the read-out tuning is kept. The 50 μm Cu wires of the LVDT coils are connected to the small shield at the side of the sensor case, where I also installed a *Lake Shore* diode thermometer in order to monitor the accelerometer temperature during the cooling.

Coil	Resistance (Ω) @ T=294 K	Resistance (Ω) @ T=20 K	Inductance (mH)
Primary (LVDT)	1.7 ± 0.1	< 0.1	$(1.7 \pm 0.1) \times 10^{-1}$
Secondary (LVDT)	194 ± 1	2.8 ± 0.1	14.9 ± 0.1
Feedback	559 ± 1	8.0 ± 0.1	177 ± 1

Table 6.1: Electric parameters of the sensor coils. Note that the resistance of the copper wire of the coils depends on the temperature T as $R(T) = R_0[1 + \alpha(T - T_0)]$, where $\alpha \approx 3.9 \times 10^{-3}$, but below 20 K it becomes almost constant due to microscopic impurities or defects in the material. The inductance variation from the room temperature value is negligible.

The system is completed by two external boards supplied through a NIM standard crate and connected to the sensor by few meters-long cables (see fig. 6.8 and 6.9). The first module hosts the preamplifier and the closure of the LVDT circuit on the above mentioned resistive trimmer, while the second one hosts the amplifier, the demodulator and the PID electronics with a bandwidth BH$\sim$ 100 Hz.

The design of these boards is based on that of the electronics provided by INFN-Pisa for the Virgo suspensions active mode damping. Moreover, the second NIM module allows the regulation of the gain and calibration factors by means of two trimmers installed on the circuit board. The circuital schemes of the NIM boards and the transfer function of the PID feedback are reported in app. D.

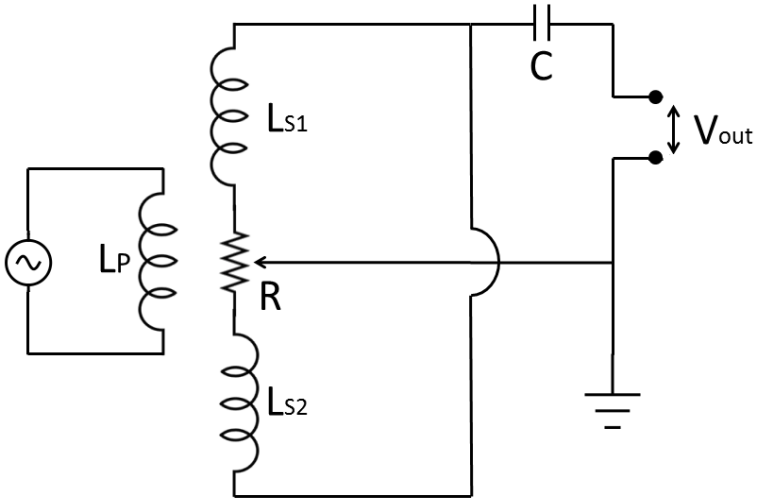

Figure 6.7: Basic scheme of the primary and secondary circuits of the LVDT displacement sensor; L_i indicates primary (P) and secondary ($S1, S2$) inductances, C the capacitor and R the resistive trimmer.

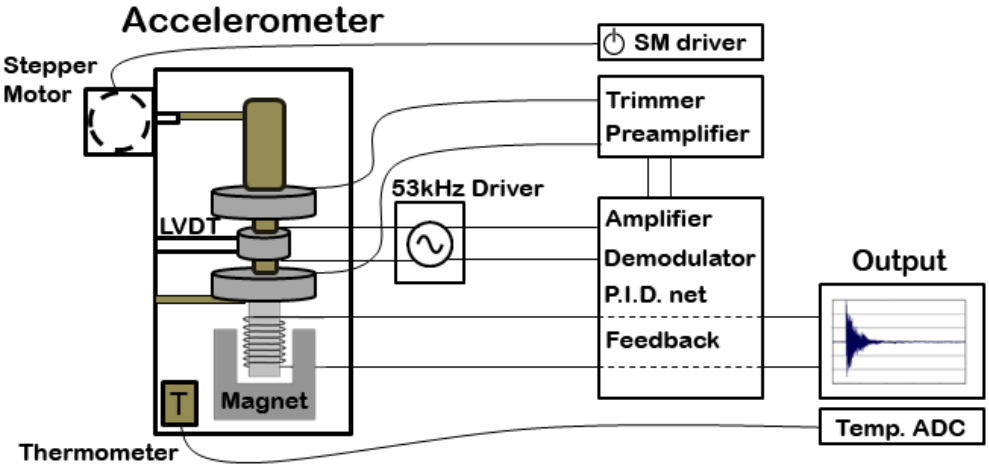

Figure 6.8: Schematic configuration of the vertical accelerometer operation.

6.2.7 Vacuum compatibility

The accelerometer is designed in order to be integrated in gravitational wave detectors, both at room and at low temperature (such as for the interferometer KAGRA,

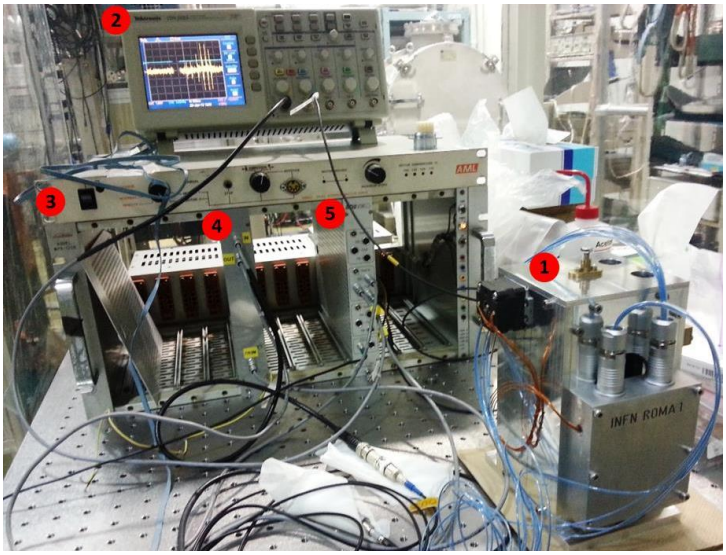

Figure 6.9: Operative configuration of the vertical accelerometer during a test: 1- accelerometer; 2- output signal seen on the oscilloscope; 3- stepper motor driver; 4- pre-amplification and resistive trimmer NIM board; 5- amplifier, demodulator, PID-feedback (ADF) NIM board.

see sec. 2.4.2 and 6.4), for this reason it was necessary to ensure its UHV compatibility and its cleanness by performing a dedicated outgassing test. A known conductance of $C = (1.21 \pm 0.01) \times 10^{-2}\ m^3/s$ was placed between the vacuum chamber and the pumping tube in order to limit the fluctuations of the effective pumping speed due to the pump itself. The vacuum chamber was evacuated using a group composed of a scroll pump plus a turbo-molecular pump, connected on the upper port of the chamber. Then, an ion pump was connected to the vacuum chamber through the conductance C (see fig. 6.10). During the outgassing test the first group of pumps was switched off. A vacuum sensor and a mass-spectrometer were connected to a third port of the chamber. After two weeks of measurements the system reached the pressure $P_{min} = (3.50 \pm 0.05) \times 10^{-5}\ Pa$, that was still reducing slowly (see fig. 6.11). Therefore the upper limit of the total outgassing rate Q_{tot} is given by:

$$Q_{tot} = Q_{acc} + Q_{chamber} = P_{min} \cdot C \tag{6.7}$$

where Q_{acc} and $Q_{chamber}$ are respectively the outgassing rate of the accelerometer and of the vacuum chamber. From eq. 6.7 we obtained $Q_{tot} = (4.20 \pm 0.07) \times 10^{-7}\ Pa \cdot m^3/s$. We measured the contribution of the chamber as equal to $Q_{chamber} = (1.20 \pm 0.07) \times 10^{-7}\ Pa \cdot m^3/s$, hence we obtained the upper limit to the outgassing due to the accelerometer $Q_{acc} = (3 \pm 0.07) \times 10^{-7}\ Pa \cdot m^3/s$. From the mass-spectrometer (fig. 6.12) we noticed the absence of significant traces of hydrocarbons, while peaks of H_2 ($P_{H_2} \approx 3.3 \times 10^{-6}\ Pa$), H_2O ($P_{H_2O} \approx 4.8 \times 10^{-6}\ Pa$) and N_2 ($P_{N_2} < 10^{-6}\ Pa$) were present. The peak due to the water is caused by two factors: first the accelerometer could not be preliminarily heated enough to eject water trapped inside its components; second there was a significant contribution coming from the vacuum chamber itself.

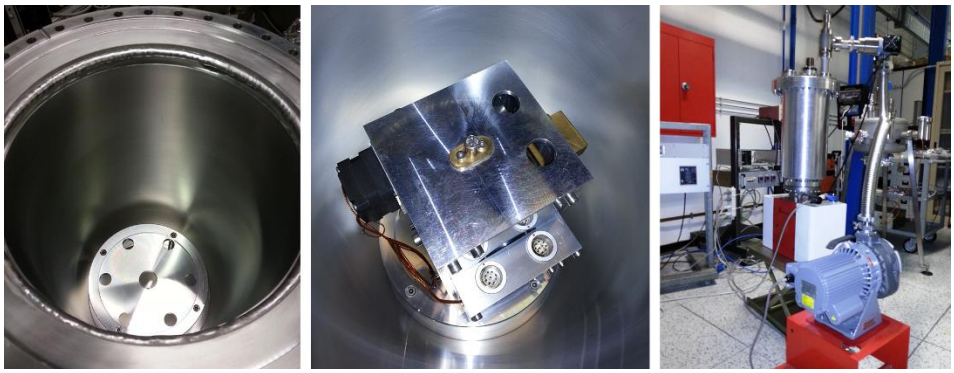

Figure 6.10: Experimental setup for the vacuum compatibility test. From left: the known conductance C clamped to the bottom of the vacuum chamber; the accelerometer fixed inside the chamber; the pumping group, composed of a scroll plus turbomolecular and ionic pumps, being the last one connected to the chamber through the conductance. A vacuum sensor plus mass spectrometer were connected to an upper port.

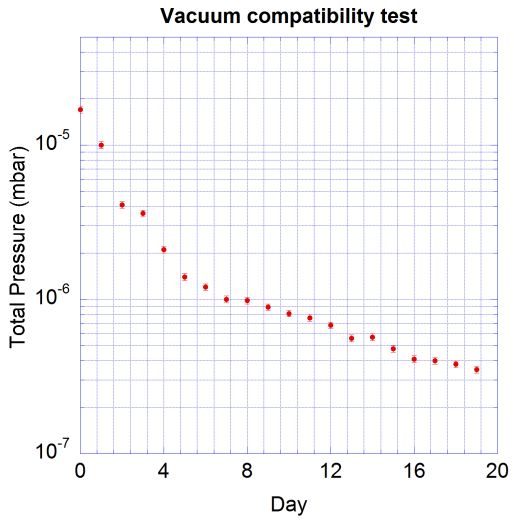

Figure 6.11: Pressure measured during the vacuum compatibility test of the accelerometer. Note that here pressures are in units of $mbar$ ($1\ bar = 10^5\ Pa$).

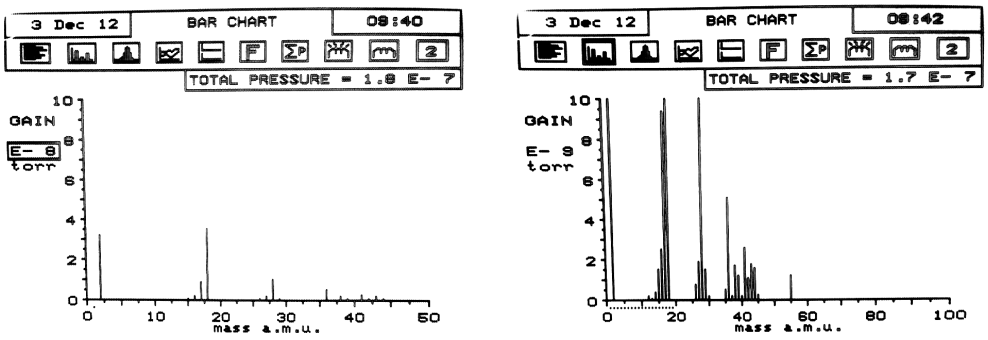

Figure 6.12: Partial pressures measured by the mass-spectrometer during the vacuum compatibility test.

6.2.8 Preliminary test

The accelerometer prototype was subject to a first test performed docking the cryogenic accelerometer together with another calibrated accelerometer over a vibrating platform at room temperature and pressure. Driving the platform with various sinusoidal signals the spectra of the two output signals were compared: the shape of the two spectra are in very good agreement (see Fig. 6.13), so that the coherence between the two signals within the considered frequency span is nearly one.

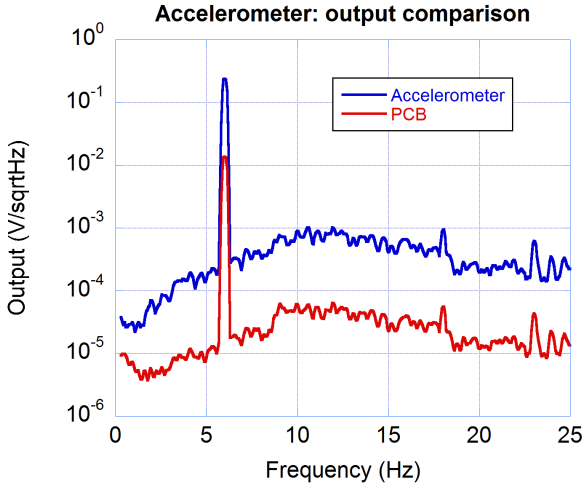

Figure 6.13: Output signal spectra from cryogenic vertical accelerometer (blue line) and another calibrated accelerometer (PCB393B12, red line), docked together on a vibrating platform. The peak at $f = 6Hz$ was intentionally generated driving the vibrating platform with a sinusoidal signal at such a frequency. Note that the PCB calibration is $1019.4mV/m/s^2$

6.3 Calibration of the accelerometer

The calibration of the sensor was checked at room temperature and at several intermediate temperatures during the cooling process. An horizontal accelerometer based on the same principle of the vertical one can be calibrated by measuring the output voltage for different tilt angles, but for this vertical prototype such a procedure could not be applied; moreover, I was interested to study the effective calibration curve of the sensor, i.e. the frequency-dependence of the conversion coefficient between voltage and acceleration: below the resonant frequency (i.e. in the range of the PT fundamental frequency) it is expected to be sufficiently flat, while at higher frequency this may be not true, since the eq. 6.6 is valid until the open loop gain is sufficiently high. Indeed I chose a low gain in order to avoid signal saturation due to environmental/technical noises and Joule heating during the cryogenic tests. According to the original project of using the accelerometer in the VFC cryostat [94], the low open loop gain, implying inter-calibration meant to flatten response, would still allow the suppression of the main disturbance due to pulse-tube cryocooler, which produce a fundamental resonance at 1 Hz.

However, also in this configuration, a point-by-point calibration curve allows to use the sensor in a wider frequency span and the wanted linear response to acceleration. At room temperature and in vacuum condition I obtained the calibration coefficients by comparing the sensor output with that of another calibrated accelerometer. At low temperatures it was not possible, since a calibrator sensor capable of cryogenic operations was not available, therefore a point-by-point calibration was obtained (as explained in sec. 6.3.3), using the piezoelectric actuation system of the VFC (see sec. 6.1.2), given the unitary coherence between the actuators and the inner chamber at the driving frequency (see the following sec. 6.3.1). During the first cooling test the sensor showed a temperature-dependent output for a given acceleration. This unattractive feature was then avoided redesigning the electric read-out circuit on-board (i.e. the electric part which is cooled down with the sensor) in order to keep at room temperature all the possible circuital components, leaving on-board just the capacitor of the resonant LVDT circuit and the coil connections. In this way the output proved to be temperature-independent.

6.3.1 VFC actuation system

Since the calibration of the accelerometer at low temperature has been performed using the VFC cryostat, it was necessary to check the coherence between the piezoelectric actuators acting on the upper platform (fig. 6.14) and the inner chamber, where the cryogenic accelerometer was installed. In order to ensure the feasibility of this low-temperature calibration, the expected coherence should be unitary at the actuation driving frequency.

Before the coherence check, I studied the mechanical response of the VFC actuation system: three PCB-393B12 accelerometers, previously cross-calibrated, were placed at the corners of the platform (indicated by A,B,C in fig. 6.14), in coincidence with the position of the piezoelectric actuators. The actuators were driven by a dedicated labVIEW-based code, which allows to inject noise or periodic signals, and adjust the gain α of each actuator. By generating a sinusoidal signal

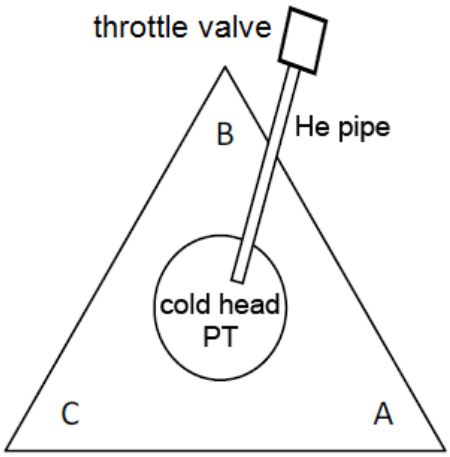

Figure 6.14: Sketch of the triangular upper platform of VFC, seen from the top.

with given amplitudes, and measuring the accelerations at A, B and C on the platform, I found the optimal gain which should be used in order to produce the same acceleration across the entire platform: $\alpha_A = 1.03$, $\alpha_B = 0.84$, and $\alpha_C = 0.90$. In this configuration the coherence among the accelerometers was measured in sinusoidal regime at given frequencies where the pulse tube was not expected to inject disturbance, finding values close to unity at the peaks; an example is given in fig. 6.15.

In order to check the coherence between the upper platform, the inner chamber, and the outer chamber, which is grounded, I fixed two PCB accelerometer externally on the platform and on the top of the outer chamber, while the cryogenic accelerometer prototype was clamped inside the inner chamber. Subsequently, the piezoelectric actuators were driven with a sinusoidal signal. As expected from previous studies, the coherence between the platform and the inner chamber is unitary at the driving frequency (see fig. 6.16), therefore it is possible to calibrate the cryogenic accelerometer by means of piezoelectric actuators, since the upper platform and the inner chamber are coherently accelerated. The coherence between the platform and the outer chamber on the ground is quite low (~ 0.6), and from the ratio between the displacements of those elements (see fig. 6.17) it is possible to evaluate a transfer function of the order of ~ 0.1, which represents the recoil through the piezoelectric-ground-outer chamber channel[1]. In the last check, I placed the PCB accelerometers on the triangle sides, and I measured the vibrations of each side when the pulse tube refrigerator was activated without the feedback piezoelectric actuation; in fig. 6.18 the fundamental peak at 1 Hz and higher order harmonics are clearly visible, moreover the BC side results to be less noisy than the other two sides.

[1]piezoelectric actuators are placed on the top of columns, which have the same mechanical ground of the outer chamber.

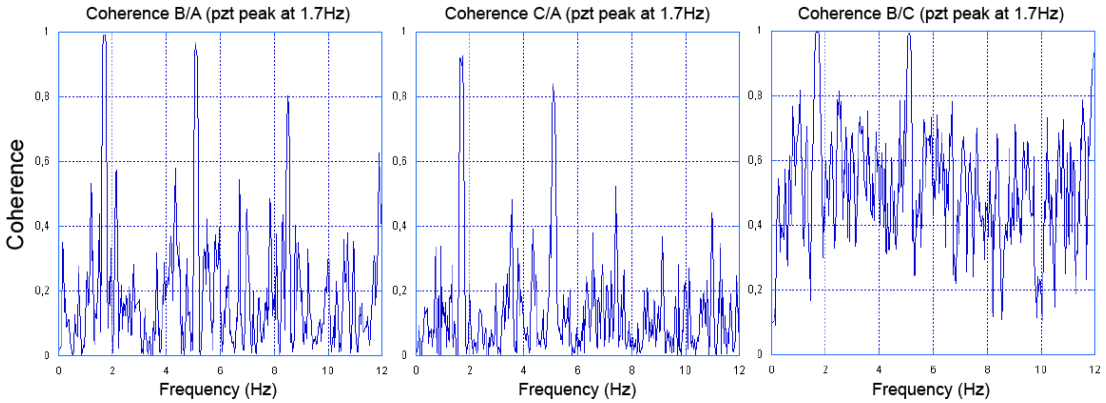

Figure 6.15: Coherence between the corners of the VFC upper platform when the piezoelectric actuators are driven with a sinusoidal signal at $f = 1.7\ Hz$ and amplitude $A = 1.2\ Hz$.

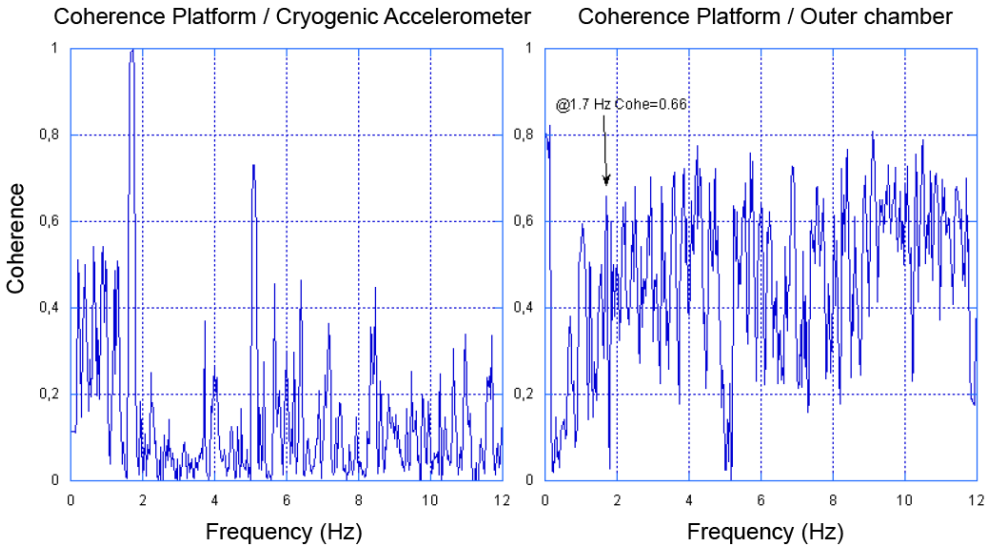

Figure 6.16: Left: coherence between VFC upper platform and the inner chamber; right: coherence between VFC upper platform and the outer chamber. Piezoelectric actuators were sinusoidally driven at $f = 1.7\ Hz$ with amplitude $A = 1.2\ Hz$.

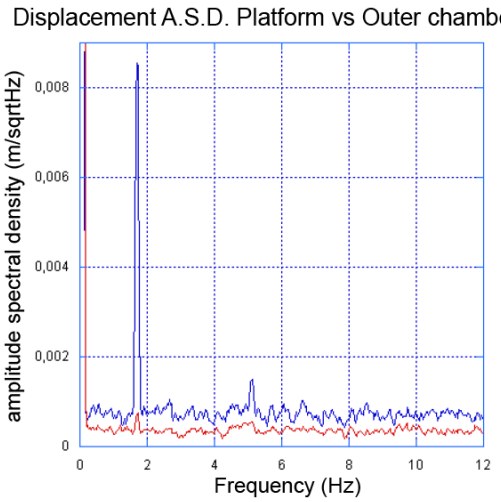

Figure 6.17: Displacement amplitude spectral density of the VFC platform (blue line) and outer chamber (red line), with the piezoelectric actuators driven with a sinusoidal signal ($f = 1.7\ Hz$ and $A = 1.2\ Hz$); the ratio between the peaks at the driving frequency is about $\mathcal{T} \sim 0.1$.

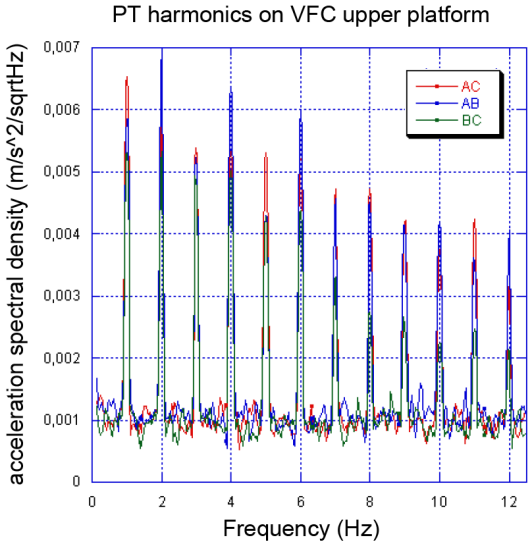

Figure 6.18: Acceleration amplitude spectral density measured on the three sides of the VFC platform, when the pulse tube cryocooler is active. The fundamental harmonic is at $f_0 = 1\ Hz$.

6.3.2 Calibration at room temperature

The accelerometer output was calibrated at room temperature by comparing it with that of the commercial accelerometers above mentioned, using the experimental configuration described in sec. 6.2.8. The calibration coefficients, for the $0 - 25\ Hz$ frequency span, are shown in fig. 6.19. Around 1 Hz it is sufficiently flat to foresee a future implementation in the VFC control closed-loop.

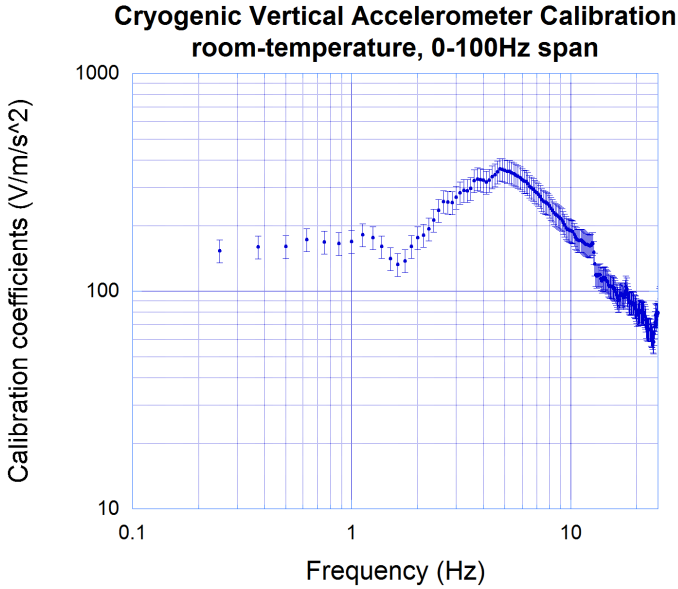

Figure 6.19: Intercalibration of the cryogenic vertical accelerometer at room temperature in $0 - 25\ Hz$ frequency span. At $f = 4.8\ Hz$ it is visible the resonance peak of the natural frequency of the oscillator, due to the low open-loop gain chosen. The main contribution to error bars comes from the uncertainty of the accelerometer used as calibrator.

6.3.3 Calibration at cryogenic temperature

In order to study the sensor output during cryogenic operations, the accelerometer was docked to the inner wall of the experimental chamber of the VFC (see sec. 6.1.2). Since it was not available a calibrator or another vertical accelerometer capable of operating at low temperatures, I developed a point-by-point calibration procedure. Driving the piezoelectric actuators of the VFC at several frequencies with certain voltage amplitudes, given the constancy of the transfer function between the upper flange and the inner chamber of the cryostat during the cooling, the accelerometer underwent the same accelerations in three different configurations:

1. the accelerometer was docked together with the calibrated one to the inner chamber of the cryostat, in vacuum and at room temperature;

2. the accelerometer was docked to the inner chamber in vacuum condition,

and the calibrated one was fixed outside to the upper flange of the cryostat. Subsequently, the accelerometer was cooled down to 20 K (see fig. 6.21);

3. same configuration of the precedent point, but with the accelerometer slowly re-heated to room temperature.

The last point is necessary to cross-check that, moving from point (1) to point (2), the mechanical transfer function of the VFC is unchanged. Adopting this three-steps procedure we verified that the first-designed prototype was characterized by a temperature-dependent output, as mentioned above, but, once I re-designed the on-board electric wiring of the accelerometer, the temperature-dependent change of the calibration factor was negligible (see fig. 6.20).

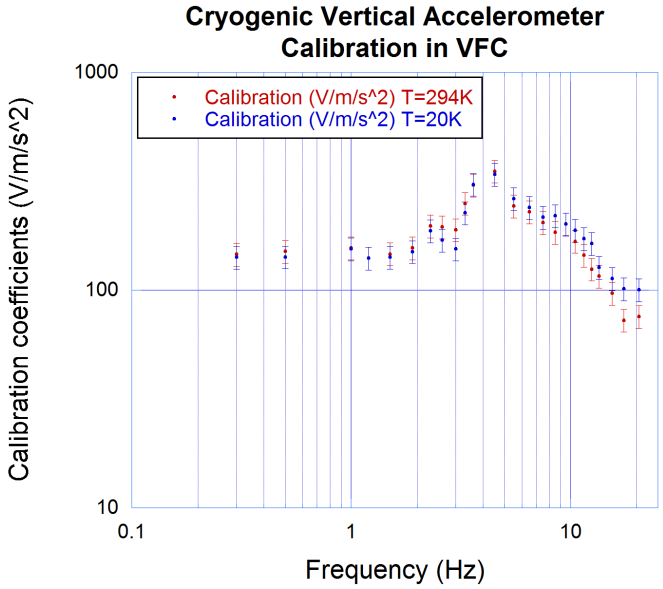

Figure 6.20: Intercalibration of the cryogenic vertical accelerometer at $T = 294\ K$ and $T = 20\ K$ into the VFC cryostat. The calibration points are consistent to those obtained comparing the output of the accelerometer with another commercial sensor in fig. 6.19. The main contribution to error bars comes from the uncertainty of the accelerometer used as calibrator.

6.3.4 Sensitivity

As reported in [152] for the accelerometers used in the SA of Virgo, a main limitation to the sensitivity of this kind of sensor comes from the Johnson noise of the LVDT secondary circuit and from the amplifier noise, which sums up in quadrature. I measured these sources of noise in the amplifier/PID network board as $N_e \sim 10^{-6}\ V/\sqrt{Hz}$ while the carrier generator (53 kHz) was disconnected from the primary coil of the LVDT sensor (see Fig. 6.22).
This electronic noise is injected through the feed-back actuator resulting in acceleration noise of the suspended mass: it can be calculated from the deconvolution of the electronic spectral noise through the mechanical transfer function, shown

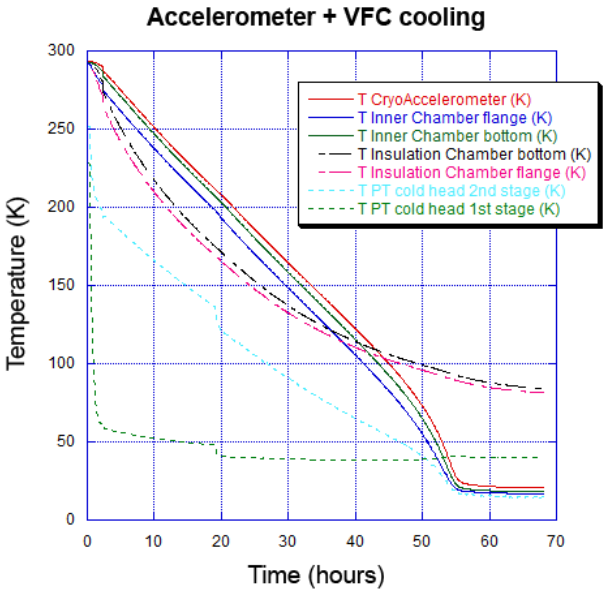

Figure 6.21: Temperature of the accelerometer compared to those measured in th VFC during the cooling test.

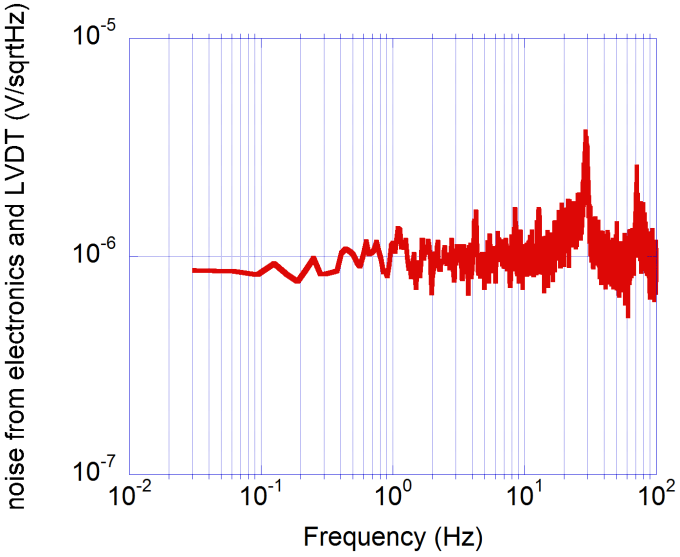

Figure 6.22: Voltage noise from the amplifier/PID network electronics and the secondary coils of the LVDT circuit.

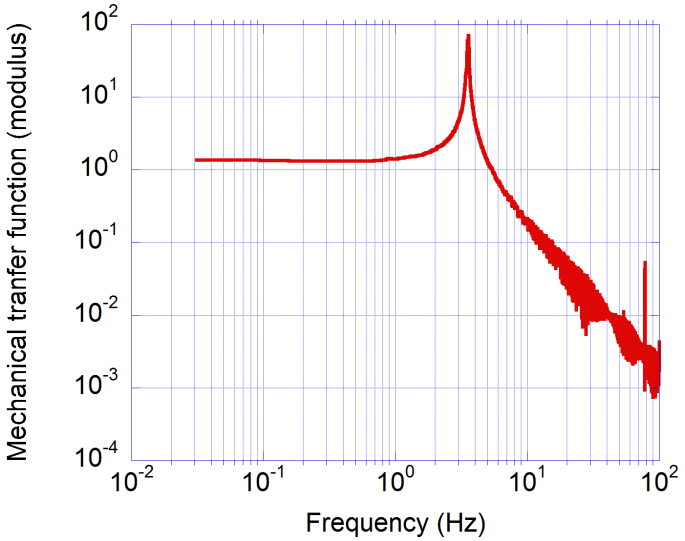

Figure 6.23: Mechanical transfer function modulus of the floating mass of the accelerometer, obtained injecting white noise through the control actuator. The mechanical resonant frequency is $f_r = 3.55 \pm 0.15\ Hz$; the quality factor at room temperature and atmospheric pressure is $Q \sim 100$.

in fig. 6.23, having considered the proper amplification and calibration factors. The acceleration noise turns out to be $2 \times 10^{-8} m/s^2/\sqrt{Hz}$ below the resonant frequency. Therefore the minimum spectral acceleration that can be measured with the accelerometer is the one which produces an output signal equal to the considered noise. Thus from the measurement of the noise we traced the sensitivity curve shown in fig. 6.25.

The achieved sensitivity is adequate for the position sensing and control of the PT-refrigerator cold head motion ($\sim 10^{-4}\ m/\sqrt{Hz}$ @1 Hz for the top platform and $\sim 2 \times 10^{-6} m/\sqrt{Hz}$ @1 Hz at the inner VFC chamber), and even to measure the seismic background noise.

Note that in the previous estimate I neglected other possible sources of noise, such as thermal dissipations, Barkhausen noise [156] and hysteresis effects. The overall noise on the sensor output arises from the contribution of all these noise sources plus the electronic contribution shown in fig. 6.25, but a theoretical estimate is not trivial. However, the overall intrinsic noise of the accelerometer can be empirically estimated by measuring the sensor output once suspended by a suitable N-stage seismic isolation system acting as a low-pass mechanical filter with attenuation factor proportional to f^{-2N}. For this purpose I used a suspension composed of $N = 2$ stages connected to each other by maraging steel-made triangular blades and coil springs (see fig. 6.26). I measured the calibrated acceleration spectral amplitudes when the accelerometer was placed on the ground and on the second stage of the suspension. Hence I compared the spectra with those measured by a commercial piezoelectric accelerometer (a *PCB-393C*). The result of these measurements are shown in fig. 6.27.

From the spectra taken on the ground I note that the cryogenic vertical accelerometer is suitable for measuring the seismic background noise up to $\sim 40\ Hz$, being

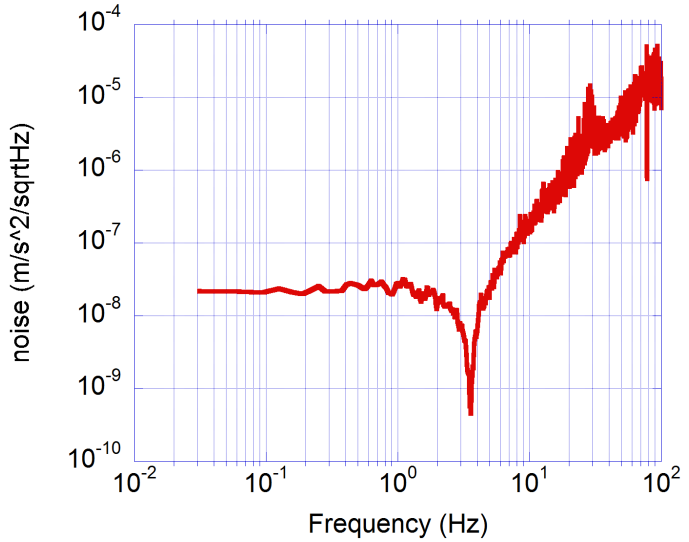

Figure 6.24: Sensitivity curve of the cryogenic vertical accelerometer obtained from the deconvolution of electronic and Johnson noises and considering the mechanical transfer function of the suspended mass, at room temperature and atmospheric pressure. Note that at low temperature the Johnson noise contribution from the cooled LVDT circuit decreases as it depends on R and T.

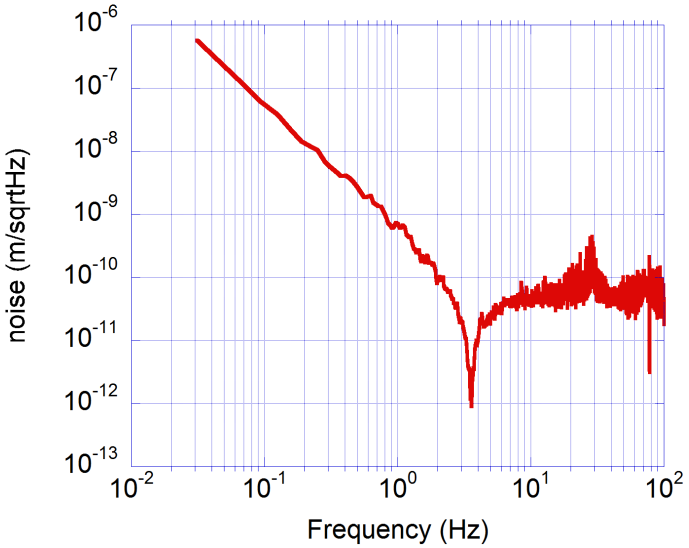

Figure 6.25: Sensitivity curve (in displacement units) of the cryogenic vertical accelerometer obtained from the deconvolution of electronic and Johnson noises and considering the mechanical transfer function of the suspended mass, at room temperature and atmospheric pressure.

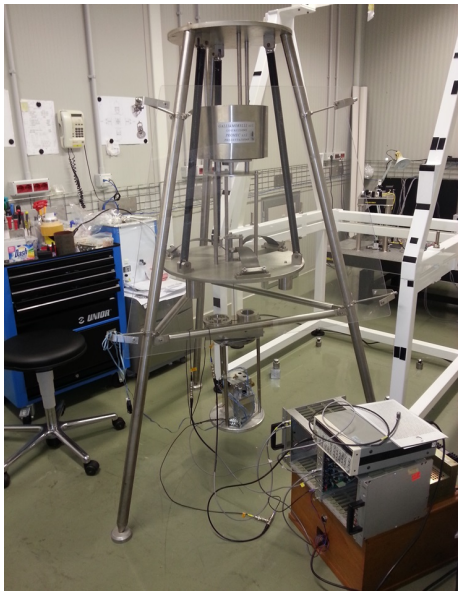

Figure 6.26: The 2-stage mechanical suspension used for measuring the overall intrinsic noise of the cryogenic vertical accelerometer. In this picture the accelerometer was fixed to the second stage during its set-up for the measurements.

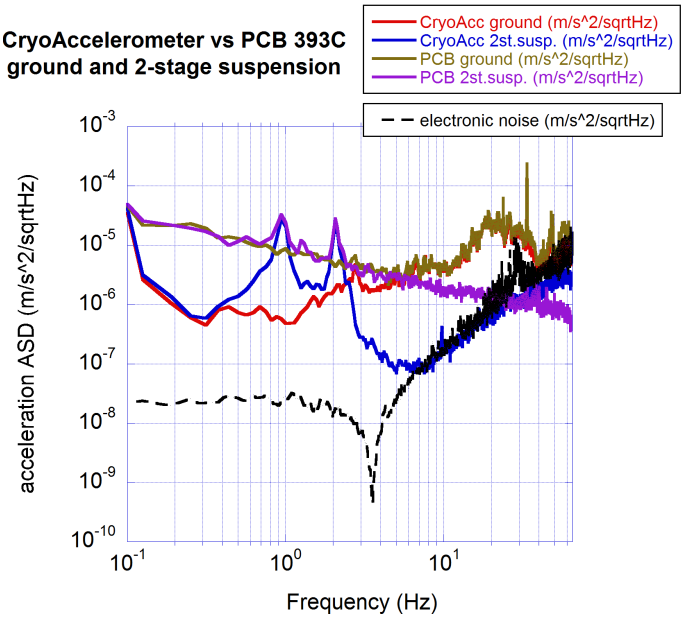

Figure 6.27: Acceleration amplitude spectral densities measured with the cryogenic vertical accelerometer and with a commercial piezoelectric accelerometer (PCB-393C) on the ground and on the second stage of a mechanical low-pass filter. The electronic noise is also reported.

the spectrum coincident with that measured by the commercial accelerometer; moreover for $f < 1\ Hz$ it turns out to be characterized by a better sensitivity respect to that of *PCB 393C*, by a factor at least ~ 30. When the accelerometers are placed on the second stage of the mechanical suspension it is clear the high sensitivity at low frequency compared to that of the commercial accelerometer: the two resonant peaks corresponds to the natural frequencies of the mechanical seismic insulator at $f_1 \sim 0.9\ Hz$ and $f_2 \sim 2\ Hz$, while at higher frequencies the low-pass filter shape is evident. The sensitivity of the cryogenic accelerometer is better than that of the *PCB 393C* by a factor ~ 800 for $f < 1\ Hz$ and ~ 50 at $f = 5\ Hz$. Finally, comparing the spectrum taken on the suspension second stage with the noise curve shown in fig. 6.25, I note that at higher frequencies the main limit to the sensitivity of the sensor comes from the electronic noise. I also remark that these measurements were performed using a primary LVDT signal of $2\ V$, but choosing a higher voltage on the primary coil it is possible to increase the sensitivity and the signal-to-noise ratio of the sensor.

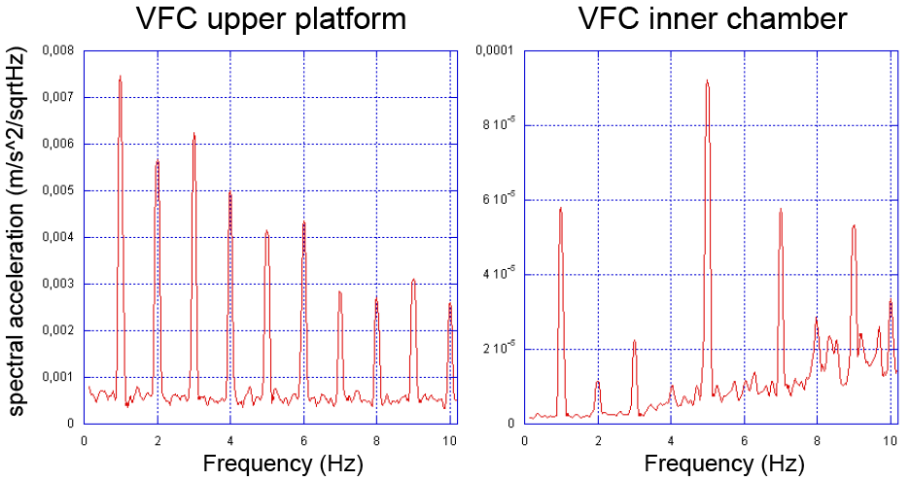

Figure 6.28: Acceleration amplitude spectral density measured on the VFC upper platform (left, with a PCB accelerometer) and inside the VFC inner chamber (right, with the calibrated cryogenic vertical accelerometer), during PT-cryocooler operations in open loop. The resonance at $f = 5\ Hz$ observed inside is produced by a mechanical couplings, such that between dampers and chamber suspension wires.

6.3.5 Measurement of PT-induced vibrations into the VFC

Through a fitting function of the calibration points, it is possible to convert directly the voltage output of the sensor into accelerations. With the cryogenic vertical accelerometer clamped inside the inner chamber of the VFC, and the PCB accelerometer placed on the upper platform, I measured the noise produced by the PT refrigerator in open loop operation (i.e. without the feedback actuation) inside the cryostat at $T = 20\ K$. The amplitude spectral densities of acceleration and displacement are reported in fig. 6.28 and 6.29.

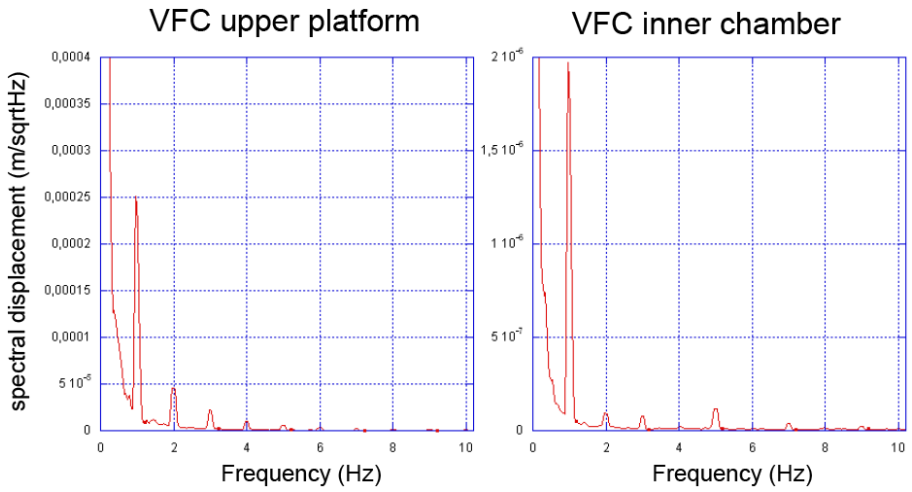

Figure 6.29: Displacement amplitude spectral density measured on the VFC upper platform (left, with a PCB accelerometer) and inside the VFC inner chamber (right, with the calibrated cryogenic vertical accelerometer), during PT-cryocooler operations in open loop.

6.4 Installation and measurements into KAGRA cryostats

In 2013 the cryogenic vertical accelerometer was installed on the inner radiation shield of the cryostats (see fig. 6.30 and fig. 6.31) dedicated to the payloads of KAGRA (see sec. 2.4.2), in order to measure the vertical vibration modes of such structures at low temperatures in the $0-100\ Hz$ frequency span, investigating the main structural modes, the effect produced by the PT-cryocoolers, whose fundamental frequency is $1.7\ Hz$, and their impact on the detector sensitivity. Moreover, this activity gave me the opportunity to check the accelerometer operations down to $T = 8\ K$ within a full scale configuration of a gravitational wave detector cryostat. Measurements were performed at the Toshiba's Keihin factory, in Yokohama (Japan), were the cryostats were assembled, during their vacuum and cooling tests. This work has been partially supported by EU ELiTES project (IRSES no.295153).

6.4.1 Cryostat vibration modes

Structural vibrations, in particular those produced by the cryocoolers, are an important issue for the development of a cryogenic gravitational wave detector such as KAGRA. They can generate noise directly through a mechanical channel, e.g. via heat-links to the payload, and indirectly through light scattering on vibrating shield and baffles, and re-coupling with the main laser. Numerical FEM analyses were performed by S. Koike at KEK (fig. 6.32), resulting in the main vibration modes of the whole cryostat and inner radiation shield, which are reported in tables 6.2 and 6.3.

Figure 6.30: Cryostats for the payloads of KAGRA under assembling and testing, at the Toshiba Keihin Product Operations in Yokohama (Japan).

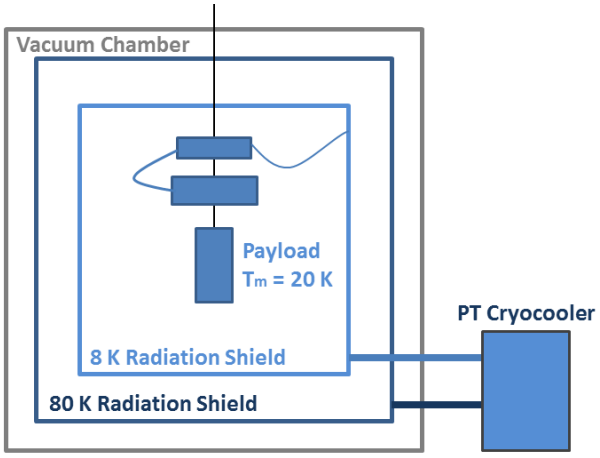

Figure 6.31: Sketch of the main cryostat elements: inside the outer vacuum chamber there are two radiation shields, the outer shield at $T = 80\ K$ and the inner shield at $T = 8\ K$. Four PT-cryocoolers for each cryostat (two connected to the shields and two to the payload through flexible heat-links) provide the refrigeration power.

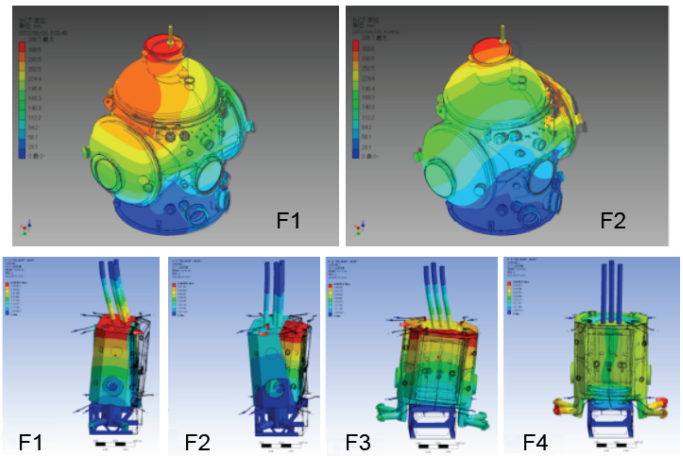

Figure 6.32: First vibration modes of the whole cryostat (upper panels) and inner radiation shield (lower panel) below 100 Hz, calculated with FEM analysis (see tables 6.2 and 6.3). Courtesy of S. Koike [157].

Vacuum chamber

Mode	Frequency (Hz)
F1	11.07
F2	22.22
F3	34.72
F4	38.03
F5	43.02
F6	44.81
F7	55.97
F8	56.14

Table 6.2: Vibration modes of the outer vacuum chamber below 60 Hz, calculated by means of FEM analysis. Courtesy of S. Koike [157].

Radiation shield

Mode	Frequency (Hz)
F1	20.71
F2	23.95
F3	24.71
F4	24.88
F5	30.84
F6	38.16
F7	42.18
F8	45.09

Table 6.3: Vibration modes of the radiation shield below 60 Hz, calculated by means of FEM analysis. Courtesy of S. Koike [157].

6.4.2 Measurements in cryostat #2

In March 2013 I installed the cryogenic vertical accelerometer inside the cryostat #2. The sensor was clamped to a dedicated platform, fixed to the inner radiation shield and in thermal contact with it (see fig. 6.33). The accelerometer was

Figure 6.33: Installation of the cryogenic vertical accelerometer into the cryostat #2 of KAGRA. From left, clockwise: installation phase in clean-room environment; the accelerometer fixed to the support platform on the radiation shield and cabled to feedthrough cables; external instrumentation setup.

cabled, from its two Fischer-connectors through a Burndy feedthrough cable, to the instrumentation placed outside the cryostat: the entire line from the sensor to the instrumentation was about 20 m-long. The output signal was monitored on the oscilloscope and acquired in parallel with a spectrum analyzer. In order to compare internal and external vibrations, a commercial RION accelerometer was placed outside the cryostat, and its output was acquired in coincidence with the cryogenic accelerometer. Before the installation, the accelerometer calibration was checked in the $0 - 100\ Hz$ frequency span by acquiring and comparing the signals from the two sensors placed side by side. Since the measurements were performed into the Toshiba Keihin factory during working hours, a certain amount of anthropic and industrial machinery-generated noise was unavoidable.

Displacement spectra

In fig. 6.34 I show the displacement amplitude spectral density (ASD) measured over a $0-100\ Hz$ frequency span, before the activation of the PT-cryocoolers, by the cryogenic vertical accelerometer clamped inside the radiation shield, compared to that measured by the RION accelerometer placed outside on the ground, at about 1 m from the cryostat. The peak observed at $f = 23\ Hz$ with the same amplitude by the two sensors can be identified as the operative frequency of the pumping group. The peak at $f = 15.25\ Hz$ is not reported in the FEM analysis (see sec. 6.4.1), but is noticeable, especially on the radiation shield. The increase of the floor level at higher frequencies may be caused by the cryostat structure: a similar effect was noticed in the cryostats of CLIO [92]. In fig. 6.35 and 6.36 I

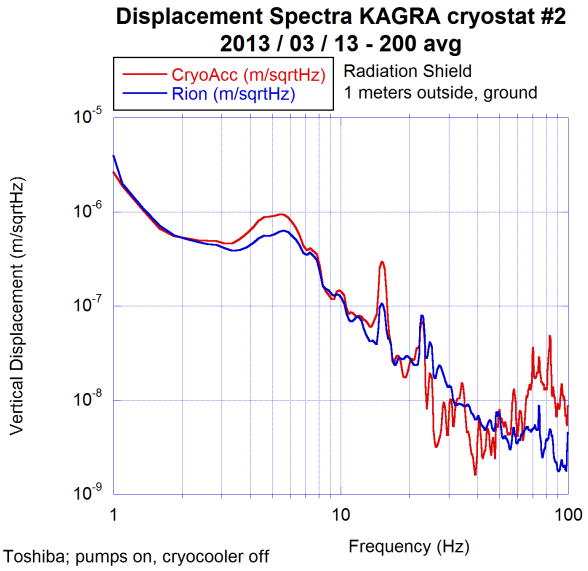

Figure 6.34: Displacement amplitude spectral densities measured on the radiation shield (with the cryogenic accelerometer, red line) and outside on the ground (with the RION accelerometer, blue line) between 1 and 100 Hz. Measurements were performed before the activation of PT-cryocoolers and with vacuum pumps active. Details in the text.

report the low-frequency displacement ASD, respectively in $0-6\ Hz$ and $0-10\ Hz$ frequency span, when the PT-cryocoolers were activated. The RION accelerometer was placed on the cryostat base flange. The fundamental harmonic of the PT-refrigerator adopted for KAGRA is expected to be at $f_0^{PT} = 1.7\ Hz$, but it is not visible on the radiation shield, while it is almost negligible on the external structure of the cryostat: the suppression of this frequency is obtained by means of the particular mechanical support-structure of PT-cryocooler and soft thermal links [91]. The two peaks at about 0.25 Hz and 0.55 Hz are produced by the microseismic activity[2]. At 6.3 Hz and 7.6 Hz two peaks are visible both inside and outside; at $f = 10\ Hz$ a peak is clearly visible at the level of the radiation

[2]the Toshiba factory is built along a quay, so that at low frequencies the seismic level is very sensitive to sea conditions

shield; at $f = 11\ Hz$ the spectrum measured on the base flange shows the peak produced by the F1 mode of vibration of the whole cryostat (see tab. 6.2). In fig. 6.37 I report the same displacement spectra over a frequency span of $0 - 50\ Hz$: here the previously-mentioned peaks are clearly visible, in particular it is possible to distinguish the inner peak at $f = 10\ Hz$ from the peak produced by the cryostat F1 mode at $f = 11\ Hz$, also observed at the level of the radiation shield with a smaller amplitude. The peak at $f = 15.25\ Hz$ is evident, while in the interval between about 20 and 25 Hz it is visible a spectral structure composed of the peaks due to vacuum pumps, and those generated by cryostat vibration mode F2 and by shield vibration modes F1, F2, F3 and F4 (see tables 6.2 and 6.3). Smaller peaks due to other vibration modes are visible at higher frequencies, while the peak at $f = 46\ Hz$ may be related to the mode F6 of the cryostat.

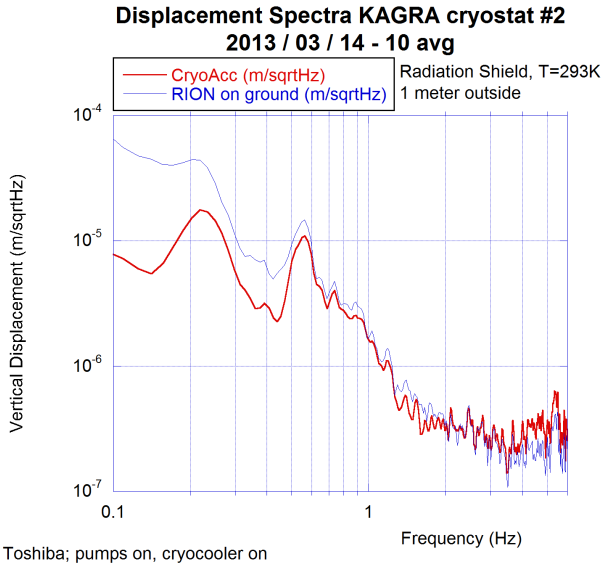

Figure 6.35: Displacement amplitude spectral densities measured on the radiation shield (with the cryogenic accelerometer, red line) and outside on the cryostat base flange (with the RION accelerometer, blue line); $0 - 6\ Hz$ frequency span. Measurements were performed with PT-cryocoolers and vacuum pumps active. Details in the text.

The vibration at $f_0^{PT} = 1.7\ Hz$ and its first overtone at $f_1^{PT} = 3.4\ Hz$, produced by the PT-cryocoolers, were visible only if the RION accelerometer was placed close to the refrigerator and on its support structure, as evident in fig. 6.38, where the related spectra are compared to that measured inside on the radiation shield.

The coherence and the frequency response between the cryogenic accelerometer, clamped on the radiation shield, and the RION accelerometer, placed on the cryostat base flange, are reported in fig. 6.39 and fig:20130314-FR: below 10 Hz it is close to unity, at higher frequencies it decreases, except for peaks related to vibration modes of both the cryostat and the shield, e.g. the peak at $f = 15.25\ Hz$.

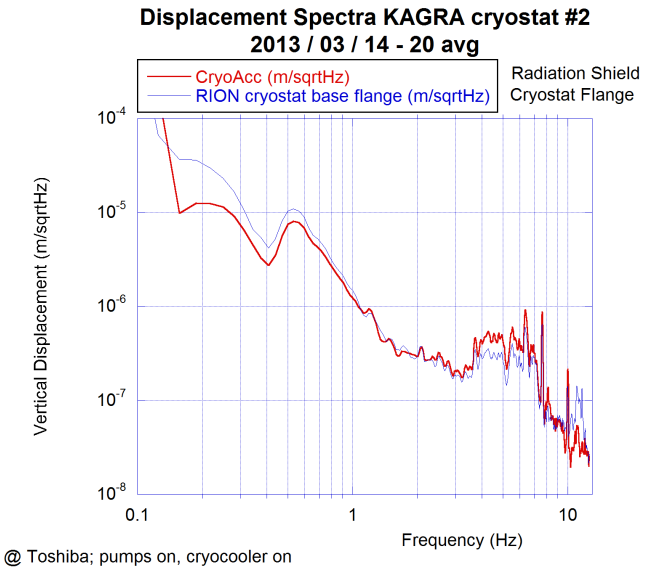

Figure 6.36: Displacement amplitude spectral densities measured on the radiation shield (with the cryogenic accelerometer, red line) and outside on the cryostat base flange (with the RION accelerometer, blue line); $0 - 10\ Hz$ frequency span. Measurements were performed with PT-cryocoolers and vacuum pumps active. Details in the text.

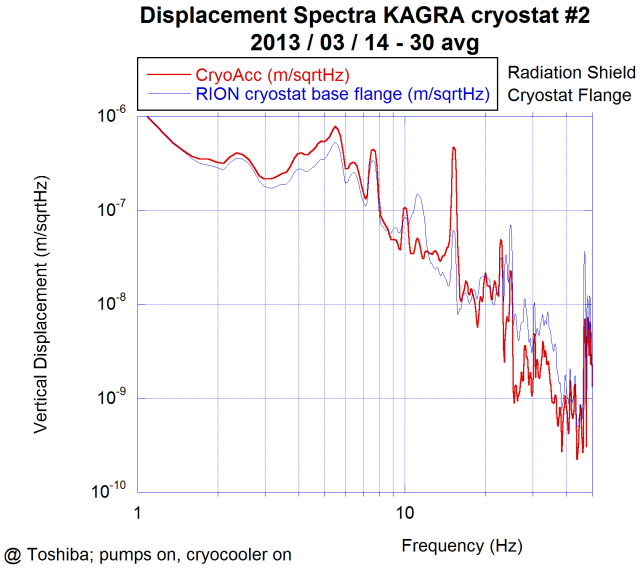

Figure 6.37: Displacement amplitude spectral densities measured on the radiation shield (with the cryogenic accelerometer, red line) and outside on the cryostat base flange (with the RION accelerometer, blue line); $1 - 50\ Hz$ frequency span. Measurements were performed with PT-cryocoolers and vacuum pumps active. Details in the text.

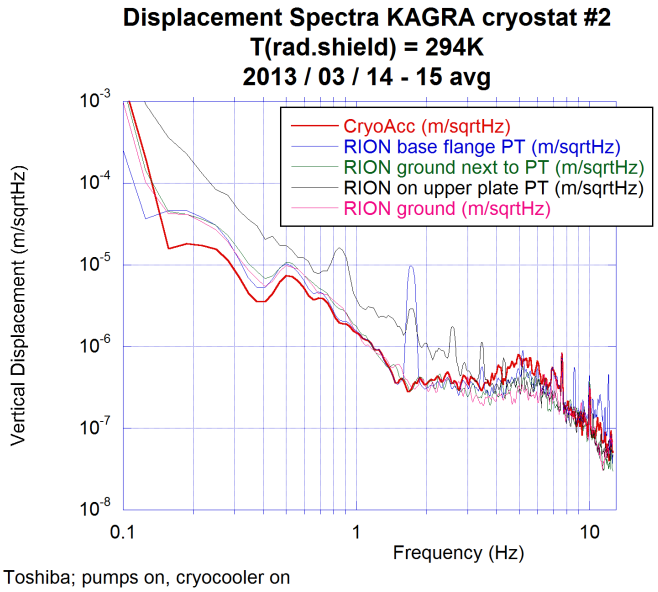

Figure 6.38: Displacement amplitude spectral densities measured on the radiation shield (with the cryogenic accelerometer, red line), on the base flange and on the upper plate of the PT (with the RION accelerometer, blue and black lines), and on the ground close to the PT and at about 1.5 m from it (with the RION accelerometer, green and pink lines); $0 - 10$ Hz frequency span. Measurements were performed with PT-cryocoolers and vacuum pumps active. See details in the text.

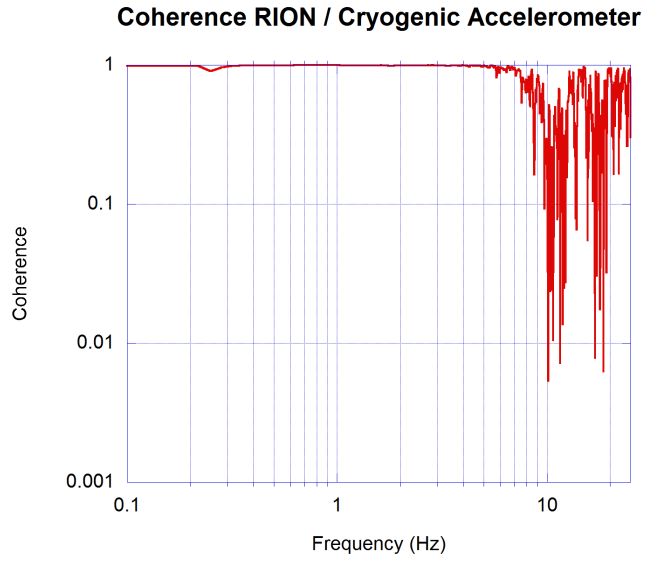

Figure 6.39: Coherence between the output of the cryogenic accelerometer, clamped on the inner radiation shield, and the RION accelerometer, placed on the base flange of the cryostat. Measurements were performed with PT-cryocoolers and vacuum pumps active. Details in the text.

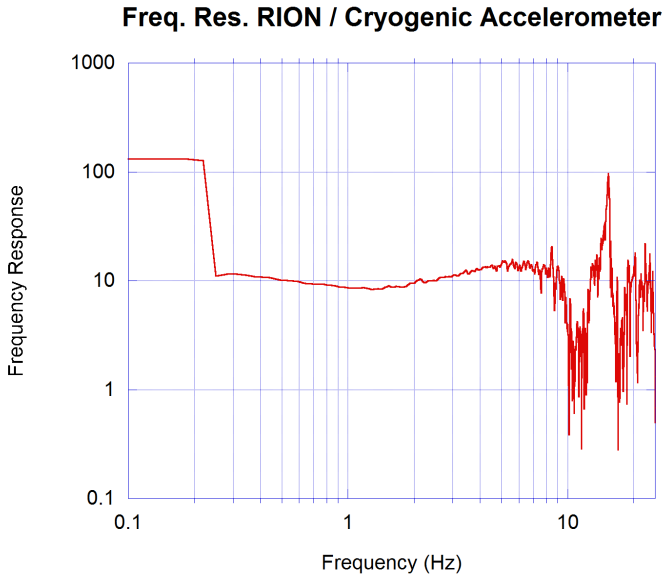

Figure 6.40: Frequency response between the output of the cryogenic accelerometer, clamped on the inner radiation shield, and the RION accelerometer, placed on the base flange of the cryostat. Measurements were performed with PT-cryocoolers and vacuum pumps active. Details in the text.

In fig. 6.41 and 6.42 I show the displacement ASD measured at $T = 111.7\ Hz$. At $f = 11\ Hz$ it is visible the cryostat mode F1, while the peak at 15.25 Hz dominates the displacement spectrum of the radiation shield. Between 20 Hz and 25 Hz are localized some modes for both the cryostat and the shield (see tables 6.2 and 6.3) in addition to the noise generated by the vacuum pumps. The cryostat mode F3 can be seen on the RION trace at $f \approx 35\ Hz$, while the peak at $f \approx 34\ Hz$ can be related to mode F5 of the shield. At $f = 41\ Hz$ and $f \approx 47\ Hz$ are noticeable the shield modes F7 and F8, while from the RION spectrum the peak at $f = 56.25\ Hz$ can be related to the cryostat mode F7 or F8. In fig. 6.43 I report a comparison between the displacement ASD measured on the radiation shield on three days during the cooling phase.
At $T = 72.6\ K$ I measured the displacement ASD in different cases:

1. with both the PT-cryocoolers and the pumps active
2. with only the pumps active and PT-cryocoolers switched off
3. with both the PT-cryocoolers and the pumps switched off
4. with only the PT-cryocoolers active, and pumps switched off

The spectra related to these different cases are shown in fig. 6.44 and 6.45: the noise level between 4 Hz and 15 Hz appears to be slightly higher in the first case, while the peak at 15.25 Hz increases in the last case when the PT-cryocooler was re-switched on. However the average noise level appears similar in all cases, except for few localized peaks.

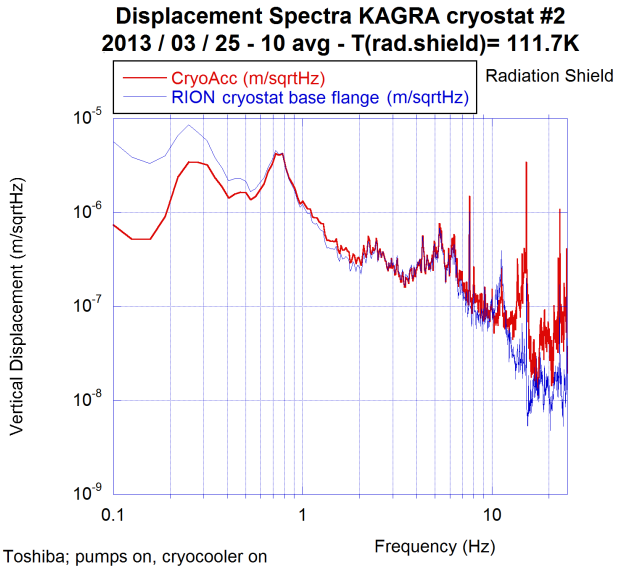

Figure 6.41: Displacement amplitude spectral densities measured on the radiation shield (with the cryogenic accelerometer, red line) and outside on the cryostat base flange (with the RION accelerometer, blue line); $0 - 25\ Hz$ frequency span. Measurements were performed with PT-cryocoolers and vacuum pumps active. Details in the text.

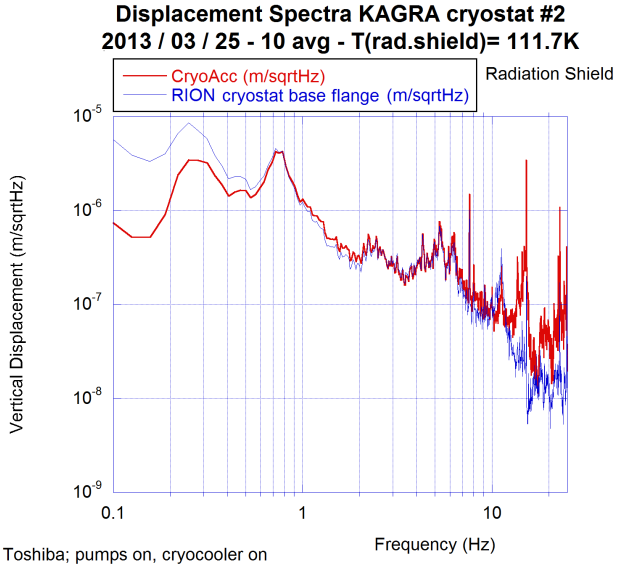

Figure 6.42: Displacement amplitude spectral densities measured on the radiation shield (with the cryogenic accelerometer, red line) and outside on the cryostat base flange (with the RION accelerometer, blue line); $0 - 100\ Hz$ frequency span. Measurements were performed with PT-cryocoolers and vacuum pumps active. Details in the text.

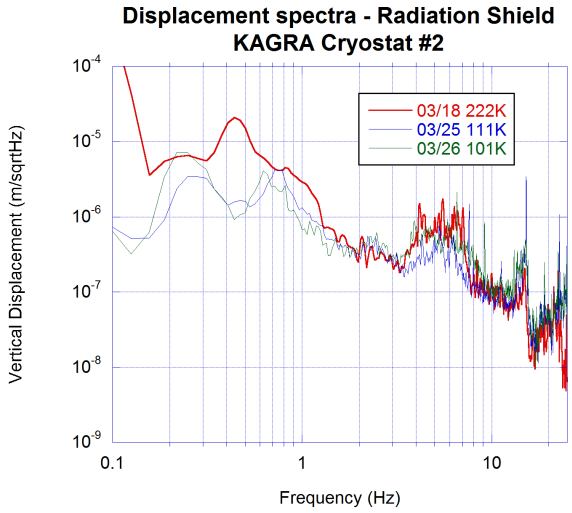

Figure 6.43: Displacement amplitude spectral densities measured on the radiation shield with the cryogenic accelerometer on three days during the cooling phase; $0 - 25\ Hz$ frequency span. Measurements were performed with PT-cryocoolers and vacuum pumps active. See details in the text.

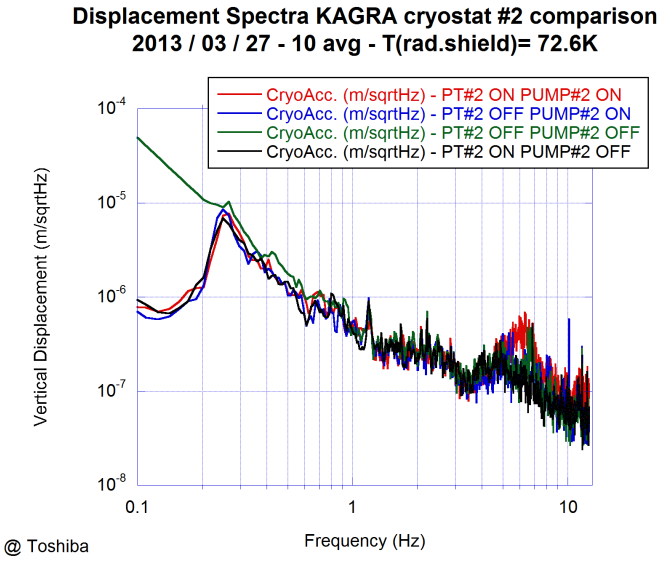

Figure 6.44: Displacement amplitude spectral densities measured on the radiation shield with the cryogenic accelerometer in different cases at $T = 72.6\ K$; $0 - 13\ Hz$ frequency span. Details in the text.

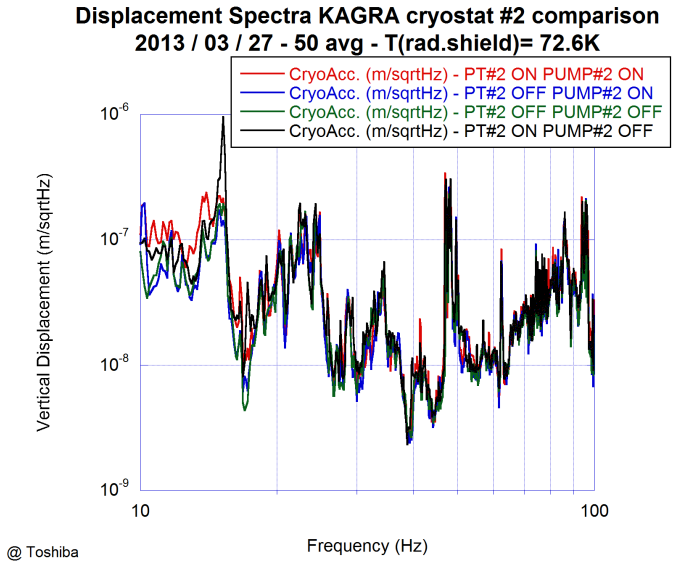

Figure 6.45: Displacement amplitude spectral densities measured on the radiation shield with the cryogenic accelerometer in different cases at $T = 72.6\ K$; $10 - 100\ Hz$ frequency span. Details in the text.

I measured the displacement ASD in the four cases above mentioned when the radiation shield reached $T = 8\ K$: the spectra are shown in fig. 6.46 and 6.47. As already noticed in the previous comparison, the re-activation of the PT-cryocooler in the last case produces a dominant peak at $f = 15.25\ Hz$, while the average noise level is slightly lower when both the pumps and the PT-cryocooler are switched off. In fig. 6.48 I show a comparison between the displacement ASD measured on the radiation shield at several temperatures during the cooling: the variability of the noise level is related to the environmental noise produced by sea waves on the near shore-line (at low frequencies) and by the working activities in the factory during the different days. It is important to note that, while I measured the vertical vibrations on cryostat #2, another cooling test (aimed to measure the horizontal vibrations) was in progress on the cryostat #3, placed a few meters away from the other one. Therefore, the measurement was repeated switching on and off also the pumps and the cryocoolers of the third cryostat: the different cases are reported in fig. 6.49 and 6.50: in the wide frequency range ($1 - 100\ Hz$) the average noise is higher when the vacuum pumps of both cryostats are active.

6.4.3 Measurements in cryostat #3

In July 2013, the cryogenic vertical accelerometer was moved inside the cryostat #3 (see fig. 6.51), clamped to the inner radiation shield, together with another interferometric horizontal accelerometer developed by D. Chen [158], in order to measure the vibration modes both on the vertical and horizontal degree of freedom, during another cooling. The instrumental configuration was similar to that used for the cryostat #2. Since only the third cryostat was under testing, the technical noise was expected to be smaller during these measurements.

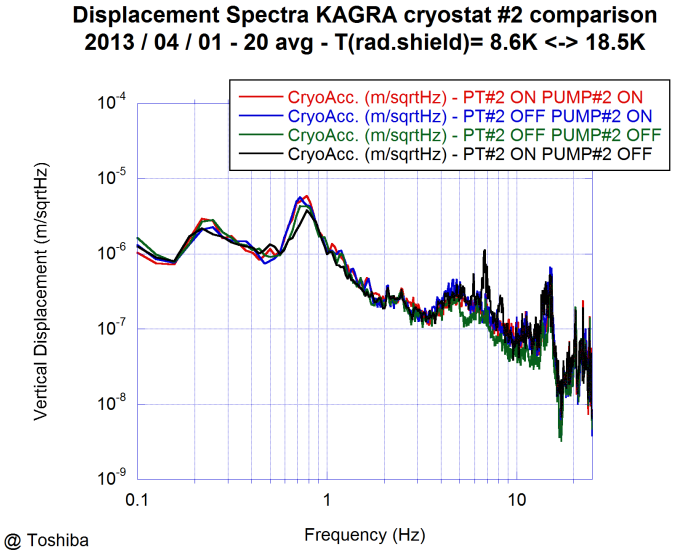

Figure 6.46: Displacement amplitude spectral densities measured on the radiation shield with the cryogenic accelerometer in different cases at $T \approx 8\ K$; $0 - 13\ Hz$ frequency span. The re-activation of the refrigerator excites the mode at $f \approx 7\ Hz$ Details in the text.

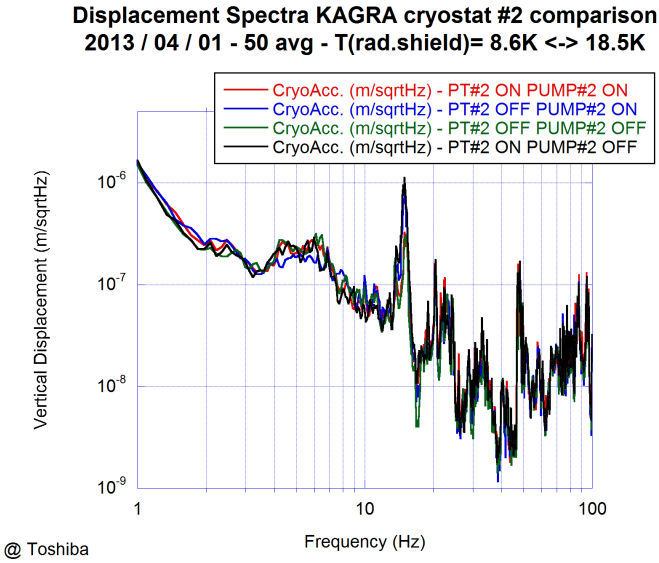

Figure 6.47: Displacement amplitude spectral densities measured on the radiation shield with the cryogenic accelerometer in different cases at $T \approx 8\ K$; $1 - 100\ Hz$ frequency span. The peak at $f \approx 15\ Hz$ is clearly visible when the refrigerator is re-activated. Details in the text.

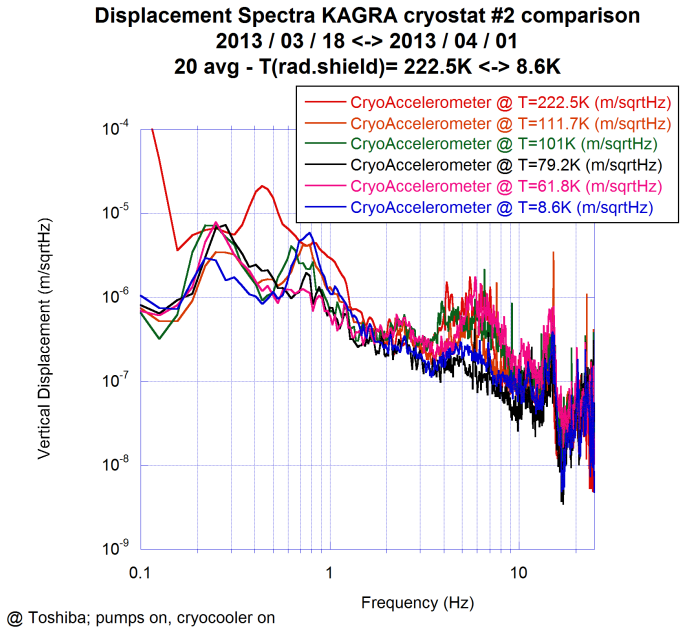

Figure 6.48: Displacement amplitude spectral densities measured on the radiation shield with the cryogenic accelerometer at several temperatures during the cooling; $0 - 13$ Hz frequency span. Measurements were performed with PT-cryocoolers and vacuum pumps active in different days (i.e. with different seismic background noises). Details in the text.

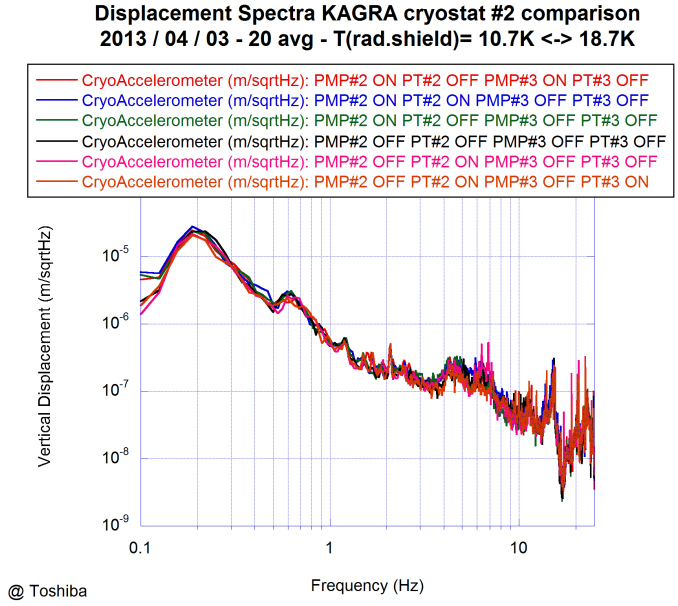

Figure 6.49: Displacement amplitude spectral densities measured on the radiation shield with the cryogenic accelerometer in several cases, switching on and off the pumps and the PT-cryocoolers of cryostat #2 and #3; $0 - 25$ Hz frequency span. Details in the text.

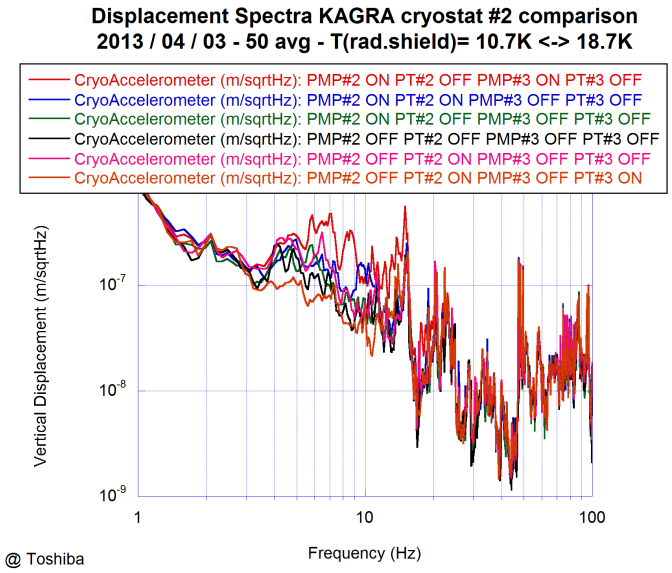

Figure 6.50: Displacement amplitude spectral densities measured on the radiation shield with the cryogenic accelerometer in several cases, switching on and off the pumps and the PT-cryocoolers of cryostat #2 and #3; $1-100\ Hz$ frequency span. Details in the text.

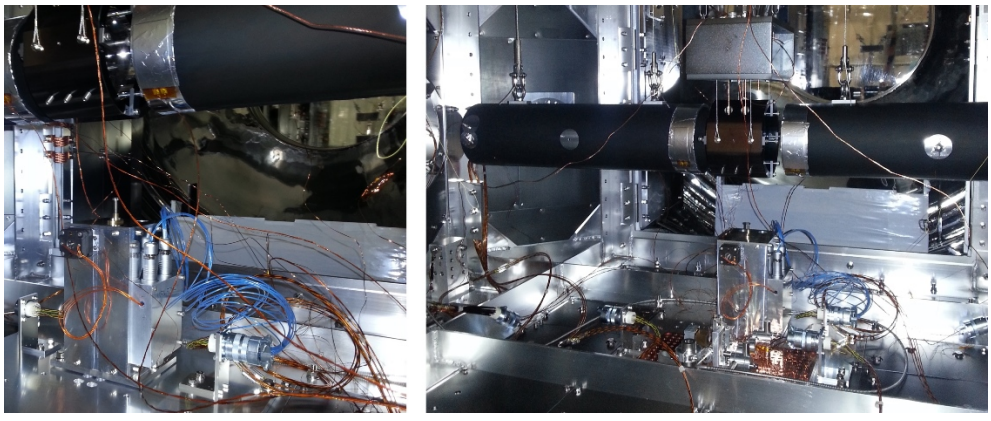

Figure 6.51: The cryogenic vertical accelerometer installed into the cryostat #3 of KAGRA. Inside the cryostat there were also an horizontal interferometric accelerometer [158] (on the same plate clamped to the radiation shield) and a dummy payload suspended above the instruments, for other parallel measurements.

Displacement spectra

In fig. 6.52 I show the displacement ASD at the start of cryostat #3 cooling test, measured whit the PT-cryocoolers switched on and off. The noise level increases of almost one order of magnitude between 4 Hz and 10 Hz and above 65 Hz when the refrigerators are activated. This effect may be partially due to a transient technical noise, in fact in other spectra taken during the cooling the broadband increase was not so high. Two peaks are visible at $f = 6.25$ Hz and $f = 10$ Hz, especially when the PT-cryocoolers are switched off, while the cryostat mode F1 can be observed with a smaller amplitude at $f \approx 11$ Hz. Similarly to cryostat #2, there is a peak at 15.25 Hz, whose amplitude is larger when the PT-cryocooler is active. The peak at $f = 18.6$ Hz may be related to the shield mode F1; between 20 Hz and 25 Hz there are peaks due to vacuum pumps and to some shield modes (see tab. 6.3). Two other peaks at $f = 33$ Hz and $f = 46$ Hz may be related to shield modes F5 and F8.

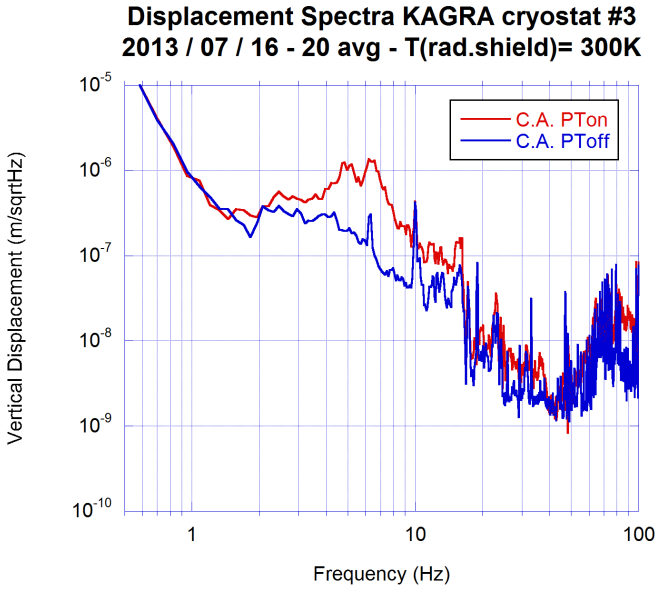

Figure 6.52: Displacement amplitude spectral densities measured on the radiation shield with the cryogenic accelerometer at the cooling start in two cases: with PT-cryocoolers active and with them switched off; $0 - 100$ Hz frequency span. The broadband noise increase may be due to a transient technical noise. Details in the text.

A slightly smaller noise increase with the PT-cryocoolers active is also visible in the spectra taken at $T = 144$ K, shown in fig. 6.53 and 6.54. Peaks are evident at $f = 7.6$ Hz, $f = 10$ Hz, $f = 15.25$ Hz and between 20 Hz and 25 Hz, while it is noticeable the noise increment around 13.5 Hz and 46 Hz when the refrigerator is activated; the last peak can be related to shield mode F8.

The four PT-cryocoolers which provide the refrigeration power to the cryostat are connected to different elements:

- PT-1 and PT-3 are connected to the radiation shield;

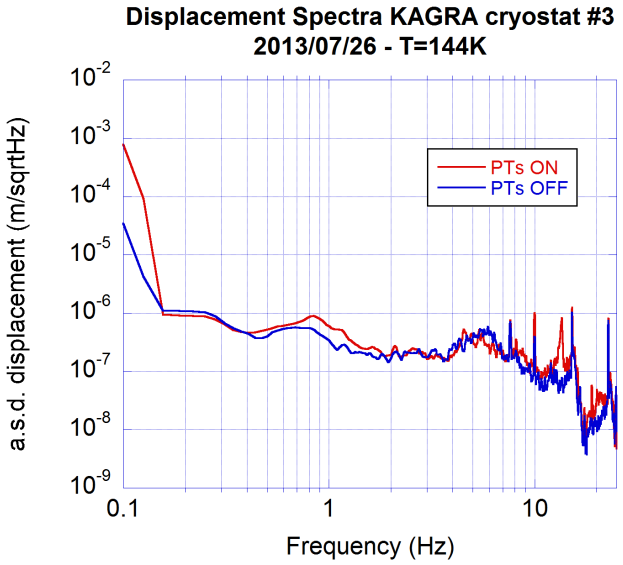

Figure 6.53: Displacement amplitude spectral densities measured on the radiation shield with the cryogenic accelerometer in two cases: with PT-cryocoolers active and with them switched off; $0 - 25\ Hz$ frequency span. Details in the text.

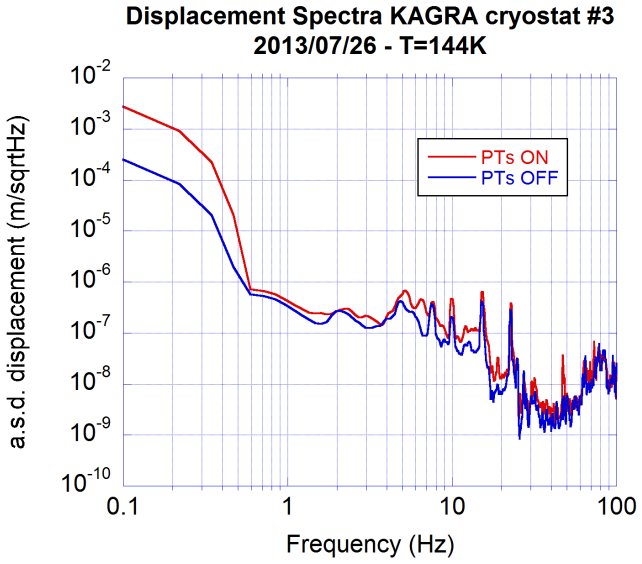

Figure 6.54: Displacement amplitude spectral densities measured on the radiation shield with the cryogenic accelerometer in two cases: with PT-cryocoolers active and with them switched off; $0 - 100\ Hz$ frequency span. Details in the text.

- PT-2 and PT-4 are connected to the cryogenic payload, i.e. to the suspended elements into the cryostat.

In order to check the contribution of every single PT-cryocooler to the overall vibration of the inner radiation shield, where the cryogenic vertical accelerometer is clamped, different spectra were taken at $T = 10\ K$ with the refrigerators alternatively activated or switched off. The characteristic peaks above mentioned seems to remain stable in the different cases, but the overall noise, especially in the band $3 - 15\ Hz$, increases up to a factor ~ 4 when all the PT-cryocoolers are active. Noticeably, the main contribution to this increase comes from PT-2 and PT-4, those not connected to the radiation shield: therefore, a mechanical transmission channel, from the heat-links connected to the payload and the inner shield, must be identified.

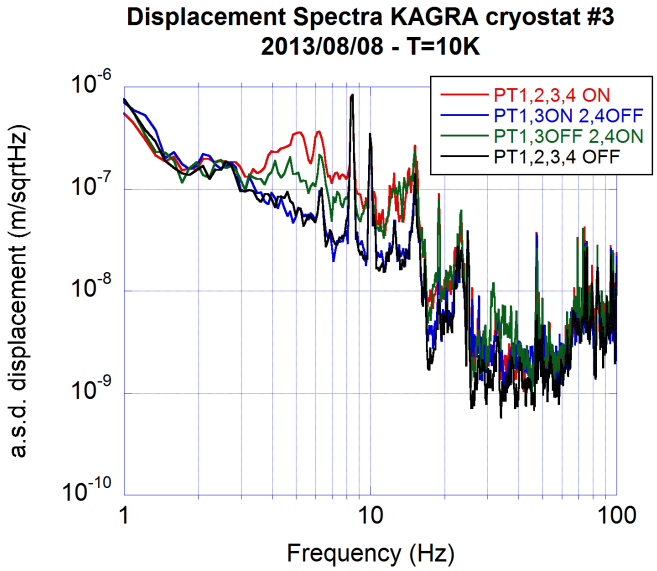

Figure 6.55: Displacement amplitude spectral densities measured on the radiation shield with the cryogenic accelerometer at $T = 10\ K$ in four cases: a) with all PT-cryocoolers active; b) with only PT-1,3 active; c) with only PT-2,4 active; d) with all the refrigerator switched off. $0 - 100\ Hz$ frequency span. Details in the text.

However, the broadband noise increase between 3 and 15 Hz can be related to a transient noise during this measure: in order to check this hypothesis, keeping the inner radiation shield at $T = 10\ K$, measurements were repeated switching on and off all the PT-cryocoolers. The spectra from the cryogenic vertical accelerometer, clamped to the inner radiation shield, and the RION accelerometer, placed on the cryostat base flange, are shown in fig. 6.56 and 6.57. The dominant peak below 1 Hz is due to the microseism produced by the sea, while for $f > 2\ Hz$ there is a slight increase of the noise level when the PT-cryocooler are active, observed also with the RION placed outside, but it is not so drastic as in fig. 6.55. In particular, refrigerating operations seems to excite vibration modes at $f \approx 5.5\ Hz$ and $f = 11.5\ Hz$ (i.e. the shield mode F1). In these spectra, the peak at 15.25 Hz

is not observed outside by the RION accelerometer. During the following heating of the cryostat, another comparison was made at $T = 48\ K$, shown in fig. 6.58: the radiation shield shows dominant peaks at $f = 10\ Hz$, $f = 15.25\ Hz$ (also seen by the RION accelerometer outside, with a smaller amplitude), $f = 19\ Hz$ (excited by PT-cryocooler activation), between 20 Hz and 25 Hz (vacuum pumps and shield modes $F1 - 4$), $f = 32.8\ Hz$, $f = 38\ Hz$ (shield mode F6), $f = 41.8\ Hz$ (shield mode F7, excited by PT-cryocooler activation), $f = 47.6\ Hz$ (maybe related to shield mode F8, excited by PT-cryocooler activation). From $f \approx 40\ Hz$ the noise level on the radiation shield is higher than outside the cryostat: a similar effect was reported in the cryostat of CLIO [92].

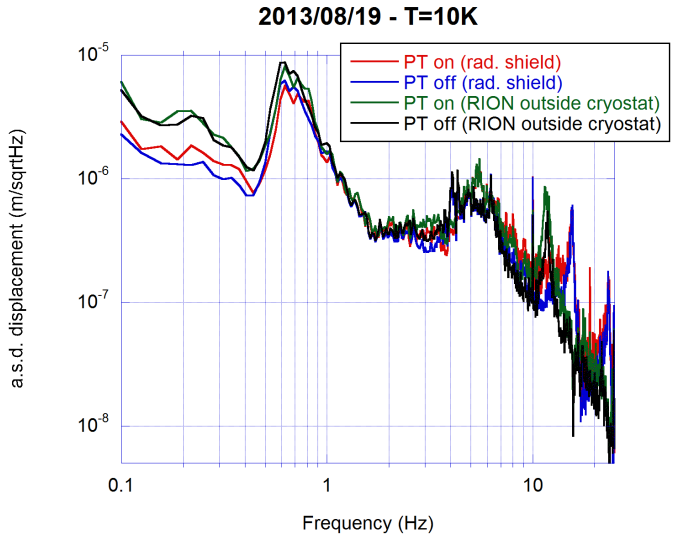

Figure 6.56: Displacement amplitude spectral densities measured on the radiation shield at $T = 10\ K$, with the cryogenic accelerometer, and outside the cryostat, with the RION accelerometer, in two cases: with PT-cryocoolers active and with them switched off; $0 - 25\ Hz$ frequency span. Details in the text.

6.4.4 Impact on the sensitivity curve

The vibrations of the radiation shield, caused by the PT-cryocoolers, can affect the cryogenic payload of KAGRA through the heat-links which provide the refrigeration power the the last stage of the suspension. In order to estimate the impact of the measured vibrations on the design sensitivity curve of the detector, the ratio between the spectra taken with the PT refrigerators switched on and off is considered (fig. 6.59), from the data represented in fig. 6.58. Taking a threshold value from this ratio, and applying the multiplicative parameters listed in tab. 6.4, the sensitivity curve with the addition of the vibrational noise transmitted through the heat-links is calculated by means of a code developed by T. Sekiguchi within the KAGRA collaboration.

I show the design sensitivity curve of KAGRA overlapped to the noise transmitted through the heat-links in fig. 6.60. The vibrational noise affects the sensi-

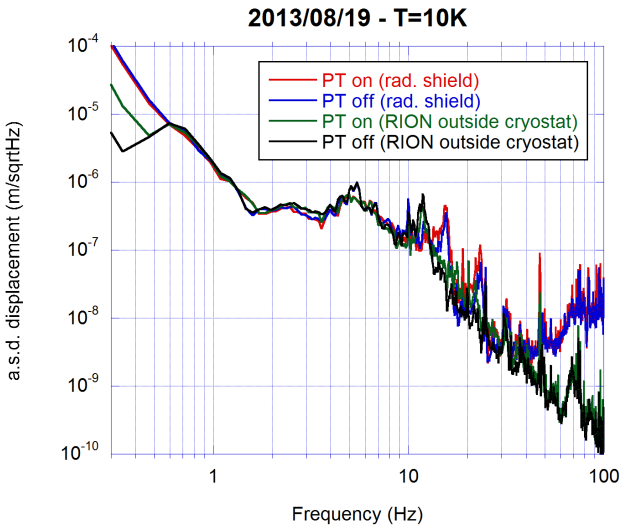

Figure 6.57: Displacement amplitude spectral densities measured on the radiation shield at $T = 10\ K$, with the cryogenic accelerometer, and outside the cryostat, with the RION accelerometer, in two cases: with PT-cryocoolers active and with them switched off; $0 - 100\ Hz$ frequency span. From $f \approx 40\ Hz$ the noise level on the radiation shield is higher than outside the cryostat. Details in the text.

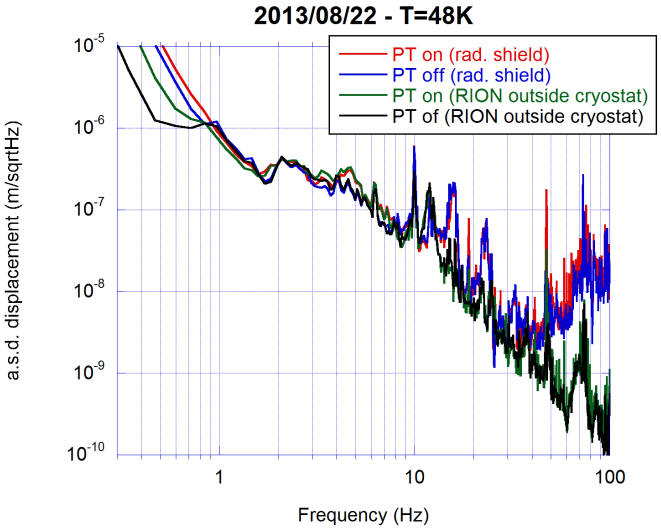

Figure 6.58: Displacement amplitude spectral densities measured on the radiation shield at $T \approx 48\ K$ (during the heating), with the cryogenic accelerometer, and outside the cryostat, with the RION accelerometer, in two cases: with PT-cryocoolers active and with them switched off; $0 - 100\ Hz$ frequency span. From $f \approx 40\ Hz$ the noise level on the radiation shield is higher than outside the cryostat. Details in the text.

KAGRA multiplicative transmission parameters

Value	Cause
1/300	slope of the tunnel
1/3000	length of the arm
$\sqrt{2}$	number of heat-links
$\sqrt{4}$	number of mirrors

Table 6.4: Multiplicative parameters used in the code developed by T. Sekiguchi in order to calculate the sensitivity curve of KAGRA considering the radiation shield vibrational noise transmitted through the heat-links to mirrors.

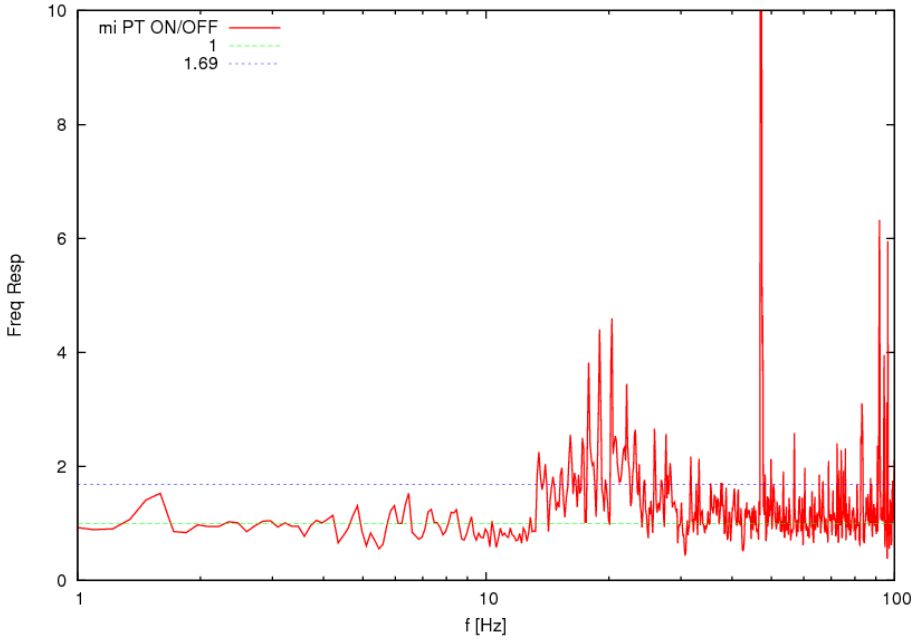

Figure 6.59: The ratio between the displacement amplitude spectral densities, measured by the cryogenic vertical accelerometer at $T = 10\ K$, switching on and off the PT-cryocoolers. Two threshold values are taken into account for the calculation of the impact on the design sensitivity curve of KAGRA.

tivity curve especially around 15 Hz, suggesting that the development a vertical-vibration filter dedicated to heat-links may be needed.

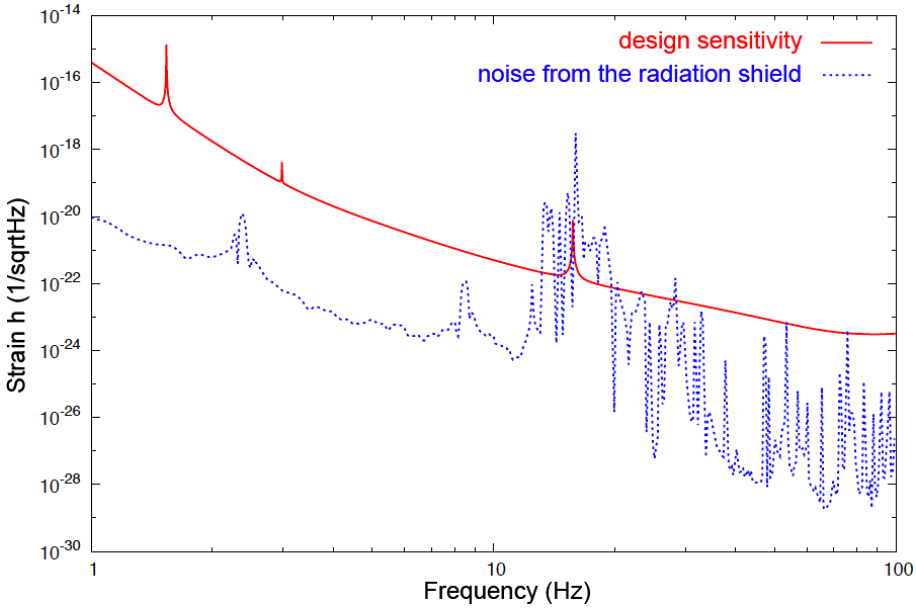

Figure 6.60: The design sensitivity curve of KAGRA overlapped to the noise caused by the vibrations of the radiation shield, transmitted through the heat-links. The vibrational data was obtained by the measurements made with the cryogenic vertical accelerometer; the plot was calculated using the dedicated code developed by T. Sekiguchi. Courtesy of D. Chen.

Conclusions

The development of routine gravitational astronomy will require a third generation of interferometric detectors. The investigation in this field has led to the proposal of the Einstein Telescope (ET), a European detector characterized by a considerably improved sensitivity respect to initial and advanced interferometers, whose construction is expected to begin before the 2020. Since many interesting astronomical sources emit gravitational radiation in the range of few Hz (e.g. rotating neutron stars), the bandwidth of third generation detectors will be extended to the low frequencies, down to $\sim 1 - 2\ Hz$. In this range the sensitivity of the interferometer is limited by two main sources of noise: the seismic noise, which perturbs the detector test masses through ground vibrations and seismically-induced fluctuating gravity gradient (known as *Newtonian noise*, NN), and the thermal noise, which perturbs the mechanical and optical parts of the detector. Therefore, the suppression of these noises is a fundamental task for the development of gravitational astronomy.

The seismic noise can be limited by choosing a suitable site characterized by a low seismic background and low population density. The purely vibrational seismic noise will be attenuated by means of vertical and horizontal suspension filters, similar to those used in the previous generations of detector (e.g. the superattenuator of Virgo). However, the seismically-induced NN couples directly to the test masses, short-circuiting all the attenuator stages: to overcome this limit third generation detectors will be hosted in underground structures, where Rayleigh waves are attenuated and the surrounding rock layers are more homogeneous and stable, resulting in reduced density fluctuations. Moreover, NN subtraction techniques are under development and will require adequate seismic surveys in order to set-up the necessary seismic arrays. The other low-frequency limit due to the thermal noise will be overcome by cooling down the test masses of the interferometer, introducing large cryostats and dedicated cryocoolers. The noise injected by such a cryogenic apparatus must be monitored, so that low-frequency cryogenic sensors for positioning control and damping will be required.

The work presented in this thesis is focused on the improvement of low-frequency detector sensitivity through the suppression of the above-mentioned seismic and thermal noises. In such a context, I worked on the seismic characterization of a potential site for ET and on the development of a vertical accelerometer suitable for cryogenic operations.

In the first experimental activity, I built an underground measuring station, part of a still-growing array of seismometers and environmental sensors, in the former mine of Sos Enattos (Sardinia - Italy). In this station I installed a high-sensitivity

three-axial seismometer (a *Trillium 240*) for long-period measurements. It took data from July 2012 to June 2013, covering about one year of observation. I analyzed the seismic stability of the site and seasonal effects produced by local and global weather conditions. In particular, I studied the correlation between the Tyrrhenian sea meteorological state and the microseismic activity measured in the underground station. As expected, the main contribution to the low-frequency seismic noise arises from sea-generated microseisms, but starting from $\sim 1\ Hz$ (i.e. in the detection bandwidth of ET) the seismic background approaches the Peterson's low noise model with a good stability during the whole year of observation, validating the site as a low seismic noise environment suitable for the construction of a third generation interferometric detector. In the next future the seismic array will be extended by integrating other underground stations equipped with high-sensitivity seismometers developed by the University of Salerno; the optical fiber network already installed in the site will ensure a common timing for all the seismometers, allowing further detailed seismic studies, e.g. coherence analyses between the stations, that will contribute to the development of ad-hoc NN subtraction techniques.

In the second part of my experimental activity I developed a vertical accelerometer suitable for cryogenic operation. It is derived from a kind of room-temperature sensors used in the suspension control of Virgo, based on the displacement sensing between a suspended mass and a suspending structure, with the aid of a feedback control loop that keeps the constant distance between the mass and the structure, so that the acceleration applied to the sensing mass is directly measured from the force actuation signal to the mass. Thermal contractions and electric unbalancing are the main concern when cooling down such kind of a device, since they produce a shift of the working point and signal saturation. In order to compensate such effects, I installed a stepper motor which allows the adjustment of the suspended mass position, and an external resistive trimmer which is used to reach the fine tuning of the displacement LVDT sensor. The calibration check at low temperature, in absence of commercial sensors working in parallel, plays a crucial role, therefore I calibrated the accelerometer in a dedicated cryostat (the vibration free cryostat, VFC), equipped with piezoelectric actuators. Finally, I installed the cryogenic vertical accelerometer into the inner radiation shield of cryostat #2 and #3 of the gravitational wave detector KAGRA, presently under construction in Japan, in order to measure the vertical vibrations produced by the cryogenic apparatus: these measurements confirmed the versatility of the sensor and its proper operation at $T = 8\ K$; moreover this experimental test provided an estimate of the impact of the cryostat vibrational modes on the detector sensitivity. A foreseeable development of the cryogenic accelerometer presented in this work is the implementation of the sensor into the control system of the VFC for the inertial position sensing of the pulse-tube refrigerator *cold head*. Figuring out a variety of future applications in other research areas that require cryogenics in precision measurements, the compactness of the sensor is one of the main issues to be dealt: in a future version, the accelerometer volume can be further and significantly reduced in height by changing the floating-mass shape and, if necessary, the read-out sensor, keeping the motorized regulation of the set-point, which has proven to be

reliable. An horizontal accelerometer can be easily obtained from the vertical scheme presented in this work with minor changes.

Conclusioni

Nei prossimi anni i rivelatori interferometrici di terza generazione apriranno finalmente l'era dell'astronomia gravitazionale di precisione. Le ricerche condotte in questo ambito hanno già portato alla proposta di un rivelatore europeo, denomeniato Einstein Telescope (ET) e caratterizzato da una più alta sensibilità rispetto ai primi rivelatori interferometrici nella loro versione iniziale e avanzata. Il progetto di ET è stato presentato nel design study del 2011, prevedendo l'inizio della costruzione del rivelatore entro il 2020. Poichè molte sorgenti astronomiche di onde gravitazionali emettono a bassa frequenza (come ad esempio molte stelle di neutroni rotanti), il limite inferiore della banda di rivelazione degli interferometri di terza generazione sarà esteso fino a $1 - 2\ Hz$. In questa banda la sensibilità dei rivelatori interferometrici è limitata da due principali sorgenti di rumore: dal rumore sismico, che perturba le masse di test del rivelatore, direttamente per mezzo delle vibrazioni sismiche del terreno e indirettamente attraverso il gradiente gravitazionale variabile indotto dalle fluttuazioni di densità di massa prodotte dalle stesse onde sismiche (rumore newtoniano), e dal rumore termico, che perturba le parti meccaniche e ottiche del sistema. Di conseguenza la soppressione di queste sorgenti di rumore a bassa frequenza è uno degli aspetti principali che devono essere trattati per rendere possibile lo sviluppo dell'astronomia gravitazionale.

Il rumore sismico può essere limitato scegliendo per la costruzione del rivelatore un sito caratterizzato da una ridotta sismicità e da una bassa densità di popolazione nelle aree circostanti. Il rumore sismico puramente vibrazionale sarà attenuato per mezzo di sospensioni meccaniche (che agiscono da filtri bassa-passo verticali e orizzontali) dello stesso tipo di quelli usati nelle prime generazioni di rivelatori, come ad esempio il superattenuatore di Virgo. Nonostante questa attenuazione diretta delle vibrazioni sismiche, il rumore newtoniano da queste generato agisce direttamente sulle masse di test, cortociruitando tutta la catena di filtri: per fronteggiare questa limitazione, i rivelatori di terza generazione saranno costruiti all'interno di infrastrutture sotterranee, dove le onde di Rayleigh sono sufficientemente attenuate dall'ambiente costituito di strati rocciosi più omogenei e stabili, e di conseguenza da fluttuazioni di densità di massa più limitate che in superficie. Inoltre sono in fase di studio delle tecniche di sottrazione del rumore newtoniano che richiederanno approfonditi studi sismici dei siti proposti per ottimizzare la disposizione dei sensori necessari. L'altro limite alla sensibilità a bassa frequenza è causato dal rumore termico, la cui riduzione richiederà il raffreddamento criogenico delle masse di test dell'interferometro, collocando parte dell'esperimento all'interno di grandi criostati e integrando nei sistemi i necessari criorefrigeratori. L'adozione della criogenia negli interferometri di terza generazione introdurrà un ulteriore sorgente

di rumore vibrazionale che dovrà essere controllato, di conseguenza sarà necessario sviluppare nuovi sensori di posizione di precisione, sensibili alle basse frequenze e compatibili con le temperature criogeniche a cui dovranno operare.

Il lavoro che presento in questa tesi è focalizzato al miglioramento della sensibilità dei futuri rivelatori interferometrici attraverso la soppressione dei suddetti rumori sismico e termico. In questo contesto ho lavorato alla caratterizzazione sismica di uno dei siti potenziali per la costruzione di ET e allo sviluppo di un accelerometro verticale compatibile con l'utilizzo in criogenia.

Nella prima attività sperimentale mi sono occupato della costruzione di una stazione sotterranea di misura, parte di una rete di sismometri e sensori ambientali tutt'ora in espansione, nella ex miniera di Sos Enattos in Sardegna. In questa stazione ho installato un sismometro triassiale caratterizzato da un'alta sensibilità alle basse frequenze (un Trillium 240), per ottenere una serie di misure su lungo periodo. La stazione di misura ha acquisito dati dal luglio 2012 a giugno 2013, coprendo un periodo di quasi un anno di osservazione. Ho analizzato la stabilità sismica del sito e gli effetti stagionali prodotti dalle condizioni meteorologiche locali e globali. In particolare ho studiato la correlazione tra lo stato meteorologico del mar Tirreno e l'attività microsismica misurata nella stazione sotterranea. Come previsto il principale contributo al rumore sismico a bassa frequenza deriva dai microsismi generati dall'onda marina, ma a partire da circa 1 Hz (cioè nella banda di rivelazione di ET) il rumore sismico misurato si avvicina al modello di minima sismicità di Peterson (NLNM) mostrando una buona stabilità nell'arco dell'intero anno di osservazione, e verificando che la miniera di Sos Enattos è caratterizzata da una bassa sismicità ambientale compatibile con la costruzione di un interferometro di terza generazione quale ET. Nel prossimo futuro la rete sismica del sito sarà integrata con altre stazioni sotterranee equipaggiate con sismometri ad alta precisione sviluppati dall'Università di Salerno; la rete di connessione in fibra ottica già installata nel sito provvederà a fornire a tutti i sensori un comune riferimento temporale, permettendo ulteriori studi dettagliati, come ad esempio l'analisi di coerenza tra le varie stazioni, contribuendo allo sviluppo delle necessarie tecniche di sottrazione del rumore newtoniano.

Nella seconda parte della ricerca sperimentale presentata in questa tesi, ho lavorato allo sviluppo di un accelerometro verticale per applicazioni criogeniche. Questo sensore è derivato dal tipo di accelerometri utilizzati nel controllo della sospensione delle masse di test in Virgo, basati sulla misura dello spostamento di una massa sospesa rispetto alla struttura di sospensione, con l'applicazione di un controllo in feedback che mantiene la massa centrata, cosicché l'accelerazione inerziale sperimentata dalla massa è proporzionale dalla forza prodotta dall'attuatore elettromagnetico che chiude il controllo. Le contrazioni termiche e lo sbilanciamento elettrico sono i principali problemi da affrontare quando un sensore di questo tipo viene raffreddato a temperature criogeniche, poichè causano uno spostamento del punto di lavoro e conseguentemente la saturazione del segnale di uscita. Per compensare questi effetti termici ho installato un motore passo-passo che permette di riportare la massa sospesa nel punto di lavoro, e un trimmer resistivo esterno che può essere utilizzato per annullare lo sbilanciamento elettrico sul circuito secondario del sensore di posizione LVDT. La verifica della calibrazione a tempe-

rature criogeniche, in assenza di sensori commerciali di pari sensibilità capaci di operare nelle stesse condizioni, gioca un ruolo fondamentale, perciò ho calibrato l'accelerometro in un criostato dedicato (il vibration free cryostat VFC), equipaggiato con attuatori piezoelettrici. Successivamente ai test criogenici e di calibrazione, ho installato il sensore all'interno dello schermo termico dei criostati #2 e #3 del rivelatore di onde gravitazionali KAGRA, attualmente in costruzione in Giappone, in modo tale da misurare le vibrazioni verticali prodotte dall'apparato criogenico: queste misure hanno confermato la versatilità dell'accelerometro e il suo corretto funzionamento a T=8 K; inoltre questo test sperimentale ha fornito una stima dell'impatto che avrà l'adozione della criogenia sulla sensibilità complessiva del rivelatore. Un futuro sviluppo dell'accelerometro criogenico presentato in questo lavoro sarà l'implementazione del sensore nel sistema di soppressione attiva delle vibrazioni del VFC, per il controllo inerziale di posizione della testa fredda del refrigeratore a tubo pulsato. Prevedendo altre applicazioni in altri campi di ricerca che richiedono misure di precisione in condizioni di criogenia, la compattezza del sensore sarà una delle principali questioni da affrontare: in una versione futura, il volume dell'accelerometro potrà essere ridotto in altezza cambiando il profilo della massa sospesa e, se necessario, il sensore di posizione, mantenendo la regolazione motorizzata del punto di lavoro, che si è dimostrata affidabile in tutti i cicli di raffreddamento a cui il sensore è stato sottoposto. Un accelerometro orizzontale basato sullo stesso schema di quello verticale presentato in questa tesi può essere ottenuto mediante piccole modifiche di questo progetto.

Part IV

Appendices

Appendix A

Spectral densities in interferometers

Let us consider the signal $X(t)$ related to the physical quantity $x(t)$. The **root mean square value** (RMS), is given by:

$$X_{RMS} = \sqrt{\lim_{T\to\infty} \frac{1}{2T} \int_{-T}^{+T} X^2(t)dt} \tag{A.1}$$

In order to separate the contributions to the signal $X(t)$ coming from different frequencies we can define the **power spectral density** (PSD) of the signal. By means of the Wiener-Khinchin theorem [159, 160], the PSD can be expressed as the Fourier transform of the auto-correlation of the signal $X(t)$:

$$S(\omega) = \mathcal{F}\{R_{XX}(\tau)\}(\omega) = \int_{-\infty}^{+\infty} e^{-i\omega\tau} R_{XX}(\tau)d\tau \tag{A.2}$$

where $\omega = 2\pi f$ and the auto-correlation $R_{XX}(\tau)$ is given by:

$$R_{XX}(\tau) = \lim_{T\to\infty} \int_{-T}^{+T} X(t)X(t+\tau)dt \tag{A.3}$$

For most physical signals the PSD can be also defined as:

$$S(\omega) = \lim_{T\to\infty} \frac{1}{2T} \left| \int_{-T}^{+T} X(t)e^{-i\omega t}dt \right|^2 \tag{A.4}$$

If the physical units of the signal are $[X]$, then the PSD will be given in $[X]^2/Hz$ units.

Considering instead two signals $X(t)$ and $Y(t)$, each of which with its PSD $S_i(\omega)$, we can define a **cross-spectral density** (CSD) as the Fourier transform of the cross-correlation between the two signals:

$$S_{XY}(\omega) = \mathcal{F}\{R_{XY}(\tau)\}(\omega) = \int_{-\infty}^{+\infty} e^{-i\omega\tau} R_{XY}(\tau)d\tau \tag{A.5}$$

where the cross-correlation function $R_{XY}(\tau)$ between $X(t)$ and $Y(t)$ is given by:

$$R_{XY}(\tau) = \lim_{T\to\infty} \int_{-T}^{+T} X(t)Y(t+\tau)dt \tag{A.6}$$

Therefore, the PSD is a special case of the CSD with $X(t) = Y(t)$.

The **amplitude spectral density** (ASD) of the signal $X(t)$ is defined as the root square of the PSD:

$$\tilde{X}(\omega) = \sqrt{S(\omega)} \tag{A.7}$$

and it is given in $[X]/\sqrt{Hz}$ units.

In interferometric detectors it is convenient to use the strain **equivalent spectral density** in h, related to the gravitational wave strain noise ASD $\tilde{X}(\omega) = \tilde{x}(\omega)$. It is defined as the amplitude $\tilde{h}$ that an incoming gravitational wave must have in order to produce the same output as detector internal noise, that is to have a SNR=1. For an interferometer with arms of length L, the contribution of the strain noise $\tilde{x}(\omega)$ to the effective gravitational wave noise is defined by:

$$\tilde{h}_x(\omega) = \frac{\tilde{x}(\omega)}{L} \tag{A.8}$$

The equivalent spectral density $\tilde{h}_x(\omega)$ is given in the typical units of the strain sensitivity, $Hz^{-1/2}$.

Appendix B

Trillium-240 data elaboration

The *Trillium 240* seismometer, made by Nanometrics Inc., is a sensor suitable for microseismic measurements between 10 mHz and $5 - 10$ Hz, as shown in fig. 5.14, where the sensor intrinsic noise is compared to the Peterson's NLNM [99]. This kind of seismometer is sensitive to both the magnetic fields and temperature variations. For this reason, the environmental conditions must be monitored, and the sensor must be properly insulated with a thermal shield. Moreover, the calibration of the sensor output must be performed when he seismometer has reached the thermal equilibrium with the environment, i.e. at least $12 - 24$ h after the installation in the site. Before the data acquisition, it is also necessary to perform the sensor's mass centering, by means of a dedicated command sent to the device.

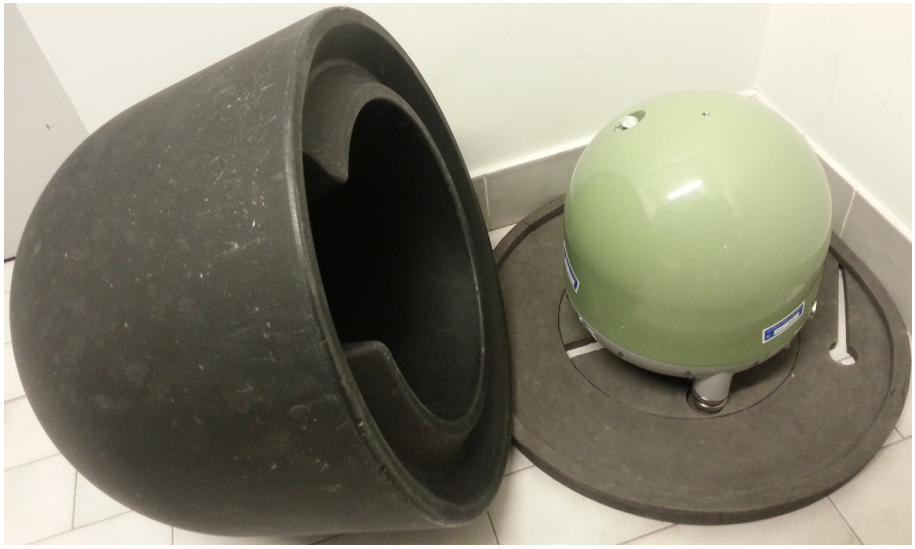

Figure B.1: The Trillium 240 seismometer with its thermal shield.

The seismometer sensing elements are oriented along the three orthogonal axes u, v and w, that are rotated respect to the x, y and z directions (see fig. B.2); therefore, in order to obtain the seismic measure along cardinal and vertical direction, the output signal must be transformed through a rotation matrix, which is reported

in the following eq. B.1.

$$\begin{bmatrix} x \\ y \\ z \end{bmatrix} = \frac{1}{\sqrt{6}} \cdot \begin{bmatrix} 2 & -1 & -1 \\ 0 & \sqrt{3} & -\sqrt{3} \\ \sqrt{2} & \sqrt{2} & \sqrt{2} \end{bmatrix} \cdot \begin{bmatrix} u \\ v \\ w \end{bmatrix} \tag{B.1}$$

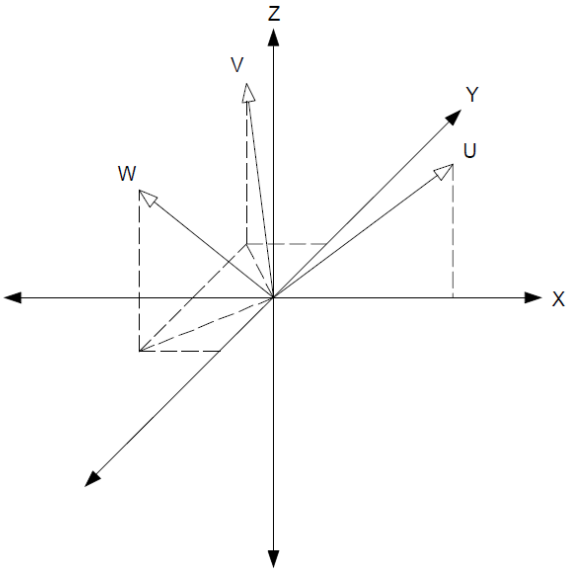

Figure B.2: The orientation of sensing elements in the Trillium 240 seismometer.

The data produced by the three channels of the sensor is acquired by the *Taurus* DAQ system (made by Nanometrics Inc.), based on a Linux kernel, and stored in the local memory, into the Linux Ext3 compressed file format *.store*. In order to extract a time-series from the stored data it is necessary to elaborate the *.store* files through the server *Apollo*, made by Nanometrics, which provide an output file in MiniSEED, seisan or ASCII format (see fig. B.3 and B.4). Selecting

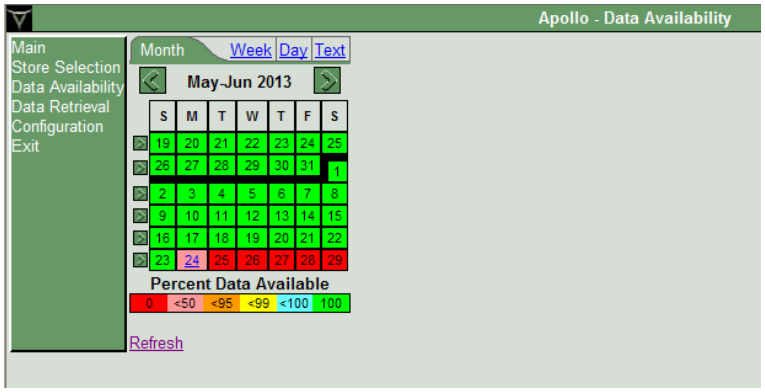

Figure B.3: The graphical user interface of the Apollo server which handles the Taurus-generated *.store* files. Here the data availability is displayed.

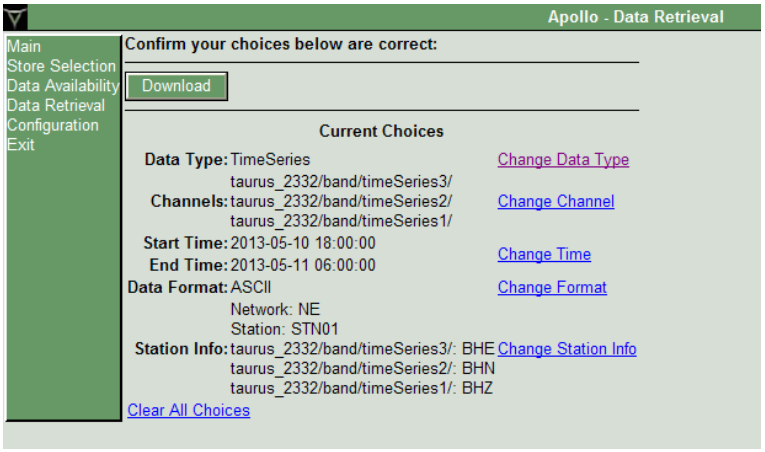

Figure B.4: The graphical user interface of the Apollo server which handles the Taurus-generated *.store* files. Here the data retrieval is displayed.

the ASCII format, the *.txt* output file contains the counts output data listed at the selected sampling frequency for each channel, interspersed with headers. I chose the sampling frequency of $\nu = 40\ Hz$ and the sensitivity $G = 1.196 \times 10^9\ counts/m/s$. The ASCII output file produced by *Apollo* appears as follows:

Listing B.1: example of ASCII Apollo output file.

```
StnLocChn: STN01    BHZ
NetWork ID: NE
Site Name: STN01
Comment: ...
Sensor Type: ...
Data Format: ...
Latitude: 40.445555
Longitude: 9.456944
        Elevation: 227
        Depth: ...
        Azimuth: ...
Dip: ...
Sensitivity: ...
        Sens Freq: ...
        Sens Units: ...
        Calib Units: ...
Sample Rate: 40
Max Clock Drift: ...
Channel Flags: ...
Update Flag: ...
        Start Valid Time: ...
        End Valid Time: ...
Response File: ...
   Start Time: 2013-05-30_17:59:51.6500
```

```
    End Time: 2013-05-31_06:00:01.9250
Number of Samples: 412
DC Offset: ...
     Max Amplitude: ...
     Min Amplitude: ...
Format: YFILE
        578,        574,        560,        552,        540,
        525,        513,        493,        485,        470,
            ...
```

In order to remove the useless interspersed headers from the standard Apollo output file, I used the following C-based code:

Listing B.2: The C-based code which removes the headers from the Apollo output files *BHZ.txt*.

```
1  //#include <TROOT.h>
2  //#include <TStyle.h>
3  //#include <TString.h>
4  //#include <TMath.h>
5  //#include <TLine.h>
6  //#include <TFile.h>
7  //#include <TList.h>
8  //#include <TClassEdit.h>
9  //#include <TObject.h>
10 //#include <TSystem.h>
11 //#include <TSystemDirectory.h>
12 //#include <TClass.h>
13 //#include <TObjString.h>4
14
15 #include <stdlib.h>
16 #include <stdio.h>
17 #include <iostream>
18 #include <iomanip>
19 #include <fstream>
20 #include <sstream>
21 #include <iterator>
22 #include <string>
23 #include <math.h>
24
25 using namespace std;
26
27 int main () {
28   int counts;
29   ifstream file1("BHZ.txt");
30   ofstream file_out("BHZoutput.txt");
31   cout<<"open file"<<endl;
32   char line1[100];
```

```
33    char *line2, *line3;
34    int j=0;
35    while (file1){
36      file1.getline(line1,100);
37      line2=line1;
38
39      //cout<<"line 1= "<<line1<<endl;
40      // cout<<"line 2= "<<line2<<endl;
41      counts=atoi(line2);
42      // cout<<"counts = "<<counts<<endl;
43      if(counts >0 || counts <0){
44        //cout<<"if counts > 0 : line 1"<<line1<<endl;
45        int size =strlen(line1);
46        // cout<<"size = "<<size<<endl;
47         int len=(size)/11;
48         // cout<<"len ="<<len<<endl;
49        //from here numbers string separed by space and comma
50
51        char *parline[5];
52        parline[0]=strtok (line1," ,");
53        //cout<<parline[0]<<endl;
54        if ((atoi(parline[0]))< 20000 && (atoi(parline[0]))> -20000)
55            file_out<<parline[0]<<endl;
56         if(len>1){
57          for(int i=1;i<len;i++){
58            parline[i]=strtok(NULL," ,");
59            //cout<<parline[i]<<endl;
60            if((atoi(parline[i]))< 20000 && (atoi(parline[i]))> -20000)
61              file_out<<parline[i]<<endl;
62          }
63         }
64      }
65    }
66    file_out.close();
67    file1.close();
68    return 0;
69  }
```

At this point the output file contains only the time-series values, listed with the selected sampling frequency. This output can be easily handled with a FFT (Fast Fourier Transform) analysis to obtain the related spectra. As an example I report here the MatLab code that can be used to obtain the PSD in $m^2/s^4/Hz$ and the spectrogram from the ASCII output file:

Listing B.3: Example of MatLab-based code which derive the PSD and the spectrogram along the Z axis from the time-series ASCII output file.

```
1 %spectral analysis
```

```
close all;
clear all;
N = 65536; %num events single spectrum multiple of 2^n
Sys =1.196*10^9; %system sensitivity in m/s
sampl = 40; %sampling rate
data = load ('BHZoutput.txt' , '-ascii');
%%%%%%%%%%%%%%%
BH_ms = (data)./(Sys); %%divide count by system sensitivity in m/s
f=sampl*(1:N)/N;
f_t= transpose(f);
f_plot=sampl*(0:(N/2))/N;
w = hann(N);
wnorm = sum(w.^2)/N;
numspetr=floor(length(BH_ms)/N);
for j=1:numspetr;
BH_mean=0;
for i=1:N; % multiple of 2^n,
BH(i,j)=BH_ms(((j-1)*N+1*i),1);
BH_mean = BH_mean + BH_ms(((j-1)*N+1*i),1)/N;
f_tt(i,j)= f_t(i,1);
end
BH(:,j) = (BH(:,j)-BH_mean).*w;
end
%------FFT-------
TF=fft(BH,N); % FFT from 1 to N events
TF_acc=2*pi*TF.*f_tt;
%------ PSD -------
PS_acc=2*TF_acc.*conj(TF_acc)/(N*sampl*wnorm); % PSD
PS_acc_mean=mean(PS_acc,2);% mean value PS_m
%%%%%%%%%% res
for j=1:numspetr;
for i=1:N;
res(i,j)=((PS_acc(i,j)-PS_acc_mean(i))/PS_acc_mean(i))^2;
end
end
sigma=sum(res)/N; %std deviation
mediana= median(sigma);
s=std(sigma);
%%%------FFT NEW-------
k=1;
for j=1:numspetr;
if sigma(j) < (mediana+1.0*s)
    PS_acc_new(:,k)=PS_acc(:,j);
  k=k+1;
end
end
```

```
48 numspetr_new=k-1;
49 PS_acc_mean_new=mean(PS_acc_new,2);% mean PSD PS_m
50 %%%%%%%%%% res 2
51 for j=1:numspetr_new;
52 for i=1:N;
53 res_new(i,j)=((PS_acc_new(i,j)-PS_acc_mean_new(i))/PS_acc_mean_new(i))^2;
54 end
55 end
56 sigma_new=sum(res_new)/N;
57 mediana_new= median(sigma_new);
58 s_new=std(sigma_new);
59 %%----FFT NEW 2----
60 k=1;
61 for j=1:numspetr_new;
62 if sigma_new(j) < (mediana_new+1.0*s_new)
63   PS_acc_new_new(:,k)=PS_acc_new(:,j);
64         k=k+1;
65 end
66 end
67 PS_acc_mean_new_new=mean(PS_acc_new_new,2);
68 % %---------- SPECTROGRAM ----------
69 t_plot = 0:0.5:numspetr;
70 logPS_acc =log10(PS_acc);
71 figure;
72  fig4=surf(t_plot(1:numspetr),f_plot',logPS_acc(1:(N/2+1),:));
73  shading interp; axis tight; colorbar;%material shiny;
74  title('Spectrogram - Z axis');
75  view(2);
76 % %----------PLOT PSD--------
77 figure;
78  fig8=loglog(f_plot,(PS_acc_mean_new_new(1:(N/2+1))));
79  loglog(f_plot,(PS_acc_mean_new_new(1:(N/2+1))));
80  xlim([0.03 20]);
81  grid on;
82  title('PSD - Z axis');
83  xlabel ('Frequency (Hz)');
84  ylabel ('PSD (m^2/s^4/Hz)');
85  view(2);
```

The sampling frequency of the seismometer was set at 40 Hz, as reported in line 6; the parameter N in line 4 is a multiple of 2^n and defines the points per spectrum, after subtracting, from each of the data streams, the mean value of the time series; the data is filtered with Hann window function (see line 13), in order to get an accurate evaluation of the peak frequencies. Subsequently, the spectra are averaged: in order to study the quasi-stationary local seismic noise, spectra with spurious transient noises (e.g. due to the passage of a vehicle, related to maintenance activities in the tunnel or to small earthquakes) must be

rejected. This selection is performed by calculating the residual of each PSD from the average one (see line 34) [161]:

$$Res_j = \sum_{i=1}^{N} \frac{1}{N} \left(\frac{PSD_i - PSD_i^{mean}}{PSD_i^{mean}} \right)^2 \tag{B.2}$$

where the index i represents the single data point of the j-th spectrum, therefore the sum over the total number of data points N gives the estimation of the deviation of every spectrum from the mean one (PSD^{mean}) in the considered frequency range. The empirical rejection criterion is based on a threshold standard deviation σ, defined from the residues (see line 37): if it is larger than the median value plus $n = 1$ standard deviations (see the code between lines 42-47 and 61-66), data is rejected. This procedure is applied twice, resulting in an average neglected data of $\sim 5\%$.
The analysis presented in chapter 5 was performed with codes analogous to that reported above, in particular I obtained the spectrogram 5.37 with a cyclic code, which initially derived the daily PSD and subsequently made an ensemble of them.

Finally, the meteorological data, used in the comparison with the microseismic data provided by the Trillium 240, was obtained with a routine code, which downloads every day the *Nettuno*-generated [142] output files (one every 12 h, in ASCII format) from the FTP server of the Weather National Center of Italian Air Force (CNMCA). The data is provided in the following format:

Listing B.4: example of meteorological data output generated by the *Nettuno* model and provided by CNMCA, for the two off-shore points of tab. 5.2.

```
1  SANTA_LUCIA_off  40.560   9.9400   0.0000   1.0000   4.0000  ...
2  0.0000   0.33   275.47   4.0400   246.31   5.4000   0.0000  ...
3  3.0000   0.33   233.79   3.7000   238.95   4.7500   0.0000  ...
4  6.0000   0.26   201.31   3.7700   166.03   4.2200   0.0000  ...
5  9.0000   0.39   180.16   2.6700   188.27   2.4200   0.0000  ...
6  12.000   0.63   163.67   3.1100   148.05   3.5600   0.0000  ...
7  SOS_ALINOS_off  40.440  9.9300   0.0000   1.0000   4.0000  ...
8  0.0000   0.37   249.81   3.6400   256.25   5.4100   0.0000  ...
9  3.0000   0.34   226.61   3.4500   250.20   4.4800   0.0000  ...
10 6.0000   0.27   196.66   3.6600   188.12   4.0900   0.0000  ...
11 9.0000   0.40   180.34   2.7100   194.80   2.6900   0.0000  ...
12 12.000   0.61   164.27   3.0400   152.78   3.4700   0.0000  ...
```

where the lines 1 and 7 are the headers (location, coordinates, day, month, year and time), the first column represents the time in hours, starting from 12 AM or PM, while the other columns are described by table 5.1; note that the model provides the periods of the wave (mean value and highest peak in one-dimensional spectrum), the related frequencies are obtained taking their inverse value.

Appendix C

Einstein Telescope specifications

The specifications for the high-frequency (HF) and low-frequency (LF) interferometers of the Einstein Telescope [26] are reported in the following table C.1:

Parameter	ET-HF	ET-LF
Arm length	10 km	10 km
Input power (after IMC)	500 W	3 W
Arm power	3 MW	18 kW
Operating temperature	290 K	10 K
Mirror material	Fused silica (SiO_2)	Silicon (mono-Si)
Mirror diameter/thickness	62 cm/30 cm	62 cm/30 cm
Mirror masses	200 kg	211 kg
Laser wavelength	1064 nm	1550 nm
SR-phase	Tuned (0.0)	Detuned (0.6)
SR transmittance	10%	20%
Quantum noise suppression	10 dB	10 dB
Beam shape	LG_{33}	TEM_{00}
Beam radius	7.25 cm	12 cm
Clipping loss	1.6 ppm	1.6 ppm
Suspension	VIRGO-like Superattenuator	5×10 m
Seismic (for $f > 1$ Hz)	$1 \cdot 10^{-7}$ m/f^2	$5 \cdot 10^{-9} m/f^2$
Gravity gradient subtraction	none	~ 50

Table C.1: Specifications of ET-HF and ET-LF.

Appendix D

NIM modules of the cryogenic accelerometer

The two NIM modules dedicated to the vertical accelerometer presented in chapter 6 are:

1. **Pre-amplification** and resistive trimmer board; the preamplifier circuital scheme is reported in sec. D.2. The trimmer derivation is connected to the output signal in the amplifier scheme, and to the two branches of the secondary LVDT circuit (see fig. 6.7)
2. **Amplifier/Demodulator/Feedback** (ADF) board, of the same kind of those used for the inertial damping control of the inverted pendulum of the superattenuator in Virgo (see sec. 2.3.1); the circuital scheme and the PID feedback transfer function of this board are reported in sec. D.2.

D.1 Pre-amplifier

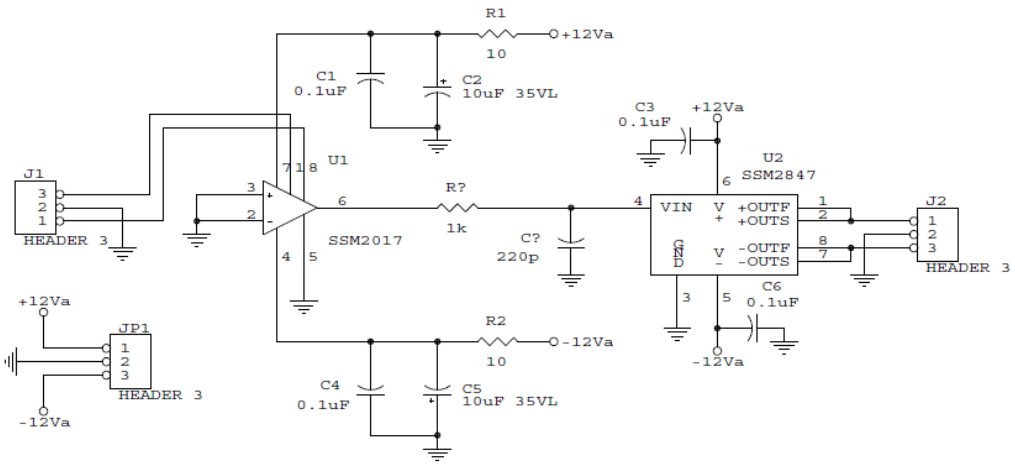

Figure D.1: Circuital scheme of the pre-amplifier used for the cryogenic vertical accelerometer (designed by F. Paoletti, INFN-Pisa/EGO).

D.2 ADF board

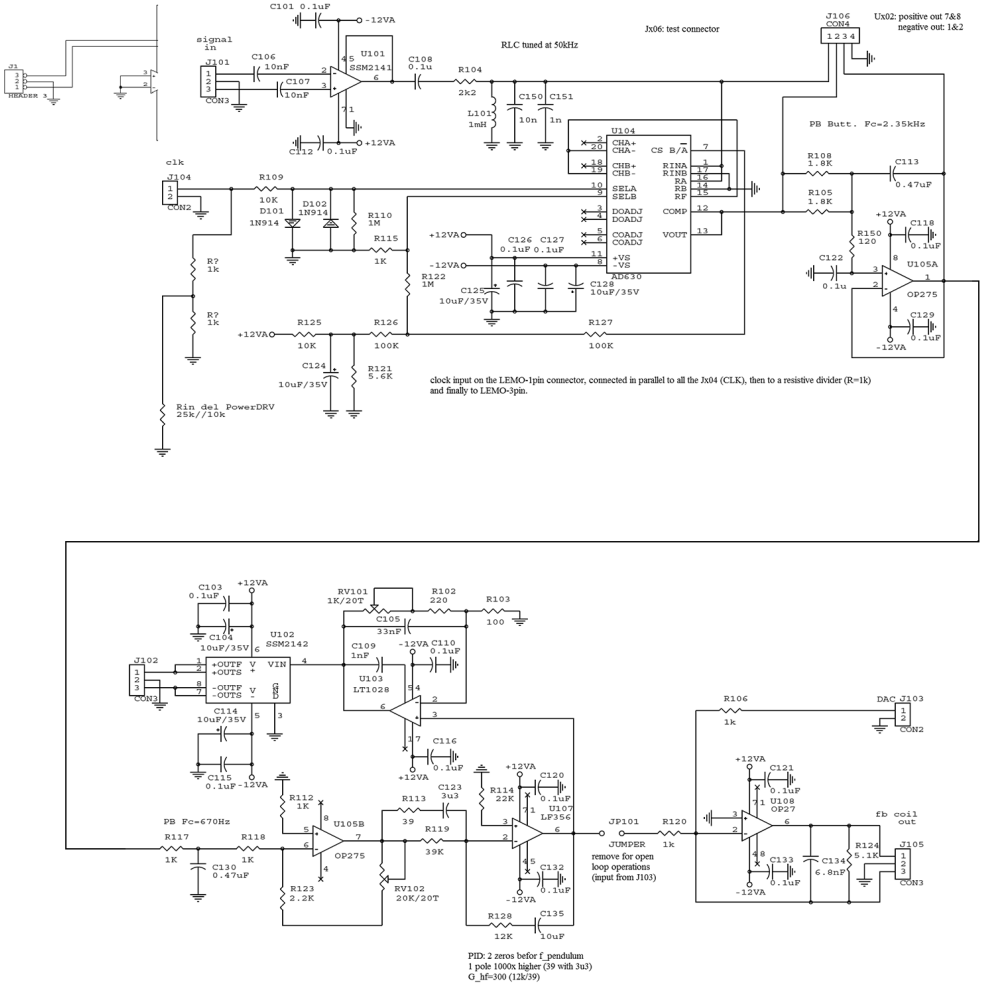

Figure D.2: Circuital scheme of the amplifier/demodulator/PID Feedback board used for the cryogenic vertical accelerometer (designed by F. Paoletti, INFN-Pisa/EGO).

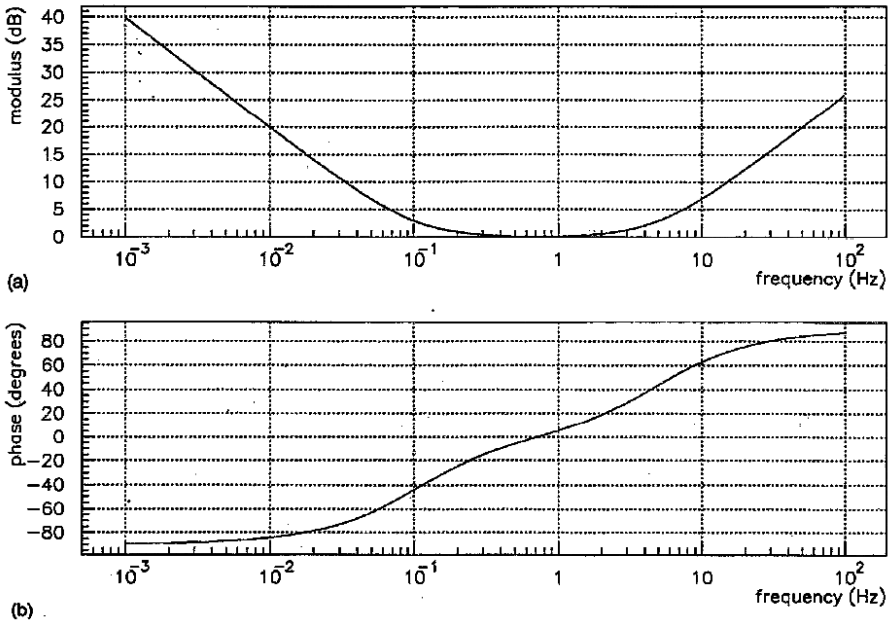

Figure D.3: Transfer function (modulus and phase) of the PID feedback on the ADF board, from [152].

List of Figures

List of Tables

Bibliography

[1] A. Einstein. Die grundlage der allgemeinen relativitätstheorie (the foundation of the general theory of relativity). *Annalen der Physick 354*, 7:769–822, 1916.

[2] B.F. Schutz. *A first course in general relativity.* Cambridge University Press, Cambridge, 1985.

[3] J.B. Camp and N.J. Cornish. Gravitational wave astronomy. *Annual Review Nuclear and Particle Science*, 54:525, 2004.

[4] K.S. Thorne, C.W. Misner, and J.A. Wheeler. *Gravitation.* W. H. Freeman publisher, 1973.

[5] K.S. Thorne. Multipole expansions of gravitational radiation. *Review of Modern Physics*, 52:299, 1980.

[6] B.S. Sathyaprakash and B.F. Schutz. Physics, astrophysics and cosmology with gravitational waves. *Living Reviews in Relativity*, 12(2), 2009. http://www.livingreviews.org/lrr-2009-2.

[7] J. Abadie et al. Predictions for the rates of compact binary coalescences observable by ground-based gravitational-wave detectors. *Classical and Quantum Gravity*, 27(17), 2010. 173001.

[8] B. Allen and J. Romano. Detecting a stochastic background of gravitational radiation: Signal processing strategies and sensitivities. *Physical Review*, 59(D), 1999. 102001.

[9] K.S. Thorne. *300 years of Gravitation.* Cambridge University Press, Cambridge 330, 1987.

[10] R.K. Sachs and A.M. Wolfe. Perturbations of a cosmological model and angular variations of the microwave background. *Astrophysical Journal*, 147:73, 1967.

[11] J.A. Miralles and D. Saez. *Some Topics on General Relativity and Gravitational Radiation.* Atlantica Seguier Frontieres, 1997.

[12] E.W. Kolb and M. Turner. *The early universe.* Addison Wesley, 1990.

[13] P.A.R. Ade et al. Planck 2013 results. xvi. cosmological parameters. arXiv:1303.5076, 2013.

[14] B. Allen. The stochastic gravity-wave background. In *Proceedings of the Les Houches School on Astrophysical Sources of Gravitational Waves*. Cambridge University Press, 1996.

[15] B. Allen. Stochastic gravity-wave background in inflationary-universe models. *Physical Review*, 37(D):2078, 1988.

[16] T. Regimbau. The astrophysical gravitational wave stochastic background. *Research in Astronomy and Astrophysics*, 11(4):369–390, 2011.

[17] M. Shibata and Y. Sekiguchi. Three-dimensional simulations of stellar core collapse in full general relativity: Nonaxisymmetric dynamical instabilities. *Physical Review*, 71(D), 2005.

[18] V. Ferrari et al. Stochastic background of gravitational waves generated by a cosmological population of young rapidy rotating neutron stars. *Monthly Notices of the Royal Astronomical Society*, 303(issue 2):258–264, 2 1990.

[19] E.Howell et al. The gravitational wave background from neutron star birth throughout the cosmos. *Monthly Notices of the Royal Astronomical Society*, 351:1237–1246, 2003.

[20] X. Zhu et al. Observational upper limits on the gravitational wave production of core collapse supernovae. *Monthly Notices of the Royal Astronomical Society*, 409(issue 1):L132, 11 2010.

[21] B.P. Abbott et al. An upper limit on the stochastic gravitational-wave background of cosmological origin. *Nature*, 460(7258):990–994, 8 2009.

[22] L. Blachet. Gravitational radiation from post-newtonian sources and inspiralling compact binaries. *Living review in Relativity*, 9, 2006.

[23] L.P. Grishchuk. *Astrophysics Update*. Springer - Praxis, 2004.

[24] R.N. Lang and S.A. Hughes. Measuring coalescing massive binary black holes with gravitational waves: the impact of spin-induced precession. *Physical Review*, 74(D):12201, 2006.

[25] M. Hannam. Status of black-hole-binary simulations for gravitational-wave detection. *Classical and Quantum Gravity*, 26:114001, 2009.

[26] M. Abernathy et al. *Einstein gravitational wave Telescope Conceptual Design Study*. 2011.

[27] D.K. Belczynski et al. Ic10 x-1/ngc300 x-1: The very immediate progenitors of bh-bh binaries. *The Astrophysical Journal*, 730(2), 2011.

[28] M.A. Gurkan et al. Massive black hole binaries from collisional runaways. *The Astrophysical Journal*, 640(L39), 2006.

[29] N. Ivanova et al. The evolution of binary fractions in globular clusters. *Monthly Notices of the Royal Astronomical Society*, 358:572–584, 2005.

[30] A.G. Riess et al. Observational evidence from supernovae for an accelerating universe and a cosmological constant. *The Astronomical Journal*, 116(3):1009, 1998.

[31] P. Astier et al. The supernova legacy survey: Measurement of omega-m omega-lambda and w from the first year data set. *Astronomy and Astrophysics*, 447:31–48, 2006.

[32] B.F. Schutz. Determining the hubble constant from gravitational wave observations. *Nature*, 323:310–311, 1986.

[33] D.E. Holz and S.A. Hughes. Using gravitational-wave standard sirens. *The Astronomical Journal*, 629:15–22, 2005.

[34] P.C. Peters and J. Mathews. Gravitational radiation from point masses in keplerian orbit. *Physical Review*, 131(Issue 1):435–440, 07 1963.

[35] J.M. Weisberg, D.J. Nice, and H. Taylor. Timing measurements of the relativistic binary pulsar psr b1913+16. *The Astrophysical Journal*, 722:1030–1034, 10 2010.

[36] J. Abadie et al. Beating the spin-down limit on gravitational wave emission from the vela pulsar. *The Astrophysical Journal*, 737:93, 08 2011.

[37] Irwin I. Shapiro. Fourth test of general relativity. *Physical Review Letters*, 13(26):789–791, 1964.

[38] B. Haskell et al. Mountains on neutron stars: accreted versus non-accreted crusts. *Monthly Notices of the Royal Astronomical Society*, 373(Issue 4):1423–1439, 2006.

[39] C.J. Horowitz and K.Kadau. Breaking strain of neutron star crust and gravitational waves. *Physical Review Letters*, 102(19):191102, 5 2009.

[40] B.J. Owen. Maximum elastic deformations of compact stars with exotic equations of state. *Physical Review Letters*, 95(21):211101, 2005.

[41] B. Haskell et al. Are neutron stars with crystalline color-superconducting cores relevant for ligo experiment? *Physical Review Letters*, 99:231101, 2007.

[42] S.K. Lander and D.I. Jones. Magnetic fields in axisymmetric neutron stars. *Monthly Notices of the Royal Astronomical Society*, 395:2162, 2009.

[43] T. Akgun and I. Wasserman. Toroidal magnetic field in type ii superconducting neutron stars. *Monthly Notices of the Royal Astronomical Society*, 383:1551–1580, 2008.

[44] J. Abadie et al. Beating the spin-down limit on gravitational wave emission from the crab pulsar. *The Astrophysical Journal*, 683:L45, 2008.

[45] N. Andersson et al. The superfluid two-stream instability and pulsar glitches. *Monthly Notices of the Royal Astronomical Society*, 354:101, 2002.

[46] B.K. Link and R.I. Epstein. Thermally driven neutron star glitches. *The Astrophysical Journal*, 457:884, 1996.

[47] A.G. Lyne and F. Graham-Smith. *Pulsar Astronomy*. Cambridge University Press, Cambridge, 1988.

[48] M. Shibata et al. The bar-mode instability in differentially rotating neutron stars: simulations in full general relativity. *The Astrophysical Journal*, 542:453–463, 2000.

[49] P.H. Roberts and K. Stewartson. On the stability of a maclaurin spheroid of small viscosity. *The Astrophysical Journal*, 137:777–790, 1963.

[50] S. Chandrasekhar. *Ellipsoidal figures of equilibrium*. Yale University Press, 1969.

[51] J.L. Friedman and B.F. Schutz. Secular instabilities of rotating newtonian stars. *The Astrophysical Journal*, 222:281–296, 5 1978.

[52] D. Lai and S.L. Shapiro. Gravitational radiation from rapidly rotating nascent neutron stars. *The Astrophysical Journal*, 442(1):259–272, 1995.

[53] N. Andersson. A new class of unstable modes of rotating relativistic stars. *The Astrophysical Journal*, 502:708–713, 1998.

[54] L. Lindblom et al. Effect of a neutron-star crust on the r-mode instability. *Physical Review D*, 62:084030, 2000.

[55] B.J. Owen. Gravitational waves from hot young rapidly rotating neutron stars. *Physical Review D*, 58:084020, 1998.

[56] H.T. Janka. Explosion mechanism of core-collapse supernovae. *Annual Review of Nuclear and Particle Science*, 62:407–451, 2012.

[57] C.D. Ott. The gravitational wave signature of core-collapse supernovae. *Classical and Quantum Gravity*, 26:063001, 2009.

[58] R. Salvaterra et al. Grb090423 at a redshift of z = 8.1. *Nature*, 461:1258–1260, 2009.

[59] L. Rezzolla et al. The missing link: merging neutron stars naturally produce jet-like structures and can power short gamma-ray bursts. *The Astrophysical Journal Letters*, 732:L6, 2011.

[60] S.Adrian-Martinez et al. A first search for coincident gravitational waves and high energy neutrinos using ligo, virgo and antares data from 2007. *Journal of Cosmology and Astroparticle Physics*, Issue 06, 2013.

[61] B. Abbott et al. Implications for the origin of grb 070201 from ligo observations. *The Astrophysical Journal*, 681:1419–1428, 2008.

[62] A. Giazzotto et al. Interferometric detection of gravitational waves. *Physics Report C*, 182:365, 1989.

[63] A. Abramovici et al. Ligo: the laser interferometer gravitational-wave observatory. *Science*, 256:325–333, 1992.

[64] R.L. Forward. Wideband laser-interferometer gravitational-radiation experiment. *Physical Review D*, 17(2):379, 1978.

[65] M. Rakhmanov, J.D. Romano, and J.T. Whelan. High-frequency corrections to the detector response and their effect on searches for gravitational waves. *Classical and Quantum Gravity*, 25:184017, 2008.

[66] P.S. Saulson. *Fundamentals of interferometric gravitational wave detectors*. World Scientific Publishing, 1994.

[67] J.-Y. Vinet. *The Virgo Physics Book, Vol. II*. 2004.

[68] B.J. Meers and K.A. Straub. Modulation, signal and quantum noise in interferometers. *Physical Review A*, 44:4693, 1991.

[69] M. Punturo. The virgo sensitivity curve. Technical report, Virgo internal note, 2004. VIR-NOTPER-1390-51.

[70] T. Corbitt and N. Mavalvala. Review: Quantum noise in gravitational-wave interferometers. *Journal of Optics B: Quantum and semiclassical optics*, 6(8):S675, 2004.

[71] J.Y. Vinet et al. Scattered light noise in gravitational wave interferometric detectors: a statistical approach. *Physical Review D*, 56(10):6085–6094, 11 1996.

[72] B. Canuel et al. Diffused light mitigation in virgo and constraints for virgo+ and adv. Technical report, Virgo internal note, 2009. VIR-0792A-09.

[73] T. Accadia et al. Noise from scattered light in virgo's second science run data. *Classical and Quantum Gravity*, 27:194011, 2010.

[74] F. Barone et al. Evaluation of very low pressure acoustic noise in virgo antenna. Technical report, Virgo internal note, 1996. VIR-NOT-NAP-1390-53.

[75] G. Cagnoli et al. Mechanical shot noise induced by creep in suspension devices. *Physics Letters A*, 237(1-2), 1998.

[76] A. Di Cintio et al. Dislocation movement and hysteresis in maraging blades. *Classical and Quantum Gravity*, 26:204018, 2009.

[77] G. Ballardin et al. Measurement of the virgo superattenuator performance for seismic noise suppression. *Review of Scientific Instruments*, 72(9):3643, 2001.

[78] T. Accadia et al. Advanced virgo techincal design report. Technical report, Virgo internal note, 2012. VIR-0128A-12.

[79] A. Bernardini, E. Majorana, P. Puppo, P. Rapagnani, F. Ricci, and G. Testi. Suspension last stages for the mirrors of the virgo interferometric gravitational wave antenna. *Review of Scientific Instruments*, 70:3463, 1999.

[80] A.M. Gretarsson and G.M. Harry. Dissipation of mechanical energy in fused silica fibers. *Review Scientific Instruments*, 70:4081, 1999.

[81] S. Rowan et al. The quality factor of natural fused quartz ribbons over a frequency range from 6 to 160 hz. *Physics Letters A*, 227:153–158, 1997.

[82] R. Day and J. Marque. Central heating radius of curvature correction (chrocc). Technical report, Virgo internal note, 2010. VIR-0695A-10.

[83] S. Hild and G. Losurdo. Advanced virgo design: Comparison of the advanced virgo sensitivity from bench 4 and gwinc (v1). Technical report, Virgo internal note, 2008. VIR-055A-08.

[84] M. Pitkin, S. Reid, and S. Rowan. Gravitational wave detection by interferometry (ground and space). *Living Reviews in Relativity*, 14, 2011. http://www.livingreviews.org/lrr-2011-5.

[85] P. Sutton. S3 performance for the ligo interferometers as measured by sensemonitor. Technical report, LIGO internal note, 2003. LIGO-T030276-00-Z.

[86] P. Hello. Detection rates of inspiralling neutron star - neutron star binaries. In *Proceedings of the 2nd GWDAW*, 1998.

[87] A. Manzotti and A. Dietz. Prospects for early localization of gravitational-wave signals from compact binary coalescences with advanced detectors. arXiv:1202.4031v2.

[88] M. Punturo and K. Somiya. Underground gravitational wave observatories: Kagra and et. *International Journal of Modern Physics*, D(5):1330010, 2013.

[89] R. Lawrence. *Active wavefront correction in laser interferometric gravitational wave detectors*. PhD thesis, MIT, 2003.

[90] T.L. Kelly et al. A differential hartmann wavefront sensor for accurate and precise optical testing. *Applied Optics*, (46):861–866, 2007.

[91] K. Somiya. Detector configuration of kagra - the japanese cryogenic gravitational-wave detector. *Classical and Quantum Gravity*, (29):124007, 2012.

[92] S. Miyoki et al. The clio project. *Classical and Quantum Gravity*, 23:S231, 2006.

[93] J. Mizuno et al. Resonant sideband extraction: a new configuration for interferometric gravitational wave detectors. *Physics Letters A*, 175(5):273–276, 1993.

[94] C. Caparelli et al. Vibration-free cryostat for low-noise applications of a pulse tube cryocooler. *Review of scientific instruments*, 77:095102, 2006.

[95] K. Yamamoto. Current status of cryogenic system of kagra. presented at the Einstein Telescope Meeting - Hannover - Germany, 2012.

[96] O. Jennrich. Lisa technology and instrumentation. *Classical and Quantum Gravity*, 26:153001, 2009.

[97] A. Nishizawa et al. Cosmology with space-based gravitational-wave detectors - dark energy and primordial gravitational waves. arXiv:1110.2865v2, 2011.

[98] P. Bormann. *New manual of seismological observatory practice*. German Research Center for Geosciences, Postdam, 2012.

[99] J. Peterson. *Observations and modeling of seismic background noise*. U.S. Department of interior - Geological Survey - open-file report 93-322, 1993.

[100] K.E. Bullen. *An introduction to the Theory of Seismology*. Cambridge University Press; 4th Ed., 1985.

[101] R.E. Sheriff. *Encyclopedic Dictionary of Applied Geophysics*. Society of Exploration Geophysicists; 4th Ed., 2002.

[102] W. Hassan and P.B. Nagy. Simplified expressions for the displacements and stresses produced by rayleigh wave. *Journal of the Acoustical Society of America*, 104(5):3107–3110, 1998.

[103] D.S. Kim and J.S. Lee. Propagation and attenuation characteristic of various ground vibrations. *Soil Dynamics and Earthquake Engineering*, 19:115–126, 2000.

[104] M.M. Withers et al. High frequency analysis of seismic background noise as a function of wind speed and shallow depth. *Bulletin of the Seismological Society of America*, 86(5):1507–1515, 1996.

[105] R. Schofield et al. Source and propagation of the predominant 1-50 hz seismic signal from off-site at ligo-hanford. presented at the LIGO Scientific Collaboration Meeting - LHO, Hanford, Washington - USA, 2000.

[106] I. Fiori, H. Holloway, and F. Paoletti. Studies of the 1 - 4 hz seism. Technical report, VIRGO internal note, 2003. VIR-NOT-FIR-1390-251.

[107] C. Young. A comparison of the high-frequency ($> 1\ hz$) surface and subsurface noise environment at three sites in united states. *Bulletin of the Seismological Society of America*, 86:1516–1528, 1996.

[108] R.A. Haubrich et al. Comparative spectra of microseisms and swell. *Bulletin of the Seismological Society of America*, 53:27–37, 1963.

[109] I. Young. *Wind Generated Ocean Waves*. Elsevier; 1st Ed., 1999.

[110] M.S. Longuet-Higgins. A theory of the origin of microseisms. *Philosophical transactions of the Royal Society of London*, 243:1–35, 1950.

[111] H. Bradner and J.G. Dodds. Comparative seismic noise on the ocean bottom and on land. *Journal of Geophysical Research*, 69:4339–4348, 1964.

[112] G.V. Latham and A.A. Nowroozi. Waves, weather, and ocean bottom microseisms. *Journal of Geophysical Research*, 73:3945–3956, 1968.

[113] G.H. Sutton and N. Barstow. Ocean-bottom ultralow-frequency (ulf) seismoacoustic ambient noise: 0.002 to 0.4 hz. *Journal of the Acoustical Society of America*, 87:2005–2012, 1990.

[114] G.G. Sorrells et al. Earth motion caused by local atmospheric pressure changes. *Geophysical Journal of the Royal Astronomical Society*, 26:83–98, 1971.

[115] R. Beauduin et al. The effects of the atmospheric pressure changes on seismic signals or how to improve the quality of a station. *Bulletin of the Seismological Society of America*, 86(6):1760–1769, 12 1996.

[116] P.R. Saulson. Terrestrial gravitational noise on a gravitational wave antenna. *Physical Review D*, 30(4):732–736, 1984.

[117] S.A. Hughes and K.S. Thorne. Seismic gravity-gradient noise in interferometric gravitational-wave detectors. *Physical Review D*, 58(12):122002, 1998.

[118] M.G. Beker et al. Improving the sensitivity of future gw observatories in the $1 - 10\ hz$ band: Newtonian and seismic noise. *General Relativity and Gravitation*, 43:623–656, 2011.

[119] K. Pepper, R. Adhikari, and P. Willems. Newtonian noise simulation and suppression for gravitational wave interferometers. Technical report, CalTech, 2007. LIGO-T070192-00-R.

[120] J. Harms et al. Simulation of underground gravity gradients from stochastic seismic fields. *Physics Letters D*, 80(12):122001, 2007.

[121] R. Brown. A brief account of microscopical observations made in the months of june, july and august, 1827, on the particles contained in the pollen of plants and the general existence of active molecules in organic and inorganic bodies. *Philosophical Magazine*, 4:161–173, 1828.

[122] A. Einstein. Über die von der molekularkinetischen theorie der wärme geforderte bewegung von in ruhenden flüssigkeiten suspendierten teilchen (the motion of small particles suspended in liquids at rest, according to theory of heat). *Annalen der Physick*, 322(8):549–560, 1905.

[123] A. Einstein. *Investigations on the Theory of the Brownian movement*. Dover Publications, inc., New York, 1956.

[124] H. Nyquist. Thermal agitation of electric charge in conductors. *Physical Review*, 32:110–113, 1928.

[125] H.B. Callen and R.F. Greene. On the theorem of irreversible thermodynamics. *Physical Review*, 86:702–710, 1952.

[126] R.F. Greene and H.B. Callen. On a theorem of irreversible thermodynamics. ii. *Physical Review*, 88:1387–1391, 1952.

[127] R.F. Greene and H.B. Callen. On the formalism of thermodynamic fluctuation theory. *Physical Review*, 83:1231–1235, 1951.

[128] H.B. Callen, M.L. Barasch, and J.L. Jackson. Statistical mechanics of irreversibility. *Physical Review*, 88:1382–1386, 1952.

[129] P.R. Saulson. Thermal noise in mechanical experiments. *Physical Review D*, 42:2437–2445, 1990.

[130] L.D. Landau and E.M. Lifshitz. *Theory of elasticity*. Addison-Wesley Pub. Co., 1959.

[131] Y.L. Huang and P.R. Saulson. Dissipation mechanisms in pendulums and their implications for gravitational wave interferometers. *Review of Scientific Instruments*, 69:544, 1997.

[132] C. Zener. Internal friction in solids, i. theory of internal friction in reeds. *Physical Review*, 52:230–235, 1937.

[133] C. Zener. Internal friction in solids, ii. general theory of thermoelastic internal friction. *Physical Review*, 53:90–99, 1938.

[134] G.I. Gonzalez and P.R. Saulson. Brownian motion of a mass suspended by an anelastic wire. *Journal of Acoustic Society of America*, 96:207–212, 1994.

[135] V.B. Braginsky et al. Thermodynamical fluctuations and photo-thermal shot noise in gravitational wave antennae. *Physics Letters A*, 264:1–10, 1999.

[136] W. Winkler et al. Heating by optical absorption and the performance of interferometric gravitational-wave detectors. *Physical Review A*, 44:7022–7036, 1991.

[137] J.A. McCaulley et al. Temperature dependence of the near-infrared refractive index of silicon, gallium arsenide, and indium phosphide. *Physical Review B*, 49(11):7408–7417, 1994.

[138] F. Basti et al. A cryogenic payload for the 3rd generation of gravitational wave interferometers. *Astroparticle Physics*, 35(2):67–75, 2011.

[139] I. Troen and E.L. Petersen. *European Wind Atlas*. Risø National Laboratory, Roskilde, 1989.

[140] F. Barone and G. Giordano. Low frequency folded pendulum with high mechanical quality factor, and seismic sensor utilizing such a folded pendulum. International application published under the patent cooperation treaty (PCT) WO 2011/004413 A3.

[141] D.E. McNamara and R.P. Buland. Ambient noise levels in the continental united states. *Bulletin of the Seismological Society of America*, 94(4):1517–1527, 8 2004.

[142] C. De Simone et al. Il sistema di previsione del mare "nettuno" (the sea forecasting system "nettuno"). *Rivista di meteorologia aeronautica*, 70:25–36, 2010.

[143] S. Hasselmann et al. The wam model: a third generation ocean wave prediction model. *Journal of Physical Oceanography*, 18:1775–1810, 1998.

[144] N. Booij et al. A third-generation model for coastal regions. part 1: Model description and validation. *Journal of Geophysical Research*, 104:7649–7666, 1999.

[145] F. Ardhuin et al. Comparison of wind and wave measurements and models in the western mediterranean sea. *Ocean Engineering*, 34:526–541, 2007.

[146] Y. Gusdal et al. Validation of the operational wave model wam at met.no. Technical report, Norwegian Meteorological Institute - Oceanography, 2011. no. 14/2011 ISSN: 1503-8025.

[147] F. Fidecaro et al. Caratterizzazione del clima acustico e vibrazionale dell'interferometro per onde gravitazionali virgo (characterization of the acoustic and vibrational noise in the interferometer for gravitational waves virgo). Technical report, Virgo internal note, 2012. VIR-0264A-12.

[148] F. Acernese et al. The commissioning of the central interferometer of the virgo gravitational wave detector. *Astroparticle Physics*, 20:629–640, 2004.

[149] J. Harms et al. Characterization of the seismic environment at the sanford underground laboratory, south dakota. *Classical and Quantum Gravity*, 27:225011, 2010.

[150] F. Frasconi, E. Majorana, L. Naticchioni, F. Paoletti, and M. Perciballi. A vertical accelerometer for cryogenics implementation in third-generation gravitational-wave detectors. *Measurement Science and Technology*, 25, 2014. Accepted by the journal, to be published.

[151] National Instruments. *LabVIEW user manual*, 2003. http://www.ni.com/pdf/manuals/320999e.pdf.

[152] S. Braccini et al. Low noise wideband accelerometer using an inductive displacement sensor. *Review of Scientific Instruments*, 66:2672, 1995.

[153] F. Acernese et al. Measurements of superattenuator seismic isolation by virgo interferometer. *Astroparticle Physics*, 33:182–189, 2010.

[154] L.B.J. LaCoste. A simplification in the conditions for the zero-length-spring seismograph. *Bulletin of the Seismological Society of America*, 25(2):176–179, 1935.

[155] H. Tariq et al. The linear variable differential transformer (lvdt) position sensor for gravitational wave interferometer low-frequency controls. *Nuclear Instruments and Methods in Physics Research A*, 489:570–576, 2002.

[156] G. Durin. The barkhausen effect: new perspectives for an old problem. In C. Claeys and E. Simoen, editors, *4th International Conference on Noise in Physical Systems and 1/f Fluctuations*. World Scientific, Singapore, 1997.

[157] S. Koike. Design of kagra cryostat. Technical report, KAGRA internal note, 2013. JGW-G1201971-v1.

[158] D. Chen et al. Measurement of the vibration in the radiation shield of kagra. In *20th International Conference on General Relativity and Gravitation, and 10th Amaldi Conference on Gravitational Waves*. Warsaw, 2013.

[159] N. Wiener. Generalized harmonic analysis. *Acta Mathematica*, 55:117–258, 1930.

[160] A. Khintchine. Korrelationshteorie der stationären stochastichen prozesse (correlation theory of stationary stochastic processes). *Mathematische Annalen*, 109(1):604–615, 1934.

[161] A. di Cintio et al. Characterization of four italian seismic fields. Technical report, ET internal note, 2010. ET-0094A-10.

Acknowledgment

First of all I want to thank Fulvio Ricci, Ettore Majorana and Piero Rapagnani, with whom I conceived the the work presented in this thesis, and for their help during the several experimental activities. I also want to thank all the staff of the gravitational wave research group G23 at physics dept. of Sapienza - University of Rome for the helpful interaction in the various topics addressed in this thesis, and Maurizio Perciballi for his technical and "photographic" support.
I also thank Fausto Acernese and Valeria Malvezzi for their help in the experimental setup realization in the Sos Enattos former mine and in the following data analysis; I am grateful to the staff members of the mine for their crucial technical support, in particular to G. Loddo and P. Calia of IGEA S.p.A.; I also have to thank the Italian *Servizio Meteorologico dell'Aeronautica Militare*, in particular Col. M. Ferri, T. Col. R. Tajani and Gen. P. Pagano for providing the meteorological data analyzed in this work and for their support to this activity.
The development of the accelerometer presented in sec. 6 and the measurements within the KAGRA collaboration were supported by the Istituto Nazionale di Fisica Nucleare and the EU ELiTES project. For this part of my experimental work I want to thank Franco Frasconi and Federico Paoletti for their kindly assistance at EGO-Virgo; V. Lollo and P. Chimenti for the vacuum compatibility tests performed at LNF-INFN; K. Yamamoto and D. Chen from ICRR of the University of Tokyo and N. Kimura from KEK for providing the opportunity of using the sensor developed in this work during the vacuum and cryogenic validation tests of the cryostats that will be used in the gravitational wave detector KAGRA, and for their assistance during the related experimental activities.

what an astrophysicist actually does - Sos Enattos site, 2012.